LOCAL PEAK PRESSURES AND WIND FORCES ACTING ON SUPER-TALL BUILDINGS WITH VARIOUS CONFIGURATIONS

A dissertation by

Eswara Kumar Bandi

Submitted to the Graduate School of Engineering

Tokyo Polytechnic University

In Partial fulfillment of the requirements

for the Degree of

DOCTOR OF PHILOSOPHY

Under the Supervision of

Prof. Yukio Tamura, Director

Graduate School of Engineering

Tokyo Polytechnic University

Japan

September 2013

ABSTRACT

Local peak pressures and wind forces acting on super-tall buildings with various configurations

Construction of tall buildings is becoming more widespread in urban areas. Wind-induced load is an important and essential design issue for tall buildings, cable suspension bridges, electricity transmission towers, telecommunication towers and chimneys. For real structures, the flow field is very complex in nature; hence, experimental studies are mandatory. However, they pose design challenges for structural engineers, particularly when building heights increase. The variety of heights and shapes of new building designs pose various design problems for architects, engineers and developers. Their design needs a comprehensive study and understanding. This dissertation aims to study local peak pressures on claddings and aerodynamic characteristics of super-tall buildings with various configurations. In particular, it concentrates on the effects of corner modifications; tapering; twisting angle of helical models; combination of twisting, corner modification and taper; and increasing numbers of surfaces (various polygonal shapes) on local peak pressures, wind forces and responses.

The present trend in design of tall buildings is toward unconventional shapes. Most previous researches have provided information on pressure distributions on low-rise buildings and aerodynamic force characteristics on tall buildings with basic shapes. However, most have focused on one aerodynamic modification, such as corner-modifications and tapering. Although there have been some reports on different aerodynamic modifications, none have comprehensively investigated aerodynamic characteristics of various types of super-tall buildings with various configurations. Systematic wind tunnel experiments were conducted on pressure models with various cross-sectional shapes for urban (power law index, α=0.27) flow. The parameters used in

these experiments are mainly twisting angle, corner modifications, tapering and combinations of the above parameters. Finally, most extensive information on local peak pressures and aerodynamic force characteristics of the above models are proposed.

Eswara Kumar Bandi, Ph.D

Tokyo Polytechnic University, 2013

ACKNOWLEDGEMENTS

First of all, I would like to express my sincere gratitude to my supervisor, Prof.Yukio Tamura, who provided me the opportunity to study in Japan and continuous support, patience and encouragement during my study, although he is always busy as he is very famous professor in the world in the field of wind engineering. His patience and considerate nature made him accessible whenever I needed his assistance. I made this study successful because he served as not only an academic supervisor but also a mentor for inspiring young generations.

I am grateful to Prof. Akihito Yoshida for his support in conducting wind tunnel experiments and fruitful discussions during this study. I would like to thank other members of the doctoral committee Prof. Kawai, Prof. Masahiro Matsui, Prof. Ryuichiro Yoshie and Prof. Masaaki Ohba and for their suggestions and comments for improving this dissertation.

Special thanks goes to my colleagues, GCOE researchers, Dr.Yong Chul Kim and students at Wind Engineering Research Center of Tokyo Polytechnic University, for the cooperation during my research, for their help in everyday work and friendship, and GCOE secretaries Ms. Aya Saito and Ms. Kazuko Ando, for their kind help and assistance. Also, my special thanks goes to GCOE Associate professor Dr. Rei Okada who supported me in all aspects during my study.

The financial support, provided by the Ministry of Education, Culture, Sports, Science and Technology, Japan, through the Global Center of Excellence Program (GCOE), 2008-2013, which is gratefully acknowledged.

Last but not least, I would like to thank my father, mother and brother, and all my family members who gave their love and support throughout my life; and my wife, Madhavi Latha, who stands behind me and support me during my study and making our life happy and joyful.

Eswara Kumar Bandi

DEDICATION

– To all my family members

CONTENTS

CHAPTER I INTRODUCTION……..……..1

1.1 Literature review……..3

1.1.1 Wind pressure characteristics…….……..3

1.1.2 Wind force characteristics……..……..4

1.2 Objective of this study…….8

1.3 Organization of the chapters…….9

1.4 References……10

CHAPTER II EFFECTS OF VARIOUS CROSS-SECTIONAL SHAPE MODIFICATIONS ON LOCAL PEAK PRESSURES…….12

2.1 Experimental set-up……..……...13

2.1.1 Wind speed and turbulence intensity profiles ……..……...13

2.1.2 Description about the experimental models…….……...14

2.2 Definition and terminology……..……..18

2.3 Effect of corner modifications …….……..19

2.3.1 Largest negative local peak pressures on the surfaces…….…….……..20

2.3.2 Largest positive local peak pressures on the surfaces……..……..20

2.3.3 Effect of corner modification on local peak pressures…….……..21

2.3.4 Variation of largest negative peak pressures with wind direction (θ) ……...23

2.4 Effect of Tapering ……...……..25

2.4.1 Largest negative local peak pressures on the surfaces…….……..25

2.4.2 Largest positive local peak pressures on the surfaces……..……..26

2.4.3 Variation of largest negative peak pressures with wind direction (θ) …….……..26

2.5 Effects of number of surfaces ……..…..27

2.5.1 Largest negative local peak pressures on the surfaces……..……..27

2.5.2 Largest positive local peak pressures on the surfaces……..…….…..28

2.5.3 Variation of largest negative peak pressures with wind direction (θ) ….……..29

2.6 Summary……...……..30

CHAPTER III EFFECTS OF TWISTING ANGLE OF HELICAL MODELS ON LOCAL PEAK PRESSURES……...…33
3.1 Experimental models……..34
3.2 Largest negative local peak pressures on the surfaces…….……..34
3.3 Largest positive local peak pressures on the surfaces……..……..35
3.4 Variation of largest negative peak pressures with wind direction (θ) …….……..38
3.5 Summary……..…..39
CHAPTER IV COMBINED EFFECT OF CORNER MODIFICATION, TAPERING AND TWISTING ON LOCAL PEAK PRESSURES……...…41
4.1 Experimental models……..41
4.2 Largest negative local peak pressures on the surfaces…….……..42
4.3 Largest positive local peak pressures on the surfaces……..……..43
4.4 Variation of largest negative peak pressures with wind direction (θ) …….……..44
4.5 Maximum of largest negative peak pressure coefficients ($\hat{C}_{p,\max}$) for all the models……..46
4.6 Summary……..……..49
4.7 References……..52
CHAPTER V EFFECTS OF POLYGONAL SHPAES ON WIND FORCES……..…55
5.1 Overturning moment coefficients (o.t.m) …….…..56
5.1.1 Effects of wind directions on o.t.m coefficients……..…..56
5.2 Vertical variations of local wind forces for the specified wind directions……..….59
5.2.1 Mean local wind force coefficients……..…..60
5.2.2 Fluctuating local wind force coefficients…….……..61
5.2.3 Maximum mean and fluctuating OTM coefficients in along-wind and crosswind directions……..……..63
5.2.4 Maximum mean Vs Fluctuating OTM coefficients in along-wind and crosswind directions……...……..64
5.3 Effect of various building plan shapes on Power spectrum of wind forces…….……..64
5.3.1 Power spectral densities in along-wind and crosswind directions……..64
5.3.2 Power spectral densities of crosswind local wind force coefficients……..66
5.3.3 Maximum spectral values for 500-yr and 1-yr return periods …….……..68

5.3.4 Vertical variation of peak local reduced frequencies of crosswind force coefficients...70
5.4 Summary.....72

CHAPTER VI EFFECTS OF TWISTING ANGLE OF HELICAL MODELS ON WIND FORCES.....74
6.1 Overturning moment coefficients (o.t.m) 75
6.1.1 Effects of wind directions on o.t.m coefficients.....75
6.2 Vertical variations of local wind forces for the specified wind directions.....76
6.2.1 Mean local wind force coefficients.....77
6.2.2 Fluctuating local wind force coefficients.....78
6.2.3 Maximum mean and fluctuating OTM coefficients in along-wind and crosswind directions.....79
6.2.4 Relation between the overturning moment coefficients 80
6.3 Effect of various building plan shapes on Power spectrum of wind forces.....81
6.3.1 Power spectral densities in along-wind and crosswind directions.....81
6.3.2 Power spectral densities of crosswind local wind force coefficients.....83
6.3.3 Maximum spectral values for 500-yr and 1-yr return periods 84
6.3.4 Variation of peak crosswind spectral values.....86
6.3.5 Variation of Bandwidth of a crosswind power spectral densities.....86
6.3.6 Vertical variation of peak local reduced frequencies of crosswind force coefficients.....87
6.4 Comparison of maximum o.t.m coefficients.....88
6.5 Summary.....91
6.6 References.....91

CHAPTER VII WIND FORCE COMBINATIONS OF WIND FORCE COMPONENTS OF POLYGON MODELS.....94
7.1 Wind force combination of straight models with various cross-sections.....95
7.1.1 Trajectories of o.t.m coefficients.....96
7.1.2 Correlation and absolute value correlations 99
7.1.3 Simultaneous wind loadings.....101

7.2 Wind force combination of helical models with various cross-sections ……..…111
7.2.1 Trajectories of wind force coefficients…….111
7.2.2 Cross correlations of wind force coefficients……..…….....114
7.2.3 Simultaneous wind loadings……....…116
7.3 Internal forces and peak normal stresses in columns……...…….……...…123
7.3.1 Effect of damping ratio on internal forces of columns…….125
7.3.2 Effect of wind direction on peak tensile stress of columns for ALL loading conditions and damping ratio, ζ=1%…….125
7.4 Summary…….…….128

CHAPTER VIII CONCLUSIONS……...……...130
8.1 Chapter II ……..……131
8.2 Chapter III ……..……131
8.3 Chapter IV ……..……132
8.4 Chapter V ……..…….……133
8.5 Chapter VI ……..……134
8.6 Chapter VII ……...……134

APPENDIX COMPARISON OF PEAK PRESSURES AND WID FORCES…….…...136

LIST OF TABLES

Table 2.1 Configurations of the models..... 17
Table 2.2 The Colored surfaces for the distribution of peak pressures.....17
Table 2.3 Arrangement of pressure taps and coordinate system.....18
Table 2.4 Largest negative peak pressures among all wind directions and all pressure taps – Occurrence height and wind direction.....31
Table 2.5 Largest positive peak pressures among all wind directions and all pressure taps – Occurrence height and wind direction.....32
Table 3.1 Configurations of helical models 34
Table 3.2 Largest negative peak pressures among all wind directions and all pressure taps – Occurrence height and wind direction.....40
Table 3.3 Largest positive peak pressures among all wind directions and all pressure taps – Occurrence height and wind direction.....40
Table 4.1 Composite models.....42
Table 4.2 Largest negative peak pressures among all wind directions and all pressure taps – Occurrence height and wind.....51
Table 4.3 Largest positive peak pressures among all wind directions and all pressure taps – Occurrence height and wind direction.....51
Table 5.1 Configurations of straight polygonal models.....55
Table 5.2 Configurations of corner modification models.....56
Table 6.1 Configurations of helical models.....74
Table 7.1 Effect of various loading conditions on peak tensile stress for quasi-static…….....126
Table 7.2 Effect of various loading conditions on peak tensile stress for ζ=1% …….....127
Table 7.1 Ratio of wind force coefficients to their maximum values when *CL*, *CD* and *CMT* are maximum – Helical models.....128

LIST OF FIGURES

Figure 1.1 Tall buildings in the urban world 2
Figure 1.2 Model shapes and wind direction (Kanda et.al, 1992) 5
Figure 1.3 comparison of maximum mean overturning moment coefficients 5
Figure 1.4 comparisons of maximum fluctuating overturning moment coefficients 6
Figure 1.5 Effect of twist angle for the helical square models. (a) Maximum mean overturning moment coefficients, (b) maximum fluctuating overturning moment coefficients, (c) peak values of power spectral densities and (d) bandwidths of power spectral densities (Tanaka et.al, 2012) 7
Figure 1.6 Schematic diagram of the thesis. 9
Figure 2.1 Roughness arrangement for Urban flow condition 13
Figure 2.2 Profile of mean wind speed and turbulence intensity 14
Figure 2.3 Largest negative peak pressure coefficients for Square and Triangular models 20
Figure 2.4 Largest positive peak pressure coefficients for Square and Triangular models 21
Figure 2.5 Effect of corner modification on largest negative peak pressure coefficients for Triangular corner modification models 22
Figure 2.6 Effect of corner modification on largest negative peak pressure coefficients for Square corner modification models 23
Figure 2.7 Variation of largest negative peak pressure coefficients with wind direction (θ) for Triangular corner modification models 24
Figure 2.8 Variation of largest negative peak pressure coefficients with wind direction (θ) for Square corner modification models 24
Figure 2.9(a) Distribution of largest negative peak pressure coefficients for Taper models 25
Figure 2.9(b) Distribution of largest positive peak pressure coefficients for Taper models 25
Figure 2.10 Variation of largest negative peak pressure coefficients with wind direction (θ) for Taper models 26
Figure 2.11 Largest negative peak pressure coefficients for Polygon models 28
Figure 2.12 Largest positive peak pressure coefficients for Polygon models 29
Figure 2.13 Variation of largest negative peak pressure coefficients with wind direction (θ) for Polygon models 30
Figure 3.1 Largest positive peak pressure coefficients for Triangular helical models 35
Figure 3.2 Largest negative peak pressure coefficients for Triangular helical models 35
Figure 3.3 Largest positive peak pressure coefficients for Square helical models 36
Figure 3.4 Largest negative peak pressure coefficients for Square helical models 36
Figure 3.5 Largest negative peak pressure coefficients for polygonal helical models 37
Figure 3.6 Largest positive peak pressure coefficients for polygonal helical models 37
Figure 3.7 Variation of largest negative peak pressure coefficients with wind direction (θ) for Triangular helical models 38
Figure 3.8 Variation of largest negative peak pressure coefficients with wind direction (θ) for Square helical models 39
Figure 3.9 Variation of largest negative peak pressure coefficients with wind direction (θ) for Polygonal helical models 39
Figure 4.1 Largest negative peak pressure coefficients for Combination models 43
Figure 4.2 Largest positive peak pressure coefficients for Combination models 44

Figure 4.3 Variation of largest negative peak pressure coefficients with wind direction (θ) for Square and Sq-180^{o}Hel &Corner cut model 45
Figure 4.4 Variation of largest negative peak pressure coefficients with wind direction (θ) for the Sq-Tapered and Sq-Tapered & 180^{o}Hel model 45
Figure 4.5 Variation of largest negative peak pressure coefficients with wind direction (θ) for the Sq-Tapered and Sq-Tapered & 360^{o}Hel & Corner cut model 46
Figure 4.6 Variation of largest negative peak pressure coefficients with wind direction (θ) for the Sq-Setback and Sq-Setback & 45^o Rotate 46
Figure 4.7 Comparison of maximum largest negative peak pressures ($\hat{C}_{p,\max}$) 49
Figure 5.1 Variation of mean overturning moment coefficients of polygonal models 57
Figure 5.2 Variation of mean overturning moment coefficients of corner modification models . 58
Figure 5.3 Variation of fluctuating overturning moment coefficients of polygonal models 59
Figure 5.4 Variation of fluctuating overturning moment coefficients of corner modification models 59
Figure 5.5 Vertical variation of mean local wind force coefficients for polygonal models 61
Figure 5.6 Vertical variation of mean local wind force coefficients for corner modification models 61
Figure 5.7 Vertical variation of fluctuating local wind force coefficients for the polygonal models 62
Figure 5.8 Vertical variation of fluctuating local wind force coefficients for the corner modification models 62
Figure 5.9 Maximum mean and fluctuating overturning moment coefficients in along-wind and cross wind directions 63
Figure 5.10 Maximum mean Vs Fluctuating o.t.m coefficients in along-wind and crosswind directions 64
Figure 5.11. Power spectral densities of crosswind OTM coefficients 65
Figure 5.12. Power spectral densities of along-wind o.t.m coefficients 66
Figure 5.13 Power spectral densities of crosswind local wind force coefficients 68
Figure 5.14 Peak spectral values for 500-year and 1-year return periods 69
Figure 5.15 Variation of Peak spectral values of Crosswind OTM coefficients 70
Figure 5.16 Variation of Bandwidth of PSD of Crosswind OTM coefficients with number of side surfaces 70
Figure 5.17 Variation of Bandwidth of PSD of Crosswind OTM coefficients for Triangular cross-sectional models 71
Figure 5.18 Vertical variation of peak local reduced frequencies of crosswind force coefficients 72
Figure 6.1 Variation of mean overturning moment coefficients for polygonal helical models 75
Figure 6.2 Variation of fluctuating overturning moment coefficients for polygonal helical models 76
Figure 6.3 Vertical variation of mean local wind force coefficients for polygonal helical models 78
Figure 6.4 Vertical variation of fluctuating local wind force coefficients for polygonal helical models 78

Figure 6.5 Maximum mean and fluctuating overturning moment coefficients in along-wind and cross wind directions..... 80
Figure 6.6 Maximum mean Vs Fluctuating o.t.m coefficients in along-wind and crosswind directions..... 81
Figure 6.7 Power spectral densities of crosswind OTM coefficients 82
Figure 6.8 Power spectral densities of along-wind OTM coefficients 82
Figure 6.9 Power spectral densities of crosswind local wind force coefficients 84
Figure 6.10 Peak spectral values for 500-year and 1-year return periods 85
Figure 6.11 Variation of Peak spectral values of Crosswind OTM coefficients 86
Figure 6.12 Variation of Bandwidth of PSD of Crosswind OTM coefficients with number of side surfaces and 180^o twist angle. 87
Figure 6.13 Variation of Bandwidth of PSD of Crosswind OTM coefficients with twisting angle of helical models. 87
Figure 6.14 Vertical variation of peak local reduced frequencies of crosswind force coefficients 88
Figure 6.15 Maximum mean OTM coefficients (Tanaka et.al, 2012) 90
Figure 6.16 Maximum fluctuating OTM coefficients (Tanaka et.al, 2012) 90
Figure 7.1 Trajectory of overturning moment coefficients for Triangular model at 0^o wind direction 96
Figure 7.2 Trajectory of overturning moment coefficients for Tri-Corner cut model at 0^o wind direction 97
Figure 7.3 Trajectory of overturning moment coefficients for Clover model at 0^o wind direction 97
Figure 7.4 Trajectory of overturning moment coefficients for Square model at 0^o wind direction 97
Figure 7.5 Trajectory of overturning moment coefficients for Pentagon model at 0^o wind direction 97
Figure 7.6 Trajectory of overturning moment coefficients for Hexagon model at 0^o wind direction 98
Figure 7.7 Trajectory of overturning moment coefficients for Octagon model at 0^o wind direction 98
Figure 7.8 Trajectory of overturning moment coefficients for Dodecagon model at 0^o wind direction 98
Figure 7.9 Trajectory of overturning moment coefficients for Circular model at 0^o wind direction 98
Figure 7.10 Correlation coefficient (Solid line) and absolute value correlation (dotted line) for Triangular model at 0^o wind direction 99
Figure 7.11 Correlation coefficient (Solid line) and absolute value correlation (dotted line) for Tri-Corner cut model at 0^o wind direction..... 99
Figure 7.12 Correlation coefficient (Solid line) and absolute value correlation (dotted line) for Clover model at 0^o wind direction 100
Figure 7.13 Correlation coefficient (Solid line) and absolute value correlation (dotted line) for Square model at 0^o wind direction..... 100
Figure 7.14 Correlation coefficient (Solid line) and absolute value correlation (dotted line) for Pentagon model at 0^o wind direction 100

Figure 7.15 Correlation coefficient (Solid line) and absolute value correlation (dotted line) for Hexagon model at 0^o wind direction 100
Figure 7.16 Correlation coefficient (Solid line) and absolute value correlation (dotted line) for Octagon model at 0^o wind direction 101
Figure 7.17 Correlation coefficient (Solid line) and absolute value correlation (dotted line) for Dodecagon model at 0^o wind direction 101
Figure 7.18 Correlation coefficient (Solid line) and absolute value correlation (dotted line) for Circular model at 0^o wind direction 101
Figure 7.19 Ratio of *CL* and *CMT* accompanied by maximum along-wind force *CD*max to their maximum values *CL*max and *CMT*max for Triangular model (a) *CL* (*CD*max)/*C*Lmax, and (b) *CMT* (*CD*max)/*CMT*max. 102
Figure 7.20 Ratio of *CD* and *CMT* accompanied by maximum crosswind force *CL*max to their maximum values *CD*max and *CMT*max for Triangular model (a) *CD* (*C*Lmax)/*CD*max, and (b) *CMT* (*CL*max)/*CMT*max. 103
Figure 7.21 Ratio of *CD* and *CL* accompanied by maximum torsional moment *CMT*max to their maximum values *CD*max and *CL*max for Triangular model (a) *CD* (*C*MTmax)/*CD*max, and (b) *CL* (*CMT*max)/*CL*max. 103
Figure 7.22 Ratio of *CL* and *CMT* accompanied by maximum along-wind force *CD*max to their maximum values *CL*max and *CMT*max for Tri-Croner cut model (a) *CL* (*CD*max)/*C*Lmax, and (b) *CMT* (*CD*max)/*CMT*max 103
Figure 7.23 Ratio of *CD* and *CMT* accompanied by maximum crosswind force *CL*max to their maximum values *CD*max and *CMT*max for Tri-Croner cut model (a) *CD* (*C*Lmax)/*CD*max, and (b) *CMT* (*CL*max)/*CMT*max. 104
Figure 7.24 Ratio of *CD* and *CL* accompanied by maximum torsional moment *CMT*max to their maximum values *CD*max and *CL*max for Tri-Croner cut model (a) *CD* (*C*MTmax)/*CD*max, and (b) *CL* (*CMT*max)/*CL*max 104
Figure 7.25 Ratio of *CL* and *CMT* accompanied by maximum along-wind force *CD*max to their maximum values *CL*max and *CMT*max for Clover model (a) *CL* (*CD*max)/*C*Lmax, and (b) *CMT* (*CD*max)/*CMT*max. 104
Figure 7.26 Ratio of *CD* and *CMT* accompanied by maximum crosswind force *CL*max to their maximum values *CD*max and *CMT*max for Clover model (a) *CD* (*C*Lmax)/*CD*max, and (b) *CMT* (*CL*max)/*CMT*max 105
Figure 7.27 Ratio of *CD* and *CL* accompanied by maximum torsional moment *CMT*max to their maximum values *CD*max and *CL*max for Clover model (a) *CD* (*C*MTmax)/*CD*max, and (b) *CL* (*CMT*max)/*CL*max. 105
Figure 7.28 Ratio of *CL* and *CMT* accompanied by maximum along-wind force *CD*max to their maximum values *CL*max and *CMT*max for Square model (a) *CL* (*CD*max)/*C*Lmax, and (b) *CMT* (*CD*max)/*CMT*max. 105
Figure 7.29 Ratio of *CD* and *CMT* accompanied by maximum crosswind force *CL*max to their maximum values *CD*max and *CMT*max for Square model (a) *CD* (*C*Lmax)/*CD*max, and (b) *CMT* (*CL*max)/*CMT*max 106
Figure 7.30 Ratio of *CD* and *CL* accompanied by maximum torsional moment *CMT*max to their maximum values *CD*max and *CL*max for Square model (a) *CD* (*C*MTmax)/*CD*max, and (b) *CL* (*CMT*max)/*CL*max. 106

Figure 7.31 Ratio of *CL* and *CMT* accompanied by maximum along-wind force *CD*max to their maximum values *CL*max and *CMT*max for Pentagon model (a) *CL* (*CD*max)/*C*Lmax, and (b) *CMT* (*CD*max)/*CMT*max. 106
Figure 7.32 Ratio of *CD* and *CMT* accompanied by maximum crosswind force *CL*max to their maximum values *CD*max and *CMT*max for Pentagon model (a) *CD* (*C*Lmax)/*CD*max, and (b) *CMT* (*CL*max)/*CMT*max. 107
Figure 7.33 Ratio of *CD* and *CL* accompanied by maximum torsional moment *CMT*max to their maximum values *CD*max and *CL*max for Pentagon model (a) *CD* (*C*MTmax)/*CD*max, and (b) *CL* (*CMT*max)/*CL*max. 107
Figure 7.34 Ratio of *CL* and *CMT* accompanied by maximum along-wind force *CD*max to their maximum values *CL*max and *CMT*max for Hexagon model (a) *CL* (*CD*max)/*C*Lmax, and (b) *CMT* (*CD*max)/*CMT*max. 107
Figure 7.35 Ratio of *CD* and *CMT* accompanied by maximum crosswind force *CL*max to their maximum values *CD*max and *CMT*max for Hexagon model (a) *CD* (*C*Lmax)/*CD*max, and (b) *CMT* (*CL*max)/*CMT*max. 108
Figure 7.36 Ratio of *CD* and *CL* accompanied by maximum torsional moment *CMT*max to their maximum values *CD*max and *CL*max for Hexagon model (a) *CD* (*C*MTmax)/*CD*max, and (b) *CL* (*CMT*max)/*CL*max. 108
Figure 7.37 Ratio of *CL* and *CMT* accompanied by maximum along-wind force *CD*max to their maximum values *CL*max and *CMT*max for Octagon model (a) *CL* (*CD*max)/*C*Lmax, and (b) *CMT* (*CD*max)/*CMT*max. 108
Figure 7.38 Ratio of *CD* and *CMT* accompanied by maximum crosswind force *CL*max to their maximum values *CD*max and *CMT*max for Octagon model (a) *CD* (*C*Lmax)/*CD*max, and (b) *CMT* (*CL*max)/*CMT*max. 109
Figure 7.39 Ratio of *CD* and *CL* accompanied by maximum torsional moment *CMT*max to their maximum values *CD*max and *CL*max for Octagon model (a) *CD* (*C*MTmax)/*CD*max, and (b) *CL* (*CMT*max)/*CL*max. 109
Figure 7.40 Ratio of *CL* and *CMT* accompanied by maximum along-wind force *CD*max to their maximum values *CL*max and *CMT*max for Dodecagon model (a) *CL* (*CD*max)/*C*Lmax, and (b) *CMT* (*CD*max)/*CMT*max. 109
Figure 7.41 Ratio of *CD* and *CMT* accompanied by maximum crosswind force *CL*max to their maximum values *CD*max and *CMT*max for Dodecagon model (a) *CD* (*C*Lmax)/*CD*max, and (b) *CMT* (*CL*max)/*CMT*max. 110
Figure 7.42 Ratio of *CD* and *CL* accompanied by maximum torsional moment *CMT*max to their maximum values *CD*max and *CL*max for Dodecagon model (a) *CD* (*C*MTmax)/*CD*max, and (b) *CL* (*CMT*max)/*CL*max..... 110
Figure 7.43 Ratio of *CL* and *CMT* accompanied by maximum along-wind force *CD*max to their maximum values *CL*max and *CMT*max for Circular model (a) *CL* (*CD*max)/*C*Lmax, and (b) *CMT* (*CD*max)/*CMT*max. 110
Figure 7.44 Ratio of *CD* and *CMT* accompanied by maximum crosswind force *CL*max to their maximum values *CD*max and *CMT*max for Circular model (a) *CD* (*C*Lmax)/*CD*max, and (b) *CMT* (*CL*max)/*CMT*max. 111
Figure 7.45 Ratio of *CD* and *CL* accompanied by maximum torsional moment *CMT*max to their maximum values *CD*max and *CL*max for Circular model (a) *CD* (*C*MTmax)/*CD*max, and (b) *CL* (*CMT*max)/*CL*max. 111

Figure 7.46 Trajectory of overturning moment coefficients for Tri-60°Hel model at 40° wind direction 112
Figure 7.47 Trajectory of overturning moment coefficients for Tri-180°Hel model at 20° wind direction 112
Figure 7.48 Trajectory of overturning moment coefficients for Tri-360°Hel model at 65° wind direction 112
Figure 7.49 Trajectory of overturning moment coefficients for Sq-180°Hel model at 30° wind direction 113
Figure 7.50 Trajectory of overturning moment coefficients for Penta-180°Hel model at 50° wind direction 113
Figure 7.51 Trajectory of overturning moment coefficients for Hexa-180° model at 70° wind direction 113
Figure 7.52 Trajectory of overturning moment coefficients for Octa-180°Hel model at 75° wind direction 113
Figure 7.53 Trajectory of overturning moment coefficients for Dodeca-180°Hel model at 80° wind direction 114
Figure 7.54 Correlation coefficient (Solid line) and absolute value correlation (dotted line) for Tri-60°Hel model at 40° wind direction 114
Figure 7.55 Correlation coefficient (Solid line) and absolute value correlation (dotted line) for Tri-180°Hel model at 20° wind direction 115
Figure 7.56 Correlation coefficient (Solid line) and absolute value correlation (dotted line) for Tri-360°Hel model at 65° wind direction 115
Figure 7.57 Correlation coefficient (Solid line) and absolute value correlation (dotted line) for Sq-180°Hel model at 30° wind direction 115
Figure 7.58 Correlation coefficient (Solid line) and absolute value correlation (dotted line) for Penta-180°Hel model at 50° wind direction 115
Figure 7.59 Correlation coefficient (Solid line) and absolute value correlation (dotted line) for Hexa-180°Hel model at 70° wind direction 116
Figure 7.60 Correlation coefficient (Solid line) and absolute value correlation (dotted line) for Octa-180°Hel model at 75° wind direction 116
Figure 7.61 Correlation coefficient (Solid line) and absolute value correlation (dotted line) for Dodeca-180°Hel model at 80° wind direction 116
Figure 7.62 Ratio of *CL* and *CMT* accompanied by maximum along-wind force *CD*max to their maximum values *CL*max and *CMT*max for Tri-180°Hel model (a) *CL* (*CD*max)/*C*Lmax, and (b) *CMT* (*CD*max)/*CMT*max 117
Figure 7.63 Ratio of *CD* and *CMT* accompanied by maximum crosswind force *CL*max to their maximum values *CD*max and *CMT*max for Tri-180°Hel model (a) *CD* (*C*Lmax)/*CD*max, and (b) *CMT* (*CL*max)/*CMT*max. 118
Figure 7.64 Ratio of *CD* and *CL* accompanied by maximum torsional moment *CMT*max to their maximum values *CD*max and *CL*max for Tri-180°Hel model (a) *CD* (*C*MTmax)/*CD*max, and (b) *CL* (*CMT*max)/*CL*max 118
Figure 7.65 Ratio of *CL* and *CMT* accompanied by maximum along-wind force *CD*max to their maximum values *CL*max and *CMT*max for Sq-180°Hel model (a) *CL* (*CD*max)/*C*Lmax, and (b) *CMT* (*CD*max)/*CMT*max. 118

Figure 7.66 Ratio of *CD* and *CMT* accompanied by maximum crosswind force *CL*max to their maximum values *CD*max and *CMT*max for Sq-180°Hel model (a) *CD* (*C*Lmax)/*CD*max, and (b) *CMT* (*CL*max)/*CMT*max. 119
Figure 7.67 Ratio of *CD* and *CL* accompanied by maximum torsional moment *CMT*max to their maximum values *CD*max and *CL*max for Sq-180°Hel model (a) *CD* (*C*MTmax)/*CD*max, and (b) *CL* (*CMT*max)/*CL*max..... 119
Figure 7.68 Ratio of *CL* and *CMT* accompanied by maximum along-wind force *CD*max to their maximum values *CL*max and *CMT*max for Penta-180°Hel model (a) *CL* (*CD*max)/*C*Lmax, and (b) *CMT* (*CD*max)/*CMT*max..... 119
Figure 7.69 Ratio of *CD* and *CMT* accompanied by maximum crosswind force *CL*max to their maximum values *CD*max and *CMT*max for Penta-180°Hel model (a) *CD* (*C*Lmax)/*CD*max, and (b) *CMT* (*CL*max)/*CMT*max. 120
Figure 7.70 Ratio of *CD* and *CL* accompanied by maximum torsional moment *CMT*max to their maximum values *CD*max and *CL*max for Penta-180°Hel model (a) *CD* (*C*MTmax)/*CD*max, and (b) *CL* (*CMT*max)/*CL*max..... 120
Figure 7.71 Ratio of *CL* and *CMT* accompanied by maximum along-wind force *CD*max to their maximum values *CL*max and *CMT*max for Hexa-180°Hel model (a) *CL* (*CD*max)/*C*Lmax, and (b) *CMT* (*CD*max)/*CMT*max..... 120
Figure 7.72 Ratio of *CD* and *CMT* accompanied by maximum crosswind force *CL*max to their maximum values *CD*max and *CMT*max for Hexa-180°Hel model (a) *CD* (*C*Lmax)/*CD*max, and (b) *CMT* (*CL*max)/*CMT*max. 121
Figure 7.73 Ratio of *CD* and *CL* accompanied by maximum torsional moment *CMT*max to their maximum values *CD*max and *CL*max for Hexa-180°Hel model (a) *CD* (*C*MTmax)/*CD*max, and (b) *CL* (*CMT*max)/*CL*max..... 121
Figure 7.74 Ratio of *CL* and *CMT* accompanied by maximum along-wind force *CD*max to their maximum values *CL*max and *CMT*max for Octa-180°Hel model (a) *CL* (*CD*max)/*C*Lmax, and (b) *CMT* (*CD*max)/*CMT*max..... 121
Figure 7.75 Ratio of *CD* and *CMT* accompanied by maximum crosswind force *CL*max to their maximum values *CD*max and *CMT*max for Octa-180°Hel model (a) *CD* (*C*Lmax)/*CD*max, and (b) *CMT* (*CL*max)/*CMT*max. 122
Figure 7.76 Ratio of *CD* and *CL* accompanied by maximum torsional moment *CMT*max to their maximum values *CD*max and *CL*max for Octa-180°Hel model (a) *CD* (*C*MTmax)/*CD*max, and (b) *CL* (*CMT*max)/*CL*max..... 122
Figure 7.77 Ratio of *CL* and *CMT* accompanied by maximum along-wind force *CD*max to their maximum values *CL*max and *CMT*max for Dodeca-180°Hel model (a) *CL* (*CD*max)/*C*Lmax, and (b) *CMT* (*CD*max)/*CMT*max. 122
Figure 7.78 Ratio of *CD* and *CMT* accompanied by maximum crosswind force *CL*max to their maximum values *CD*max and *CMT*max for Dodeca-180°Hel model (a) *CD* (*C*Lmax)/*CD*max, and (b) *CMT* (*CL*max)/*CMT*max. 123
Figure 7.79 Ratio of *CD* and *CL* accompanied by maximum torsional moment *CMT*max to their maximum values *CD*max and *CL*max for Dodeca-180°Hel model (a) *CD* (*C*MTmax)/*CD*max, and (b) *CL* (*CMT*max)/*CL*max..... 123
Figure 7.80 Frame model for Square model 124
Figure 7.81 Effect of damping ratios on phase plane expression of internal forces for *ALL* loading condition ($\theta=0^o$) – Square model 125

Figure 7.82 Effect of wind direction on peak tensile stress for *ALL* loading condition, and damping ratio, ζ=1% – Square model 125
Figure A.1 Largest negative peak ($C_{p,\max}^{\check{}}$) among all wind directions and all pressure taps of all the models..... 137
Figure A.2 Largest positive peak ($C_{p,\max}^{\hat{}}$) among all wind directions and all pressure taps of all the models 137
Figure A.3 Comparison of mean overturning moment coefficients among all wind directions of all models 138
Figure A.4 Comparison of fluctuating overturning moment coefficients among all wind directions of all models 139

NOMENCLATURE

$C_p(t)$	Wind pressure coefficients
$\check{C}_p$	The largest negative peak pressure coefficient among all tap locations at each wind direction, θ
$\hat{C}_p$	The largest positive peak pressure coefficient among all tap locations at each wind direction, θ
$\check{C}_p(i)$	The largest negative peak pressure coefficients of all wind directions of each pressure tap
$\hat{C}_p(i)$	The largest positive peak pressure coefficients of all wind directions of each pressure tap
$\check{C}_{p,0.85H}$	The largest negative peak pressure coefficients at $0.85H$
$C_{p,\max}^{\check{}}$	Maximum of largest negative peak pressure coefficients of each model (Largest negative peak among all wind directions and all pressure taps
$C_{p,\max}^{\hat{}}$	Maximum of largest positive peak pressure coefficients of each model (Largest negative peak among all wind directions and all pressure taps
OTM	Overturning moment
$\overline{C}_{MD}$	Mean OTM coefficients in Along-wind direction
$\overline{C}_{ML}$	Mean OTM coefficients in Crosswind direction
C'_{MD}	Fluctuating OTM coefficients in Along-wind direction
$\overline{M}_D$	Mean OTM in Along-wind direction
$\overline{M}_L$	Mean OTM in Crosswind direction
M'_D	Fluctuating OTM in Along-wind direction

M'_L	Fluctuating OTM in Crosswind direction
$\overline{C}_{FD,local}$	Mean local wind force coefficients in Along-wind direction
$\overline{C}_{FL,local}$	Mean local wind force coefficients in Crosswind direction
$C'_{FD,local}$	Fluctuating local wind force coefficients in along-wind direction
$C'_{FL,local}$	Fluctuating local wind force coefficients in Crosswind direction
$\overline{F}_{D,local}$	Local mean wind forces in Along-wind direction
$\overline{F}_{L,local}$	Local mean wind forces in Crosswind direction
$F'_{D,local}$	Local fluctuating wind forces in Along-wind direction
$F'_{L,local}$	Local fluctuating wind forces in Crosswind direction
B	Width of a model
q_H	Mean velocity pressure at model height, H
A	Frontal area of building at each level.
z	Height of each pressure measurement level
$U_{P,500}$	Wind speed corresponding to 500-year Return period
$U_{P,1}$	Wind speed corresponding to 1-year Return period
B_w	Bandwidth of Crosswind force power spectrum
Fx	Force in Along-wind direction
Fy	Force in Crosswind direction
Mz	Torsional Moment in z-direction
ζ	Damping ratio

Chapter I

INTRODUCTION

The economy of the country and the availability of the space with increase number of population make the engineers think about the construction of the tall buildings. Construction of tall buildings is common in the urban world. However, they pose design challenges for structural engineers, particularly when they are situated in seismically active regions or when the underlying soils have geotechnical risk factors such as high compressibility. Wind is a main phenomenon to introduce major complexity because of the many flow situations arising from the interaction of wind with structures. Some structures, particularly those that are taller or slender, respond dynamically to the effects of wind. The generation of the largest negative peak pressures under reattaching shear layers has long been recognized as a major cause of damage to low-rise building roofs and cladding on high-rise buildings.

They also pose serious challenges to firefighters during emergencies. New building designs and plans are common among architects, engineers and developers, and the variety of heights and shapes pose various design problems. Therefore, their design needs a comprehensive study and understanding of the plans. The present trend towards design

of tall buildings is toward unconventional shapes such as various cross sections. Figure 1.1 shows some of the tall buildings in urban areas around the world.

Wind-induced load is an important and essential design issue for tall buildings, cable suspension bridges, electricity transmission towers, telecommunication towers and chimneys. For real structures, the flow field is very complex in nature; hence, experimental studies are mandatory. Many researchers have tested wind pressures on irregular plan buildings (Anim and Ahuja, 2008), different rectangular cross sections (Ning et al., 2005), tapered building models with taper ratios of 5% and 10%, and building models with set-back at mid-height (Kim and Kanda, 2010) etc., but, there have been very few studies on triangular cross-section tall buildings.

Figure 1.1 Tall buildings in the urban world

1.1 Literature review

1.1.1 *Wind pressure characteristics*

To explore the high peak suctions developed on building models and their relationship with building shape and the characteristics of the oncoming simulated atmospheric flow is very important especially for cladding design for high-rise buildings. For real structures within real environments, the fluid mechanical aspects are complex; hence the heavy reliance on experimental methods. Nonetheless, there is a continuing need to explore the fundamental nature of the fluid mechanics involved. D.Surry & D.Djakovich (1995) pointed out that the model geometry did not strongly influence the magnitude and location of the most severe values observed peaks, although it did alter the most important wind directions. In contrast, the structure of the peak suctions was strongly influenced by the simulated terrain. Furthermore, the peak event always coincides with a vortex shedding peak. An increase in turbulence intensity, associated with a more built-up terrain simulation, deteriorates the periodicity of vortex shedding, but the peak relationship with the remaining randomized vortex shedding appears to be maintained.

W.H.Melbourne (1993) mentioned that the occurrence of very high peak pressures on the surfaces on which cladding is designed, the crosswind response of towers and buildings, the vertical response of a bridge deck or roof canopy, are all examples of activities which have their origin in the leading edge phenomenon. The generation of large negative peak pressures under reattaching shear layers has long been recognized as a major cause of damage to lo-rise building roofs and cladding on high-rise buildings. An increase in turbulence was shown increase the magnitude of pressure fluctuations. N.J.Jamieson et.al (1992) investigated the effect of the different corner configurations on the magnitude and distribution of the peak pressure coefficients and it is common practice to perform wind tunnel tests for tall buildings to determine the design wind pressures for the cladding. The modification of the edge is very effective to reduce the peak suction, as it controls effectively the separation of the shear layer (H.Kawai, 2002). Many researchers investigated the effect of corner modifications on peak pressure coefficients, Jamieson et.al (1992); Ohtake Kazuo (2000); Katagiri Junji et.al (1992).

Kareem et.al (1984) investigated, spatio-temporal measurements of a fluctuating pressure filed acting on the side faces of a square prism of finite height in boundary-layer flows are presented for 0^o angle of attack. Two typical neutral atmospheric flow conditions were simulated in the wind tunnel to represent open country and urban flow environments.

1.1.2 *Wind force characteristics*

Wind is a phenomenon of great complexity because of the many flow situations arising from the interaction of wind with structures. Wind is composed of multitude of eddies of varying sizes and rotational characteristics carried along in a general stream of air moving relative to the earth's surface. These eddies give wind its gusty or turbulent character. The gustiness of strong winds in the lower levels of the atmosphere largely arises from interaction with surface features. Some structures, particularly those that are tall or slender, respond dynamically to the effects of wind. The best known structural collapse due to wind was Tacoma Narrows Bridge which occurred in 1940 at a wind speed of only about 19 m/s. It failed after it had developed a coupled torsional and flexural mode of oscillation. One way to minimize wind-induced vibrations of tall buildings is to focus more on their shapes in the design stage. Hayashida et.al (1990) studied the effects of building plan shape on aerodynamic forces, and displacement responses have been studied for super-high-rise buildings with square and triangular cross-sections with corner modifications. Kim et.al (2002) discussed aerodynamic modifications of building shape, such as by changing the cross-section with height through tapering, which alters the flow pattern around tall buildings, and can reduce wind-induced excitations. Many researchers have tested wind pressures on buildings with irregular plans (Amin et.al., 2008), with plan shapes that change with height (Harikrishna et.al., 2009), with different rectangular cross-sections (Lin et.al., 2005), and with tapers with taper ratios of 5% and 10%, and with set-back at mid-height (Kim et.al., 2010a, 2010b, 2011).

Kanda et.al (1992) investigated the dynamic wind force components on 3-D cylinders with typical sectional shapes, i.e. square, rectangle, triangle and diamond, were

measured in three simulated boundary layers in a wind tunnel shown in Figure 1.2. These models also have a same sectional area of 0.01 m^2.

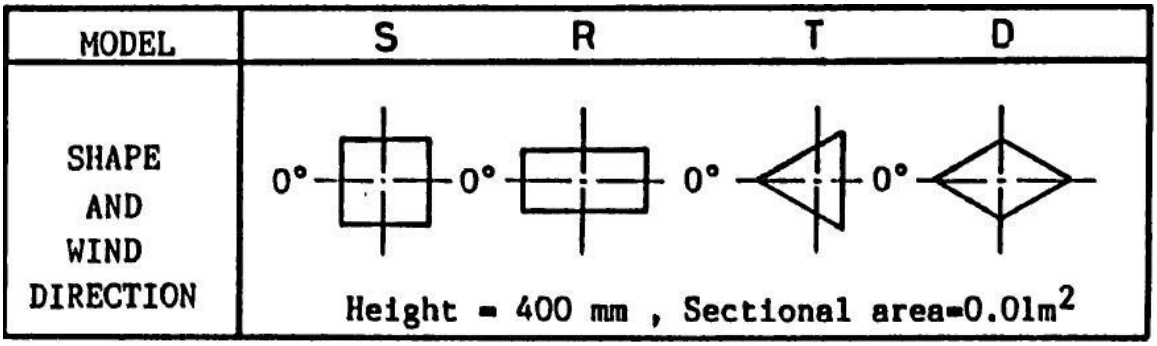

Figure 1.2 Model shapes and wind direction (Kanda et.al, 1992)

Tanaka et.al (2012) investigated aerodynamic forces and wind pressures acting on tall buildings with various unconventional configurations. All the models considered here are square cross-sections. A series of wind tunnel experiments have been carried out to determine aerodynamic forces and wind pressures acting on square-plan tall building models with various configurations: corner cut, setbacks, helical and combinations of corner cut, setbacks and helical. Figure 1.3 and Figure 1.4 show the maximum values of the mean and fluctuating along-wind and crosswind overturning moment coefficients considering all wind directions.

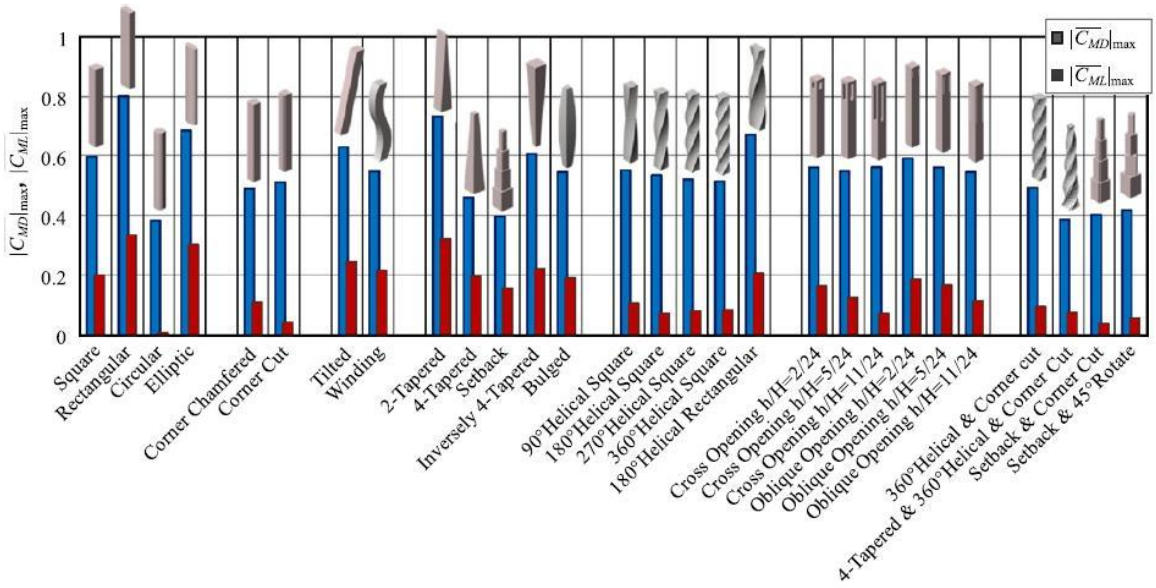

Figure 1.3 comparison of maximum mean overturning moment coefficients

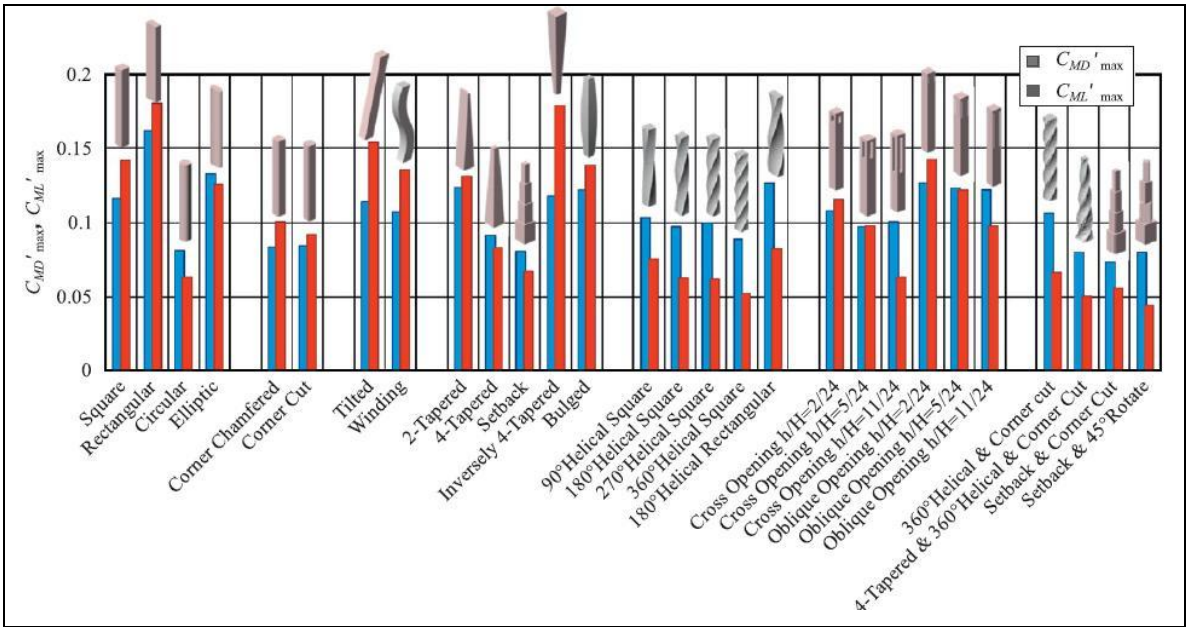

Figure 1.4 comparisons of maximum fluctuating overturning moment coefficients

Based on his study he concluded that the helical models are better than those of other models with single modification, detailed comparisons are summarized in Figure 1.5. From Figure 1.5(a)-(c) , the overturning moment coefficients and the spectral peak values show the tendency to decrease with increasing twist angle, and the decrease in the fluctuating component of crosswind is significant, as shown in Figure 1.5(b) and (c). But note that there are small differences in overturning moment coefficients, spectral peaks and band widths when the twist angle is larger than 180^o. From this, it can be assumed that the effects of twist angle on regular vortex shedding appear mostly when the twist angle is less than 90^o, and the relative effects of twist angle become smaller at larger twist angle.

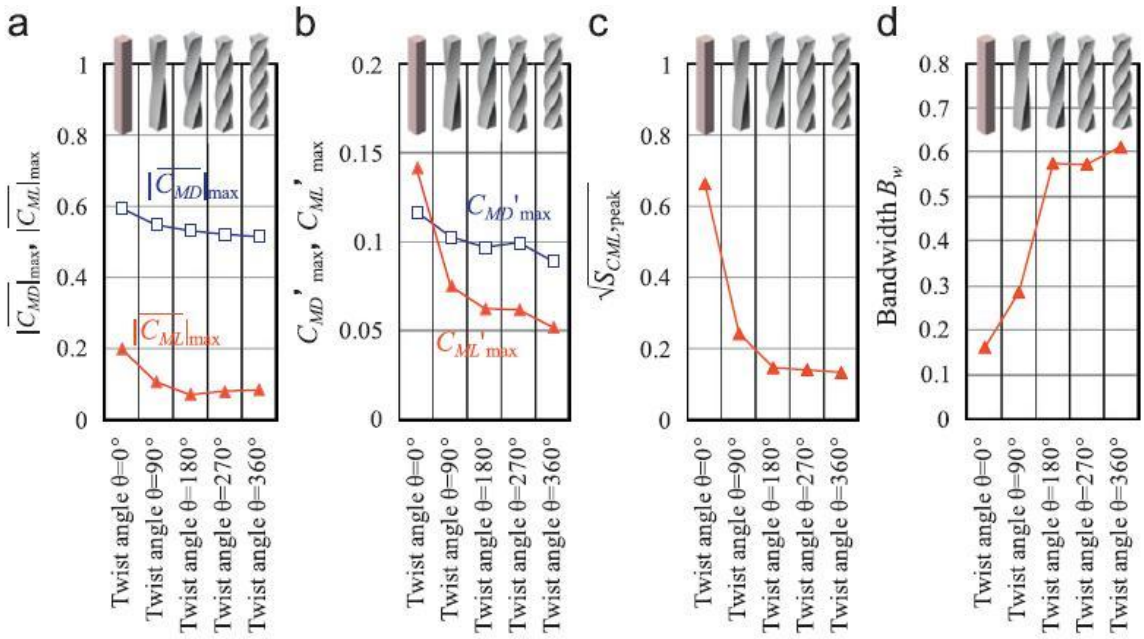

Figure 1.5 Effect of twist angle for the helical square models. (a) Maximum mean overturning moment coefficients, (b) maximum fluctuating overturning moment coefficients, (c) peak values of power spectral densities and (d) bandwidths of power spectral densities (Tanaka et.al, 2012)

1.2 Objective of this study

Figure 1.6 shows the schematic diagram of the thesis. The main objectives of the thesis are

(1) To investigate the characteristics of local peak pressures for the design of cladding and aerodynamic characteristics of various tall building models with various configurations.

(2) To investigate the effects of corner modifications, twisting angle of helical models and combination of corner modifications and twisting on local peak pressure coefficients.

(3) To investigate the effects of corner modifications and twisting angle of helical models on wind forces.

(4) Summarize the most efficient configurations based on the above investigations.

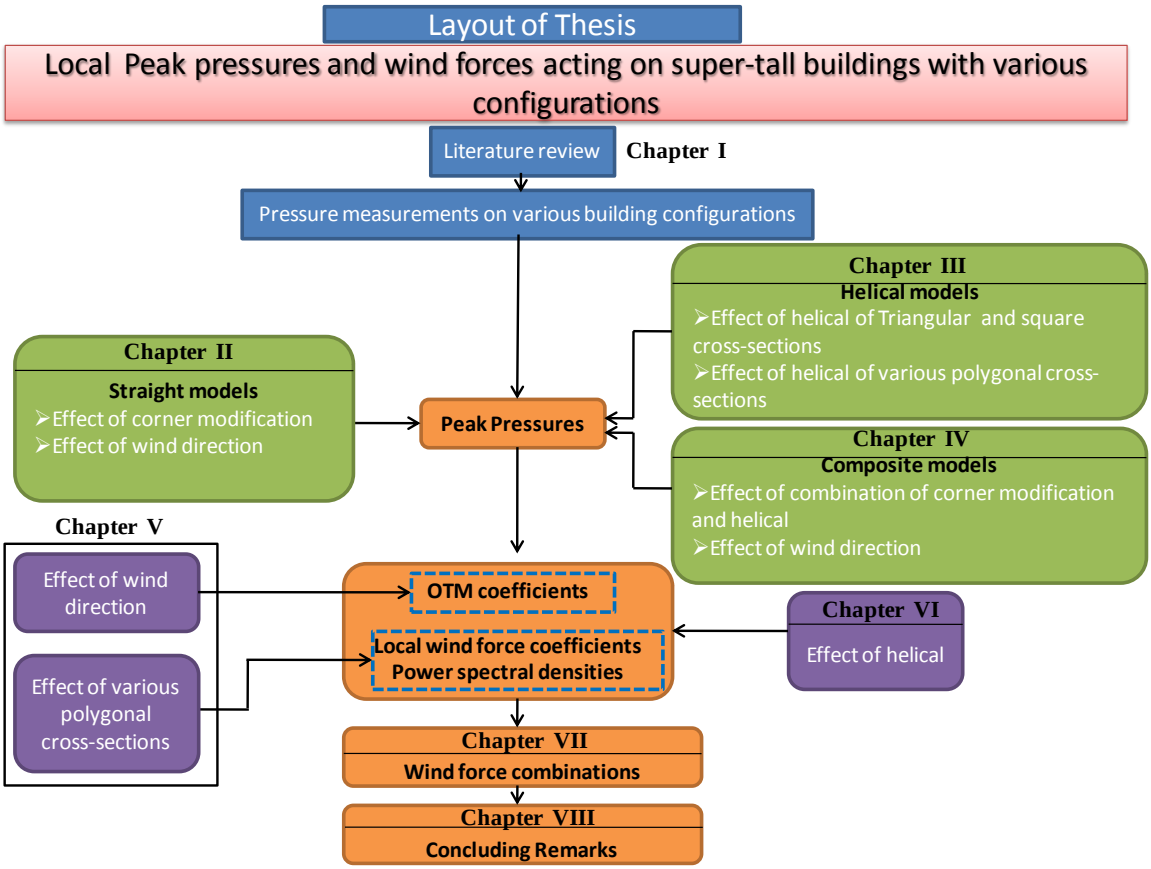

Figure 1.6 Schematic diagram of the thesis.

1.3 Organization of the thesis

The thesis is divided into 8 chapters as follows.

Chapter II introduces the experimental setup, various experimental models and mainly the effect of corner modifications, effects of taper, effects of number of surface increased on local peak pressures investigated in this chapter.

Chapter III discusses the effect of twisting angle on local peak pressure coefficients.

Chapter IV discusses the combined effect of corner modification, tapering and twisting angle on local peak pressure coefficients.

Chapter V discusses the effect of triangular models with corner modification and the effect of number of surfaces on local and total wind forces and power spectral densities.

Chapter VI discusses the effect of twisting angle of helical models and number of surfaces with twisting able of 180^{o} on local and total wind forces and power spectral densities.

Chapter VII discusses the wind force combinations.

Chapter VIII Conclusions of the current study.

1.4 References

1. Amin, J.A., Ahuja, A.K., 2008, Experimental study of wind pressures on irregular plan shape buildings, BBAA VI, 20-24.
2. Emil Simiu, Robert H.Scanlan, Wind effects on Structures, Fundamentals and applications to Design, Third Edition.
3. Harikrishna, P., Abraham, A., Arunachalam, S., Selvi Rajan, S., Ramesh Babu, G., Lakshmanan, N., 2009, Pressure measurement studies on a model of a tall building with different plan shapes along the height, APCWE-VII.
4. Hayashida, H., Iwasa, Y., 1990, Aerodynamic shape effects of tall building for vortex induced vibration, Journal of Wind Engineering and Industrial Aerodynamics, 33, 237-242.
5. Jamieson, N.J. & Carpenter, P. & Cenek, P.D. (1992), Wind induced external pressures on a tall building with various corner configurations, Journal of Wind Engineering and Industrial Aerodynamics, 41-44, 2401-2412.
6. John D. Holmes, Wind loading of structures
7. Kanda, J., Choi, H., 1992, Correlating Dynamic Wind Force Components on 3-D cylinders, Journal of Wind Engineering and Industrial Aerodynamics, 41-44, 785-796.
8. Kawai, H., (2002), "Local peak pressure and conical vortex on building, Journal of Wind Engineering and Industrial Aerodynamics, 90, 251-263.
9. Kareem, A., Cermak, J.E., 1984, Pressure fluctuations on a square building model in boundary-layer flows, Journal of Wind Engineering and Industrial Aerodynamics, 16, 17-41.

10. Kim, Y.C., Kanda, J., 2010a, Characteristics of aerodynamic force and pressures on square plan buildings with height variations, Journal of Wind Engineering and Industrial Aerodynamics, 98, 449-465.
11. Kim, Y.C., Kanda, J., 2010b, Effects of taper and set-back on wind force and wind-induced response of tall buildings, Wind and Structures, 13(6), 499-517.
12. Kim, Y.C., Kanda, J., Tamura, Y., 2011, Wind-induced coupled motion of tall buildings with varying square plan with height, Journal of Wind Engineering and Industrial Aerodynamics, 99, 638-650.
13. Kim, Y.M., You, K.P., 2002, Dynamic responses of a tapered tall building to wind loads, Journal of Wind Engineering and Industrial Aerodynamics, 90, 1771-1782.
14. Lin, N., Letchford, C., Tamura, Y., Liang, B., Nakamura, O., 2005, Characteristics of wind forces acting on tall buildings, Journal of Wind Engineering and Industrial Aerodynamics, 93, 217-242.
15. Melbourne, W.H., 1993, Turbulence and the Leading Edge Phenomenon, Journal of Wind Engineering and Industrial Aerodynamics, 49, 45-64.
16. Peter A. Irwin., Wind Engineering Research Needs, Building Codes and Project specific Studies, 11th Americas Conference on Wind Engineering – San Juan, Puerto Rico., June 22-26, 2009.
17. Surry, D. & Djakovich, D., 1995, Fluctuating pressures on models of tall buildings, Journal of Wind Engineering and Industrial Aerodynamics, 58, 81-112.
18. Tanaka, H., Tamura, Y., Ohatake, K., Nakai, M., Kim, Y.C., 2012, Experimental investigation of aerodynamic forces and wind pressures acting on tall buildings with various unconventional configurations, Journal of Wind Engineering and Industrial Aerodynamics, 107-108, 179-191.

Chapter II

EFFECT OF VARIOUS CROSS-SECTIONAL SHAPES ON LOCAL PEAK PRESSURES

Tall buildings are very common now in urban areas all over the world. It is very important to study peak suctions on roofs and walls, because it causes frequent damages by the peak suctions under strong wind conditions. In turbulent flows, peak suctions occurs occasionally near the corner of walls and roofs (W.H.Melbourne, 1993). Saathoff et.al (1989) investigated the occurrence of large negative peak pressures near the leading edge of sharp-edged bluff bodies. Stathopoulos et.al (1991) studied local pressure coefficients on multi-span gabled (folded) roofs of low buildings. Surry et.al (1995) studied the high peak suctions developed on building models and their relationship with building shapes. Jamieson et.al (1992) investigated the effect of the different corner configurations on the magnitude and distribution of the peak pressure coefficients. Kim et.al (2010) also studied the wind pressures of Square, Taper and Setback models to investigate the aerodynamic force reduction. This study investigates effect of various aerodynamic shapes on local peak pressures based on the pressure measurement of wind tunnel tests. Also, this chapter introduces the experimental set-ups and the basic models used for this study.

2.1 Experimental set-up

2.1.1 *Wind speed and turbulence intensity profiles*

Wind tunnel tests on various configurations were conducted in a boundary layer wind tunnel at the Wind Engineering Research Center, Tokyo Polytechnic University, Japan. The wind tunnel test section was 19m long with a cross-section 2.2m wide by 1.8m high. A length scale of 1/1000 and a time scale of 1/167 were assumed. The velocity scale is 1/6.

The experiments were conducted for an urban (power–law exponent, α=0.27) flow, by changing the wind directions. Figure. 2.1 show the roughness arrangement in the wind tunnel for this study. Figure. 2.2 show the mean wind speed and turbulence intensity profiles for this study. The wind velocity and turbulence intensity at the top of the model are about 12-m/s and 11%, respectively for an urban flow condition. The turbulence integral scale near the model top is about 0.42m.

All the pressures were measured simultaneously with a sampling frequency of 781Hz, and a low pass-filter with a cut-off frequency of 300 Hz was cascaded in each data acquisition channel to eliminate aliasing effects. The measuring time was adjusted such that 33 samples were obtained which correspond to 10 min-long samples in full scale. The tubing effects were numerically compensated by the gain and phase-shift characteristics of the pressure measuring system (Irwin et al., 1979).

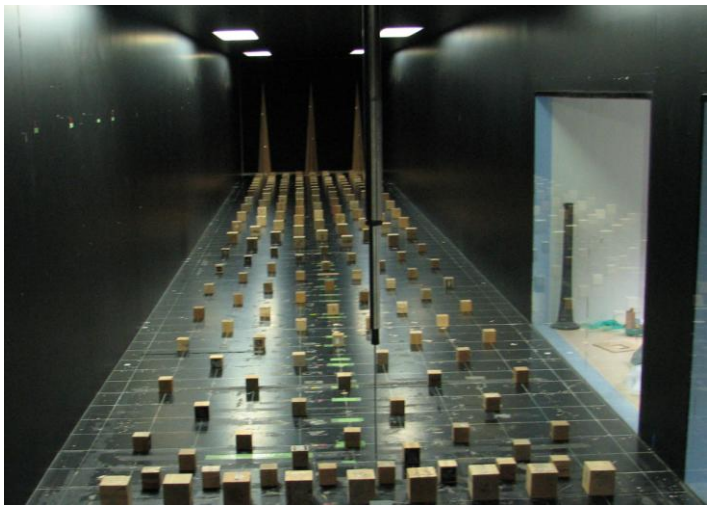

Figure 2.1 Roughness arrangement for Urban flow condition

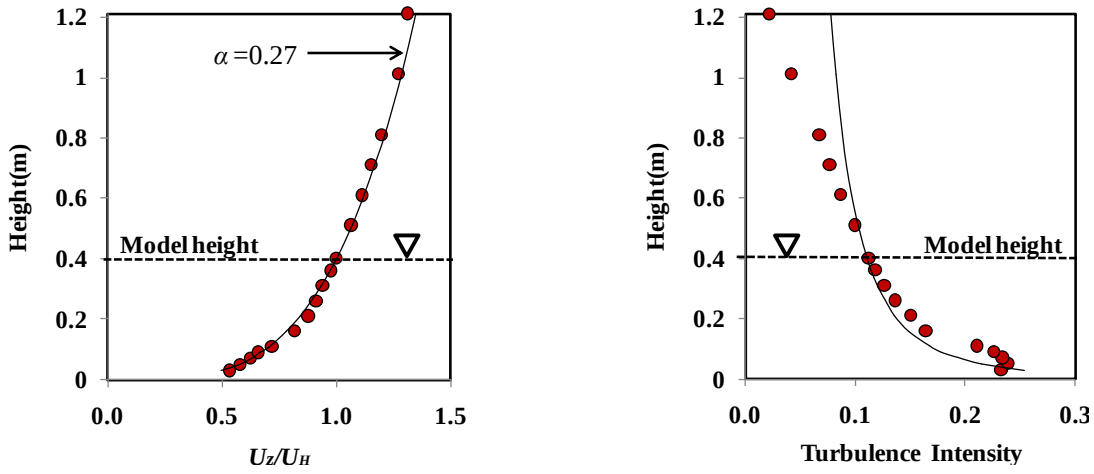

(a) Mean wind speed (b) Turbulence intensity

Figure 2.2 Profile of mean wind speed and turbulence intensity

2.1.2 *Experimental models*

The tall building models used for this study are shown in Table 2.1(a-c). The full-scale height and the total volume of each building model are set at H=400 m and 10^6 m^3. The width *B* of the Square model shown in Table 2.1 is 50m and the aspect ratio *H/B* is 8. The Reynolds number (R_e) obtained from the diameter of the Circular model used in the wind tunnel experiment is R_e=4.4 × 10^4. All the models had the same volume, and Triangular, Tri-Corner cut, Clover, Square, Sq-Corner cut, Sq-chamfered, Sq-Tapered, Sq-Setback, Pentagon, Hexagon, Octagon, Dodecagon, Circular, Tri-60^{o}Helical, Tri-180^{o}Helical, Tri-360^{o}Helical, Sq-90^{o}Helical, Sq-180^{o}Helical, Penta-180^{o}Helical, Octa-180^{o}Helical, Dodeca-180^{o}Helical, Sq-180^{o}Hel &Corner cut, Sq-Tapered & 180^{o}Hel, Sq-Tapered & 360^{o}Hel & Corner cut and Sq-Setback & 45^o Rotate models were tested to identify their aerodynamic characteristics. The colored surfaces shown in Table 2.2 are those shown as straight surfaces for the distribution of largest negative peak and largest positive peak pressures. There were about 21 measurement points for the Triangular models and 24 measurement points for the Tri-Corner cut and Clover models on each level on three surfaces as shown in the following Table 2.3, and the measurement points were instrumented at 10 levels giving about 210 measurement points for the Triangular models and about 240 measurement points for the Tri-Corner cut and Clover models. All the pressure models discussed in this paper have the measurement points at 10 levels and the height of each level for all the models is same. The total number of measurement points for each model varies from 184 to 250.

In this chapter, the straight polygon models, corner modification models and tapered models were considered. These models are shown in Table 2.2 (a-b) and Table 2.2(d).

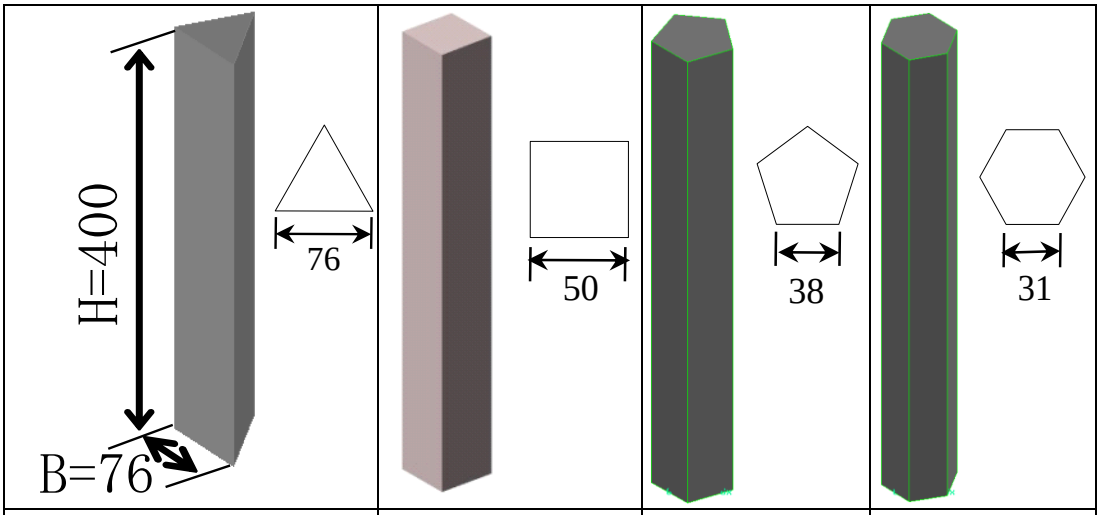

Triangular	Square	Pentagon	Hexagon

(a) Straight Polygonal models

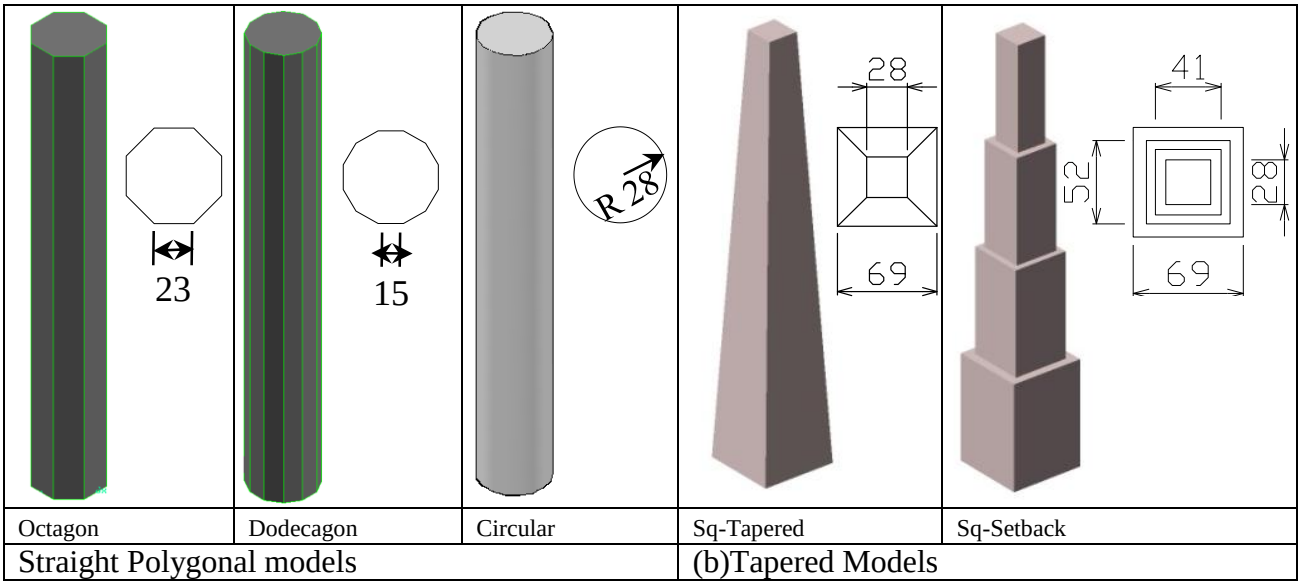

Octagon	Dodecagon	Circular	Sq-Tapered	Sq-Setback

Straight Polygonal models (b)Tapered Models

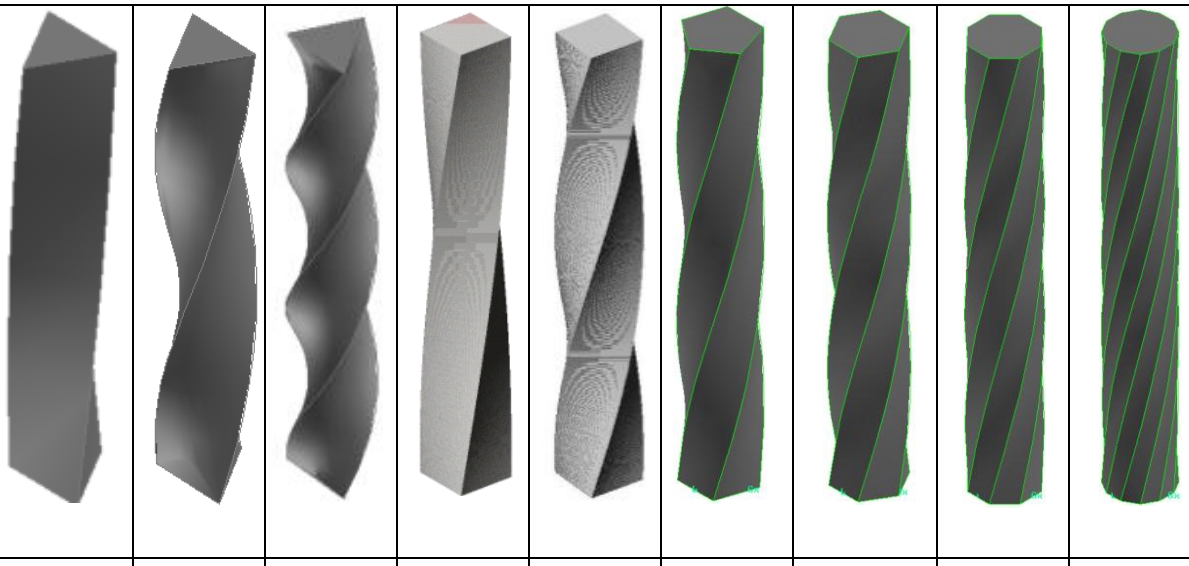

Tri-60°Hel	Tri-180°Hel	Tri-360°Hel	Sq-90°Hel	Sq-180°Hel	Penta-180°Hel	Hexa-180°Hel	Octa-180°Hel	Dodeca-180°Hel

(c) Helical models

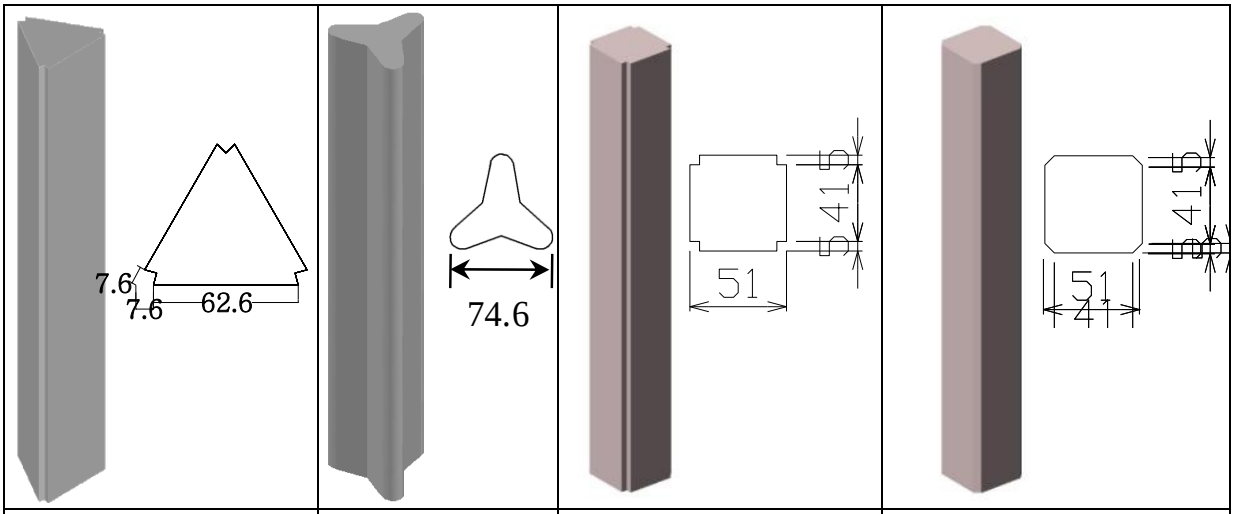

Octagon	Dodecagon	Circular	Sq-Tapered

(d) Corner modified models

			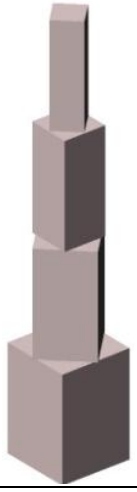
Sq-180^{o}Hel &Corner cut	Sq-Tapered & 180^{o}Hel	Sq-Tapered& 360^{o}Hel & Corner cut	Sq-Setback & 45^{o} Rotate
(e) Composite models			
Table 2.1 Configurations of the models			

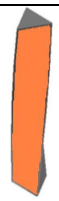											
Tri-60^{o}Hel	Tri-180^{o}Hel	Tri-360^{o}Hel	Sq-90^{o}Hel	Sq-180^{o}Hel	Sq-180^{o}Hel &Corner cut	Sq-Tapered & 180^{o}Hel	Sq-Tapered & 360^{o}Hel &Corner cut	Penta-180^{o}Hel	Hexa-180^{o}Hel	Octa-180^{o}Hel	Dodeca-180^{o}Hel
Table 2.2 The Colored surfaces for the distribution of peak pressures											

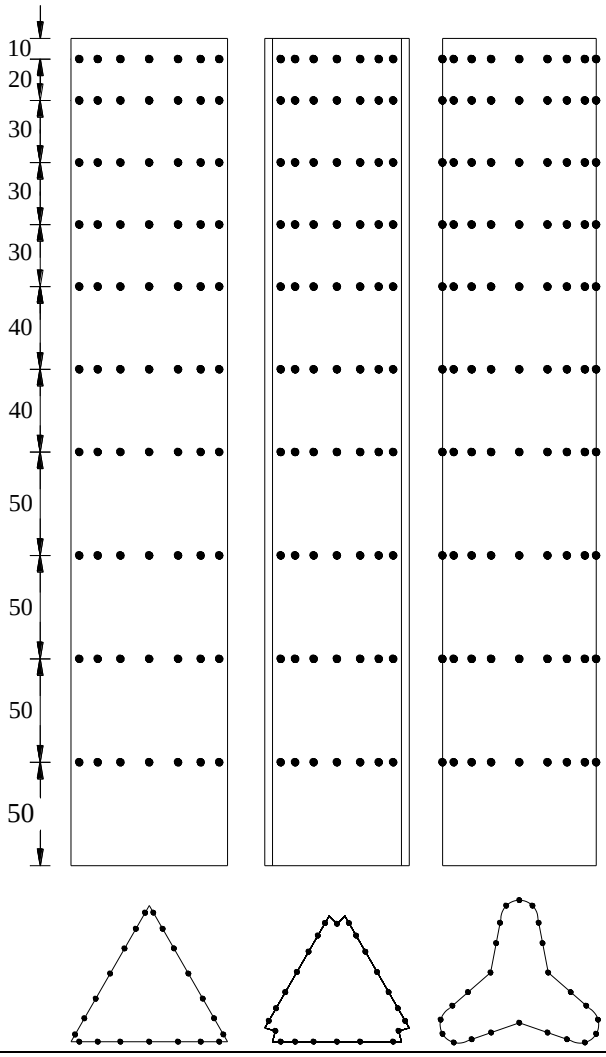

Table 2.3 Arrangement of pressure taps and coordinate system (Unit: mm)

2.2 **Definition and terminology**

Wind pressure coefficients are calculated for the time series of each pressure tap, $C_p(t)$ using Eq. (1).

$$C_p(t) = \frac{p(t)}{0.5\rho(U_H)^2} \tag{1}$$

$$\check{C}_p = \min(C_p(t), \theta)$$

$$\hat{C}_p = \max(C_p(t), \theta)$$

Where $p(t)$ is the time series of wind pressure; ρ the air density (1.25 kg/m3); U_H the mean wind speed at the top of the building models; θ is wind direction; $\check{C}_p$ the largest negative peak pressure coefficient among all tap locations at each wind direction; $\hat{C}_p$ the largest positive peak pressure coefficient among all tap locations at each wind direction; The maximum and minimum wind pressure coefficients shown in the paper are ensemble averages of 9 samples, and one sample corresponds to 10 min in full time scale.

2.3 **Effect of corner modifications**

This section, considers corner modification models of Triangular and Square cross-sections. The models considered were Triangular, Tri-Corner cut, Clover, Square, Sq-Corner cut and Sq-Chamfered models, as shown Table 2.1(d). The largest negative and positive peak pressures were selected for all wind directions.

2.3.1 *Largest negative local peak pressure coefficients* ($\check{C}_P(i)$)

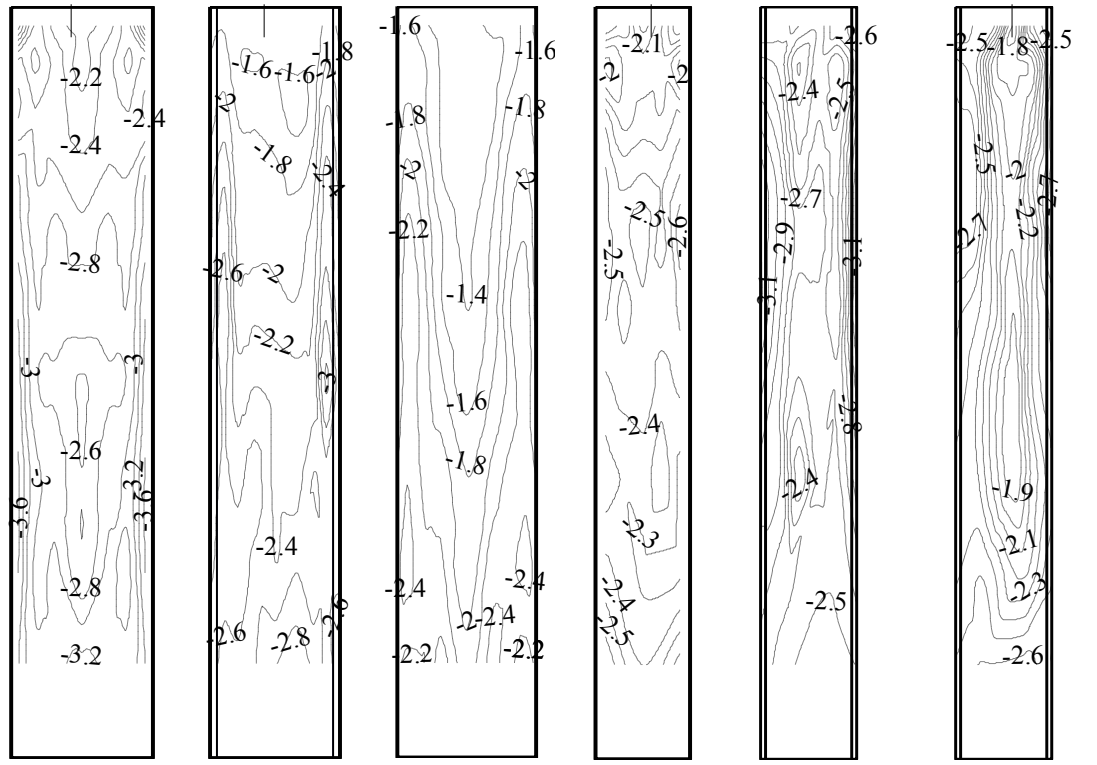

(a) Triangular (b)Tri-Corner cut (c) Clover (d) Square (e)Sq-Corner cut (f)Sq-Chamfered

Figure 2.3 Largest negative peak pressure coefficients for Square and Triangular models

Figure 2.3 show the distribution of largest negative local peak pressure coefficients ($\check{C}_P(i)$). The $\check{C}_P(i)$ distributions vary smoothly from corner regions to the center of the surfaces for all models. The largest peak suctions occur close to the corner regions for all the models, and it occurs between 0.4*H*-0.78*H* for the Tri-Corner cut, Clover, Square, Sq-Corner cut and Sq-Chamfered models, whereas for Triangular model it occurs at 0.98*H*. The absolute largest negative peak pressure coefficients of all wind directions and tap locations were Triangular: 3.75, Tri-Corner cut: 3.12, Clover: 3.13, Square: 2.68, Sq-Corner cut: 3.20, and Sq-Chamfer: 2.75.

2.3.2 *Largest positive local peak pressure coefficients ($\hat{C}_P(i)$) distribution on the surfaces*

Figure 2.4 shows the distribution of largest positive local peak pressure coefficients ($\hat{C}_P(i)$). The $\hat{C}_P(i)$ distributions vary smoothly for all models. The maximum $\hat{C}_P(i)$ values occur at up-

per levels for all models. The $\hat{C}_P(i)$ distribution varies smoothly from lower to the higher values from corner regions to the center of the surfaces for the Tri-Corner cut and Clover models whereas $\hat{C}_P(i)$ is almost constant for the Square models. The absolute largest positive peak pressure coefficients of all wind directions and tap locations were Triangular: 1.79, Tri-Corner cut: 1.64, Clover: 1.62, Square: 1.44, Sq-Corner cut: 1.43, and Sq-Chamfer: 1.45.

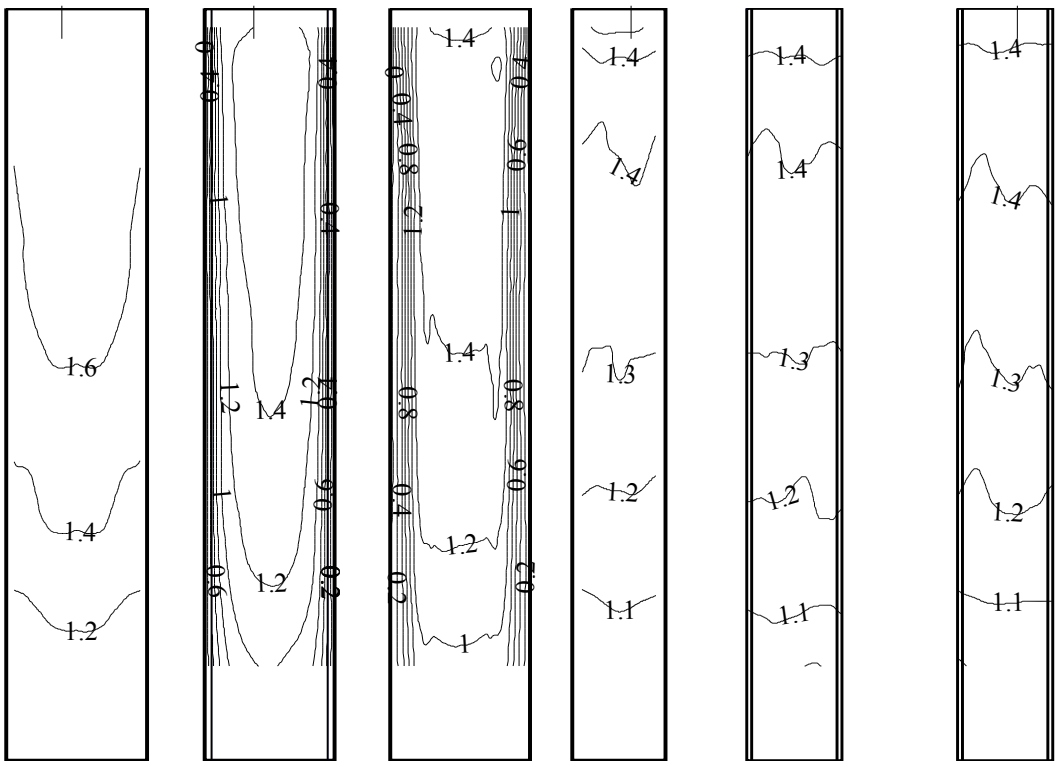

(a) Triangular (b)Tri-Corner cut (c) Clover (d) Square (e)Sq-Corner cut (f)Sq- Chamfered

Figure 2.4 Largest positive peak pressure coefficients for Square and Triangular models

2.3.3 *Effect of corner modification on peak pressures*

The effect of corner modifications on $\check{C}_{p,0.85H}$ has been investigated for all wind directions at 0.85*H* for the Triangular, Tri-Corner cut, Clover, Square, Sq-Corner cut and Sq-Chamfered models. Points a, b, c, d and e in Figure 2.5 and Figure 2.6 are where the maximum $\check{C}_P$ occurred on the side surface at 0.85*H*. Figure 2.5 and Figure 2.6 show the variation of $\check{C}_{p,0.85H}$ with wind direction of the above mentioned points. Figure 2.5, show clearly that $\check{C}_{p,0.85H}$ reduces for the Tri-Corner cut for most of wind directions except 0° to 25°, 70° to 185° and 320° to 360°, whe-

reas for the Clover model $\hat{C}_{p,0.85H}$ reduces for all wind directions. The $\hat{C}_{p,0.85H}$ values for the Tri-Corner cut model are less than the maximum value for the Triangular model. The $\hat{C}_{p,0.85H}$ values are equal for the Triangular and Clover models at 30° wind direction where the flow is parallel to one of the surfaces of the Triangular model. The $\hat{C}_{p,0.85H}$ $\hat{C}_P$ values are equal for the Triangular, Tri-Corner cut and Clover models at 25° and 285° to 315° wind directions. As shown in Figure 5, for the square cross-sections, the $\hat{C}_{p,0.85H}$ values reduce for the Sq-Corner cut and Sq-Chamfered models at point c and point e for most of wind directions. The location of the peak suctions shifts downstream on the surface for the Sq-Corner cut model compared with those of the Square, Triangular and Tri-Corner cut models, whereas the corner regions for the Sq-Corner cut and Sq-Chamfer models showed larger $\hat{C}_{p,0.85H}$ values when the flow was perpendicular (around 90° Wind direction) to the surface. The $\hat{C}_{p,0.85H}$ values followed the same trend and were almost the same for all wind directions except 60° to 160° for the Sq-Corner cut and Sq-Chamfered models at the specified locations. The $\hat{C}_{p,0.85H}$ values followed the same trend between 60° and 185° for the Tri-Corner cut, Sq-Corner cut and Sq-Chamfered models.

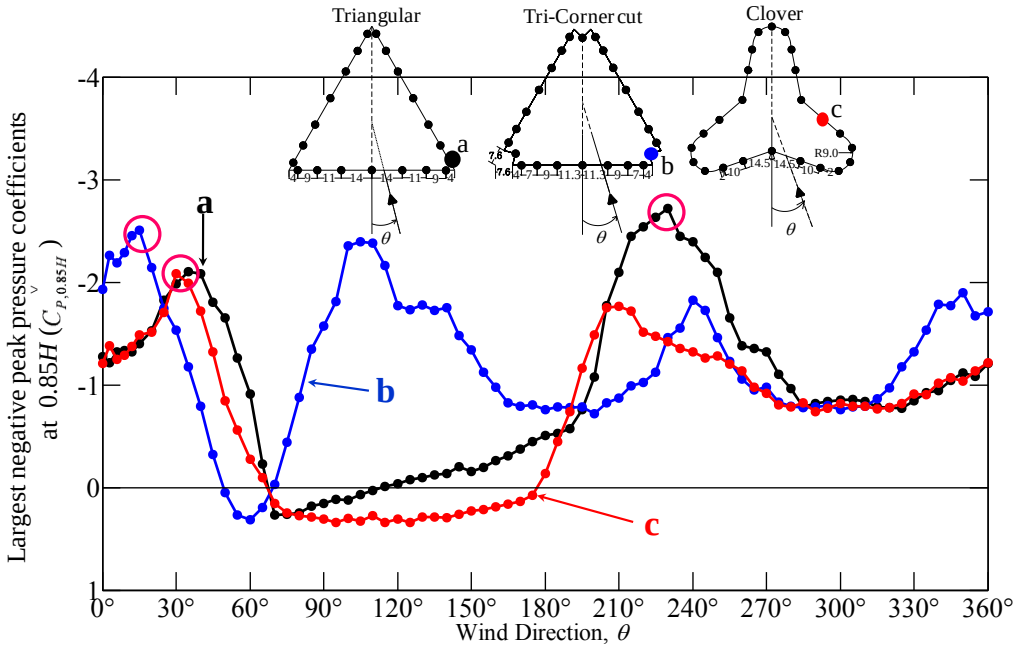

Figure 2.5 Effect of corner modification on largest negative peak pressure coefficients for Triangular corner modification models

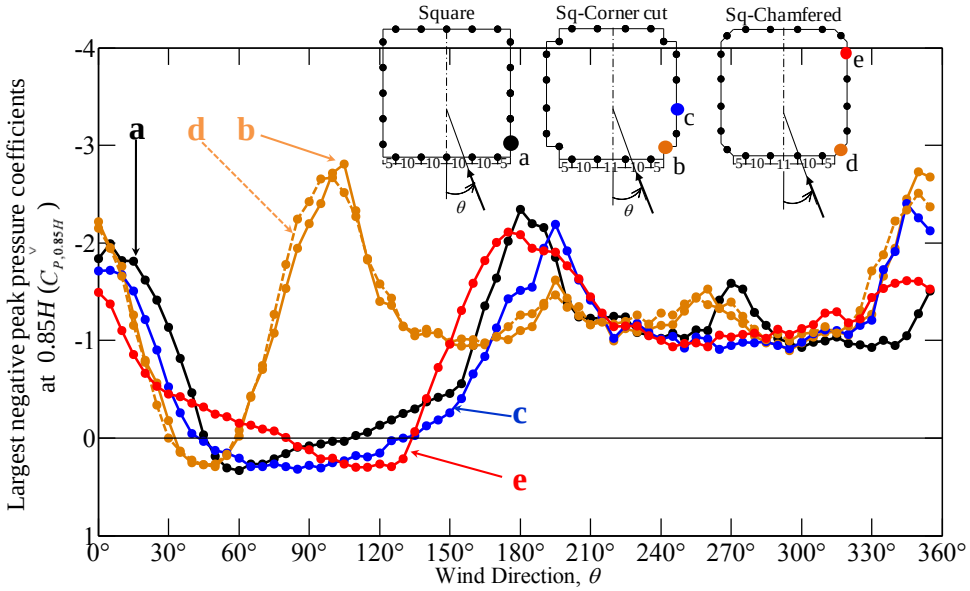

Figure 2.6 Effect of corner modification on largest negative peak pressure coefficients for Square corner modification models

2.3.4 *Variation of largest negative peak pressures with wind direction* (θ)

Figs 2.7 and 2.8 show the maximum $\hat{C}_P$ from all the pressure taps for each wind direction. As shown in Figure 2.7, the largest and smallest $\hat{C}_P$ occurred for the Triangular model. The smallest $\hat{C}_P$ occurred for the Tri-Corner cut and Clover models when the corners of the models were perpendicular to the flow at wind directions close to 60°. Figure 2.8 shows the variation of $\hat{C}_P$ for all wind directions for the Square, Sq-Corner cut and Sq-Chamfered models. Sq-Corner cut shows larger and smaller values than Square and Sq-Chamfered models. The $\hat{C}_P$ values were the same for the Square, Sq-Corner cut and Sq-Chamfered when the flow was perpendicular to the surface (θ=0°) and corners (θ=45°). Also, the $\hat{C}_P$ values were the same for the Tri-Corner cut and Clover models when the flow was perpendicular to the corner (θ=60°)

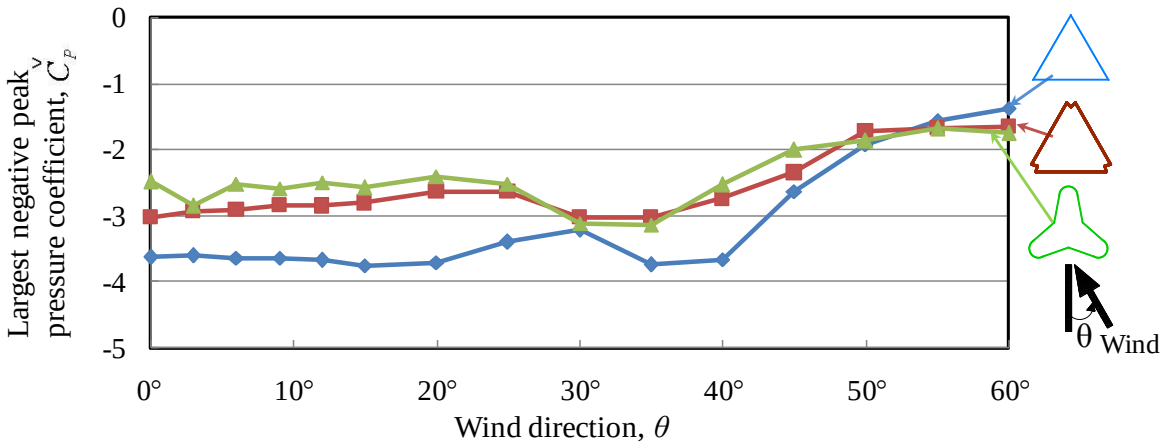

Figure 2.7 Variation of largest negative peak pressure coefficients with wind direction (θ) for Triangular corner modification models

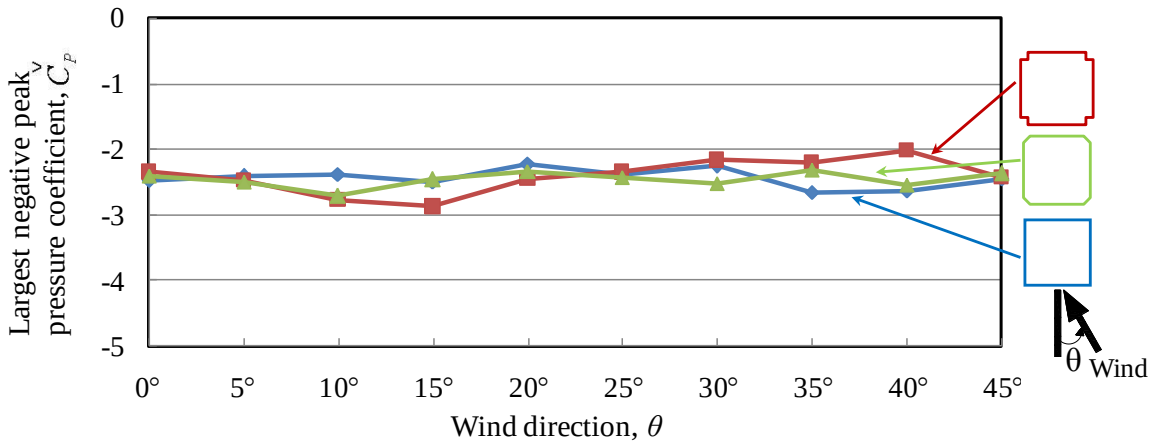

Figure 2.8 Variation of largest negative peak pressure coefficients with wind direction (θ) for Square corner modification models

2.4 **Effect of Tapering**

This section considers the tapered models with square cross-sections and compares them with the Square model. The models are Square, Sq-Tapered and Sq-Setback shapes, as shown in Table 2.1(b).

2.4.1 *Largest negative local peak pressure coefficients* ($\breve{C}_P(i)$)

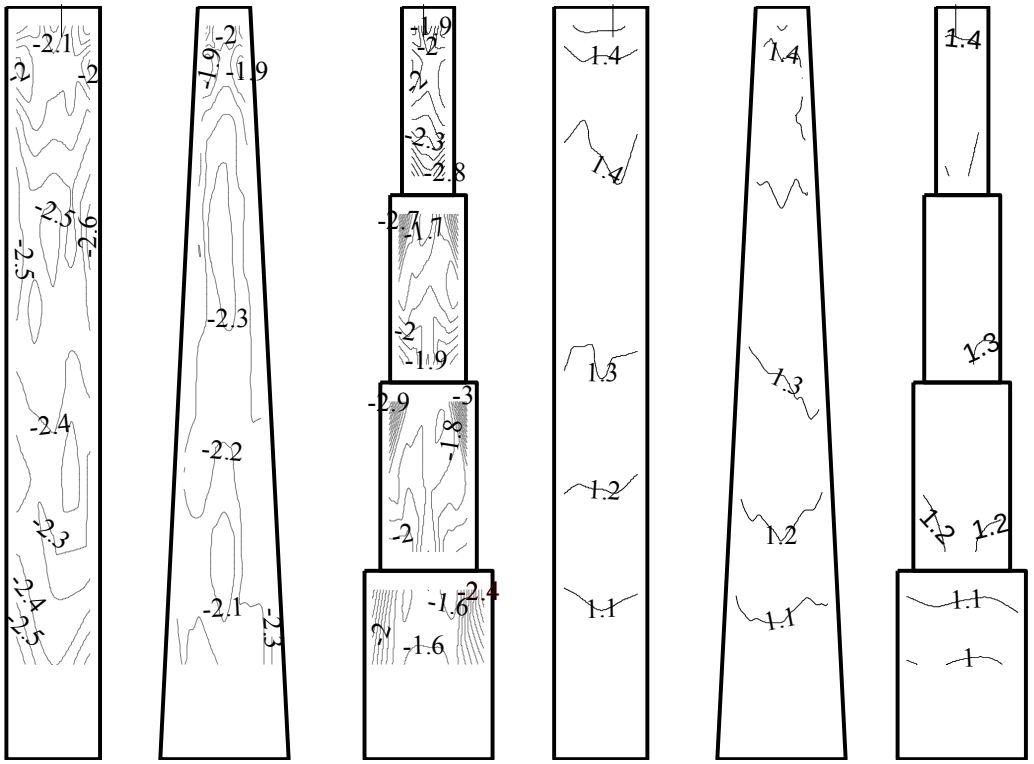

(a) Square (b) Sq-Tapered (c)Sq-Setback
Figure 2.9(a) Distribution of largest negative peak pressure coefficients for Taper models

(a) Square (b)Sq-Tapered (c)Sq-Setback
Figure 2.9(b) Distribution of largest positive peak pressure coefficients for Taper models

Figure 2.9(a) shows the $\breve{C}_P(i)$ distribution for the models mentioned in 3.2.1. They vary smoothly for all models. The peak suctions occur close to the corner regions for the Square and Setback models whereas for the Taper model, the largest values occur at mid height of the center region and at 0.125*H* of the corner region. The largest suctions occur at the top corner regions of

each step of the Sq-Setback model. The absolute largest negative peak pressure coefficients of all wind directions and tap locations were Sq-Taper: 2.34, and Sq-Setback: 3.05.

2.4.2 *Largest positive local peak pressure coefficients* ($\hat{C}_P(i)$)

Figure 2.9(b) shows the $\hat{C}_P(i)$ distribution for the Square, Sq-Tapered and Sq-Setback models. They vary smoothly for all models. For all models, the $\hat{C}_P(i)$ values increase with height. The $\hat{C}_P(i)$ distribution varies almost constantly for the Square and Sq-Taper models whereas for the Sq-Setback model, they are larger at the corner regions as in the case of $\hat{C}_P(i)$ values. The absolute largest positive peak pressure coefficients of all wind directions and tap locations were Sq-Taper: 1.43, and Sq-Setback: 1.44.

2.4.3 *Variation of largest negative peak pressures with wind direction* (θ)

Figure 2.10 shows the maximum $\check{C}_P$ for each wind direction. The largest and smallest $\check{C}_P$ values occur for the Sq-Setback model and the largest values occur for wind directions 0^o to 10^o when the flow is perpendicular to the surface. The variation between the largest and smallest values is larger than for the Square and Sq-Tapered models, whereas they vary between -1.88 and -2.34 for the Sq-Tapered model.

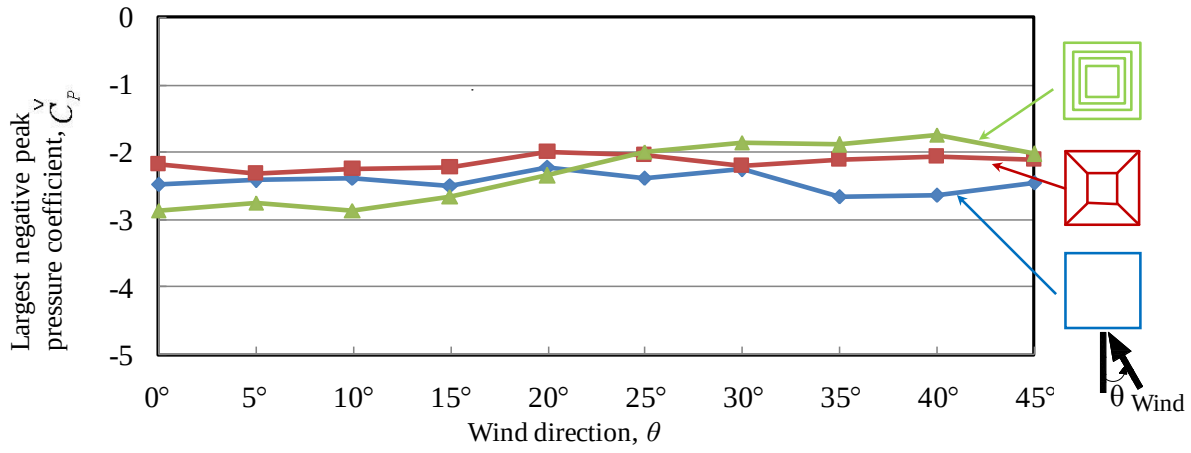

Figure 2.10 Variation of largest negative peak pressure coefficients with wind direction (θ) for Taper models

2.5 **Effect of number of surfaces**

This section, considers the polygonal models of Triangular, Square, Pentagon, Hexagon, Octagon, Dodecagon and Circular cross-sections, as shown in Table 2.1(a), and the effect of increasing number of surfaces on local peak pressures.

2.5.1 *Largest negative local peak pressure coefficients* ($\check{C}_P(i)$)

Figure 2.11 shows the $\check{C}_P(i)$ distributions for all the polygonal models with increase in number of surfaces. They vary smoothly for all models. The largest peak suctions occur close to the corner regions for all models at various heights. The peak suctions occur at 0.6*H*, 0.78*H*, 0.125*H*, 0.98*H*, 0.98*H*, 0.98*H* and 0.125*H* for the Triangular, Square, Pentagon, Hexagon, Octagon, Dodecagon and Circular models. For the Pentagon model, the peak suctions occurs at the acute bottom corner whereas for the Hexagon model, they occur at the top and at the acute bottom corners as well. The absolute largest negative peak pressure coefficients of all wind directions and tap locations were Pentagon: 3.13, Hexagon: 2.65, Octagon: 2.56, Dodecagon: 2.85, and Circular: 2.33.

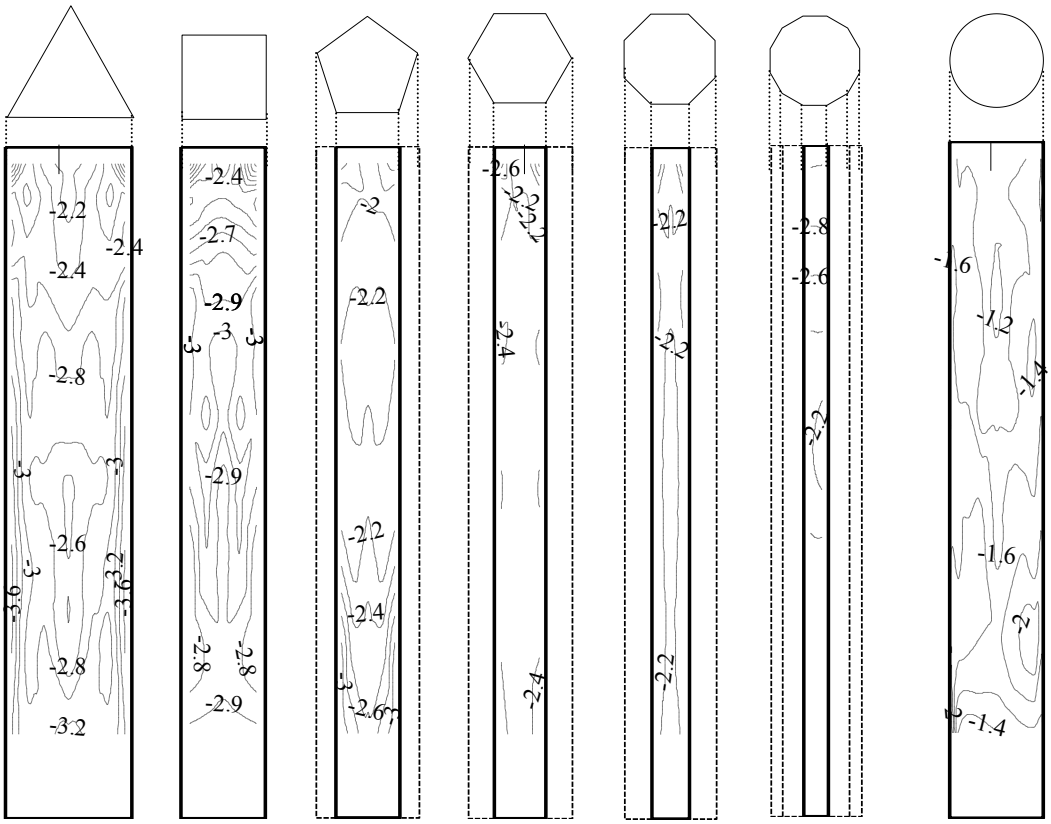

(a) Triangular (b) Square (c) Pentagon (d) Hexagon (f) Octagon (g)Dodecagon (h)Circular

Figure 2.11 Largest negative peak pressure coefficients for Polygon models

2.5.2 *Largest positive local peak pressure coefficients* ($\hat{C}_P(i)$)

Figure 2.12 shows the $\hat{C}_P(i)$ distributions for all the polygonal models with increasing of number of surfaces. They vary smoothly for all models. $\hat{C}_P(i)$ values occur at heights from 0.85H to 0.925H for all models, whereas for the Pentagon model a slightly higher $\hat{C}_P(i)$ also occurs even at the acute bottom corner (0.125H). $\hat{C}_P(i)$ values decrease as the width of the surface decreases for the Triangular, Square, Pentagon and Hexagon models, as seen in the Figure.11. The absolute largest positive peak pressure coefficients of all wind directions and tap locations were Pentagon: 1.64, Hexagon: 1.62, Octagon: 1.68, Dodecagon: 1.66, and Circular: 1.53.

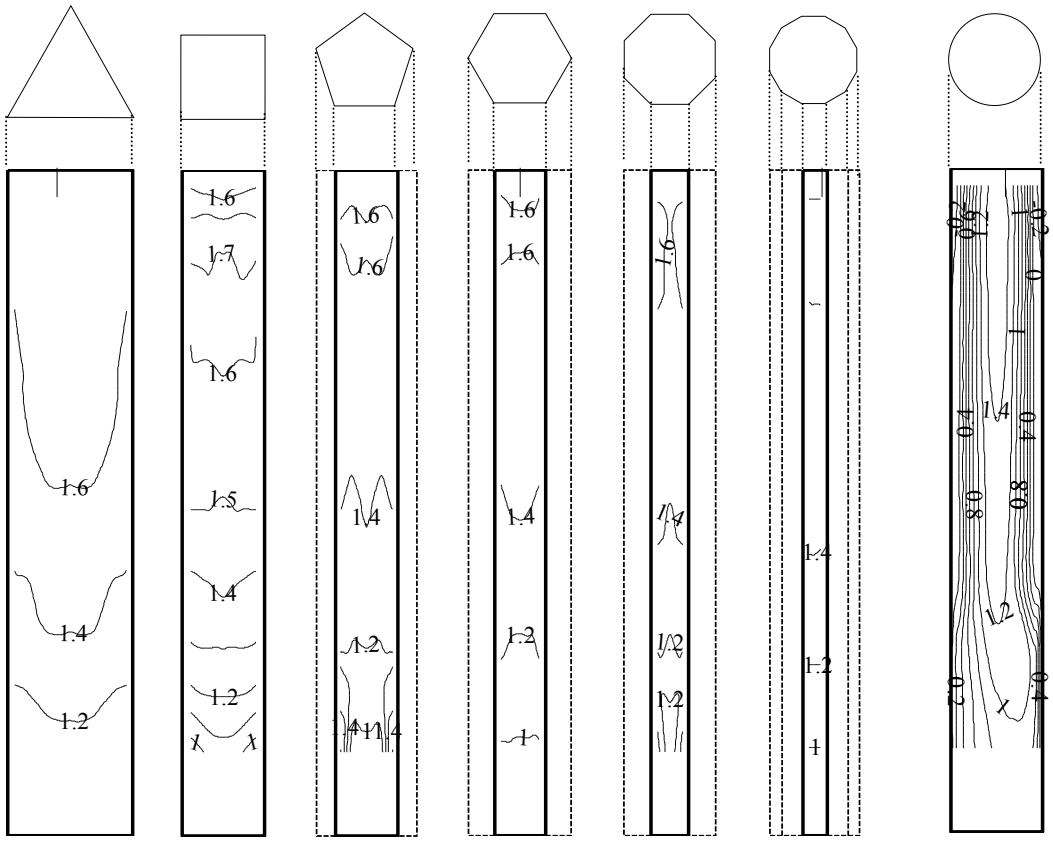

(a) Triangular (b) Square (c) Pentagon (d) Hexagon (f) Octagon (g) Dodecagon (h)Circular

Figure 2.12 Largest positive peak pressure coefficients for Polygon models

2.5.3 *Variation of largest negative peak pressures with wind direction* (θ)

Figure 2.13 shows the maximum $\hat{C}_P$ for each wind direction for all the polygonal models. As shown in the Figure 2.13, the largest and smallest $\hat{C}_P$ values occur for the Triangular model. When the flow is perpendicular to one of the surfaces (wind direction, θ=0^o), the $\hat{C}_P$ value is maximum for the Triangular model and it reduces when the number of surfaces increases, but the largest $\hat{C}_P$ is around -2.2 for the Pentagon, Hexagon, Octagon and Circular models.

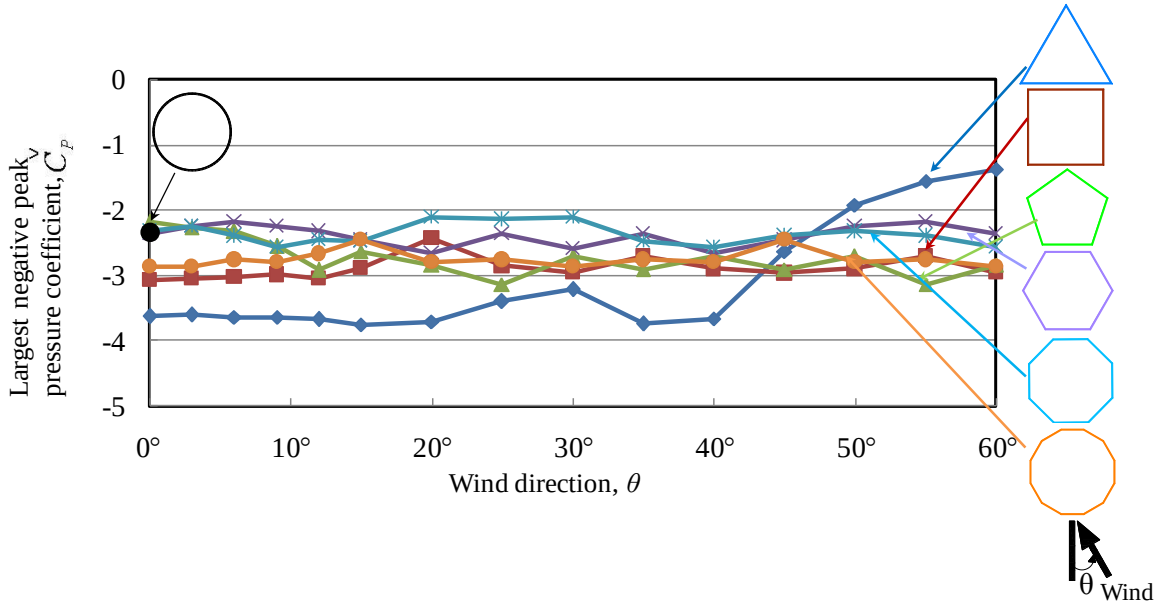

Figure 2.13 Variation of largest negative peak pressure coefficients with wind direction (θ) for Polygon models

2.6 **Summary**

The experimental facilities and models for pressure measurement tests were introduced. The effects of corner modification, tapering, increasing number of surfaces (Polygonal models) on local peak pressures were investigated. Also the effects of wind direction on local peak pressures were investigated. In this chapter, the straight polygon models, corner modification models and tapered models were considered. These models are shown in Table 2.2 (a-b) and Table 2.2(d).

1. For the models Triangular, Tri-Corner cut, Clover, Square, Sq-Corner cut, Sq-Chamfered model, the $\check{C}_P$ occurred at the corner regions. For Sq-Tapered model, the $\check{C}_P$ occurred even at the center of the surface at around 0.5H to 0.6H whereas for Sq-Setback model, the $\check{C}_P$ occurred upper side corners of each step. The maximum of $\check{C}_P$ occurred for Triangular model among all the straight polygonal models.
2. For all the models, the $\hat{C}_P$ varies very smoothly for all the models.

2.6.1 Largest negative peak pressures among all wind directions and all pressure taps – Occurrence height and wind direction

Model	$C_{p,\max}^{\vee}$	Wind direction	Height (z/H)
Triangular	-3.75	15^o	0.50
Square	-3.06	0^o	0.78
Pentagon	-3.14	25^o	0.13
Hexagon	-2.65	20^o	0.98
Octagon	-2.56	9^o	0.98
Dodecagon	-2.85	3^o	0.93
Circular	-2.34	0^o	0.25
Tri-Corner cut	-3.12	115^o	0.25
Clover	-3.13	35^o	0.98
Square	-2.68	130^o	0.13
Sq-Corner cut	-3.21	170^o	0.60
Sq-Chamfered	-2.76	190^o	0.70
Sq-Tapered	-2.34	95^o	0.70
	-2.34	115^o	0.13
Sq-Setback	-3.05	280^o	0.48

Table 2.4 Largest negative peak pressures among all wind directions and all pressure taps – Occurrence height and wind direction

2.6.2 Largest positive peak pressures among all wind directions and all pressure taps – Occurrence height and wind direction

Model	$\hat{C}_{p,\max}$	Wind direction	Height (z/*H*)
Triangular	1.80	9^o	0.93
Square	1.72	15^o	0.93
Pentagon	1.64	12^o	0.93
Hexagon	1.62	20^o	0.93
Octagon	1.68	15^o	0.85
Dodecagon	1.66	9^o	0.93
Circular	1.54	0^o	0.93
Tri-Corner cut	1.64	15^o	0.93
Clover	1.62	105^o	0.93
Square	1.44	30^o	0.93
Sq-Corner cut	1.43	205^o	0.93
Sq-Chamfered	1.45	355^o	0.93
Sq-Tapered	1.44	200^o	0.85
Sq-Setback	1.45	5^o	0.93

Table 2.5 Largest positive peak pressures among all wind directions and all pressure taps – Occurrence height and wind direction

Chapter III

EFFECTS OF TWISITING ANGLE OF HELICAL MODELS ON LOCAL PEAK PRESSURES

In this chapter, the helical models with various twisting angles were considered to investigate the effect of twisting on local peak pressure coefficients. The important aspect is, the complicated sectional shapes are basically good with regard to aerodynamic properties for crosswind responses which are key issue in tall-building wind-resistant design. The sectional shapes of the helical models were triangular, square, pentagonal, hexagonal, octagonal, dodecagonal and circular and the twisting angles are 60^o, 180^o and 360^o for triangular cross-sectional model, 90^o and 180^o for square cross-sectional model and 180^o for all polygonal models mentioned in the above.

3.1 **Experimental models**

The tall building models used for this study are shown in Table 3.1. All the models had the same volume, and Tri-60^{o}Hel, Tri-180^{o}Hel, Tri-360^{o}Hel, Sq-90^{o}Hel, Sq-180^{o}Hel, Penta-180^{o}Hel, Hexa-180^{o}Hel, Octa-180^{o}Hel, and Dodeca-180^{o}Hel.

			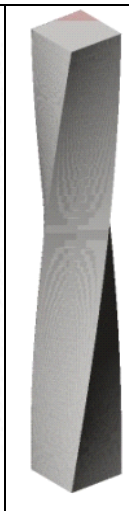	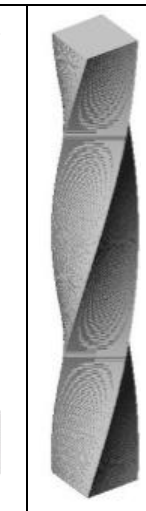				
(a)Tri-60^{o}Hel	(b) Tri-180^{o}Hel	(c) Tri-360^{o}Hel	(d) Sq-90^{o}Hel	(e)Sq-180^{o}Hel	(f) Penta-180^{o}Hel	(g) Hexa-180^{o}Hel	(h) Octa-180^{o}Hel	(i) Dodeca-180^{o}Hel

Table 3.1 Configurations of helical models

3.2 **Largest negative local peak pressure coefficients ($\hat{C}_P(i)$)**

$\hat{C}_P(i)$ distributions were discussed for the helical models shown in Table 3.1. Figure 3.2, Figure 3.4 and Figure 3.5 show the $\hat{C}_P(i)$ distributions for all helical models. They vary smoothly for the Triangular and Square models as can be seen in Figure 2.11, but for the helical models they vary widely, showing larger differences between the corner regions and on the surfaces. $\hat{C}_P(i)$ increases as the twisting angle of the Helical model increases for both Triangular and Square cross-sectional models. Occurrence height of peak suctions also increases with twisting angle of the Helical models. The maximum $\hat{C}_P(i)$ occur at heights $0.85H$ - $0.925H$ for all the helical models of polygonal shapes, whereas it occurs at $0.125H$ for the Penta-180^{o}Hel model.

The variation of $\check{C}_P(i)$ between upper and lower levels of the models reduces as the number of surfaces increases for the 180°Helical polygon models.

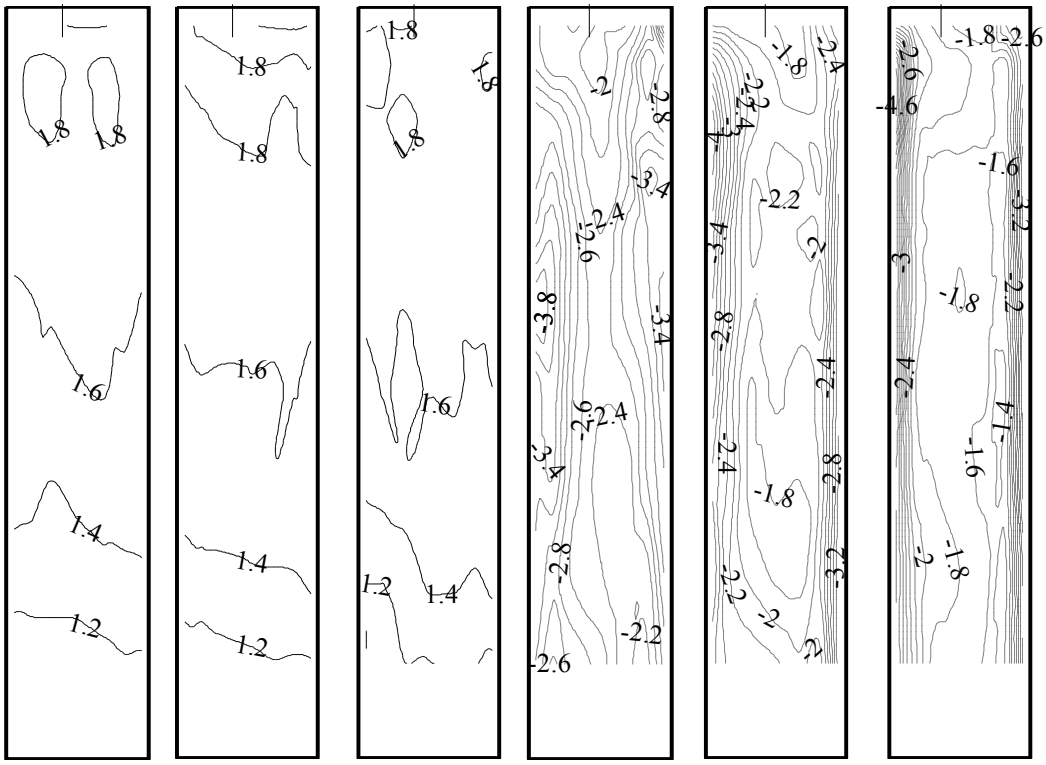

(a) Tri-60°Hel (b)Tri-180°Hel (c) Tri-360°Hel
Figure 3.1 Largest positive peak pressure coefficients for Triangular helical models

(a) Tri-60°Hel (b) Tri-180°Hel (c) Tri-360°Hel
Figure 3.2 Largest negative peak pressure coefficients for Triangular helical models

3.3 **Largest positive local peak pressure coefficients ($\hat{C}_P(i)$)**

Figure 3.1, Figure 3.3 and Figure 3.6 show the $\hat{C}_P(i)$ distributions for the helical models of Triangular cross-section (Tri-60°Hel, Tri-180°Hel, and Tri-360°Hel), Square cross-section (Sq-90°Hel and Sq-180°Hel), and polygonal models (Tri-180°Hel, Sq-180°Hel, Penta-180°Hel, Hexa-180°Hel, Octa-180°Hel, and Dodeca-180°Hel). They vary smoothly for the Triangular and Square models as we can seen from Figure 10, but for the Helical models they also vary smoothly and increase towards upper levels. The $\hat{C}_P(i)$ values are higher for the helical models of Tri-

angular cross-sections than for the helical models of Square cross-sections. The maximum $\hat{C}_P(i)$ values occur at 0.125*H* for Penta-180°Hel as in the case of the straight Pentagon model.

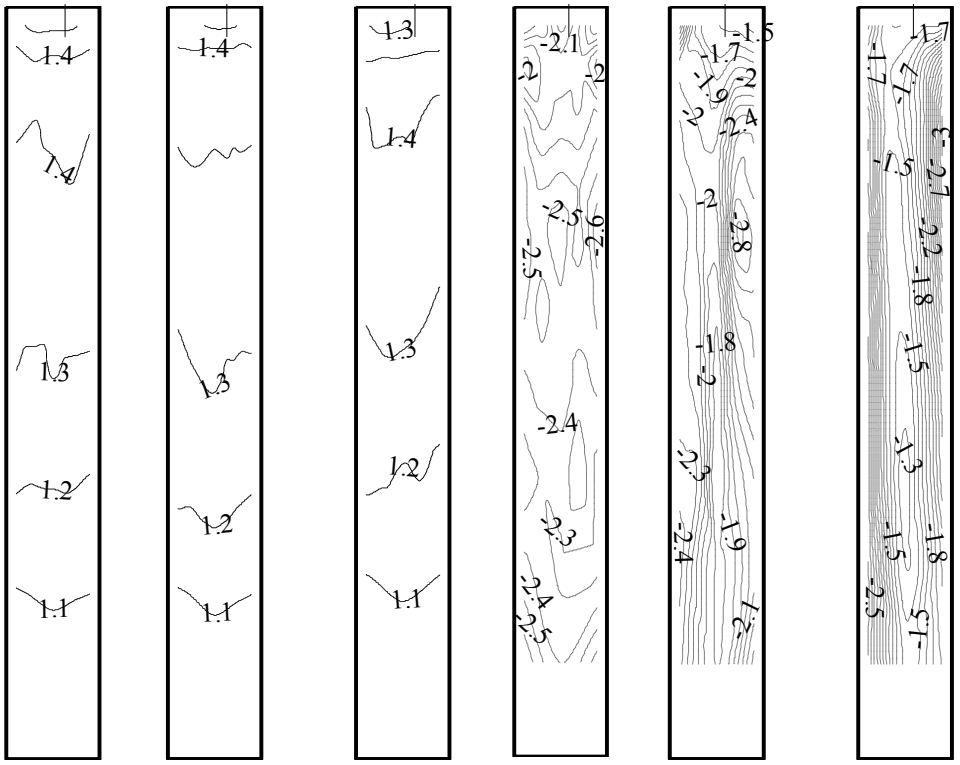

(a) Square (b) Sq-90°Hel (c) Sq-180°Hel

Figure 3.3 Largest positive peak pressure coefficients for Square helical models

(a) Square (b) Sq-90°Hel (c) Sq-180°Hel

Figure 3.4 Largest negative peak pressure coefficients for Square helical models

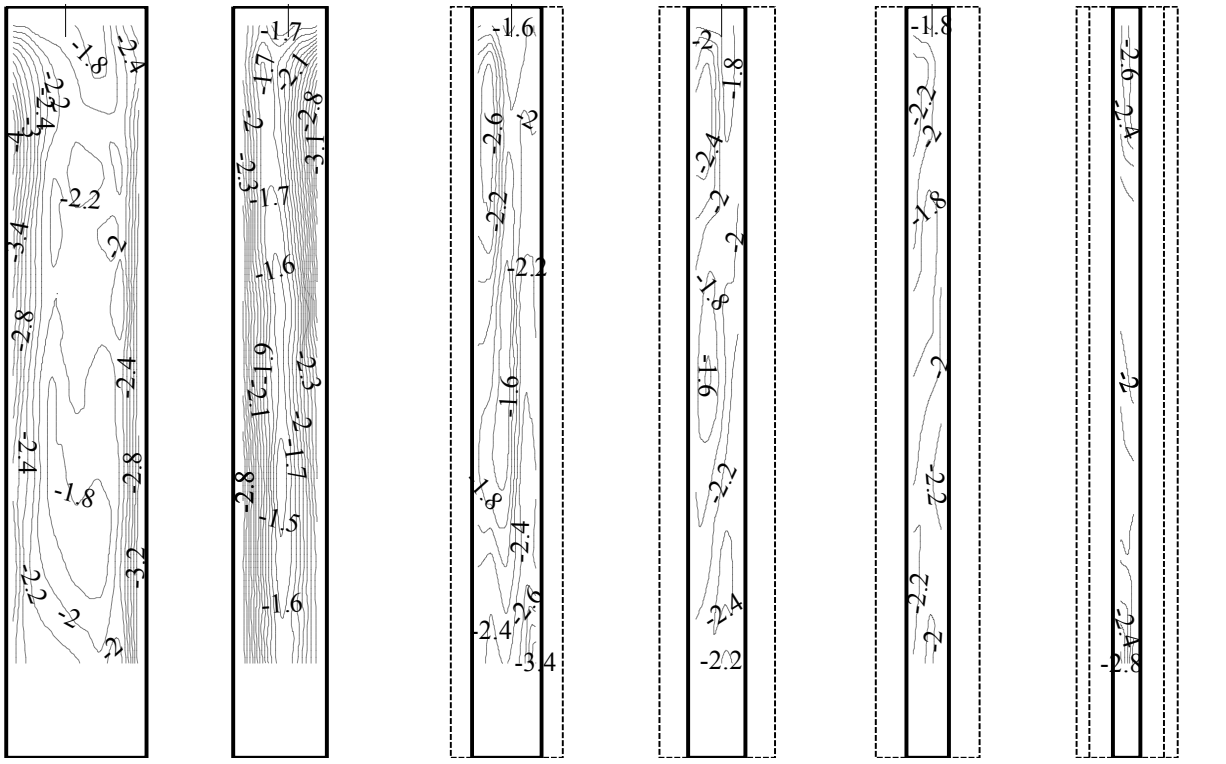

(a) Tri-180°Hel (b)Sq-180°Hel (c)Penta-180°Hel (d)Hexa-180°Hel (e)Octa-180°Hel (f)Dodeca-180°Hel

Figure 3.5 Largest negative peak pressure coefficients for polygonal helical models

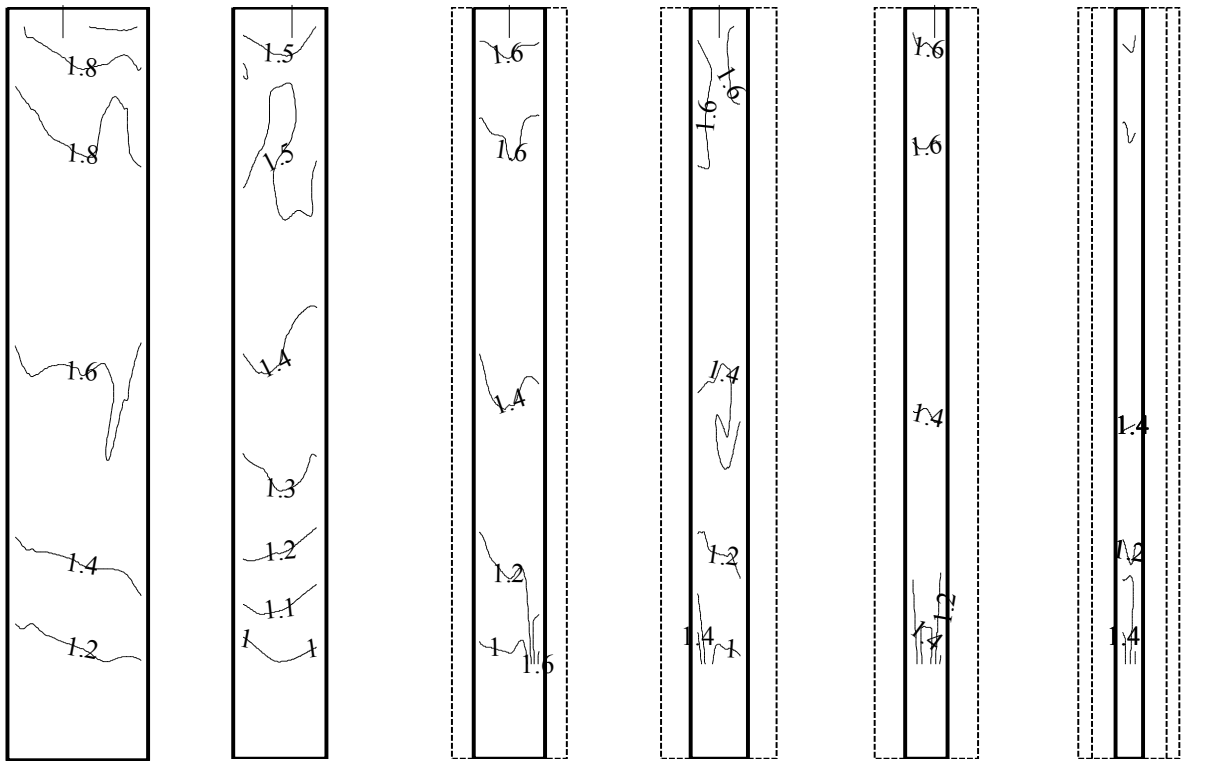

(a) Tri-180°Hel (b)Sq-180°Hel (c)Penta-180°Hel (d)Hexa-180°Hel (e)Octa-180°Hel (f)Dodeca-180°Hel

Figure 3.6 Largest positive peak pressure coefficients for polygonal helical models

3.4 **Variation of largest negative peak pressures with wind direction (θ)**

Figs 3.7-3.9 show the maximum $\hat{C}_P$ for each wind direction for all the helical models. At 0^o wind direction the $\hat{C}_P$ values are higher for the Tri-360^oHelicl model and decrease as twisting angle decreases, whereas for the Square cross-section helical models, it is the same at 0^o wind direction, as can be seen in Figure 3.8. The variation of $\hat{C}_P$ with wind direction is high for the helical models of Triangular cross-sections and the variation is low for the helical models of Square cross-sections, whereas the variation of $\hat{C}_P$ with wind direction is low for the Octa-180^oHel model compared with all polygonal helical models.

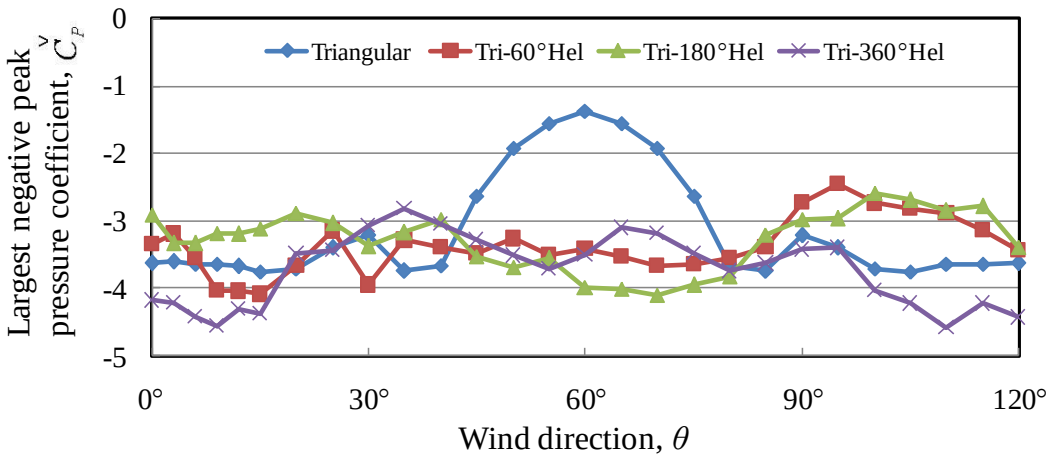

Figure 3.7 Variation of largest negative peak pressure coefficients with wind direction (θ) for Triangular helical models

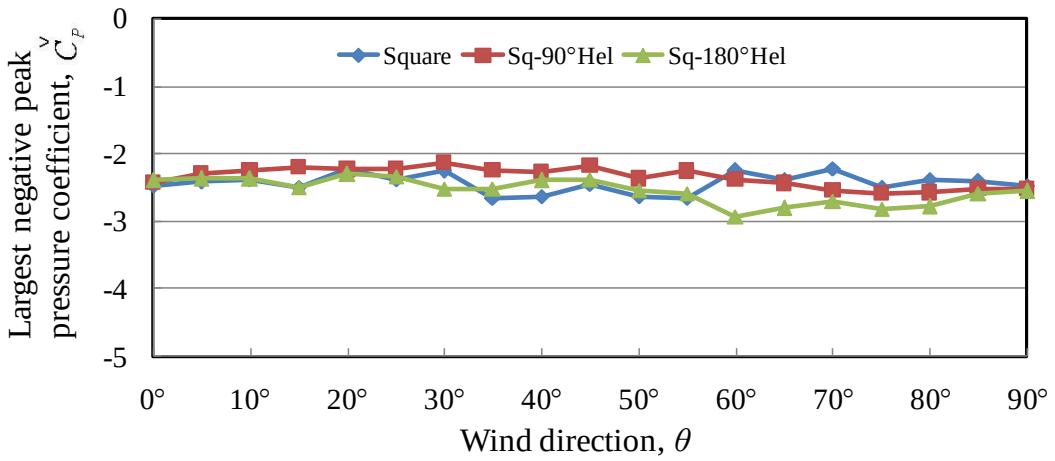

Figure 3.8 Variation of largest negative peak pressure coefficients with wind direction (θ) for Square helical models

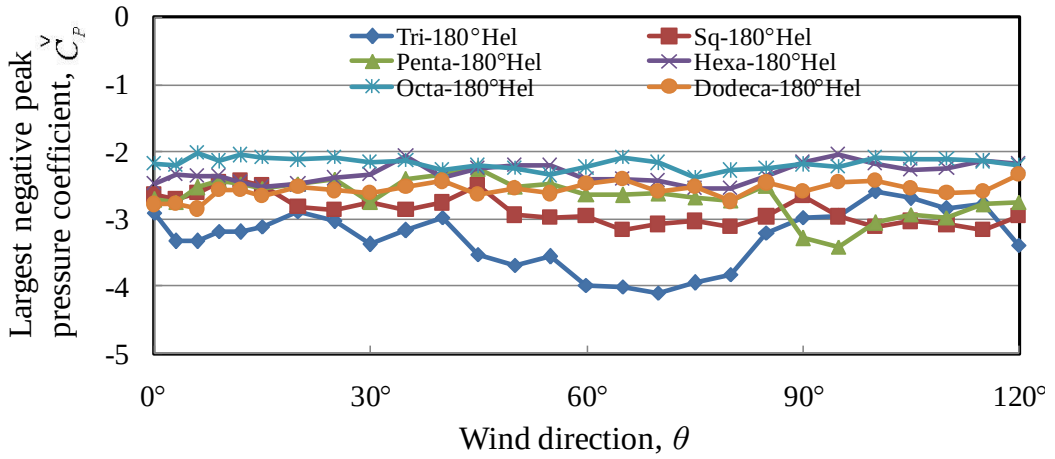

Figure 3.9 Variation of largest negative peak pressure coefficients with wind direction (θ) for Polygonal helical models

3.5 **Summary**

Helical models of various cross-sectional shapes with different twisting angles were introduced in this chapter. The effects of twisting angle of helical models of Triangular, Square, Pentagon, Hexagon, Octagon, Dodecagon and Circular models on local peak pressures were investigated.

1. For helical models, the distribution of $\check{C}_P$ varies widely and peak suctions occurred at the corners and even on the surfaces, but the area occupied by the peak suctions is very limited comparatively with the straight polygon models. When the twisting angle of helical model increases, the $\check{C}_P$ value and height at which it occurs also increases for both

Triangular and Square cross-sectional models. Helical models of polygonal models with 180^o twisting, the trend of maximum of $\check{C}_P$ is same as straight polygonal models.

2. The $\hat{C}_P$ values are very smooth for Square, Sq-90°Hel, Sq-180°Hel models than Triangular, Tri-60°Hel, Tri-180°Hel and Tri-360°Hel models.

3.5.1 Largest negative peak pressures among all wind directions and all pressure taps – Occurrence height and wind direction

Model	$\check{C}_{p,\max}$	Wind direction	Height (z/H)
Tri-60°Hel	-3.94	30°	0.60
Tri-180°Hel	-4.10	70°	0.85
Tri-360°Hel	-4.57	110°	0.85
Sq-90°Hel	-2.78	250°	0.70
Sq-180°Hel	-3.01	170°	0.85
Penta-180°Hel	-3.41	95°	0.13
Hexa-180°Hel	-2.54	75°	0.85
Octa-180°Hel	-2.38	75°	0.85
Dodeca-180°Hel	-2.84	6°	0.13

Table 3.2 Largest negative peak pressures among all wind directions and all pressure taps – Occurrence height and wind direction

3.5.2 Largest positive peak pressures among all wind directions and all pressure taps – Occurrence height and wind direction

Model	$\hat{C}_{p,\max}$	Wind direction	Height (z/H)
Tri-60°Hel	1.84	65°	0.85
Tri-180°Hel	1.95	80°	0.85
Tri-360°Hel	1.88	55°	0.85
Sq-90°Hel	1.45	260°	0.93
Sq-180°Hel	1.42	345°	0.85
Penta-180°Hel	1.69	115°	0.93
Hexa-180°Hel	1.68	6°	0.93
Octa-180°Hel	1.69	75°	0.93
Dodeca-180°Hel	1.66	12°	0.93

Table 3.3 Largest negative peak pressures among all wind directions and all pressure taps – Occurrence height and wind direction

Chapter IV

COMBINED EFFECT OF CORNER MODIFICATION, TAPERING AND TWISITING ANGLE ON LOCAL PEAK PRESSURES

In this chapter, four types of composite models were considered. The combined effects of corner modification, tapering, and twisting on local peak pressures were investigated. The combinations of twisting with corner cut, taper with twisting, taper with corner cut and twisting and setback with rotation were considered. The composite models with various twisting angles were considered to investigate the effect of combination effect on local peak pressure coefficients.

4.1 **Experimental models**

In this section, the combination models were considered which are shown in Table 4.1. The models are Sq-180^{o}Hel &Corner cut, Sq-Tapered & 180^{o}Hel, Sq-Tapered & 360^{o}Hel &Corner cut, and Sq-Setback & 45^{o}Rotate.

			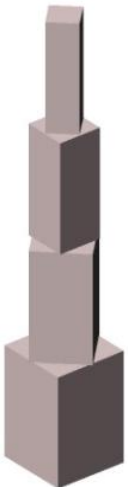
(a) Sq-180^{o}Hel &Corner cut	(b)Sq-Tapered & 180^{o}Hel	(c) Sq-Tapered & 360^{o}Hel & Corner cut	(d)Sq-Setback & 45^o Rotate
Table 4.1 Composite models			

4.2 **Largest negative local peak pressure coefficients ($\check{C}_P(i)$)**

Figure 4.1 show the distribution of the $\check{C}_P(i)$ were discussed for 180^{o}Hel &Corner cut, Tapered & 180^{o}Hel, Tapered & 360^{o}Hel &Corner cut, and Setback & 45^{o}Rotate models. $\check{C}_P(i)$ were chosen from each pressure tap from all the wind directions. The distributions of the $\check{C}_P(i)$ vary widely for all the models. Peak suctions occur above 0.5H for corner cut (180^{o}Hel &Corner cut, and Tapered & 360^{o}Hel &Corner cut) models whereas for Tapered & 180^{o}Hel and Setback & 45^{o}Rotate models peak suctions occurs even at 0.125H. For the Setback & 45^{o}Rotate model, the suction occurs at the corners of all the steps. The absolute largest negative peak pressure coefficients of all wind directions and tap locations were 180^{o}Hel &Corner cut: 2.49, Tapered & 180^{o}Hel:2.94, Tapered & 360^{o}Hel &Corner cut: 2.51, and Setback & 45^{o}Rotate:3.2.

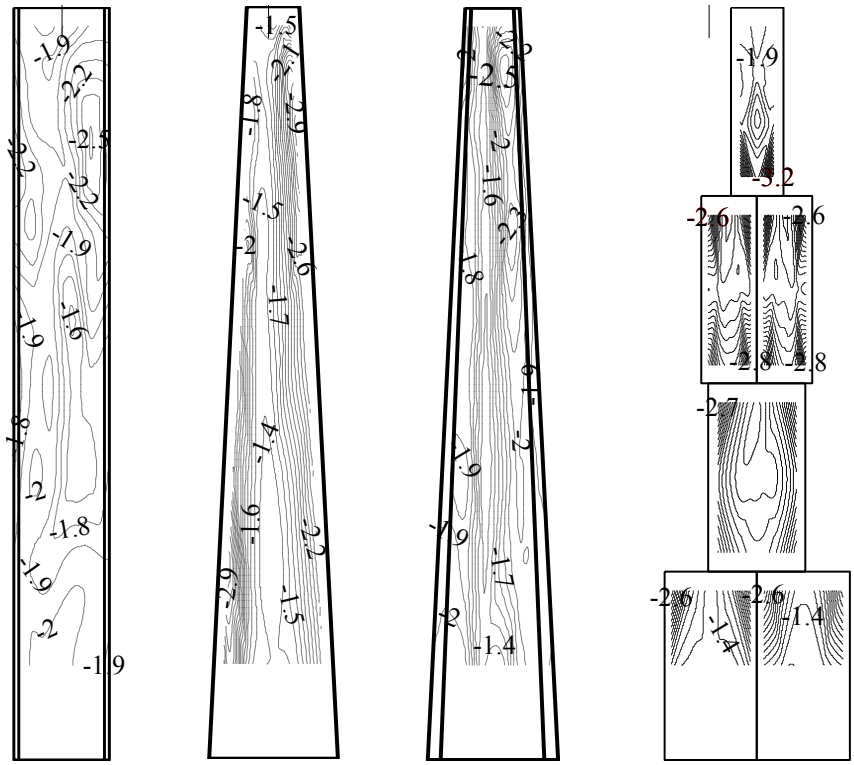

(a)Sq-180°Hel & Corner cut | (b)Sq-Tapered & 180°Hel | (c)Sq-Tapered& 360°Hel & Corner cut | (d) Sq-Setback & 45° Rotate

Figure 4.1 Largest negative peak pressure coefficients for Combination models

4.3 **Largest positive local peak pressure coefficients ($\hat{C}_P(i)$)**

Figure 4.2 show the distributions of the $\hat{C}_P(i)$ vary smoothly for all the models. The largest $\hat{C}_P(i)$ occur with the height of the model for all the models. The absolute largest positive peak pressure coefficients of all wind directions and tap locations were 180°Hel &Corner cut: 1.47, Tapered & 180°Hel:1.45, Tapered & 360°Hel &Corner cut: 1.48, and Setback & 45° Rotate: 1.51.

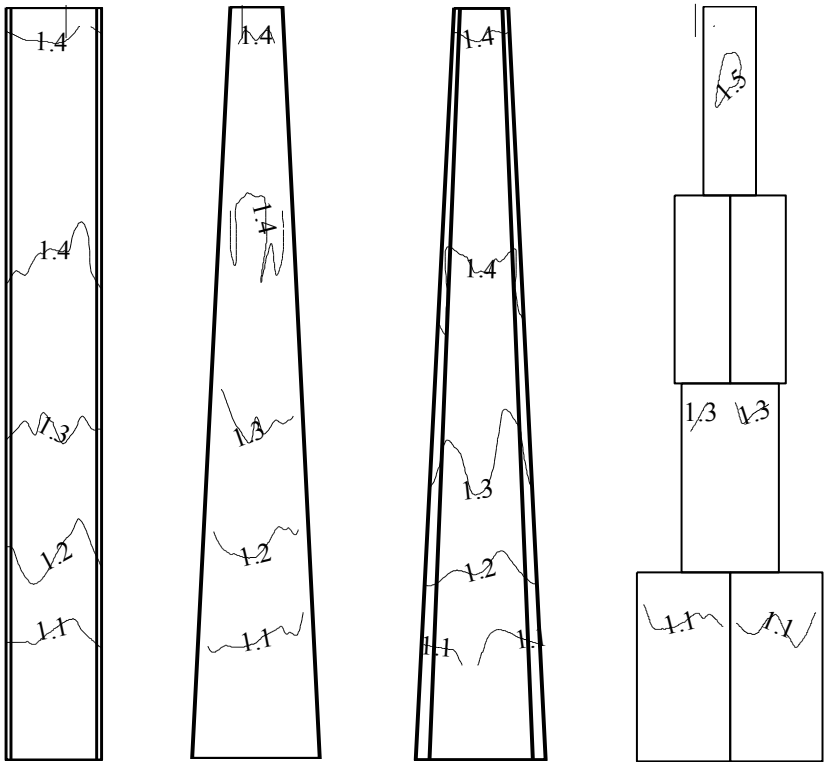

(a)Sq-180°Hel & Corner cut (b)Sq-Tapered & 180°Hel (c)Sq-Tapered& 360°Hel & Corner cut (d) Sq-Setback & 45° Rotate

Figure 4.2 Largest positive peak pressure coefficients for Combination models

4.4 **Variation of largest negative peak pressures with wind direction (θ)**

Figure 4.3, Figure 4.4, Figure 4.5 and Figure 4.6 show the variation of maximum of $\hat{C}_P$ with wind direction (θ). The comparison of $\hat{C}_P$ were made on 180°Hel &Corner cut, Tapered & 180°Hel, Tapered & 360°Hel &Corner cut, and Setback & 45°Rotate with Square, Tapered and Setback models to discuss the effect of combination of twisting and corner cut. The combination effect of corner cut & helical on $\hat{C}_P$ were shown clearly in Figure 4.3, the magnitude of the negative peak pressure coefficients of the 180°Hel &Corner cut model reduces almost for all the wind directions whereas the combination effect of taper and helical on $\hat{C}_P$ increases to higher magnitudes of $\hat{C}_P$ for the Tapered & 180°Hel model than the Tapered model as shown in Figure 4.4. The effect of 360°Hel &Corner cut of taper model shows bit higher $\hat{C}_P$ for some wind di-

rections, at the same time lower values of $\hat{C}_P$ occurred for Tapered model as shown in Figure 4.5. The Setback & 45°Rotate models shows higher values of $\hat{C}_P$ than the Setback model for all the wind directions.

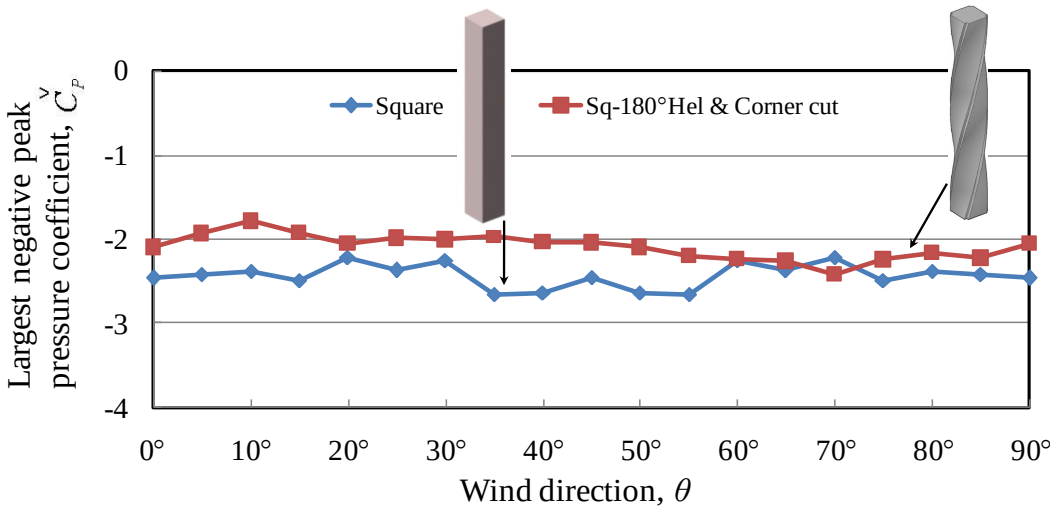

Figure 4.3 Variation of largest negative peak pressure coefficients with wind direction (θ) for Square and Sq-180°Hel &Corner cut model

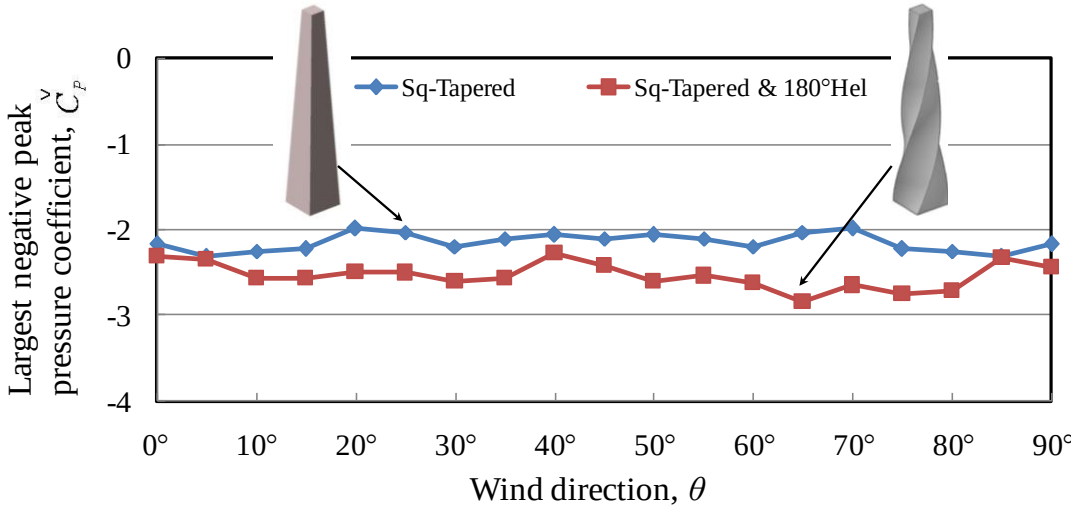

Figure 4.4 Variation of largest negative peak pressure coefficients with wind direction (θ) for the Sq-Tapered and Sq-Tapered & 180°Hel model

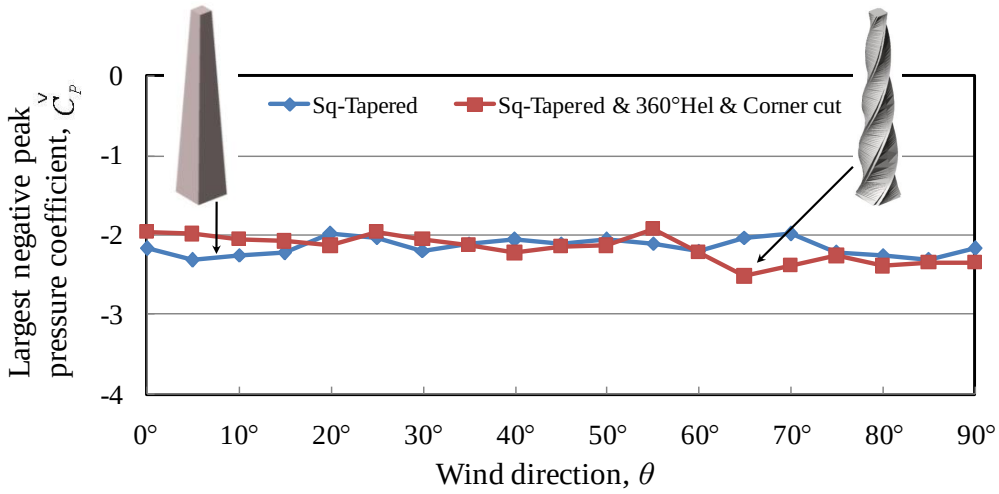

Figure 4.5 Variation of largest negative peak pressure coefficients with wind direction (θ) for the Sq-Tapered and Sq-Tapered & 360°Hel & Corner cut model

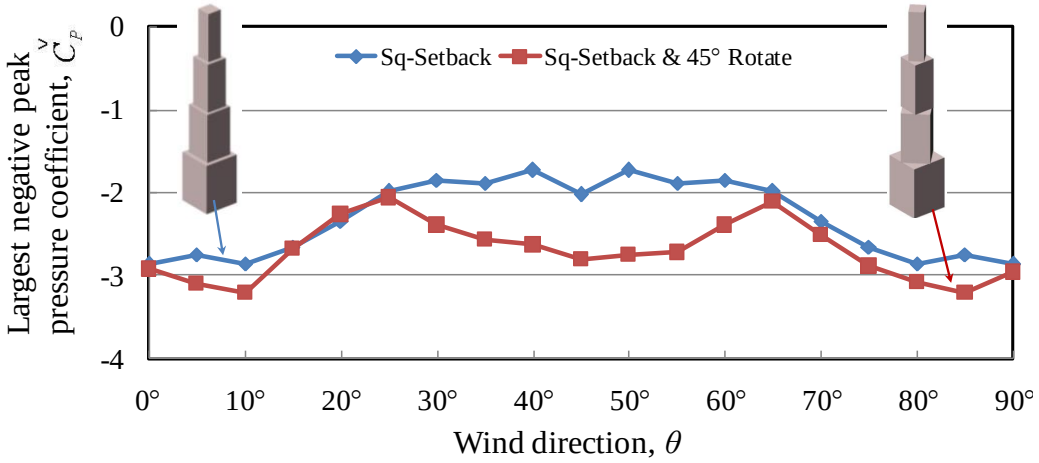

Figure 4.6 Variation of largest negative peak pressure coefficients with wind direction (θ) for the Sq-Setback and Sq-Setback & 45° Rotate

4.5 **Maximum of largest negative peak pressure coefficients ($\hat{C}_{p,\max}$)**

The maximum of the largest negative peak pressure coefficients ($\hat{C}_{p,\max}$) is the maximum value of $\hat{C}_p$ among those for all the wind directions selected for each model. Figure 4.7 (a-g) compares of $\hat{C}_{p,\max}$ for each category of models shown in Table 1. Due to the modification of corner regions, $\hat{C}_{p,\max}$ reduces and the values are equal for the Tri-Corner cut and Clover models. The $\hat{C}_{p,\max}$ value of the Sq-Corner cut model and the Sq-Setback model increases to around 16% and

12% greater than that of the Square model, as can be seen in Figure 4.7(b-c). For the Straight Polygonal models, the overall trend of $\hat{C}_{p,\max}$ decreases from Triangular model to Circular model, but the location of pressure tap may cause the slight variation in the trend for the Pentagon and Dodecagon models. As the twisting angle of the helical model increases, $\hat{C}_{p,\max}$ also increases for the Triangular and Square models, as can be seen in Figure 4.7(d). The polygonal helical models also show the same trend as the Straight Polygonal models, as can be seen in Figure 4.7(g). The combined effects of helical and corner cut (Sq-180^{o}Hel & Corner cut model) increases $\hat{C}_{p,\max}$ to 3% greater than that of the Square model. The combined effect of tapering & helical (Sq-Tapered &180^{o}Hel model) and helical & corner cut (Sq-Tapered & 360^{o}Hel & Corner cut model) increases $\hat{C}_{p,\max}$ to around 20% and 7% greater than that of the Sq-Tapered model. The Sq-Setback model with 45^o Rotation increases of $\hat{C}_{p,\max}$ to 5% greater than that of the Sq-Setback model value.

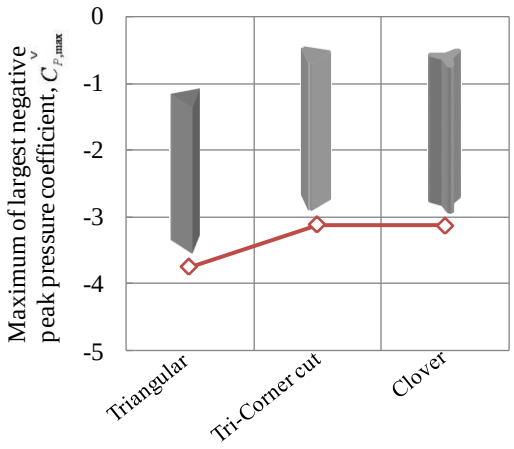

(a) Corner modification models of Triangular cross-section

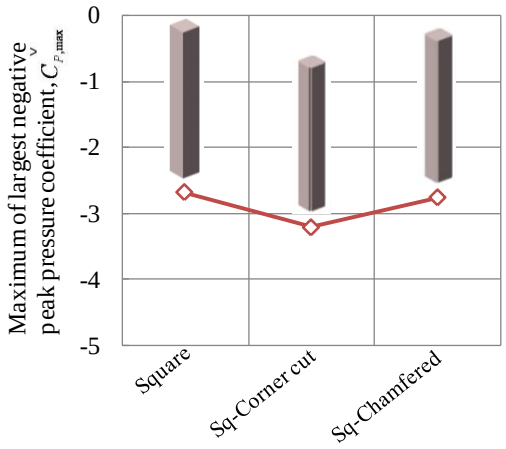

(b) Corner modification models of Square cross-section

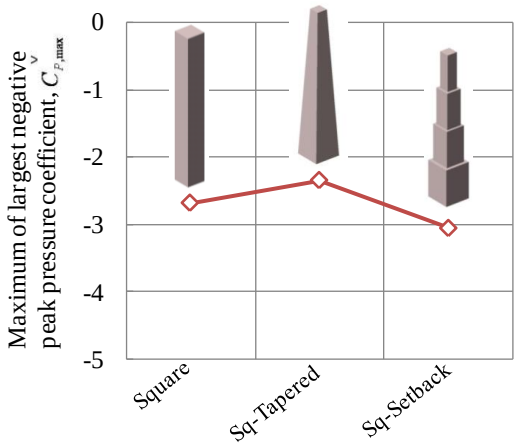

(c) Tapered models

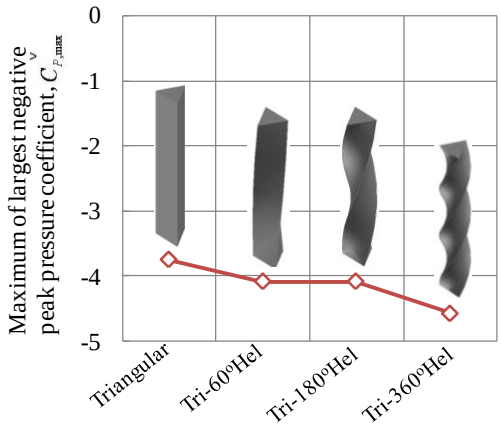

(d) Helical models of Triangular cross-section

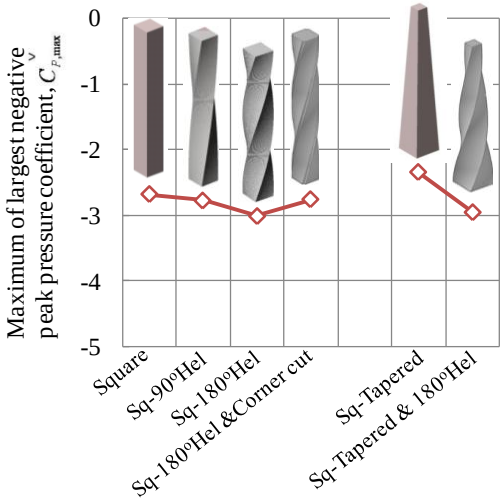

(e) Helical models of Square cross-section

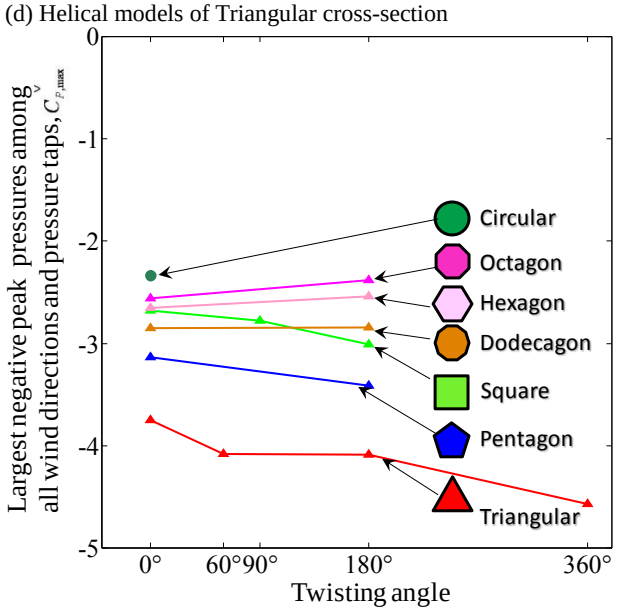

(f) Straight and 180°Helical models

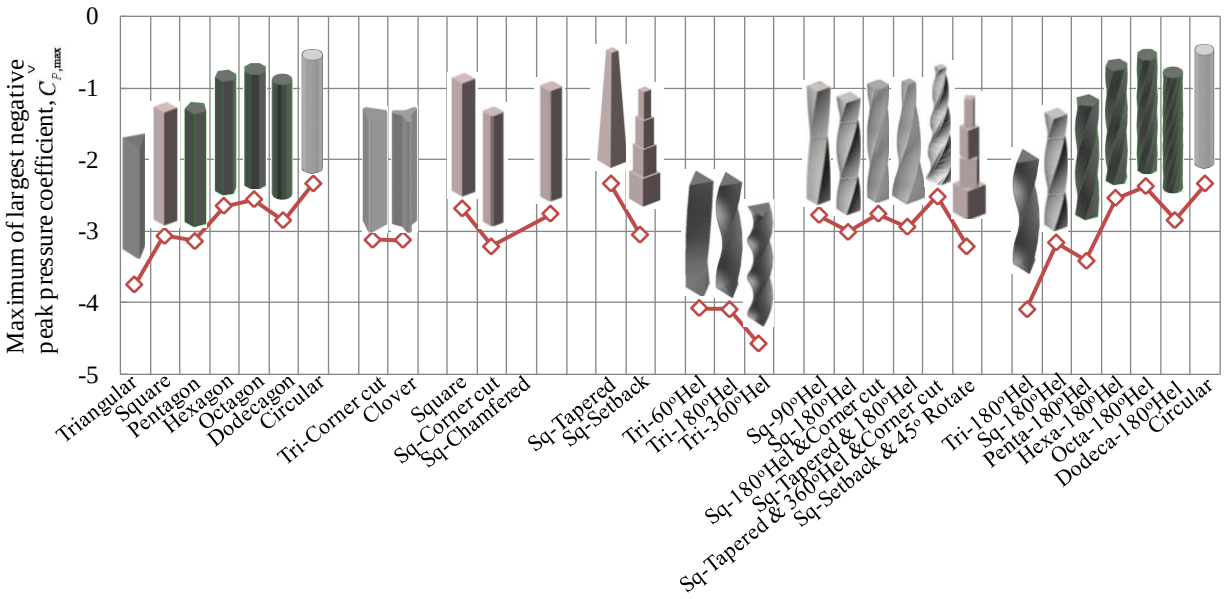

(g) All models

Figure 4.7 Comparison of maximum largest negative peak pressures ($\hat{C}_{p,\max}$)

4.6 **Summary**

Four types of composite models were considered in this chapter. The combinations of twisting with corner cut, taper with twisting, taper with corner cut and twisting and setback with rotation were considered to investigate the effects on local peak pressures. Comparisons of maximum of largest negative peak pressure coefficients of all models were made shown in Table 2.2 in Chapter-II.

1. Among all the combination models, the Setback & 45^{o}Rotate model has maximum of $\hat{C}_P$, but the distribution of $\hat{C}_P$ looks same as Setback model. The maximum of $\hat{C}_P$ value of Setback model is just 5% less than that of the Setback & 45^{o}Rotate model.

2. There is significant effect of corner cut with twisting angle of 180^{o} on the $\hat{C}_P$ value. The $\hat{C}_P$ value of Sq-180^{o}Hel & Corner cut model is around 22% less than that of Sq-Corner cut model.

3. Also there is significant effect of twisting the taper model to 180^{o}, the $\breve{C}_P$ value is increases more than around 25% than that of Sq-Tapered model.

4. The combination of corner cut with twisting has more effect on $\breve{C}_P$ value than tapered with twisting.

4.6.1 Largest negative peak pressures among all wind directions and all pressure taps – Occurrence height and wind direction

Model	$C_{p,\max}^{\vee}$	Wind direction	Height (z/*H*)
Sq-180°Hel & Corner cut	-2.50	245°	0.85
Tapered & 180°Hel	-2.90	170°	0.85
	-2.90	210°	0.25
Sq-Tapered 360°Hel & Corner cut	-2.51	65°	0.93
Sq-Setback & 45°Rotate	-3.21	10°	0.78

Table 4.2 Largest negative peak pressures among all wind directions and all pressure taps – Occurrence height and wind direction

4.6.2 Largest positive peak pressures among all wind directions and all pressure taps – Occurrence height and wind direction

Model	$C_{p,\max}^{\wedge}$	Wind direction	Height (z/*H*)
Sq-180°Hel & Corner cut	1.48	220°	0.93
Tapered & 180°Hel	1.45	255°	0.85
Sq-Tapered 360°Hel & Corner cut	1.48	170°	0.85
Sq-Setback & 45°Rotate	1.52	5°	0.93

Table 4.3 Largest negative peak pressures among all wind directions and all pressure taps – Occurrence height and wind direction

4.7 **References**

1. Bao-Shi Shiau, Ho-Chieh Chang, Measurements on the surface wind pressure characteristics of two square buildings under different wind attack angles and building gaps, BBAA VI International Colloquium on Bluff-Bodies Aerodynamics & Applications, Milano, Italy, July, 20-24, 2008.

2. Eswara Kumar Bandi, Hideyuki Tanaka, Yong Chul Kim, Kazuo Ohtake, Akihito Yoshida and Yukio Tamura, Peak pressure acting on Tall buildings with various configurations, International Journal of High-Rise Buildings, September 2013, Vol 2, No 3, 1-16.

3. Jamieson, N.J. & Carpenter, P. & Cenek, P.D., 1992, Wind induced external pressures on a tall building with various corner configurations, Journal of Wind Engineering and Industrial Aerodynamics, 41-44, 2401-2412.

4. Katagiri Junji, 1992, Wind pressure characteristics of Rectangular cylinders with Cut Corner, Summaries of technical papers of Annual Meeting, AIJ, 47-48 (in Japanese)

5. Kyle Butler, Shuyang Cao, Yukio Tamura, Ahsan Kareem, Shigehira Ozono, Surface pressure and wind load characteristics on prisms immersed in a transient gust front flow field, BBAA VI International Colloquium on Bluff-Bodies Aerodynamics & Applications, Milano, Italy, July, 20-24, 2008.

6. Ohtake Kazuo, 2000, Peak pressure coefficients for cladding of a tall building, Summaries of technical papers of Annual Meeting, AIJ, 193-194 (in Japanese)

7. Kikuchi Hirotoshi, 1997, Characteristics of peak wind pressures acting on a tall building model, Summaries of technical papers of Annual Meeting, AIJ, 209-210 (in Japanese)

8. Kim, Y.C. & Kanda, J., 2010, Characteristics of aerodynamic force and pressures on square plan buildings with height variations, Journal of Wind Engineering and Industrial Aerodynamics, 98, 449-465.

9. Masahiro Matsui, Yukio Tamura and Akihito Yoshida, Wind tunnel experiment for unsteady internal pressure in building, BBAA VI International Colloquium on Bluff-Bodies Aerodynamics & Applications, Milano, Italy, July, 20-24, 2008.

10. Melbourne, W.H., 1993, Turbulence and the Leading Edge Phenomenon, Journal of Wind Engineering and Industrial Aerodynamics, 49, 45-64.

11. Ohtake Kazuo, 2000, Peak pressure coefficients for cladding of a tall building, Summaries of technical papers of Annual Meeting, AIJ, 193-194.

12. Saathoff, P.J. & Melbourne, W.H. 1989, The generation of peak pressures in separated/reattaching flows, Journal of Wind Engineering and Industrial Aerodynamics, 32, 121-134.

13. Shuyang Cao, Yukio Tamura, Reynolds number dependence of the velocity shear effects on flow around a circular cylinder, EACWE 5, Florence, Italy, 19th – 23rd July 2009.

14. Stathopoulos, T. & Saathoff, P., 1991, Wind pressure on roofs of various geometries, Journal of Wind Engineering and Industrial Aerodynamics, 38, 273-284.

15. Sungsu Lee and Chan Wook Park, Instantaneous pressure distribution on square cylinder in Turbulent flow, BBAA VI International Colloquium on Bluff-Bodies Aerodynamics & Applications, Milano, Italy, July, 20-24, 2008.

16. Surry, D. & Djakovich, D., 1995, Fluctuating pressures on models of tall buildings, Journal of Wind Engineering and Industrial Aerodynamics, 58, 81-112.

17. Wonsul Kim, Yukio Tamura and Akihito Yoshida, Interference effects of two buildings on peak wind pressures, The seventh Asia-Pacific Conference on Wind Engineering, November 8-12, 2009, Taipei, Taiwan.

18. Ye Gao and Wan-Ki Chow, A simple method for obtaining the correct pressure coefficient at the windward frontal corner of the bluff body, The seventh Asia-Pacific Conference on Wind Engineering, November 8-12, 2009, Taipei, Taiwan.

Chapter V

EFFECTS OF POLYGONAL SHAPES ON WIND FORCES

In this chapter, nine models with various cross-sections were used to study the characteristics of wind forces on tall buildings. The models analyzed in this chapter are Triangular, Tri-Corner cut, Clover, Square, Pentagon, Hexagon, Octagon, Dodecagon and Circular models which are shown in Table 5.1-5.2. We tried to investigate the effect of these cross-sections on local, total wind forces and power spectral densities.

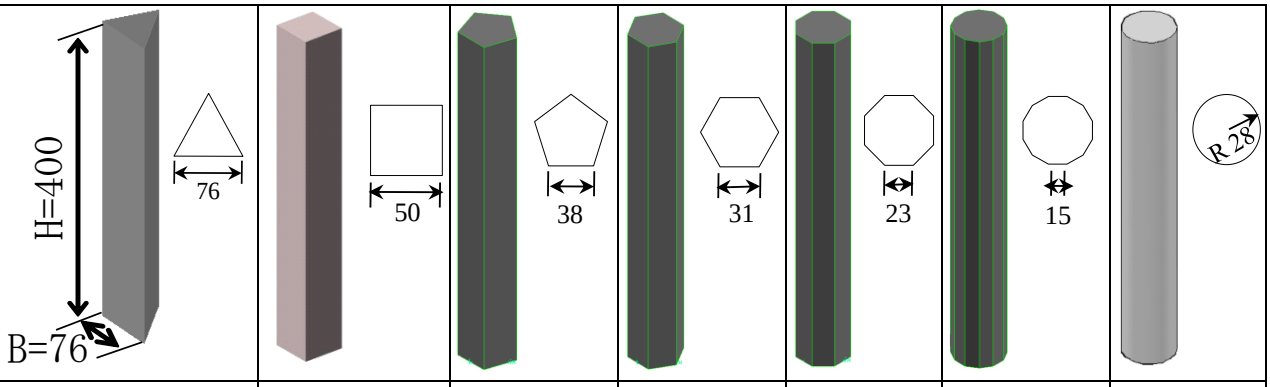

(a)Triangular	(b)Square	(c) Pentagon	(d) Hexagon	(e) Octagon	(f)Dodecagon	(g) Circular

Table 5.1 Configurations of straight polygonal models

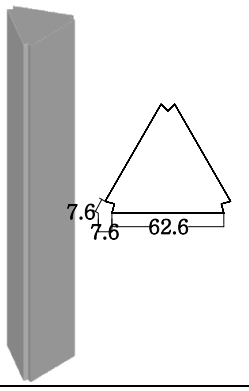

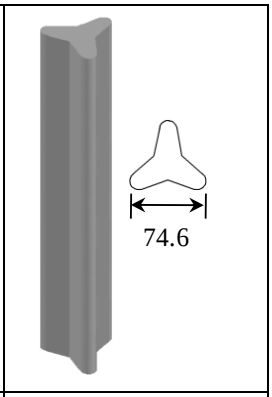

(a) Tri-Corner cut | (b) Clover

Table 5.2 Configurations of corner modification models

5.1 *Overturning moment (o.t.m) coefficients*

The mean and fluctuating overturning moment coefficients were calculated using Eq. (1).

$$\overline{C}_{MD} = \frac{\overline{M}_D}{q_H BH^2}, \quad \overline{C}_{ML} = \frac{\overline{M}_{L,}}{q_H BH^2}$$
$$C'_{MD} = \frac{M'_D}{q_H BH^2}, \quad C'_{ML} = \frac{M'_L}{q_H BH^2} \tag{1}$$

In which, $\overline{C}_{MD}$ and $\overline{C}_{ML}$ are mean OTM coefficients in along-wind and crosswind directions respectively; C'_{MD} and C'_{ML} are the corresponding fluctuating OTM coefficients. $\overline{M}_D$ and $\overline{M}_L$ are mean overturning moments in along-wind and crosswind directions, and M'_D, M'_L are fluctuating overturning moments. *B* is width of Triangular (*B*=50mm) model; *H* is model height; q_H is mean velocity pressure at model height, *H*.

5.1.1 *Effects of wind direction on over turning moment (OTM) coefficients*

Figure 5.1 shows the variation of mean along-wind OTM coefficient ($\overline{C}_{MD}$) and mean cross-wind OTM coefficient ($\overline{C}_{ML}$) with wind direction (θ). For Triangular model, shape of the $\overline{C}_{MD}$ curve is bell shaped. This shape becomes gradually almost straight line as the number of faces of the model increases from 3 faces (Triangular) to 12 faces (Dodecagon). The maximum and min-

imum values of $\overline{C}_{MD}$ are 0.98 and 0.38 for the Triangular and Dodecagon models among all the models. The maximum and minimum absolute values of $\overline{C}_{ML}$ are 0.69 and 0.002 for the Triangular and Dodecagon models among all the models. For the Dodecagon model, the absolute values of $\overline{C}_{ML}$ are around 0.002~0.07 for all wind directions. The variations in $\overline{C}_{ML}$ and $\overline{C}_{MD}$ showed similar trend, as can be seen in Figure 5.1. For the Triangular model, the minimum $\overline{C}_{MD}$ occurred at 60^o wind direction and the curve is 'U'-shaped. The variation of mean drag and mean lift force coefficients were 1.2 and 0 for the Triangular model at 0^o wind direction, which is similar to the results of Kanda et.al (1992). Figure 5.2 shows the variation of mean and fluctuating overturning moment coefficients for corner modification models (Tri-Corner cut and Clover models). $\overline{C}_{MD}$ values of the Tri-Corner cut model shows lower for all wind directions than the Triangular model. The clover model shows higher $\overline{C}_{MD}$ values than the Triangular model between wind directions 35^o and 85^o. $\overline{C}_{ML}$ values for the Triangular, Tri-Corner cut and Clover models show the similar trend for all the wind directions as shown in Figure 5.2(b). When the flow is parallel (wind direction, $\theta = 30^o$) to one of the surfaces of the Triangular, Tri-Corner cut and Clover models, $\overline{C}_{MD}$ and $\overline{C}_{ML}$ values are smaller for the Tri-Corner cut model than the Triangular and Tri-Corner cut models.

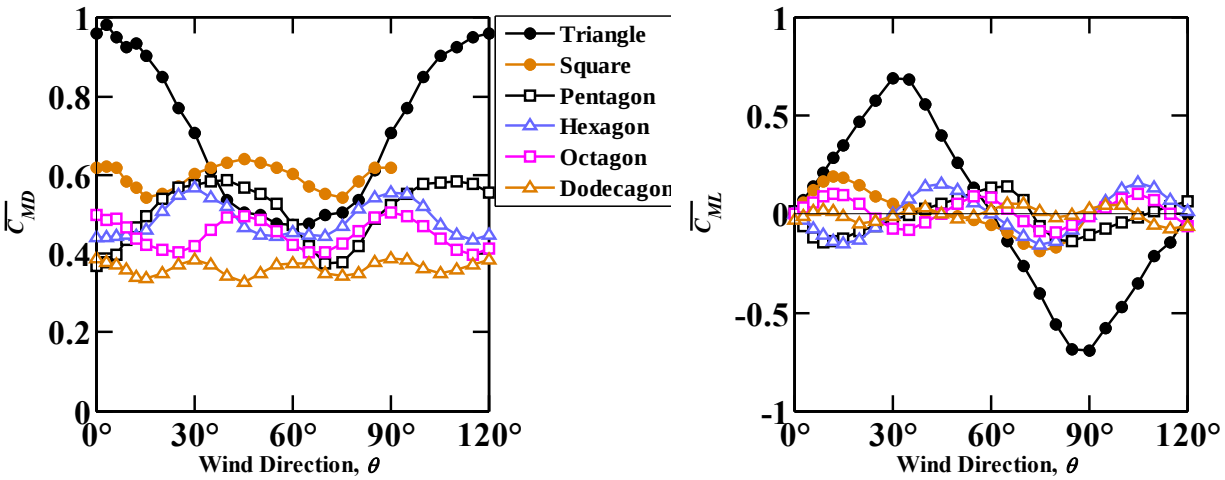

(a) Along-wind direction (b) Crosswind direction

Figure 5.1 Variation of mean overturning moment coefficients of polygonal models

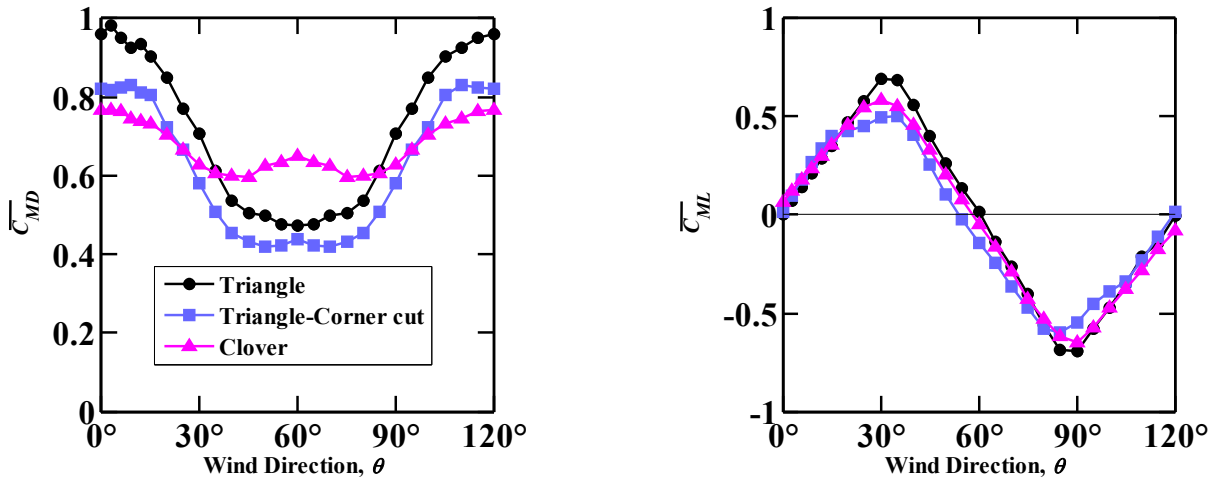

(a) Along-wind direction (b) Crosswind direction

Figure 5.2 Variation of mean overturning moment coefficients of corner modification models

Figure 5.3. shows the variation of fluctuating along-wind OTM coefficient (C'_{MD}) and fluctuating crosswind OTM coefficient (C'_{ML}) with wind direction (θ). For the Dodecagon model, the maximum C'_{MD} value is almost 97% larger than the maximum absolute C'_{ML} value. The maximum and minimum values of C'_{MD} are 0.18 and 0.08 for the Triangular model. The maximum and minimum values of C'_{ML} are 0.18 and 0.06 for the Triangular and Dodecagon models. The C'_{ML} values vary almost constantly for all wind directions for the Dodecagon model where as for C'_{MD} values vary between 0.055~0.067. Figure 5.4 show the variation of C'_{MD} and C'_{ML} with wind direction for corner modification models. C'_{MD} values are followed the same trend as $\overline{C}_{MD}$ values for the Triangular, Tri-Corner cut and Clover models as shown in Figure 5.2(a). C'_{ML} values are smaller for the Tri-Corner cut model than the Triangular model between the wind directions 20^o and 105^o as shown in Figure 5.4(b).

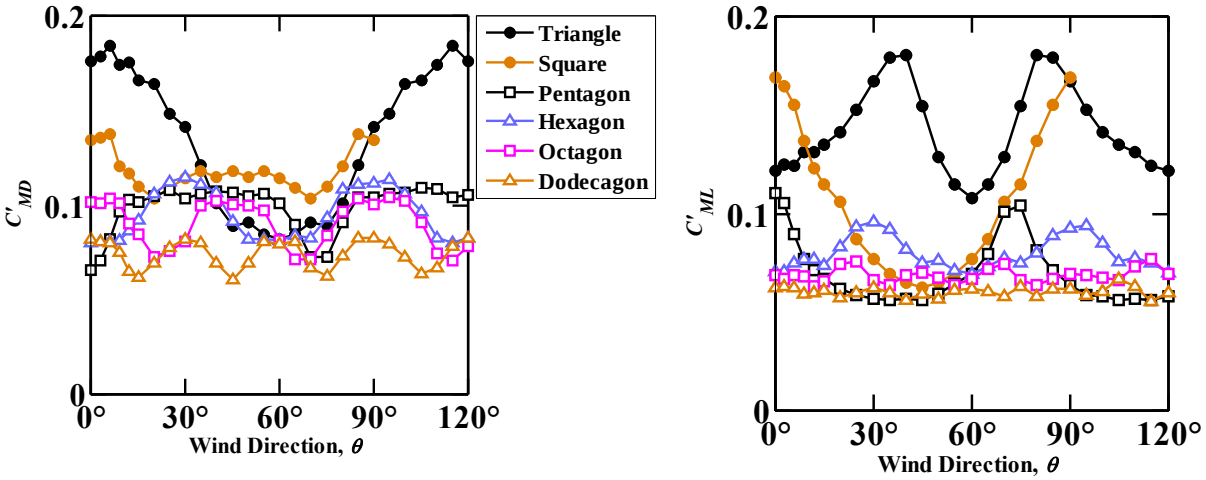

(a) Along-wind direction (b) Crosswind direction

Figure 5.3 Variation of fluctuating overturning moment coefficients of polygonal models

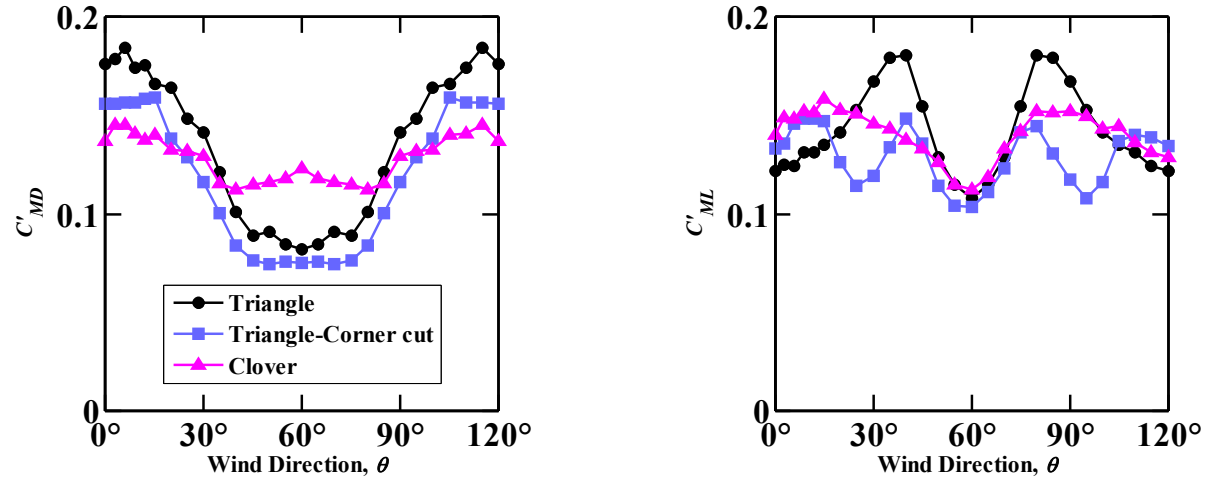

(a) Along-wind direction (b) Crosswind direction

Figure 5.4 Variation of fluctuating overturning moment coefficients of corner modification models

5.2 **Vertical variations of local wind forces**

Local wind force coefficients were calculated using the velocity pressure q_H at model height H and width B for a unit model height. Along-wind local wind force coefficients are discussed here for wind directions 3°, 9°, 0°, 45°, 40°, 30°, 90°, 95° and 0° and crosswind local wind force coefficients are discussed here for wind directions 90°, 85°, 90°, 0°, 85°, 75°, 80°, 115 ° and 0° for Triangular, Tri-Corner cut, Clover, Square, Pentagon, Hexagon, octagon, Dodecagon and Circular models, where the total mean drag and total mean lift force coefficients were maximum.

The mean and fluctuating local wind force coefficients were calculated using Eq. (2).

$$\overline{C}_{FD,local}=\frac{\overline{F}_{D,local}}{q_H A},\quad \overline{C}_{FL,local}=\frac{\overline{F}_{L,local}}{q_H A}$$
$$C'_{FD,local}=\frac{F'_{D,local}}{q_H A},\quad C'_{FL,local}=\frac{F'_{L,local}}{q_H A} \tag{2}$$

In which, $\overline{C}_{FD,local}$ and $\overline{C}_{FL,local}$ are mean local wind force coefficients in along-wind and crosswind directions, respectively; $C'_{FD,local}$ and $C'_{FL,local}$ are the corresponding fluctuating wind force coefficients. $\overline{F}_{D,local}$ and $\overline{F}_{L,local}$ are local mean wind forces in along-wind and crosswind directions, and $F'_{D,local}$, $F'_{L,local}$ are the corresponding fluctuating local wind forces. *B* is width of Square (*B*=50mm) model; q_H is mean velocity pressure at model height, *H*. *A* is frontal area of building at each level.

5.2.1 *Mean local wind force coefficients*

Figure 5.5 shows the mean local wind force coefficients for the specified wind directions. The mean local drag coefficients, $\overline{C}_{FD,local}$ of the Triangular model shows higher values than all the other models and the values reduces as the number of faces increases from Triangular (3 faces) to Dodecagon (12 faces) and Circular models. The distributions of $\overline{C}_{FD,local}$ followed the same trend for the all the models, where the Pentagon and Hexagon models showed almost same values from 0.5*H* to *H*. The $\overline{C}_{FD,local}$ values of the Clover model are around 50% less than those of the Triangular model. The $\overline{C}_{FD,local}$ values of the Tri-Corner cut model vary between those of the Triangular and Clover models. The maximum and minimum $\overline{C}_{FD,local}$ occurred at 0.93*H* and 0.13*H* for all the models. The $\overline{C}_{FL,local}$ values are same throughout the height for Square, Pentagon and Circular models. Figure 5.6 shows the mean local wind force coefficients for the corner modification models (Tri-Corner cut and Clover models). The mean local lift coefficients, $\overline{C}_{FL,local}$ of the Triangular, Tri-Corner cut and Clover models, show the almost same trend throughout the height.

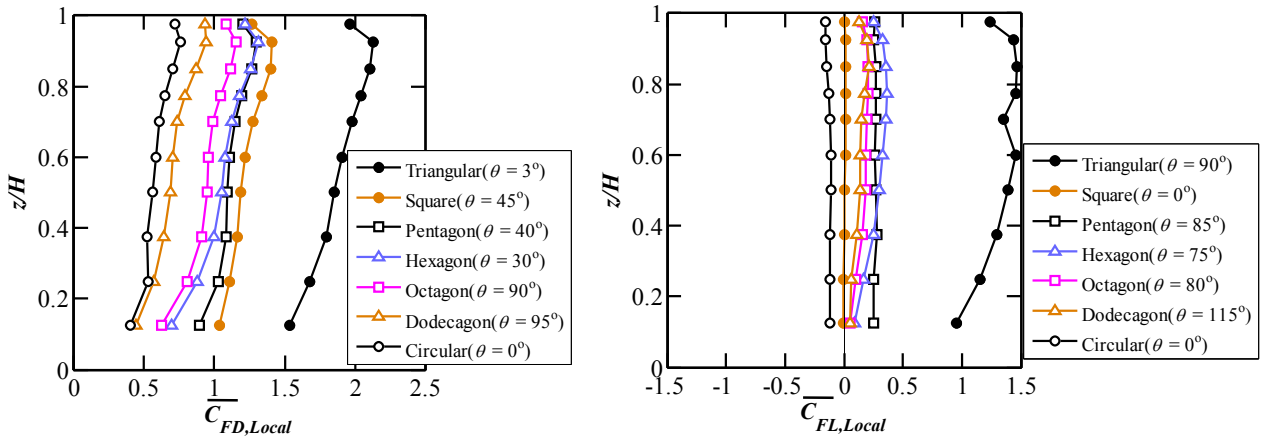

(a) Mean local drag force coefficient (b) Mean local lift force coefficient

Figure 5.5 Vertical variation of mean local wind force coefficients for polygonal models

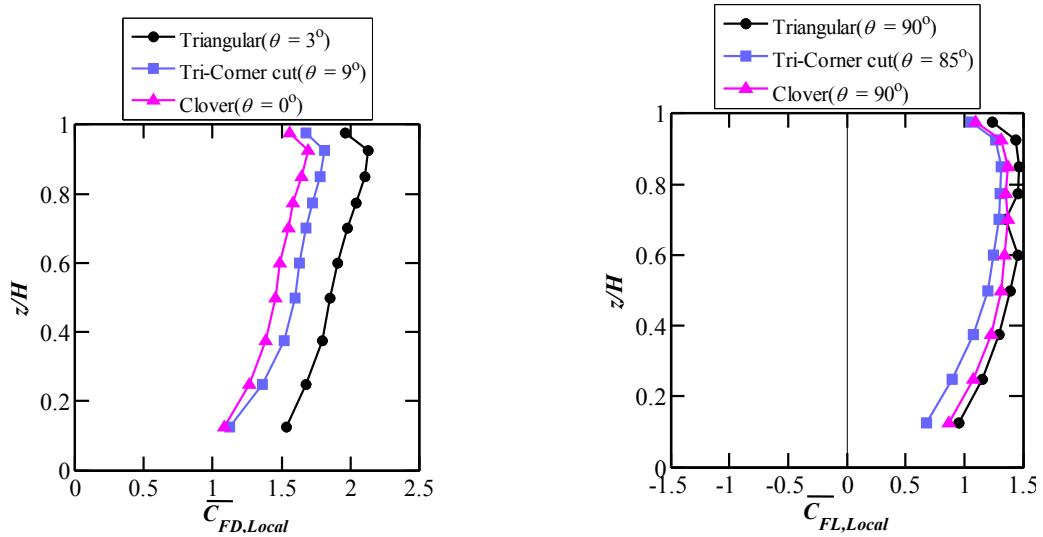

(a) Mean local drag force coefficient (b) Mean local lift force coefficient

Figure 5.6 Vertical variation of mean local wind force coefficients for corner modification models

$\overline{C}_{FD,local}$ and $\overline{C}_{FL,local}$ values are smaller for the Tri-Corner cut and Clover models than the Triangular model at all heights. $\overline{C}_{FD,local}$ values are smaller for the Clover model for all heights than the Tri-Corner cut model whereas $\overline{C}_{FL,local}$ values are smaller for the Tri-Corner cut mode than the Clover model.

5.2.2 *Fluctuating local wind force coefficients*

Figure 5.7 shows the fluctuating local wind force coefficients for the polygonal models. The fluctuating drag force coefficient $C'_{FD,local}$ was found to be maximum for the Triangular model at 0.93H as in the case of $\overline{C}_{FD,local}$. The maximum values were found at heights of 0.93H for all the

models as for $\overline{C}_{FD,local}$. The $C'_{FD,local}$ values were almost the same for the Square and Hexagon models at all heights. Figure 5.8 shows the fluctuating local wind force coefficients for the corner modification models. The $C'_{FL,local}$ curves for the Tri-Corner cut and Clover models followed the same trend but the values for the Tri-Corner cut model were around 17% less than that for the Clover model. $C'_{FD,local}$ and $C'_{FL,local}$ values are smaller for the Tri-Corner cut and Clover models than the Triangular model at all heights as in the case of mean local wind force coefficients.

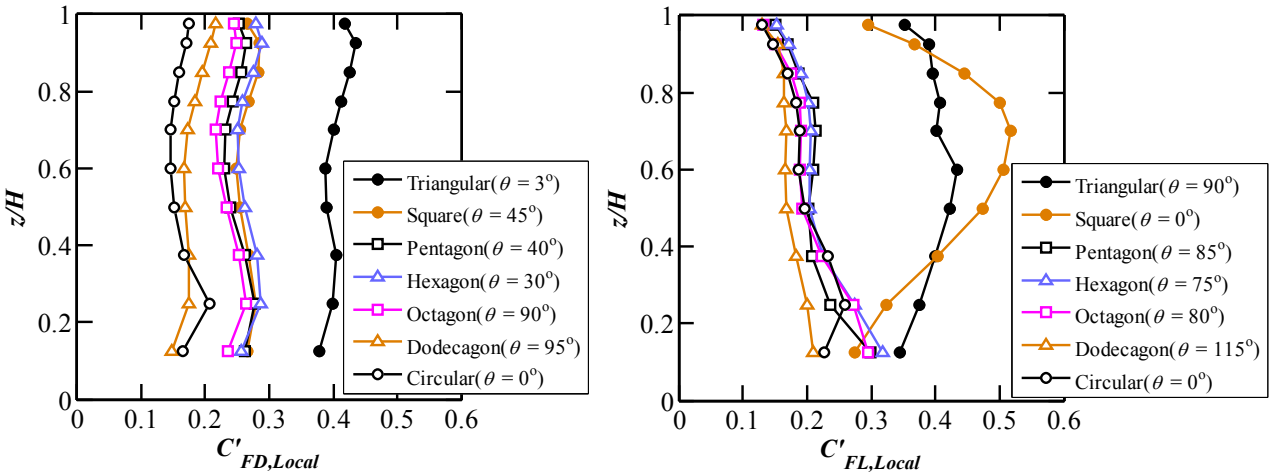

(a) Fluctuating local drag force coefficient (b) Fluctuating local lift force coefficient

Figure 5.7 Vertical variation of fluctuating local wind force coefficients for the polygonal models

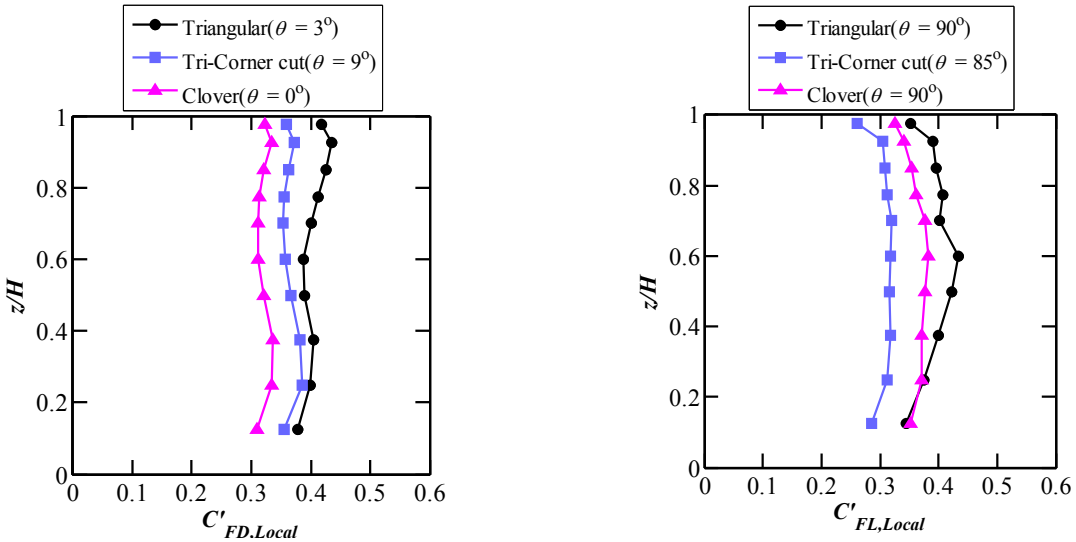

(a) Fluctuating local drag force coefficient (b) Fluctuating local lift force coefficient

Figure 5.8 Vertical variation of fluctuating local wind force coefficients for the corner modification models

$C'_{FD,local}$ values are smaller for the Clover model for all heights than the Tri-Corner cut model whereas $C'_{FL,local}$ values are smaller for the Tri-Corner cut mode than the Clover model.

5.2.3 *Maximum mean and fluctuating OTM coefficients in along-wind and crosswind directions*

Figure 5.9(a-b) shows the maximum mean and fluctuating o.t.m coefficients from all the wind directions. Maximum o.t.m coefficients have been chosen from all the wind directions for all the models. Maximum mean o.t.m coefficients in along-wind directions reduces from Triangular to Circular models where as in maximum fluctuating o.t.m coefficient of Hexagon model is slightly increases around 5% more than Pentagon model and remaining models are same as maximum mean o.tm coefficients. Maximum mean o.t.m coefficients in crosswind direction, overall trend reduces from Triangular to Circular models, but Hexagon model shows 3% higher values than Pentagon model and Clover models shows around 8% higher values than Tri-Corner cut model. Maximum fluctuating o.t.m coefficients in crosswind direction reduces as the number of faces of the model increases i.e. in the order from Triangular (3 faces), Square, Pentagon, Hexagon, Octagon, Dodecagon (12 faces) and Circular model. But Clover model shows around 6% higher values than Tri-Corner cut model.

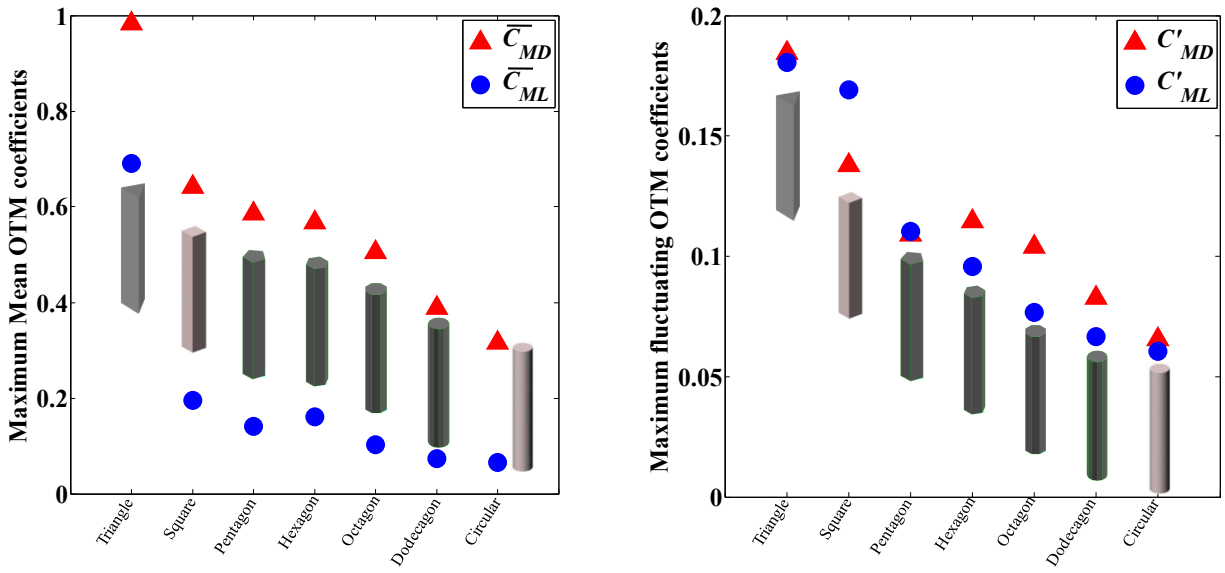

(a) Maximum mean overturning moment coefficients

(b) Maximum fluctuating over turning moment coefficients

Figure 5.9 Maximum mean and fluctuating overturning moment coefficients in along-wind and cross wind directions

5.2.4 *Relation between the overturning moment coefficients*

The relationships between maximum mean overturning moment coefficients and maximum fluctuating overturning moment coefficients for all models are plotted in Figure 5.10 (a) for the along-wind direction and Figure 5.10 (b) for the crosswind direction. From Figure 5.10 (a), a high correlation between along-wind maximum mean OTM coefficients and maximum fluctuating OTM coefficients observed. In crosswind direction also, maximum mean and fluctuating OTM coefficients shows higher correlations. Among all models, the Pentagon and Hexagon models show almost similar values in both along-wind and crosswind directions. In crosswind direction, Dodecagon and Circular model shows almost similar values where as in along-wind direction it differs slightly.

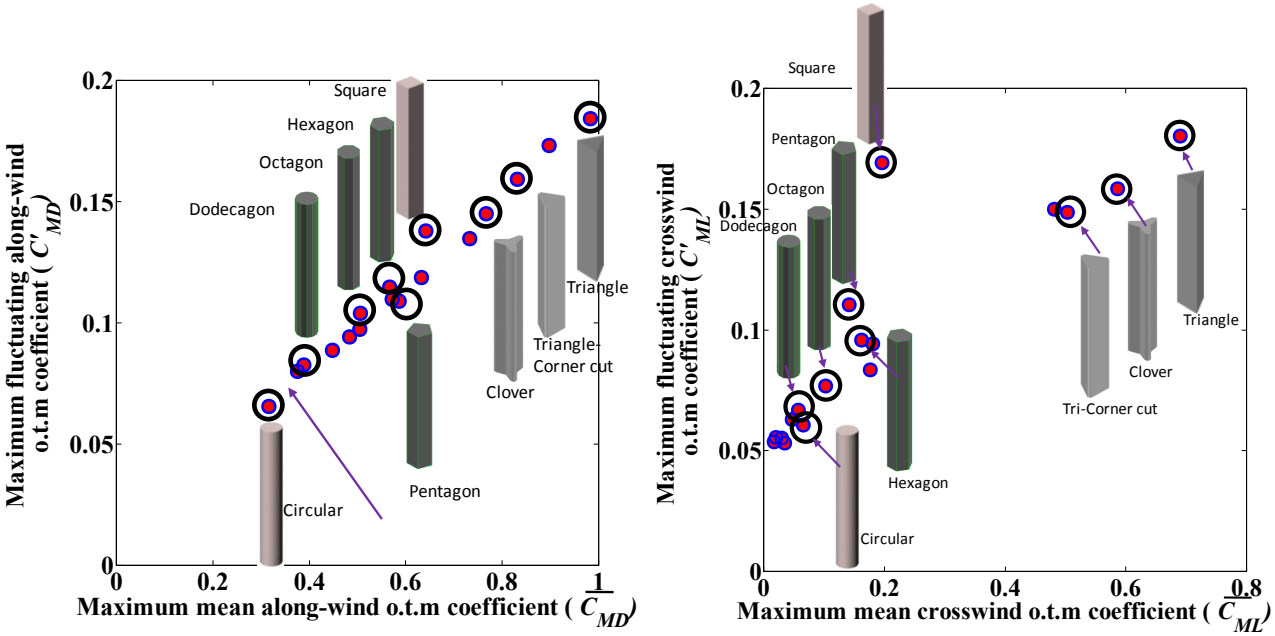

(a) Maximum mean o.t.m coefficient Vs maximum fluctuating OTM coefficient in along-wind directions

(b) Maximum mean o.t.m coefficient Vs maximum fluctuating OTM coefficient in crosswind directions

Figure 5.10 Maximum mean Vs Fluctuating o.t.m coefficients in along-wind and crosswind directions

5.3 **Effect of various building plan shapes on Power spectrum of wind forces**

5.3.1 *Power spectral densities in along-wind and crosswind directions*

Figure 5.11(a-b) shows the crosswind power spectra, fS_{CML}, for the wind directions at which the maximum peak occurred for polygonal and corner modification models. The maximum peaks occurred for crosswind spectra at θ=0°, 6°, 15° 0°, 100°, 30°, 45°, 0° and 0° for the Triangular,

Tri-Corner cut, Clover, Pentagon, Hexagon, Octagon, Dodecagon and Circular models. A sharp peak of crosswind spectrum is observed for all the models, but the maximum peak is observed for the Square model. The sharp peak is reduced drastically for the polygonal models as the number of side surfaces increases, indicating that the shedding vortices are more disturbed. But for the Tri-Corner cut and Clover models, the peak appears sharp and shifts towards slightly higher reduced frequency ranges than the Triangular model as shown in Figure 5.11(b).

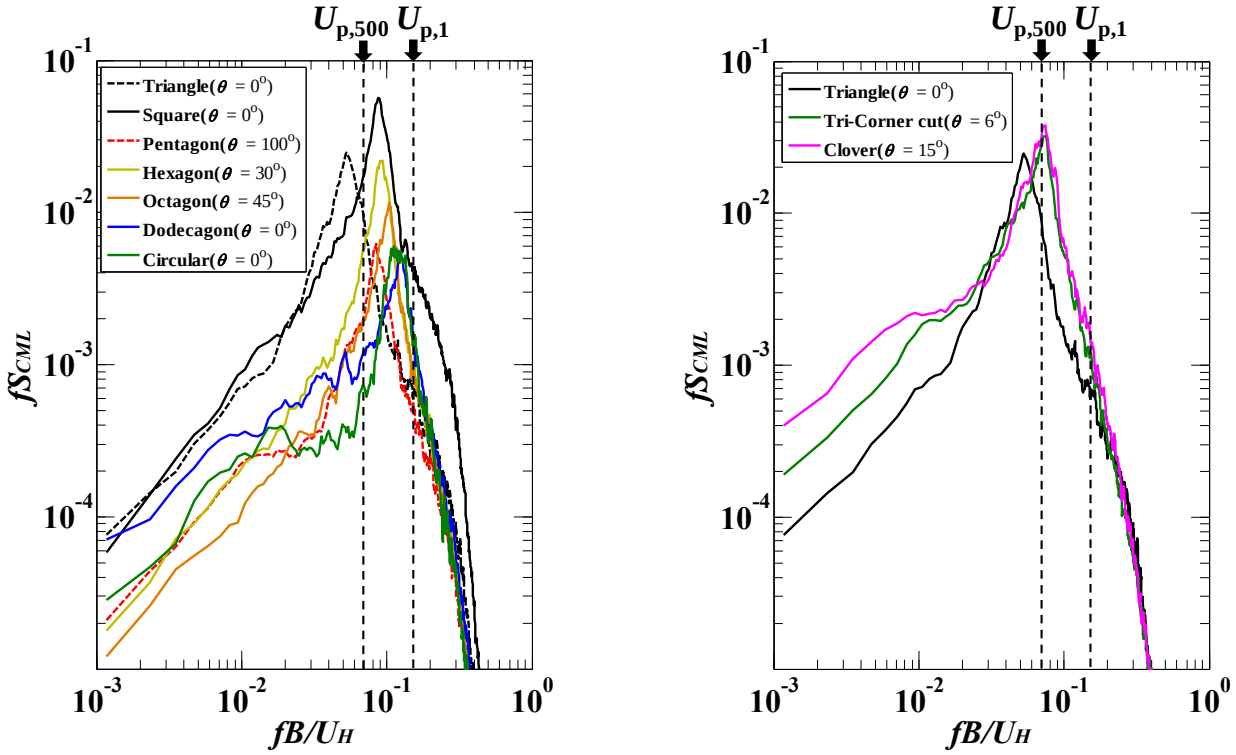

(a) Polygonal models (b) Corner modification models

Figure 5.11. Power spectral densities of crosswind OTM coefficients

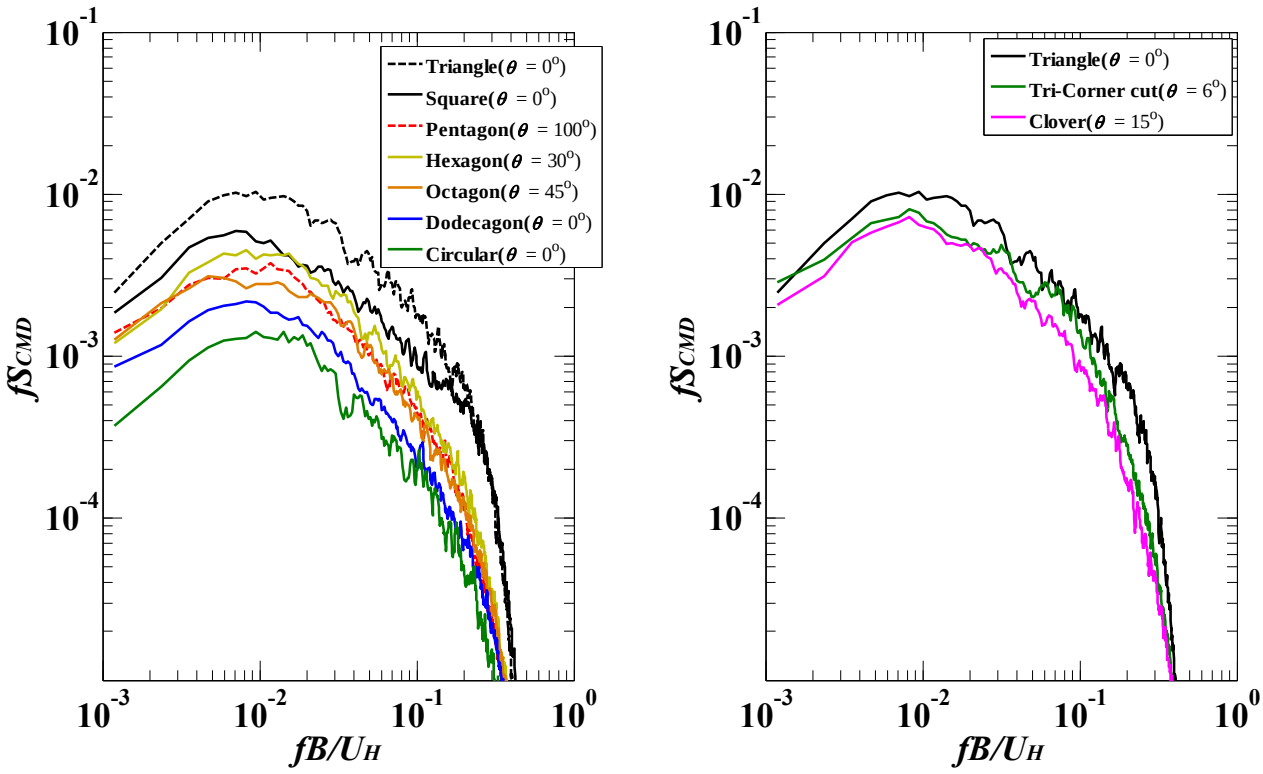

(a) Polygonal models (b) Corner modification models

Figure 5.12. Power spectral densities of along-wind o.t.m coefficients

Figure 5.12(a-b) shows the along-wind power spectra, fS_{CMD}, for the above mentioned wind directions for the polygonal models and corner modification models at which the maximum cross-wind spectra peak occurred. For all reduced frequencies, fS_{CMD} values are becoming smaller as the number of side surfaces increases except for the Pentagon and Hexagon models as shown in Figure 5.12(a). For corner modification models, fS_{CMD} values are smaller for all reduced frequencies for the Clover model than the Triangular and Tri-Corner cut models as shown in Figure 5.12(b).

5.3.2 *Power spectral densities of crosswind local wind force coefficients*

The crosswind power spectra of local wind force coefficients, fS_{CfL} are discussed for all the models from z/H = 0.5 to 0.975. The power spectral densities versus reduced frequencies are plotted in the Figure 5.8. The reduced frequencies were calculated based on the Square model width (B=50). Power spectral densities of crosswind local wind force coefficients were calculated for the wind directions corresponding to those where the maximum peak occurred for the crosswind spectra. The maximum peak of power spectra of crosswind occurred at wind direc-

tions, θ = 0°, 6°, 15°, 0°, 100°, 30°, 45°, 0° and 0° for the Triangular, Tri-Corner cut, Clover, Square, Pentagon, Hexagon, Octagon and Circular models.

The power spectra of the Triangular model showed a sharp peak near the reduced frequency fB/U_H =0.06. The crosswind spectrum showed a narrow-band peak due to vortex shedding for all the models as shown in Figure 5.13 (a)-(i). The spectral peak shifts to higher reduced frequencies from fB/U_H =0.055 to 0.13 for the models from the above mentioned order (Triangular to Circular models). The magnitude of spectral peak increased for the models Triangular, Tri-Corner cut, Clover and Square models. The magnitude of spectral peak reduces as the number of faces increase from the Square model to Dodecagon models, where as the peak spectral value of Octagon is 97% higher than that of the Pentagon model and the peak spectral value of Circular model is around 30% higher than that of the Dodecagon model.

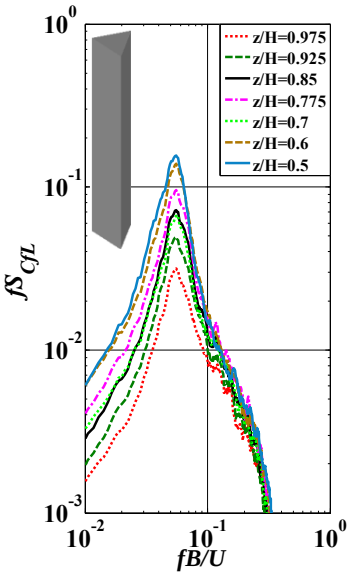

(a) Triangular (θ=0°)

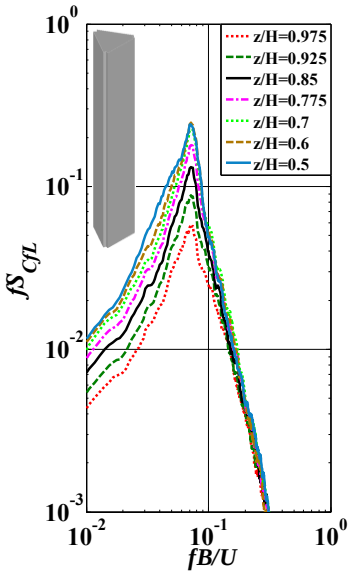

(b) Tri-Corner cut (θ=6°)

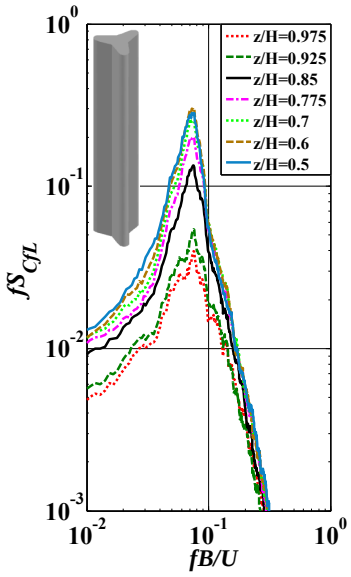

(c) Clover (θ=15°)

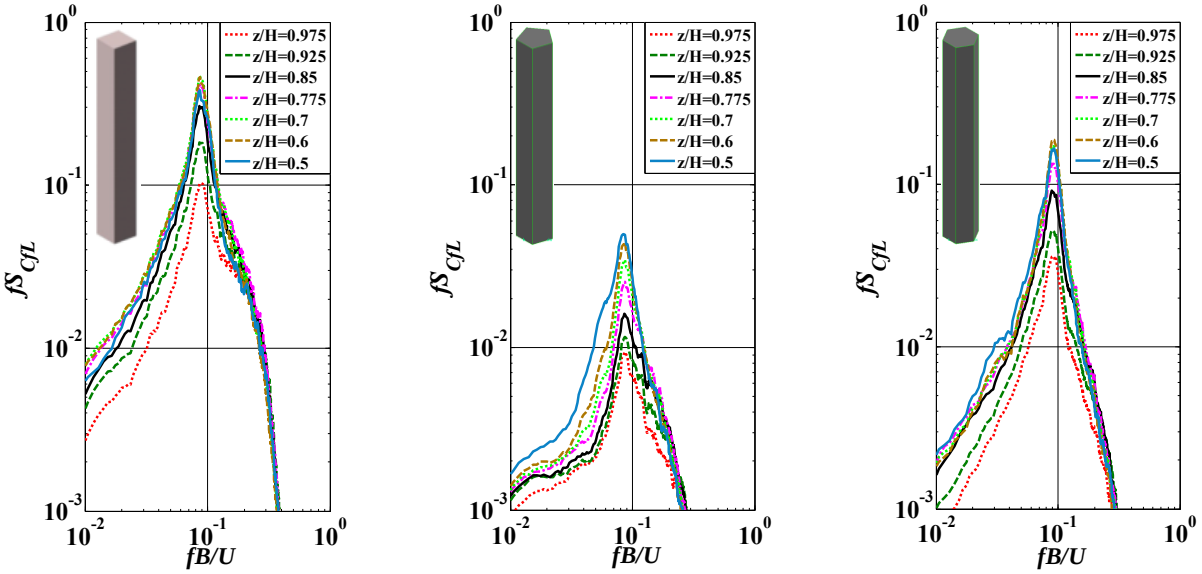

(d) Square (θ=0°) (e) Pentagon (θ=100°) (f) Hexagon (θ=30°)

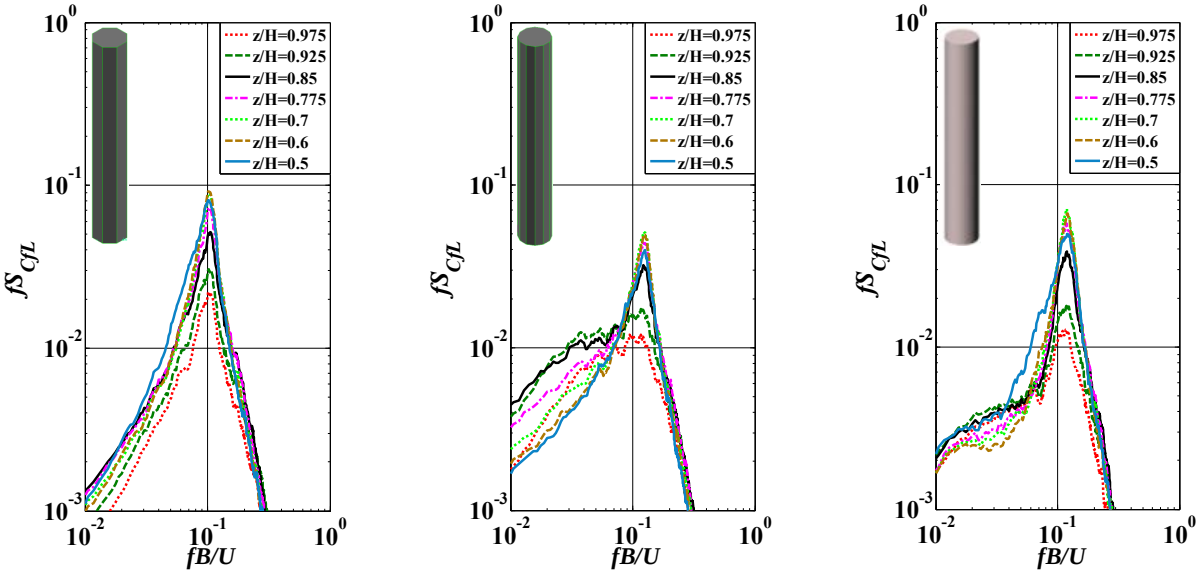

(g) Octagon (θ=45°) (h) Dodecagon (θ=0°) (i) Circular (θ=0°)

Figure 5.13 Power spectral densities of crosswind local wind force coefficients

5.3.3 *Maximum spectral values for 500-yr and 1-yr return periods*

Figure 5.14 compares in detail the square root of crosswind power spectra for the design wind speeds corresponding to higher spectral values at a 500-year return period ($U_{p,500}$) and a 1-year return period ($U_{p,1}$). Here, the first natural frequency is assumed to be f_1=0.1Hz, and the design wind speeds are assumed to be $U_{p,500}$=71m/s and $U_{p,1}$=30m/s at model height H, respectively, in the Tokyo region. Here, the square root of the power spectra for $U_{p,500}$, is the maximum value of power spectra when the reduced frequency is larger than 0.07 ($fB/U_H \geq 0.07$), and the square root

of the power spectra for $U_{p,1}$, is the maximum value of the power spectra when the reduced frequency is larger than 0.17 ($fB/U_H \geq 0.17$). Then, the corresponding spectral values were calculated. The maximum $\sqrt{S_{CML,\max}}$ value shown corresponding to $U_{p,500}$, for the Clover model than the Triangular and Tri-Corner cut model. For $U_{p,1}$, the $\sqrt{S_{CML,\max}}$ values become smaller than those for the Triangular model. The Tri-Corner cut model shows the smallest value of all.

The values of $\sqrt{S_{CML,\max}}$ for 500-year return period ($U_{p,500}$) for the Pentagon, Hexagon, Octagon, Dodecagon, and Circular Models, which show smaller than that of Square models, which are 40-70% of the Square Model, having advantages for safe design. The values $\sqrt{S_{CML,\max}}$ for 500-year return period ($U_{p,500}$) for the Pentagon model is around 35% lesser than that of Triangular model. The values of $\sqrt{S_{CML,\max}}$ for 1-year return period ($U_{p,1}$), for all the models are around 50% lesser than that for the Triangular and Square models. Tri-Corner cut, Pentagon, Hexagon, Octagon, Dodecagon and Circular models have almost same values of $\sqrt{S_{CML,\max}}$ for 1-year return period, showing that these building shapes are superior to the Square shape for habitability design.

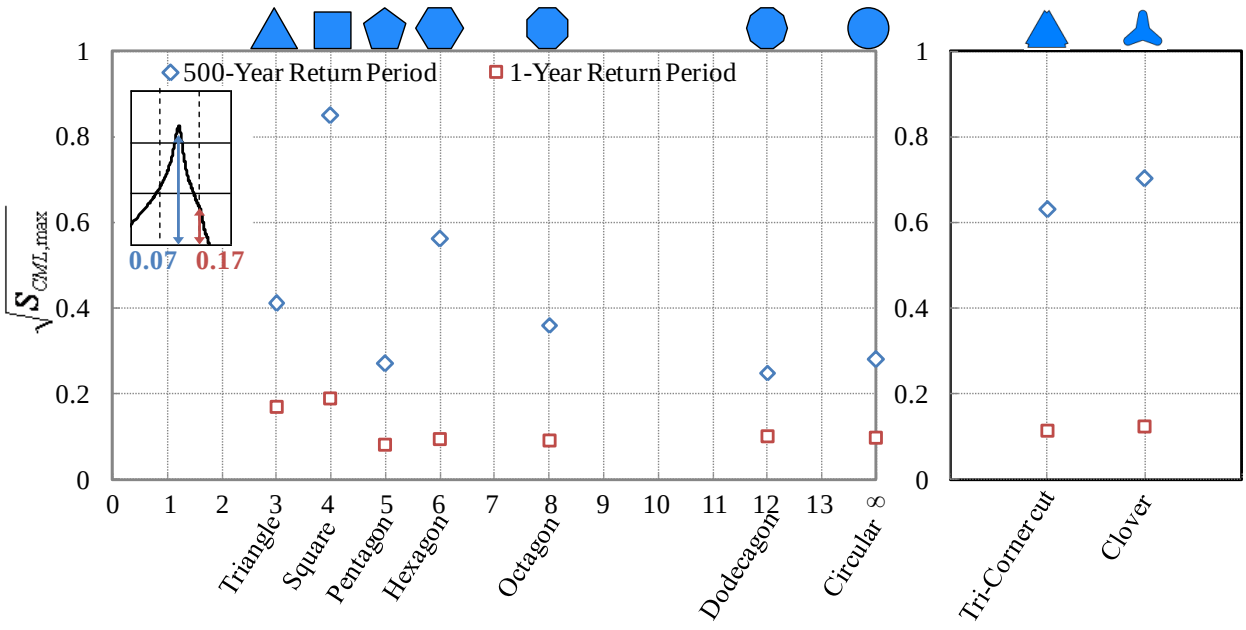

Figure 5.14 Peak spectral values for 500-year and 1-year return periods

5.3.4 *Variation of peak crosswind spectral values*

Figure 5.15 compares the variation of peak spectral values of crosswind spectra with number of side surfaces. The wind directions were selected where the maximum peak occurs for each model. The maximum value occurred for the Square model and then the value decreases as shown in Figure 5.15. The maximum peak spectral value of crosswind spectra increases for the Clover model than the Tri-Corner cut model.

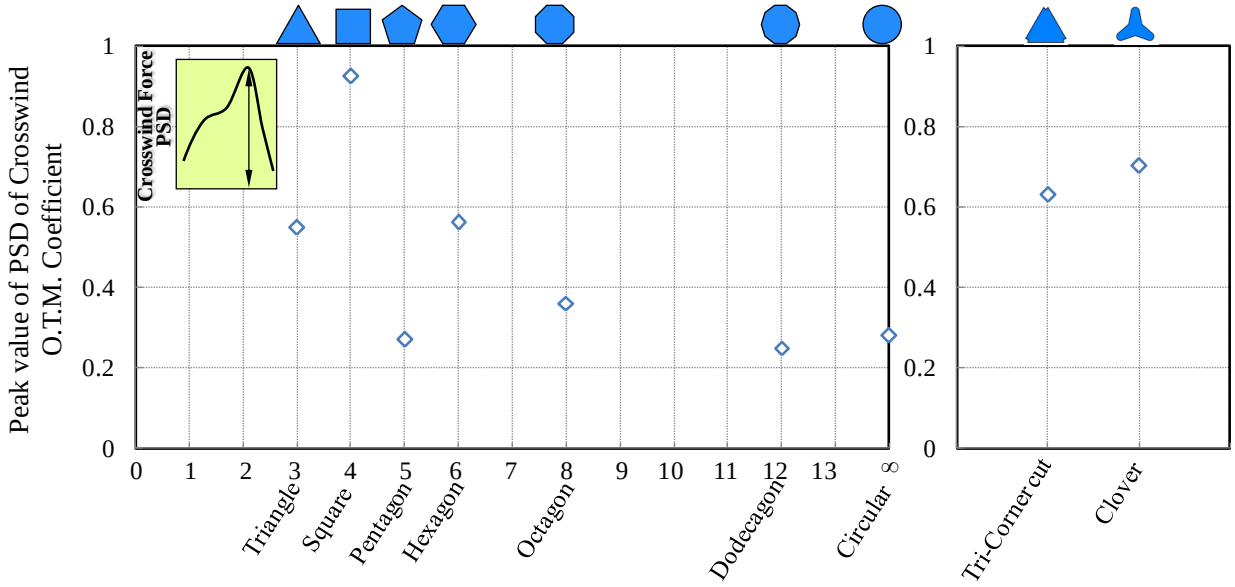

Figure 5.15 Variation of Peak spectral values of Crosswind OTM coefficients

5.3.5 *Variation of Bandwidth of a Crosswind power spectral densities*

Figure 5.16 compares the variation of bandwidth of crosswind spectra.

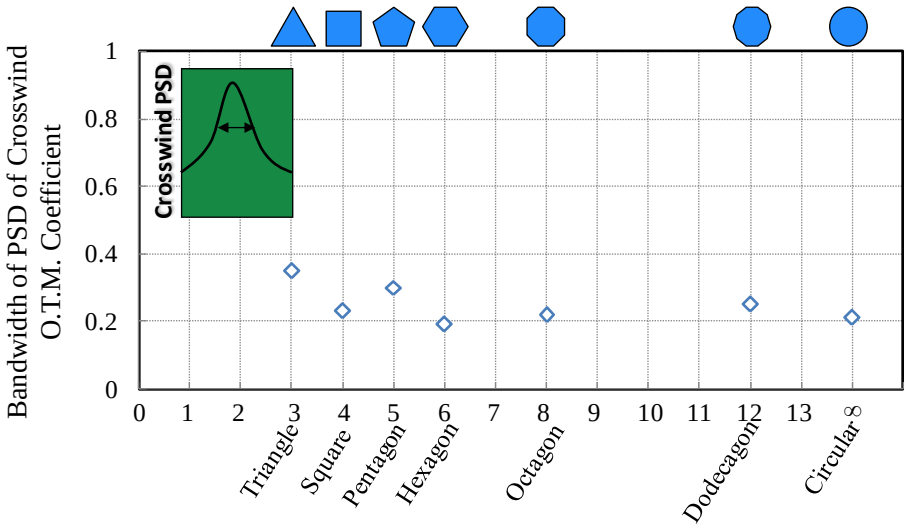

Figure 5.16 Variation of Bandwidth of PSD of Crosswind OTM coefficients with number of side surfaces

The bandwidth, B_w was obtained by approximating the power spectra, fS_{CML} to the Eq.(5.1) through the least-square method (Vickery and Clark, 1972).

$$\frac{fS_{CML}}{\sigma^2} = k\frac{f}{\sqrt{\pi}\, f_{peak} B_w}\exp\left[-\left(\frac{1-f/f_{peak}}{B_w}\right)^2\right] \tag{5.1}$$

The bandwidth is higher for the Triangular model among all the polygonal models; the overall trend shows the bandwidth decreases as the number of side surfaces increases. When the bandwidth is small, the spectral peak becomes very sharp as shown for the Square model, implying that strong vortices are shed regularly. But when the bandwidth is large, as the spectral peak becomes flat and the spectral shape becomes wide, it can be assumed that the vortex shedding becomes random and irregular. This randomness contributes largely to the smaller wind forces discussed in the previous sections. The band width reduces for the Tri-Corner cut and Clover models as shown in Figure 5.17.

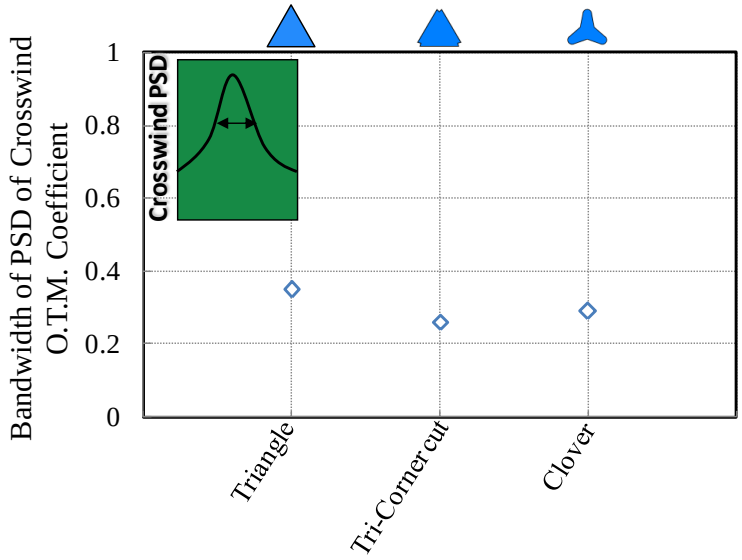

Figure 5.17 Variation of Bandwidth of PSD of Crosswind OTM coefficients for Triangular cross-sectional models

5.3.6 *Vertical variation of peak local reduced frequencies of crosswind force coefficients*

Figure 5.18 show the vertical variation of peak local reduced frequencies of crosswind force coefficients. These peak reduced frequencies have been calculated for all the models for the wind directions discussed in section 5.3.1. The peak reduced frequencies were obtained using the height at each level and the width, *B* of the Square model. The peak reduced frequencies are al-

most same for heights between 0.38*H* to 0.78*H* for all the models except Octagon, Dodecagon and Circular models. The Tri-Corner cut and Clover models behave almost the same way from 0.125*H* to 0.78*H*. This means that all the vortices shed almost the same time throughout these heights greatly exciting these models in crosswind direction. These values show increasing and decreasing trend at all heights for Octagon, Dodecagon and Circular models. This means, the shedding frequencies are different at various heights for these models, the resulting crosswind force decreases correspondingly.

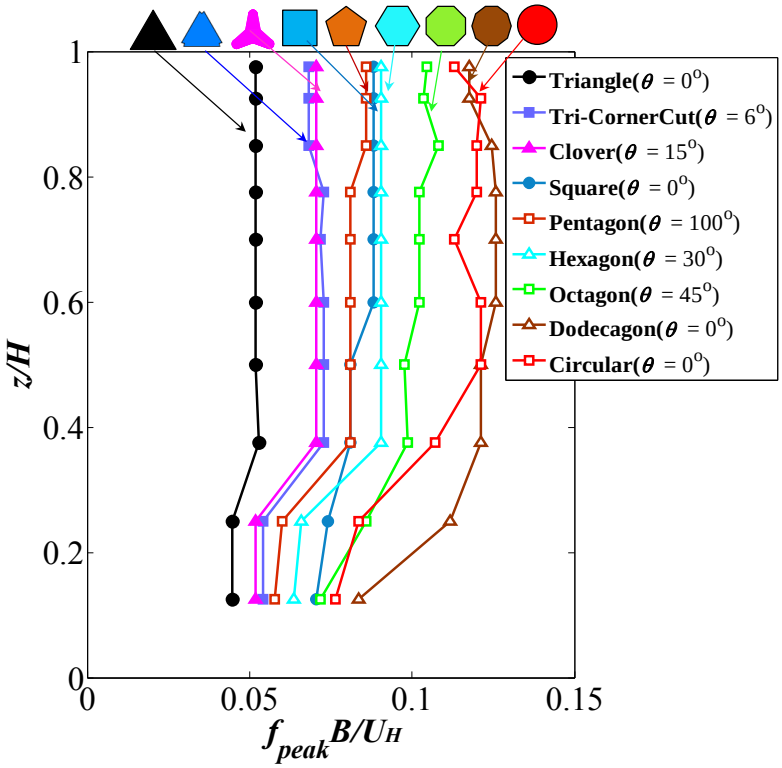

Figure 5.18 Vertical variation of peak local reduced frequencies of crosswind force coefficients

5.4 **Summary**

Seven types of various cross-sectional polygonal models and two types of corner modification models were considered in this chapter. The effect of these models on total wind forces, local wind forces and power spectral densities were studied.

Wind force coefficients were calculated based the pressure measurement experiment studies by integrating the wind pressures over the surfaces. Based on the results, the increasing number

of surfaces (polygonal models) has the significant effect on wind forces and power spectral densities.

Chapter VI

EFFECTS OF TWISTING ANGLE OF HELICAL MODELS ON WIND FORCES

In this chapter, eight models with different cross-sections with twisting angle of 180^o were used to study the characteristics of wind forces on tall buildings. The models analyzed in this chapter are Tri-60^oHel, Tri-180^oHel, Tri-360^oHel, Penta-180^oHel, Hexa-180^oHel, Octa-180^oHel and Dodeca-180^oHel models which are shown in Table 6.1. We tried to predict the effect of twisting angle on local, total wind forces and power spectral densities.

			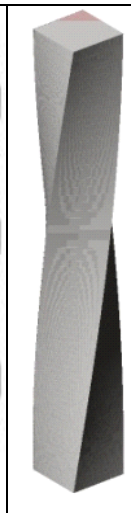					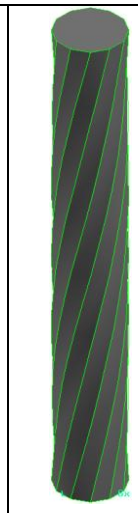
(a)Tri-60^oHel	(b) Tri-180^oHel	(c) Tri-360^oHel	(d) Sq-90^oHel	(e)Sq-180^oHel	(f) Penta-180^oHel	(g) Hexa-180^oHel	(h) Octa-180^oHel	(i) Dodeca-180^oHel

Table 6.1 Configurations of helical models

6.1 *Overturning moment (*OTM*) coefficients*

The mean and fluctuating overturning moment coefficients were calculated using equations as mentioned in section 5.1 (Chapter V).

6.1.1 *Effects of wind direction on over turning moment (o.t.m) coefficients*

Figure 6.1 shows the variation of mean along-wind OTM coefficient ($\overline{C}_{MD}$) and mean cross-wind OTM coefficient ($\overline{C}_{ML}$) with wind direction (θ). For Tri-60°Hel and Tri-180°Hel models, the $\overline{C}_{MD}$ values increase up to 40° wind direction then start decreasing. The curve shape becomes almost straight line as the number of faces of the model increases from 4 faces (Square) to 12 faces (Dodecagon). The maximum and minimum values of $\overline{C}_{MD}$ are 0.9 and 0.36 for the Tri-60°Hel and Dodeca-180°Hel models among all the models. The $\overline{C}_{MD}$ values of Tri-360°Hel and Sq-180°Hel models followed almost same for all the wind directions. Also, the $\overline{C}_{MD}$ values of Penta-180°Hel and Hexa-180°Hel models followed almost same for all the wind directions. Among all these models, Dodeca-180°Hel showed less value (~0.36) for all the wind directions. For the Tri-60°Hel model, the maximum and minimum $\overline{C}_{MD}$ occurred at 45° and 100° wind directions. The maximum and minimum absolute values of $\overline{C}_{ML}$ are 0.48 and 0.009 for the Tri-60°Hel and Dodeca-180°Hel models among all the models. For the Dodecagon model, the absolute values of $\overline{C}_{ML}$ are around 0.01~0.03 for all wind directions.

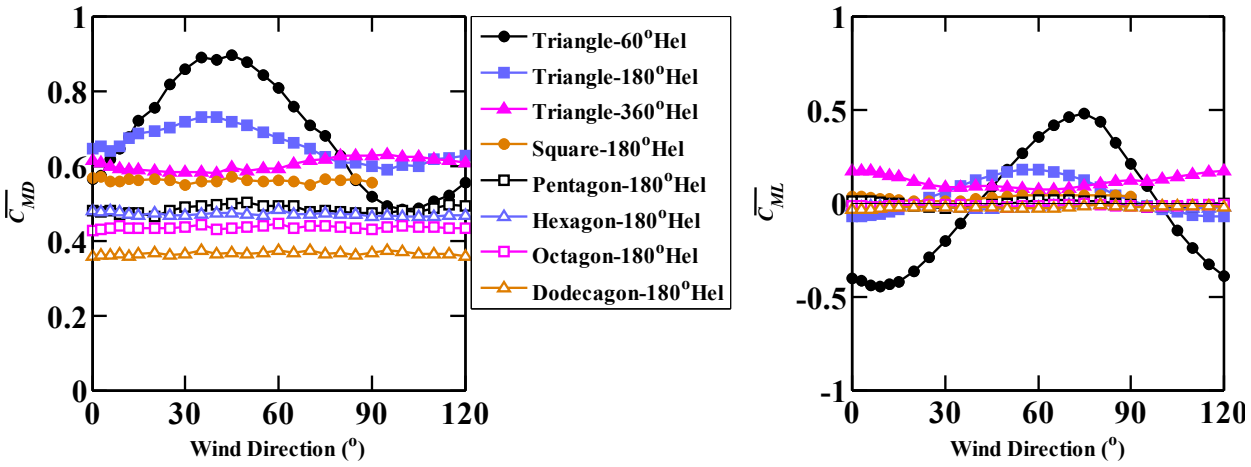

(a) Along-wind direction (b) Crosswind direction

Figure 6.1 Variation of mean overturning moment coefficients for polygonal helical models

On average, the absolute values of $\overline{C}_{ML}$ are around 0.015 for Penta-180°Hel, Hexa-180°Hel, Octa-180°Hel and Dodeca-180°Hel models. The variations in $\overline{C}_{ML}$ and $\overline{C}_{MD}$ showed similar trend, as can be seen in Figure 6.1.

Figure 6.2. shows the variation of fluctuating along-wind OTM coefficient (C'_{MD}) and fluctuating crosswind OTM coefficient (C'_{ML}) with wind direction (θ). C'_{MD} values also followed the same trend as $\overline{C}_{MD}$ values. For the Dodeca-180°Hel model, the C'_{MD} values are almost 30% larger than the absolute C'_{ML} values. Penta-180°Hel, Hexa-180°Hel and Octa-180°Hel models followed same trend and almost same values of C'_{MD} for all the wind directions. The maximum and minimum values of C'_{MD} are 0.17 and 0.08 for the Tri-180°Hel model is almost same as Tri model. The maximum and minimum values of C'_{ML} are 0.15 and 0.05 for the Tri-180°Hel and Dodeca-180°Hel models. Penta-180°Hel, Hexa-180°Hel, Octa-180°Hel and Dodeca-180°Hel models followed same trend and almost same values of C'_{ML} for all the wind directions.

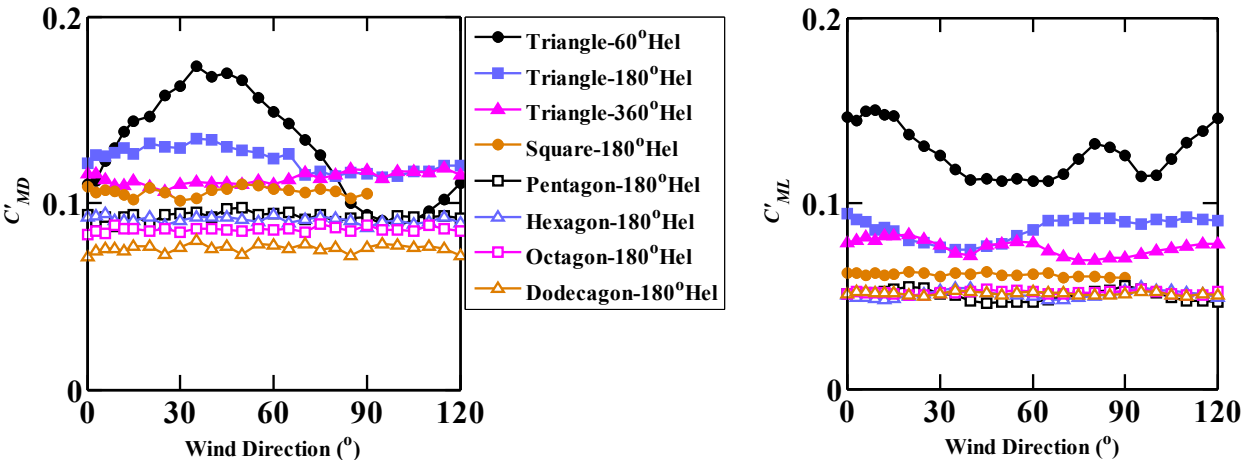

(a) Along-wind direction (b) Crosswind direction

Figure 6.2 Variation of fluctuating overturning moment coefficients for polygonal helical models

6.2 **Vertical variations of local wind forces**

Local wind force coefficients were calculated using the velocity pressure q_H at model height H and width B for a unit model height. Along-wind local wind force coefficients are discussed here for wind directions 35°, 35°, 45°, 3°, 50°, 60°, 60°, and 95° and crosswind local wind force coefficients are discussed here for wind directions 0°, 0°, 25°, 30°, 110°, 45°, 9° and 3° for Tri-60°Hel, Tri-180°Hel, Tri-360°Hel, Penta-180°Hel, Hexa-180°Hel, octa-180°Hel and Dodeca-180°Hel

models, where the total mean drag and total mean lift force coefficients were maximum. In Figure 6.3 and 6.4, the values in the parentheses are wind directions for which the local wind force coefficients were obtained.

The mean and fluctuating local wind force coefficients were calculated using based on the equations mentioned in section 4.2 in Chapter IV.

6.2.1 *Mean local wind force coefficients*

Figure 6.3 shows the mean local wind force coefficients for the specified wind directions. Mean local drag coefficients, $\overline{C}_{FD,local}$ of the Tri-180^{o}Hel model shows higher values up to 0.78H than all the other models. Maximum $\overline{C}_{FD,local}$ shows for Tri-180^{o}Hel model at 0.85H. The distributions of $\overline{C}_{FD,local}$ values of Tri-180^{o}Hel and Tri-360^{o}Hel models followed the shape of the models whereas the variation is very less for the Hel models of Square, Pentagon, Hexagon, Octagon and Dodecagon. The distributions of $\overline{C}_{FD,local}$ values of Hexa-180^{o}Hel and Octa-180^{o}Hel models shows almost similar values as in the case of $\overline{C}_{MD}$. The maximum value of $\overline{C}_{FD,local}$ are occurred between 0.78H to 0.93H for all Hel models. The maximum value of mean local lift coefficients $\overline{C}_{FL,local}$ occurred at 0.6H for Tri-60^{o}Hel model. $\overline{C}_{FL,local}$ values varies between positive to negative values and vice versa and followed the shape of the Hel models for all the models except Tri-60^{o}Hel model. The variation of $\overline{C}_{FL,local}$ values between positive to negative and vice versa reduces as the number of faces increases from Tri (3 faces) to Dodecagon (12 faces). The $\overline{C}_{FL,local}$ values of Dodeca-180^{o}Hel model varies close to the zero line for all heights where as for Dodecagon and Circular models, the values are almost same for all heights.

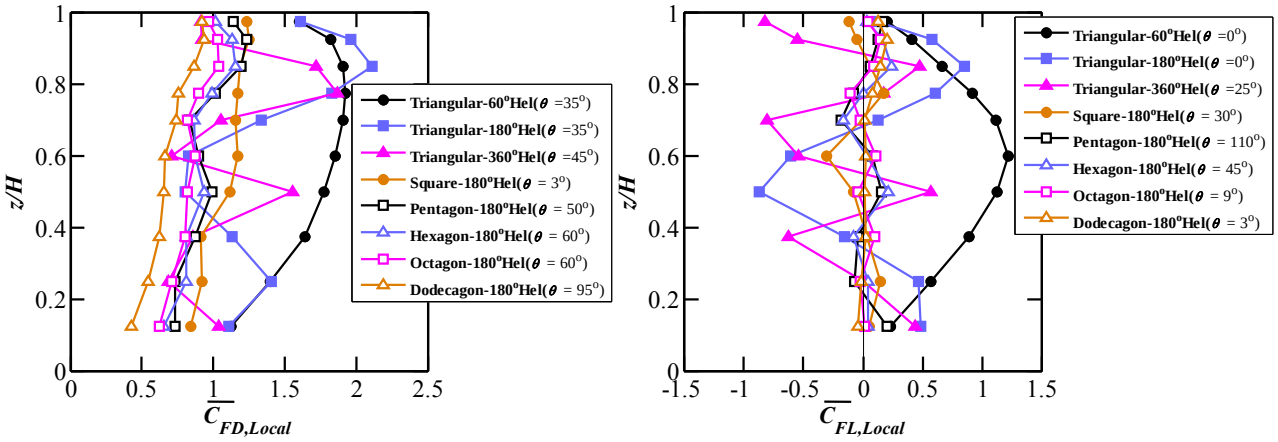

(a) Mean local drag force coefficient (b) Mean local lift force coefficient

Figure 6.3 Vertical variation of mean local wind force coefficients for polygonal helical models

6.2.2 *Fluctuating local wind force coefficients*

Figure 6.4 shows the fluctuating local wind force coefficients. The fluctuating drag force coefficient $C'_{FD,local}$ was found to be maximum for the Tri-180°Hel model at 0.85H as in the case of $\overline{C}_{FD,local}$. The maximum values were found at heights of 0.78H to 0.98H for all the models whereas at 0.5H for Sq-180°Hel model.

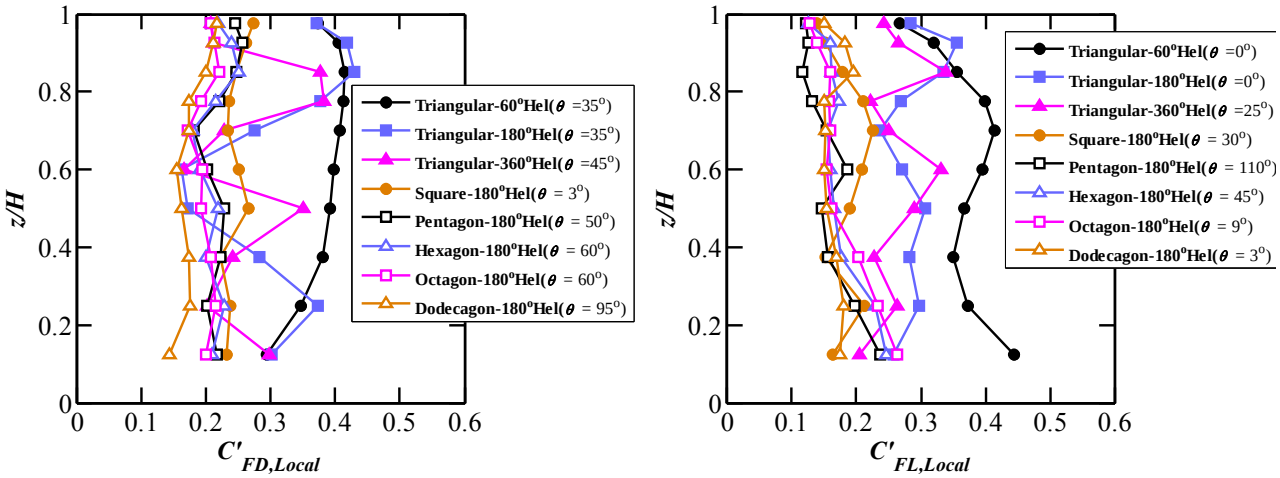

(a) Fluctuating local drag force coefficient (b) Fluctuating local lift force coefficient

Figure 6.4 Vertical variation of fluctuating local wind force coefficients for polygonal helical models

The $C'_{FD,local}$ values were almost the same for the Penta-180^{o}Hel and Hexa-180^{o}Hel models at heights 0.5H to 0.85H. The $C'_{FL,local}$ curves for the Tri-180^{o}Hel and Tri-360^{o}Hel models followed increasing and decreasing trend from positive to negative and vice versa and followed the shape of the models whereas the helical models of Pentagon, Hexagon, Octagon and Dodecagon the variation reduces to smaller values throughout their heights.

6.2.3 *Maximum mean and fluctuating OTM coefficients in along-wind and crosswind directions*

Figure 6.5(a-b) shows the maximum mean and fluctuating o.t.m coefficients from all the wind directions. Maximum o.t.m coefficients have been chosen from all the wind directions for all the models. Maximum mean o.t.m coefficients in along-wind directions reduces from Tri-180^{o}Hel to Dodeca-180^{o}Hel models where as in maximum fluctuating o.t.m coefficient of Hexa-180^{o}Hel model and Dodeca-180^{o}Hel model is slightly increases than Penta-180^{o}Hel and Octa-180^{o}Hel models. Maximum mean and fluctuating o.t.m coefficients in crosswind direction, overall trend reduces from Tri-60^{o}Hel to Dodeca-180^{o}Hel models. It is interesting to see the maximum fluctuating o.t.m coefficients are same for Hel models of Pentagon, Hexagon, Octagon and Dodecagon models. There is around 45% reduction in maximum fluctuating o.t.m coefficients between Tri-180^{o}Hel to Hel models of Pentagon, Hexagon, Octagon and Dodecagon models. And there is around 17% reduction in maximum fluctuating o.t.m coefficients between Sq-180^{o}Hel to Helical models of Pentagon, Hexagon, Octagon and Dodecagon models. There is an overall effect of twist angle on reduction in maximum o.t.m coefficients, but there is very less effect on maximum o.t.m. coefficients in crosswind direction.

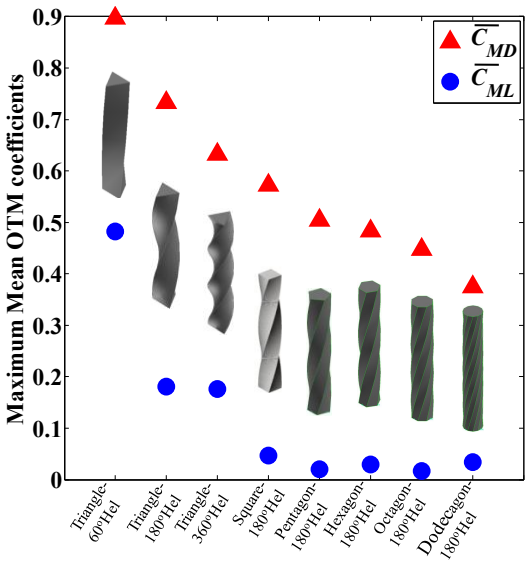

(a) Maximum mean overturning moment coefficients

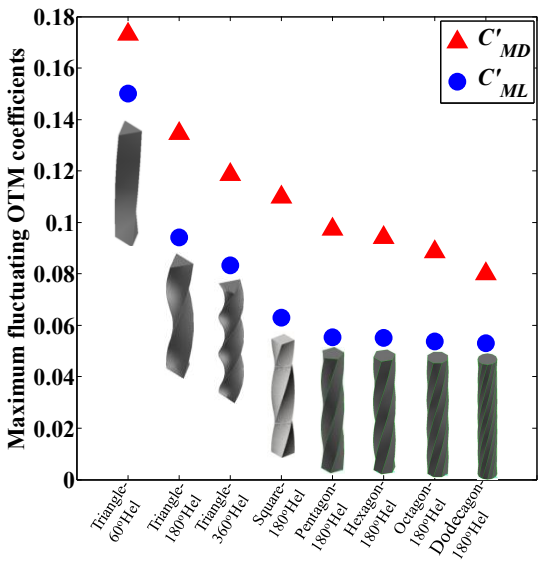

(b) Maximum fluctuating over turning moment coefficients

Figure 6.5 Maximum mean and fluctuating overturning moment coefficients in along-wind and cross wind directions

6.2.4 *Relation between the overturning moment coefficients*

The relationships between maximum mean overturning moment coefficients and maximum fluctuating overturning moment coefficients for all models are plotted in Figure 6.6 (a) for the along-wind direction and Figure 6.6 (b) for the crosswind direction. From Figure 6.6 (a), a high correlation between along-wind maximum mean coefficients and maximum fluctuating coefficients observed. In crosswind direction also, maximum mean and fluctuating o.t.m coefficients shows higher correlations. Among all the models Penta-180^{o}Hel, Hexa-180^{o}Hel, Octa-180^{o}Hel and Dodeca-180^{o}Hel models shows almost similar values in crosswind direction.

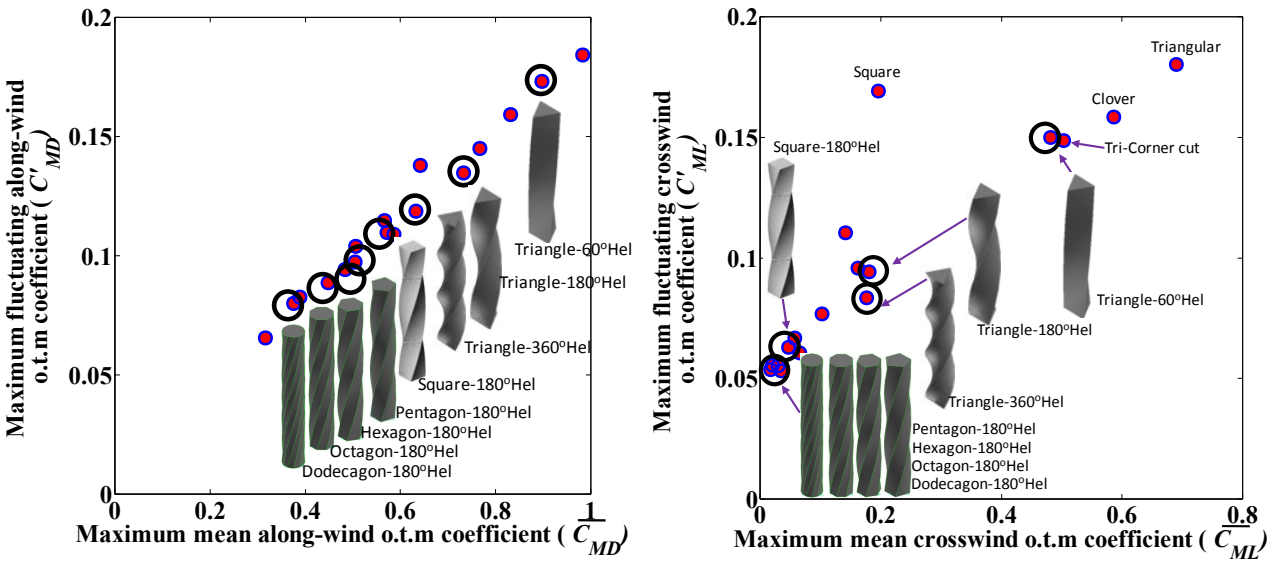

(a) Maximum mean o.t.m coefficient Vs maximum fluctuating OTM coefficient in along-wind directions

(b) Maximum mean o.t.m coefficient Vs maximum fluctuating OTM coefficient in crosswind directions

Figure 6.6 Maximum mean Vs Fluctuating o.t.m coefficients in along-wind and crosswind directions

6.3 **Effect of various building plan shapes on Power spectrum of wind forces**

6.3.1 *Power spectral densities in along-wind and crosswind directions*

Figure 6.7(a-b) shows the crosswind power spectra, fS_{CML}, for the wind directions at which the maximum peak occurred for the helical models of Triangular cross-sections and polygonal helical models. The maximum peaks occurred for crosswind spectra at θ=45°, 110°, 25°, 35°, 20°, 35°, 3° and 85° for the Tri-60°Hel, Tri-180°Hel, Tri-360°Hel, Penta-180°Hel, Hexa-180°Hel, Octa-180°Hel and Dodeca-180°Hel models. A sharp peak of crosswind spectrum is observed for the lowest twist angle. As the twist angle of helical model increases, the peak suppresses, band width increases and also the sharp peak shifts to higher reduced frequencies as shown in Figure 6.7(a). For all 180°Hel polygonal models, the peak shifts to higher reduced frequency ranges. The maximum peak occurs in the following order, i.e., Tri-180°Hel, Octa-180°Hel, Hexa-180°Hel, Dodeca-180°Hel models, Penta-180°Hel, and Sq-180°Hel as shown in Figure 6.7(b). Figure 6.8(a-b) shows the along-wind power spectra, fS_{CMD}, for the above mentioned wind directions for the polygonal models and corner modification models at which the maximum crosswind spectra peak occurred. For helical models of triangular cross-section, fS_{CMD} values reduces for all reduced frequencies as the twist angle helical model increases as shown in Figure 6.8(a).For all reduced frequencies, fS_{CMD} values are very close to each other for the Penta-180°Hel, Hexa-180°Hel and Dodeca-180°Hel models as shown in Figure 6.8(b).

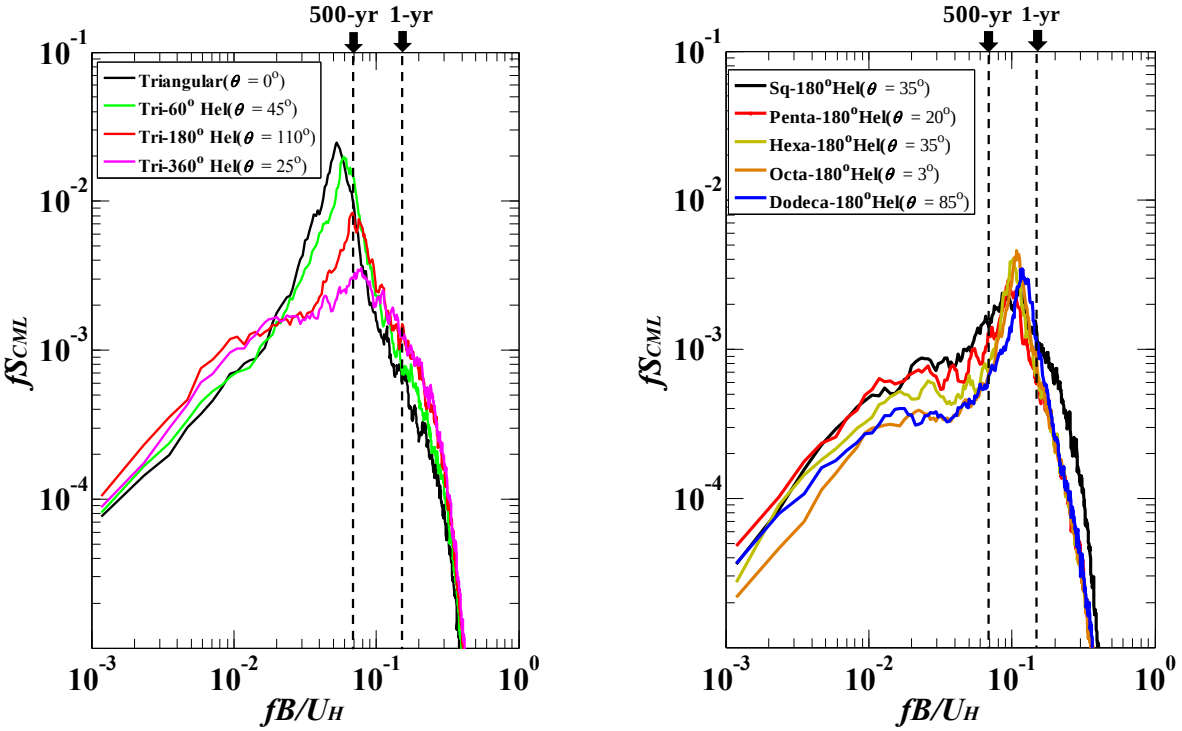

(a) Helical models of Triangular cross-section models (b) Polygonal helical models

Figure 6.7 Power spectral densities of crosswind OTM coefficients

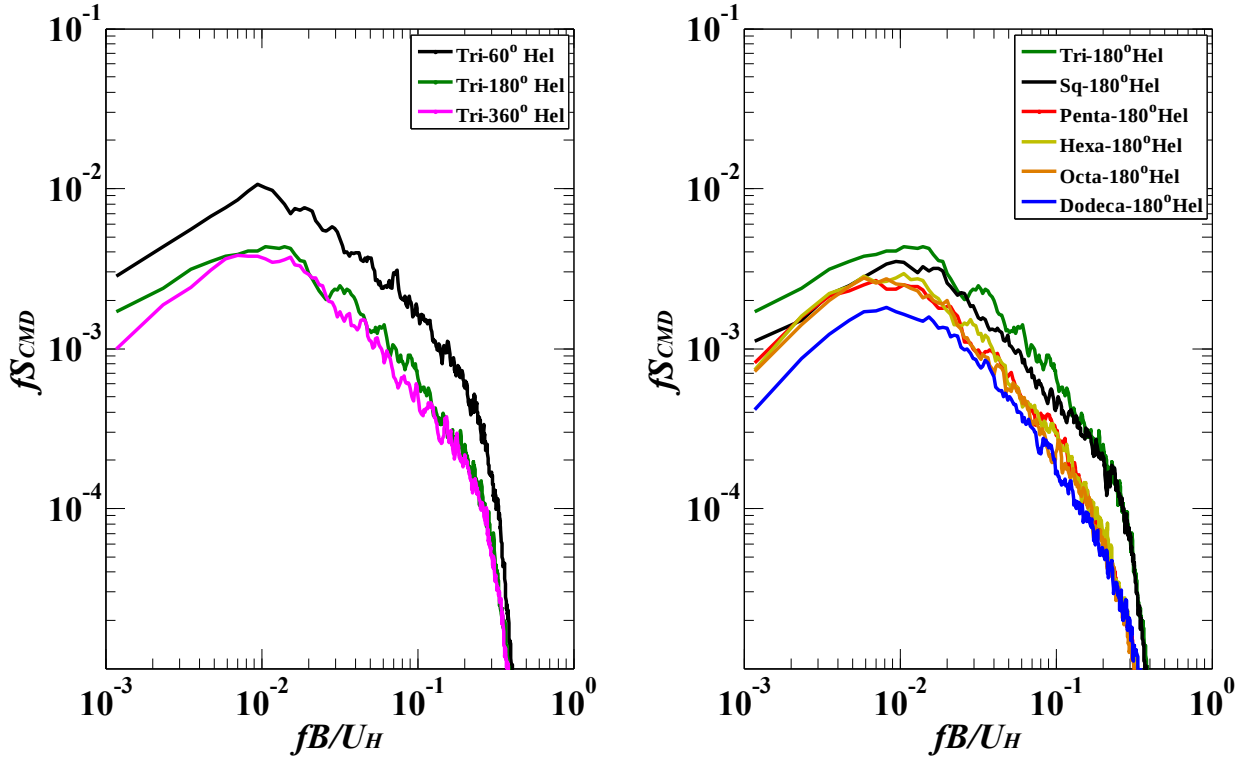

(a) Helical models of Triangular cross-section models (b) Polygonal helical models

Figure 6.8 Power spectral densities of along-wind OTM coefficients

6.3.2 *Power spectral densities of crosswind local wind force coefficients*

The crosswind power spectra of local wind force coefficients, fS_{CfL} are discussed for all the models from z/H = 0.5 to 0.975. The power spectral densities versus reduced frequencies are plotted in the Figure 6.9. The reduced frequencies were calculated based on the Square model width (B=50). Power spectral densities of crosswind local wind force coefficients were calculated for the wind directions corresponding to those where the maximum peak occurred for the crosswind spectra. The maximum peak of power spectra of crosswind occurred at wind directions, θ=45°, 110°, 25° 35°, 20°, 35°, 3° and 85° for the Tri-60°Hel, Tri-180°Hel, Tri-360°Hel, Sq-180°Hel, Penta-180°Hel, Hexa-180°Hel, Octa-180°Hel and Dodeca-180°Hel models.

The power spectra of the Tri-60°Hel model showed a sharp peak near the reduced frequency fB/U_H =0.06. The crosswind spectrum showed a narrow-band peak due to vortex shedding for all the models as shown in Figure 6.9 (a)-(h). The spectral peak shifts to higher reduced frequencies from fB/U_H =0.06 to 0.13 for the models from the above mentioned order (Tri-60°Hel to Dodeca-180°Hel models). The magnitude of spectral peak decreased for the models Tri-60°Hel, Tri-180°Hel, Tri-360°Hel, Sq-180°Hel, Penta-180°Hel models. The sharp peaks occur at z/H=0.6, 0.78, 0.7, 0.6, 0.7, 0.5 and 0.7 for the models Tri-60°Hel, Tri-180°Hel, Tri-360°Hel, Sq-180°Hel, Penta-180°Hel, Hexa-180°Hel, Octa-180°Hel and Dodeca-180°Hel models where the regular vortex shedding exists.

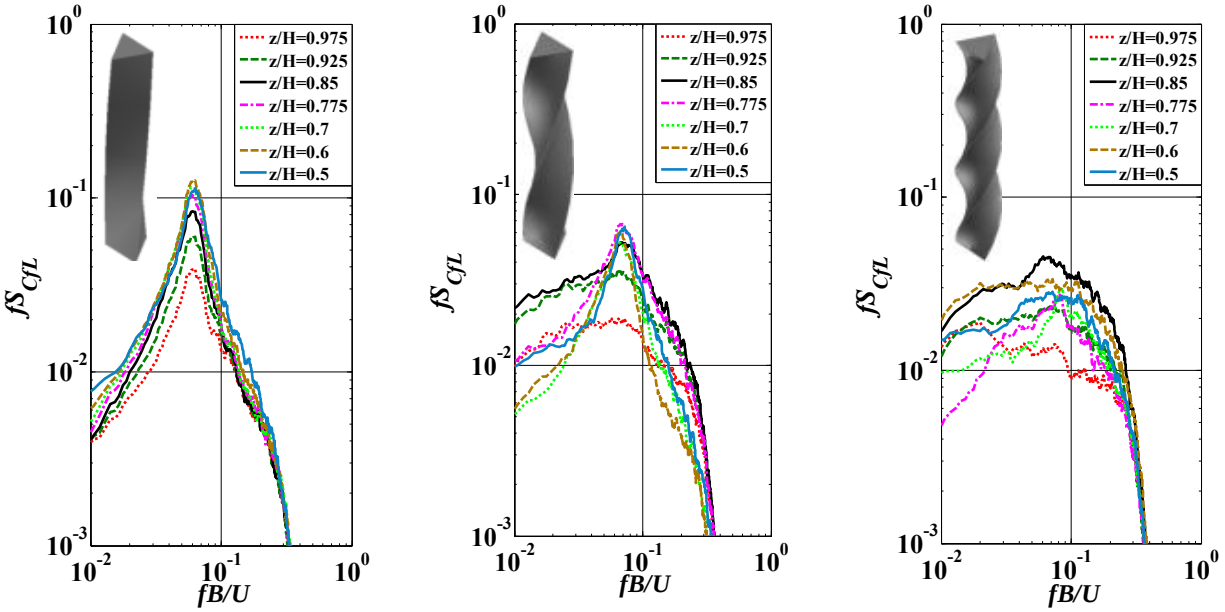

(a) Tri-60°Hel (θ=0°) (b) Tri-180°Hel (θ=0°) (c) Tri-360°Hel (θ=0°)

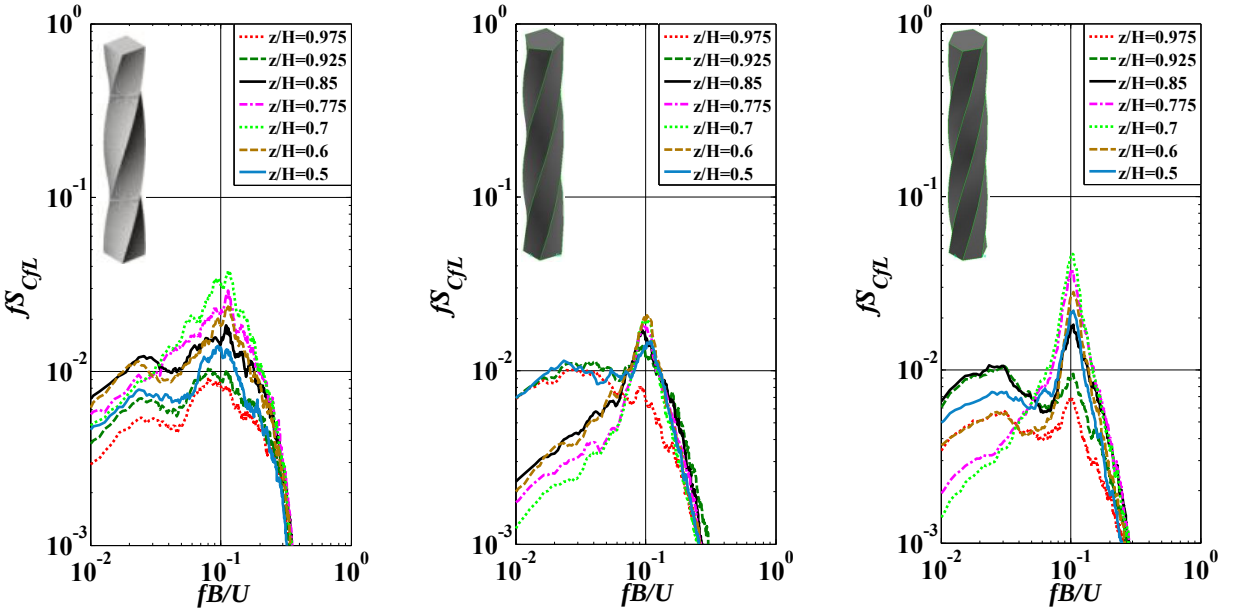

(d) Sq-180°Hel (θ=0°) (e) Penta-180°Hel (θ=100°) (f) Hexa-180°Hel (θ=30°)

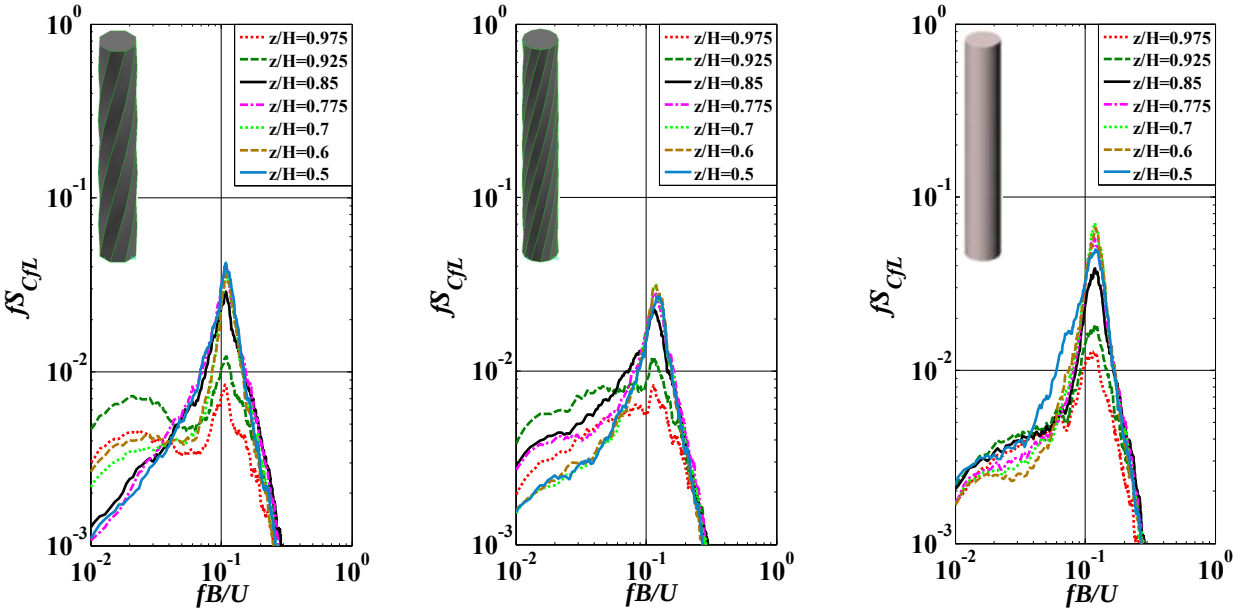

(g) Octa-180°Hel (θ=45°) (h) Dodeca-180°Hel (θ=0°) (i) Circular (θ=0°)

Figure 6.9 Power spectral densities of crosswind local wind force coefficients

6.3.3 *Maximum spectral values for 500-yr and 1-yr return periods*

Figure 6.10 compares in detail the square root of crosswind power spectra for the design wind speeds corresponding to higher spectral values at a 500-year return period ($U_{p,500}$) and a 1-year return period ($U_{p,1}$). Here, the first natural frequency is assumed to be f_1=0.1Hz, and the design wind speeds are assumed to be $U_{p,500}$=71m/s and $U_{p,1}$=30m/s at model height H, respectively, in the Tokyo region. Here, the square root of the power spectra for $U_{p,500}$, is the maximum value of

power spectra when the reduced frequency is larger than 0.07 ($fB/U_H \geq 0.07$), and the square root of the power spectra for $U_{p,1}$, is the maximum value of the power spectra when the reduced frequency is larger than 0.17 ($fB/U_H \geq 0.17$). Then, the corresponding spectral values were calculated. The $\sqrt{S_{CML,\max}}$ values decreased as the Hel angle increased for triangular models corresponding to $U_{p,500}$, but the largest value is shown for the Tri-60°Hel model.

The values of $\sqrt{S_{CML,\max}}$ for 500-year return period ($U_{p,500}$) for the Penta-180°Hel, Hexa-180°Hel, Octa-180°Hel and Dodeca-180°Hel Models, which show larger values than that of Square-180°Hel model, which are around 10-23% larger than that of the Sq-180°Hel Model. For $U_{p,1}$, $\sqrt{S_{CML,\max}}$ values become similar for Tri-180°Hel, Tri-360°Hel, Sq-180°Hel models and also similar $\sqrt{S_{CML,\max}}$ values for Penta-180°Hel, Hexa-180°Hel, Octa-180°Hel and Dodeca-180°Hel models. Hence, Penta-180°Hel, Hexa-180°Hel, Octa-180°Hel and Dodeca-180°Hel models showing that these building shapes are good for habitability design than all other models.

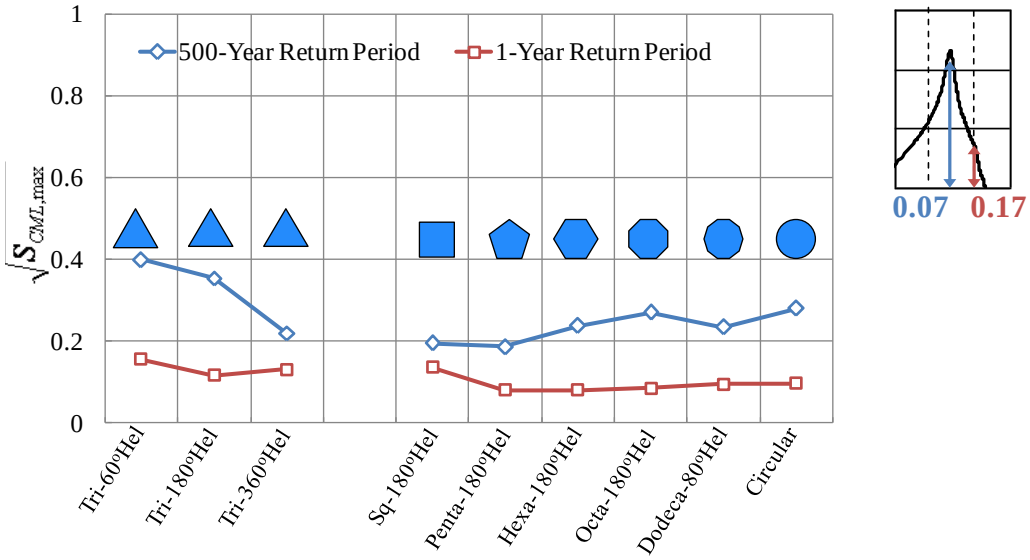

Figure 6.10 Peak spectral values for 500-year and 1-year return periods

6.3.4 *Variation of peak crosswind spectral values*

Figure 6.11 compares the variation of peak spectral values of crosswind spectra with number of side surfaces. The wind directions were selected where the maximum peak occurs for each model. The maximum value occurred for the Tri-60^{o}Hel model and then the value decreases as the twisting angle increases as shown in Figure 6.11. The maximum peak spectral value of crosswind spectra increases when the number of side surfaces increases with twist angle of 180^{o} as shown in the Figure 6.11.

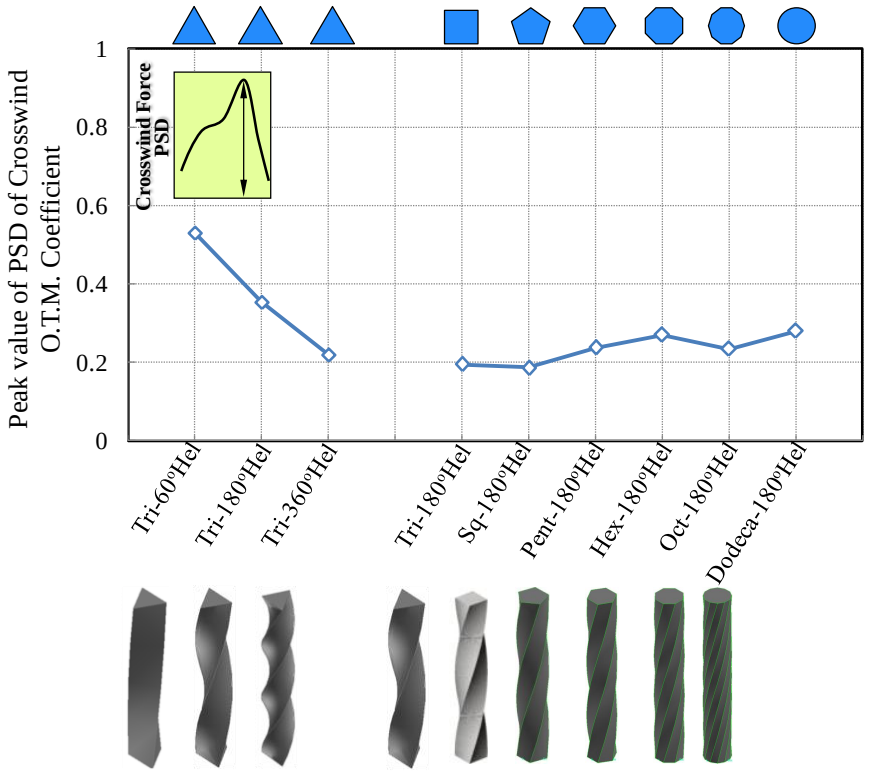

Figure 6.11 Variation of Peak spectral values of Crosswind OTM coefficients

6.3.5 *Variation of Bandwidth of a Crosswind power spectral densities*

Figures 6.12 and 6.13 compare the variation of bandwidth of crosswind spectra. The effect of number of side surfaces with 180^{o} twist angle on bandwidth shows in Figure 6.12. The bandwidth shows bit higher value for the Sq-180^{o}Hel model among all the models; but, the overall trend shows the bandwidth decreases as the number of side surfaces increases with 180^{o} twist angle. Figure 6.13 (a-b) shows the effect twisting angle of helical models on bandwidth. When

the twisting angle increases bandwidth also increases for Triangular and Square cross-sectional models.

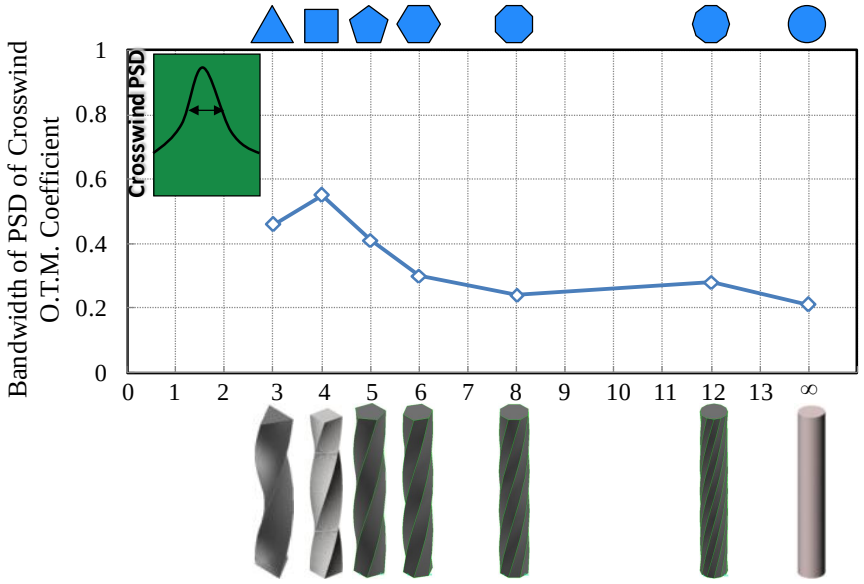

Figure 6.12 Variation of Bandwidth of PSD of Crosswind OTM coefficients with number of side surfaces and 180° twist angle.

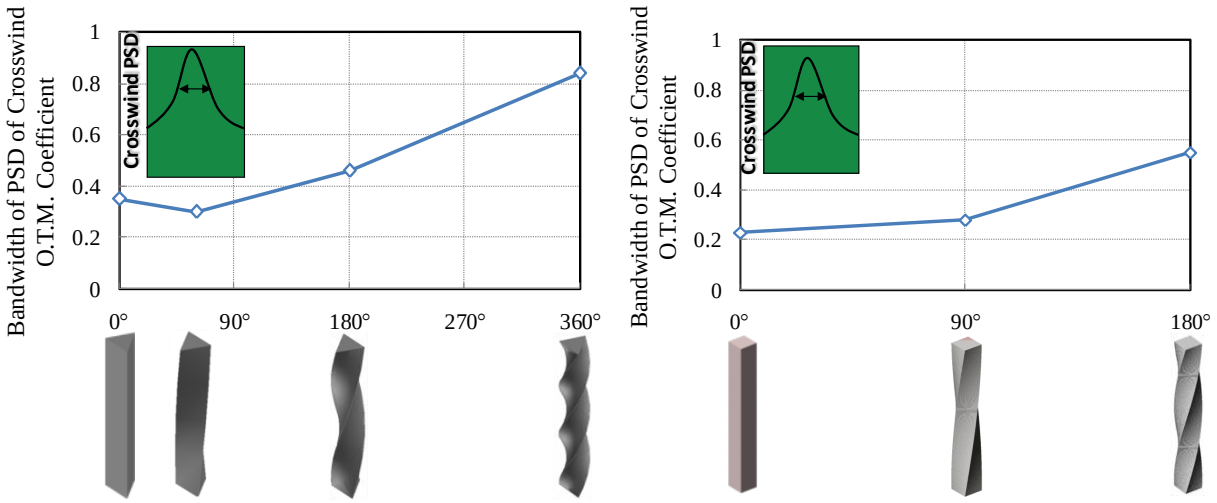

(a) Triangular models (b) Square models

Figure 6.13 Variation of Bandwidth of PSD of Crosswind OTM coefficients with twisting angle of helical models.

6.3.6 *Vertical variation of peak local reduced frequencies of crosswind force coefficients*

Figure 6.14 show the vertical variation of peak local reduced frequencies of crosswind force coefficients. These peak reduced frequencies have been calculated for all the models for the wind directions discussed in section 6.3.1. The peak reduced frequencies were obtained using the height at each level and the width, *B* of the Square model. The peak reduced frequencies are

same from 0.5*H* to 1*H* for the Tri-60°Hel model. The peak reduced frequencies are almost same for heights between 0.5*H* to 0.78*H* for all the models except Tri-180°Hel, Sq-180°Hel and Dodeca-180°Hel models. This means that all the vortices shed almost the same time throughout these heights greatly exciting these models in crosswind direction. These values show increasing and decreasing trend at all heights for Tri-360°Hel Sq-180°Hel, Pena-180°Hel and Dodeca-180°Hel models. This means, the shedding frequencies are different at various heights for these models, the resulting crosswind force decreases correspondingly.

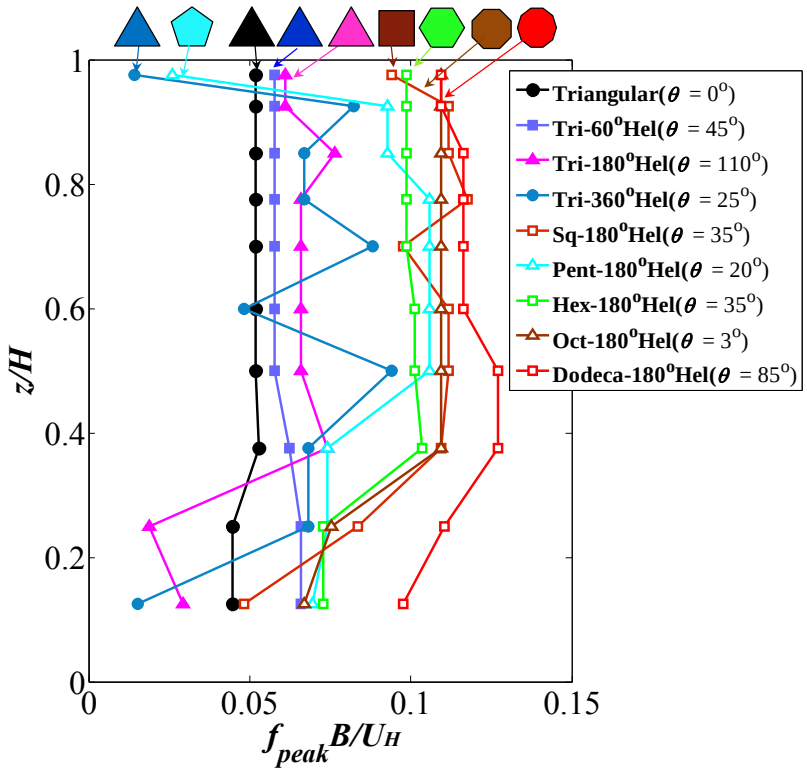

Figure 6.14 Vertical variation of peak local reduced frequencies of crosswind force coefficients

6.4 **Comparison of maximum o.t.m coefficients**

Maximum OTM coefficients have been compared with the results of Tanaka et.al (2012). In this comparison, width *B* of Square (*B*=50mm) model is considered for all the models. Maximum mean and fluctuating OTM coefficients in the along-wind and crosswind directions ($\max|\overline{C}_{MD}|$, $\max|\overline{C}_{ML}|$, $\max C'_{MD}$ and $\max C'_{ML}$) have been identified for all wind directions, as shown in Figure 6.15 and Figure 6.16. The abscissa shows the various models.

Figure 6.15 compares the maximum mean OTM coefficients. The maximum mean OTM coefficients reduce as the helical angle increases in both the along-wind and crosswind directions for triangular models. For crosswind direction, the Clover model shows 17% higher values than the Tri-Corner cut model. In the crosswind direction, the variation of maximum mean OTM coefficients is almost the same for the 180^{o}Helical and 360^{o}Helical models. The $\max|\overline{C}_{MD}|$ values of Triangular, Tri-Corner cut, Tri-180^{o}Hel, and Tri-360^{o}Hel models show around 40%, 40%, 28%, and 18% higher values than the Square, Sq-Corner cut, Sq-180^{o}Hel, and Sq-360^{o}Hel models; 71%, 92%, 61%, and 55% are the corresponding higher $\max|\overline{C}_{ML}|$ values than the Square, Sq-Corner cut, Sq-180^{o}Hel, and Sq-360^{o}Hel models.

As can be seen from Figure 6.16, the maximum fluctuating OTM coefficients reduce as the helical angle increases in both the along-wind and crosswind directions as in the case of maximum mean OTM coefficients for triangular models. The maximum fluctuating OTM coefficients in both along-wind and crosswind directions are the same for the Triangular model. In the crosswind direction, the Clover model shows a slightly higher value than the Tri-Corner cut model whereas in the along-wind direction, the Tri-Corner cut model shows a slightly higher value than the Clover model. The $\max C'_{MD}$ values of Triangular, Tri-Corner cut, Tri-180^{o}Hel, and Tri-360^{o}Hel models show around 35%, 50%, 26%, and 24% higher values than the Square, Sq-Corner cut, Sq-180^{o}Hel, and Sq-360^{o}Hel models; 22%, 39%, 36%, and 40% are the corresponding higher $\max C'_{ML}$ values than the Square, Sq-Corner cut, Sq-180^{o}Hel, and Sq-360^{o}Hel models.

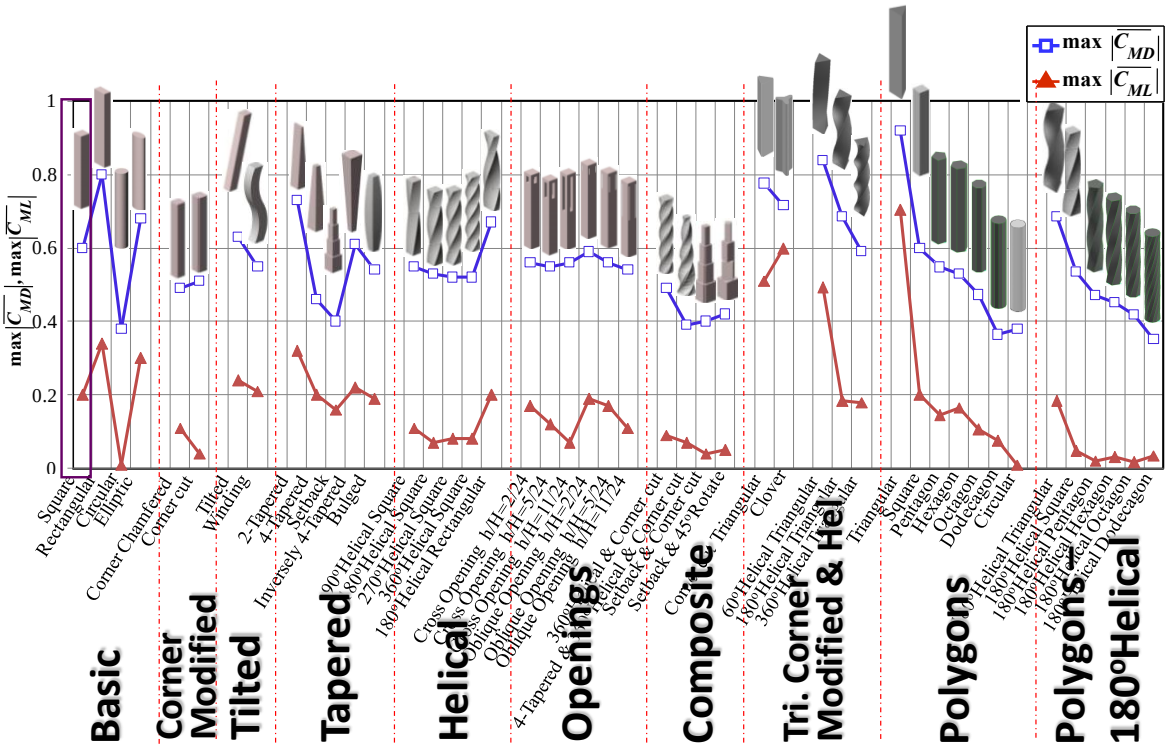

Figure 6.15 Maximum mean OTM coefficients (Tanaka et.al, 2012)

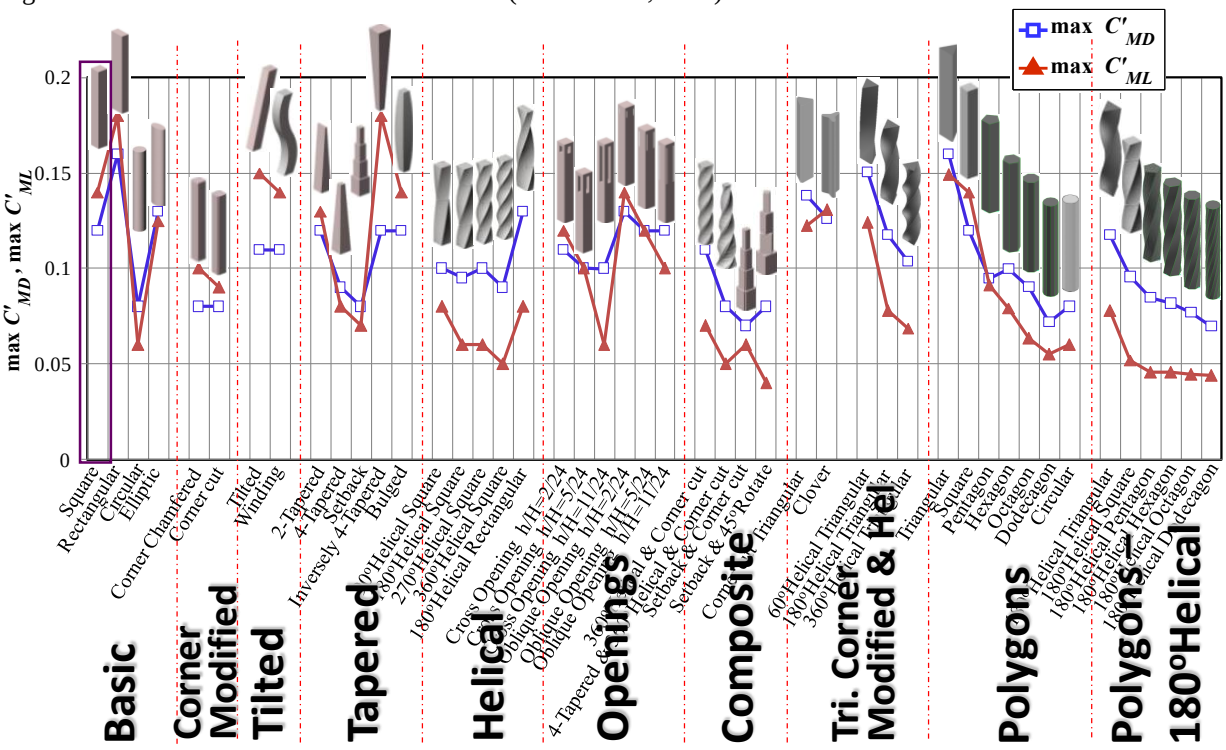

Figure 6.16 Maximum fluctuating OTM coefficients (Tanaka et.al, 2012)

6.5 **Summary**

Eight types of various cross-sectional polygonal helical models with various twisting angles were considered in this chapter. The effect of twisting angle of helical models on total wind forces, local wind forces and power spectral densities were studied.

Based on the results, the increasing number of surfaces (polygonal models) with twisting angle of 180^{o} and triangular section helical models has the significant effect on wind forces and power spectral densities. Higher twisting angle has the more significant effect on wind forces, power spectral densities and its band width.

Maximum mean and fluctuating over turning moment coefficients in along-wind and cross wind directions were compared with the square-cross sectional models (Tanaka et.al., 2012).

6.6 References

1. Akihito Yoshida, Eswara Kumar Bandi, Yukio Tamura, Yong Chul Kim, Qingshan Yang , 2012, *Experimental investigation on aerodynamic characteristics of various triangular-section high-rise buildings*, Bluff Body Aerodynamics (BBAA7), Shanghai, China.

2. Barry J. Vickery and Arthur W.Clark, Lift or Across-wind response of tapered stacks, Journal of the Structural Division, Proceedings of the American Society of Civil Engineers, January, 1972.

3. Chii-Ming Cheng, Ming-Shu Tsai, Jenmu Wang, Characteristics of alongwind loads on rectangular cylinders in turbulent boundary layer flows, BBAA VI International Colloquium on Bluff-Bodies Aerodynamics & Applications, Milano, Italy, July, 20-24, 2008.

4. D.L.Beneke and K.C.S.Knok., 1993, Aerodynamic effect of wind induced torsion on tall buildings, Journal of Wind Engineering and Industrial Aerodynamics, 50, 271-280.

5. Eswara Kumar Bandi, Yukio Tamura, Akihito Yoshida, Yong Chul Kim, Qingshan Yang, 2013, Experimental investigation on aerodynamic characteristics of various triangular-section high-rise buildings, Journal of Wind Engineering and Industrial Aerodynamics.

6. Eswara Kumar Bandi, Yong Chul Kim, Akihito Yoshida, Yukio Tamura (2011), Aerodynamic characteristics of triangular-section tall buildings with different helical angles , International Conference on Wind Engineering (ICWE13) held at Amsterdam, The Nederlands.

7. Eswara Kumar Bandi, Yukio Tamura, Akihito Yoshida, Yong Chul Kim, Qingshan Yang (2012), *Local and total wind force characteristics of triangular-section tall buildings*, The 22nd National Symposium on Wind Engineering, Tokyo, Japan.

8. Hai-Yang Wu, Shu-Guo Liang, Zheng-Qing Chen and Shu-Liang Wang, Investigation on the model of vortex-induced vibrations of rectangular super high-rise buildings, The seventh Asia-Pacific Conference on Wind Engineering, November 8-12, 2009, Taipei, Taiwan.

9. Hiroshi Hasebe, Kenji Watanabe, Yuki Watanabe and Takashi Nomura, Experimental study on the flow field between two square cylinders in tandem arrangement, The seventh Asia-Pacific Conference on Wind Engineering, November 8-12, 2009, Taipei, Taiwan.

10. Kim, Y.C., Kanda, J., 2010b, Effects of taper and set-back on wind force and wind-induced response of tall buildings, Wind and Structures, 13(6), 499-517.

11. K.M.Lam, S.Y.Wong and A.P.To, Dynamic wind loading of H-Shaped tall buildings, The seventh Asia-Pacific Conference on Wind Engineering, November 8-12, 2009, Taipei, Taiwan.

12. Lin, N., Letchford, C., Tamura, Y., Liang, B., Nakamura, O., 2005, Characteristics of wind forces acting on tall buildings, Journal of Wind Engineering and Industrial Aerodynamics, 93, 217-242.

13. M.Cheng, G.R.Liu., 2000, Effects of afterbody shape on flow around prismatic cylinders, Journal of Wind Engineering and Industrial Aerodynamics, 84, 181-196.

14. N.Bazeos & D.E.Beskos., 1996, Torsional moments on buildings subjected to wind loads, Engineering Analysis with Boundary Elements, 18, 305-310.

15. S.C.Luo, Md.G.Yazdani, Y.T.Chew, T.S.Lee., 1994, Effects of incidence and afterbody shape on flow past bluff cylinders, Journal of Wind Engineering and Industrial Aerodynamics, 53, 375-399.

16. Tanaka, H., Tamura, Y., Ohatake, K., Nakai, M., Kim, Y.C., 2012, Experimental investigation of aerodynamic forces and wind pressures acting on tall buildings with various unconventional configurations, Journal of Wind Engineering and Industrial Aerodynamics, 107-108, 179-191.

17. Tetsuro Tamura, Tetsuya Miyagi, 1999, The effect of turbulence on aerodynamic forces on a square cylinder with various corner shapes, Journal of Wind Engineering and Industrial Aerodynamics, 83-108, 135-145.

18. Yong Chul Kim, Yukio Tamura, Hideyuki Tanaka, Kazuo Ohtake, Bandi Eswara Kumar, Akihito Yoshida, 2013, *Aerodynamic characteristics of tall buildings with unconventional configurations*, 12th Americas Conference on Wind Engineering (12th ACWE), Seattel, Washington, USA.

19. Yukio Tamura, Yong Chul Kim, Bandi Eswara Kumar, Hideyuki Tanaka, Kazuo Ohtake, 2012, *Aerodynamic characteristics of Tall Building Models with Unconventional Configurations*, Structures Congress, USA.

Chapter VII

WIND FORCE COMBINATIONS OF WIND FORCE COMPONENTS OF POLYGONAL MODELS

It is commonly known that along wind force fluctuations are mainly generated by the approaching flow turbulence and the across wind force and torsional moment fluctuations are mainly due to the vortex shedding. Thus it is believed that the across wind force and torsional moment are well correlated, but the along wind force is not correlated with the other two components. Therefore in the design of structures, the along wind force is predominant, their combinations tend to be ignored (Tamura et al, 2003).

Surface pressures on buildings and structures fluctuate irregularly both in time and space, and the wind load on buildings and structures is a kind of spatial average of them over a certain area. Therefore, the surface pressures should be measured spatially and simultaneously (Ueda et al, 1994). In this research the pressure fluctuations on the surface of the building models are measured simultaneously using the multi channel pressure scanners. Then the fluctuating pressures are integrated to calculate the forces and moments acting on the model. In this chapter the detailed discussion on the wind load combinations between the forces and moments are shown in terms of trajectories, correlation coefficient, absolute value correlation and the simultaneously acting wind loads.

Capturing the necessity of the maximum wind forces was first introduced as a gust factor (Davenport, 1961). Based on the concept of the maximum wind load effects, the reliability of wind loading on low-rise buildings are discussed and suggested some important factors for its assess-

ment (Davenport, 1983). Davenport emphasized the importance of more sophisticated wind load estimation for low-rise buildings.

The full-scale and the wind tunnel relation on the Aylesbury experimental low-rise building shows in Vickery et al (1986). Recently the study on wind forces acting on the tall buildings and its characteristics are discussed in Lin et al (2005). It gives a detailed discussion about the spectral characteristics, cross-correlation, coherence, phase etc for the tall building force and moment components. It summarizes the extensive wind tunnel study on local wind forces on isolated tall building.

In this chapter, seventeen models with different cross-sections with twisting angle of 180^o were used to study the wind load combinations. The models are Triangular, Tri-Corner cut, Clover, Square, Pentagon, Hexagon, Octagon, Dodecagon, Circular, Tri-60^oHel, Tri-180^oHel, Tri-360^oHel, Sq-180^oHel, Penta-180^oHel, Hexa-180^oHel, Octa-180^oHel and Dodeca-180^oHel models.

The fluctuating pressures were integrated to obtain the forces and moments acting on the surface of the building model. They are along-wind force F_D, crosswind force F_L, along wind overturning moment M_D, across wind overturning moment M_L, and torsional moment M_T. They are expressed in non-dimensional forms based on the mean velocity pressure q_H at the model height.

Along-wind force coefficient, $C_D = \dfrac{F_D}{q_H BH}$ (7.1)

Crosswind force coefficient, $C_L = \dfrac{F_L}{q_H BH}$ (7.2)

Along-wind overturning moment coefficient, $C_{MD} = \dfrac{M_D}{q_H BH^2}$ (7.3)

Crosswind overturning moment coefficient, $C_{ML} = \dfrac{M_L}{q_H BH^2}$ (7.4)

Torsional moment coefficient, $C_{MT} = \dfrac{M_T}{q_H B^2 H}$ (7.5)

7.1 **Wind force combinations of straight models with various cross-sections**

Wind force combination in the super-tall buildings were discussed in terms of trajectories, correlation coefficient, absolute value correlation and simultaneously acting wind forces.

7.1.1 *Trajectories of various overturning moment coefficients*

Figure 7.1 to 7.9 shows the trajectories of time series of various overturning moment coefficients for Triangular, Tri-Corner cut, Clover, Square, Pentagon, Hexagon, Octagon, Dodecagon and Circular models. Trajectories of overturning moment coefficients have been plotted for wind direction where the mean over turning moment in crosswind direction ($\overline{C_{ML}}$) becomes zero.

The trajectory of C_{MD}-C_{ML} and C_{MD}-C_{MT} for the Triangular model shows a circular shape, showing that there is no correlation between them, but sometimes we can see some correlation for C_{ML}-C_{MT}. The Tri-Corner cut show almost no correlation between all overturning moment coefficients. The Clover model sometimes shows some correlation between C_{ML}-C_{MT}. The trajectory of C_{MD}-C_{ML} of Square model shows a half circle shape, implying no correlation between them. But the wedge shape also means that when C_{MD} is a maximum, the maximum value of C_{ML} may occur. There is no correlation between C_{MD}-C_{ML} for the models Pentagon, Hexagon, Octagon and Dodecagon where as some correlation in Circular model. There is no correlation between C_{MD}-C_{MT} for the models Pentagon, Octagon, Dodecagon and Circular models where as some correlation for the Hexagon model. For the Pentagon model, we can see some correlation between C_{ML}-C_{MT} as its trajectory shape looks elliptical with slight inclination angle where as for the Hexagon model we can see high correlation as its trajectory shape looks elliptic with more inclination angle. It is very interesting to note that, the trajectory shapes between C_{MD}-C_{MT} and C_{ML}-C_{MT} becomes elliptic in shape and becomes thinner and thinner and becomes very flat with abscissa as the number of faces increases from Pentagon to Circular models.

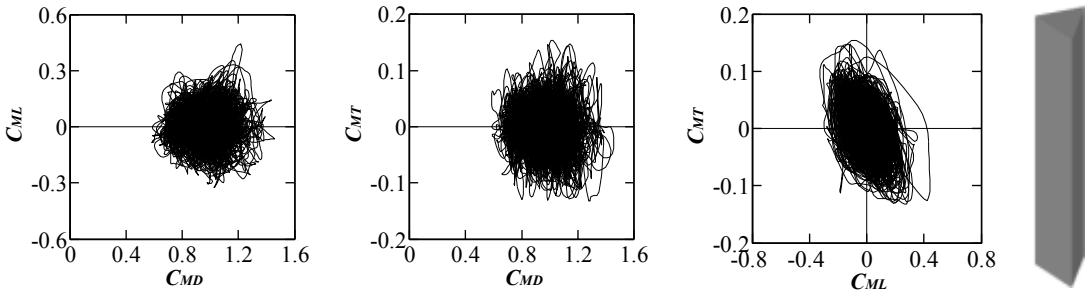

(a) C_{MD} - C_{ML} (b) C_{MD} - C_{MT} (c) C_{ML} - C_{MT}

Figure 7.1 Trajectory of overturning moment coefficients for Triangular model at 0^o wind direction

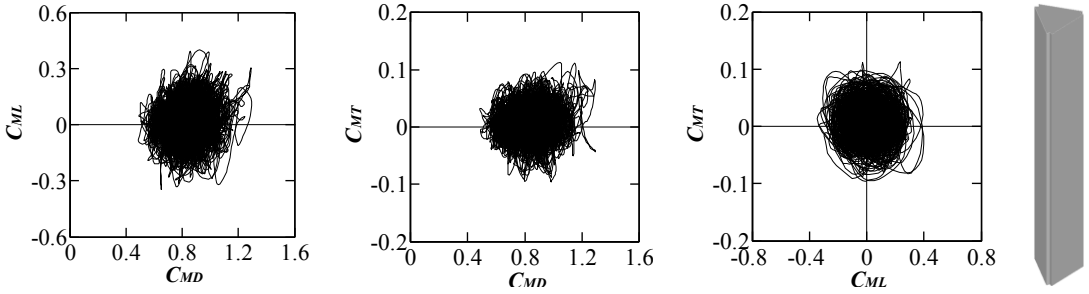

(a) C_{MD} - C_{ML} (b) C_{MD} - C_{MT} (c) C_{ML} - C_{MT}

Figure 7.2 Trajectory of overturning moment coefficients for Tri-Corner cut model at 0^o wind direction

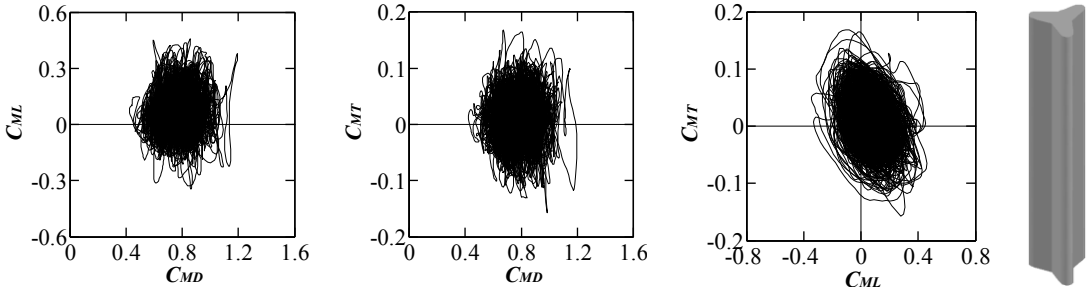

(a) C_{MD} - C_{ML} (b) C_{MD} - C_{MT} (c) C_{ML} - C_{MT}

Figure 7.3 Trajectory of overturning moment coefficients for Clover model at 0^o wind direction

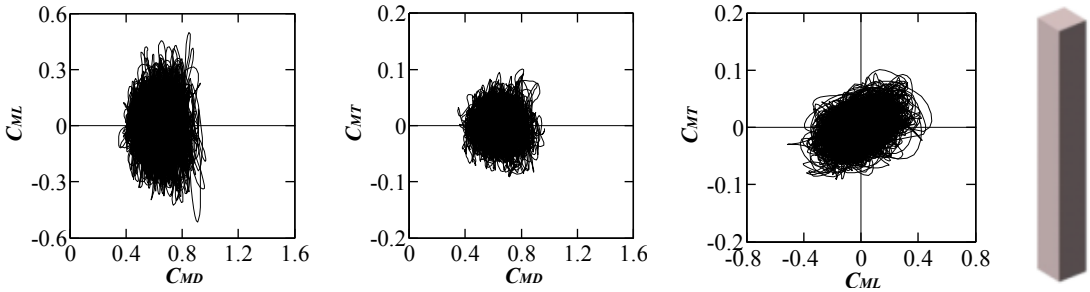

(a) C_{MD} - C_{ML} (b) C_{MD} - C_{MT} (c) C_{ML} - C_{MT}

Figure 7.4 Trajectory of overturning moment coefficients for Square model at 0^o wind direction

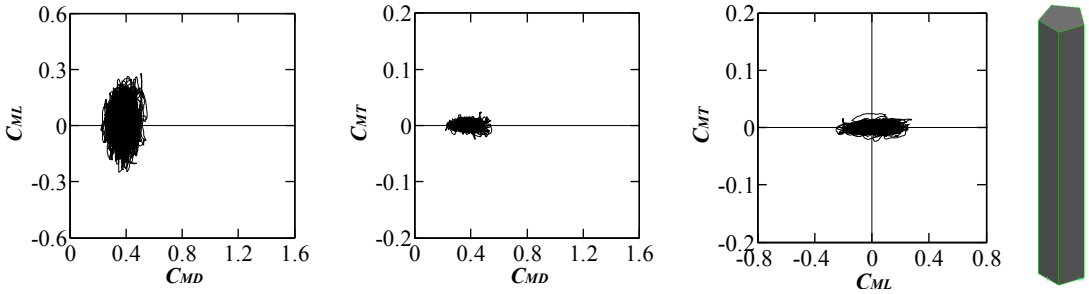

(a) C_{MD} - C_{ML} (b) C_{MD} - C_{MT} (c) C_{ML} - C_{MT}

Figure 7.5 Trajectory of overturning moment coefficients for Pentagon model at 0^o wind direction

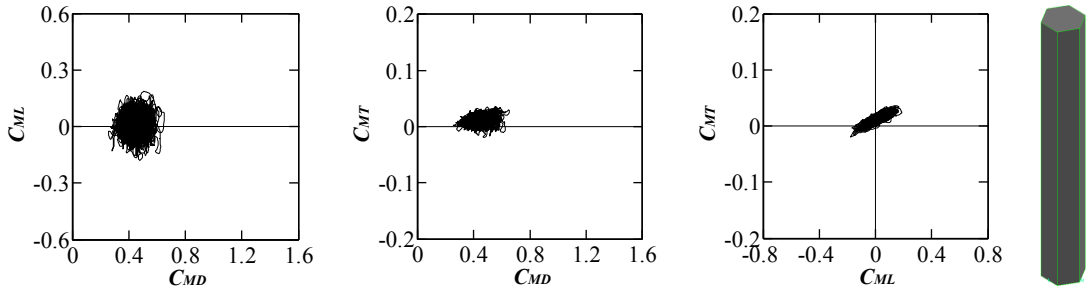

(a) C_{MD} - C_{ML} (b) C_{MD} - C_{MT} (c) C_{ML} - C_{MT}

Figure 7.6 Trajectory of overturning moment coefficients for Hexagon model at 0^o wind direction

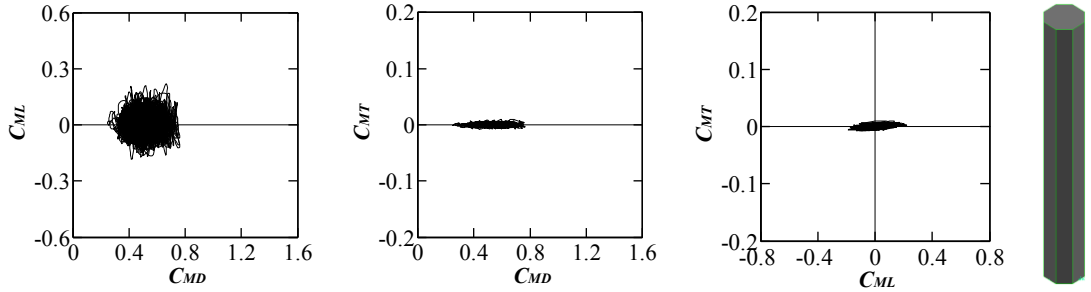

(a) C_{MD} - C_{ML} (b) C_{MD} - C_{MT} (c) C_{ML} - C_{MT}

Figure 7.7 Trajectory of overturning moment coefficients for Octagon model at 0^o wind direction

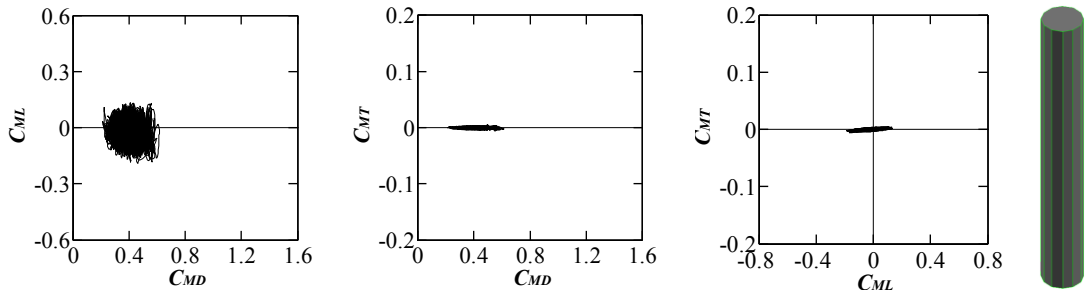

(a) C_{MD} - C_{ML} (b) C_{MD} - C_{MT} (c) C_{ML} - C_{MT}

Figure 7.8 Trajectory of overturning moment coefficients for Dodecagon model at 0^o wind direction

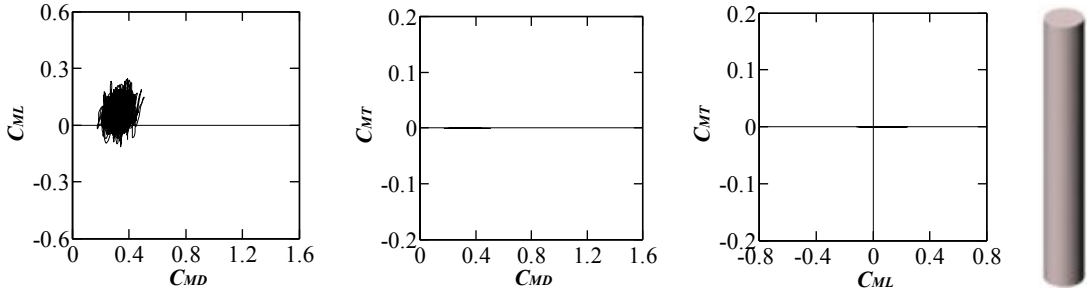

(a) C_{MD} - C_{ML} (b) C_{MD} - C_{MT} (c) C_{ML} - C_{MT}

Figure 7.9 Trajectory of overturning moment coefficients for Circular model at 0^o wind direction

7.1.2 *Correlation and absolute value correlation*

In statistics and probability, the correlation coefficient indicates the strength and the direction of the relationship between the two random variables. In order to understand the real relationship between the various overturning moments, the absolute value correlation is also calculated and shown in Figure 7.10-7.18 for the models Triangular, Tri-Corner cut, clover, Square, pentagon, Hexagon, Octagon, Dodecagon and Circular models respectively. The value of the correlation coefficient can be well compared with the shape of the trajectories of overturning moments discussed in section 7.1.1. In the following figures, solid line shows correlation curve and dotted line shows absolute value correlation. Considering the absolute value correlation, there is some correlation between C_{MD}-C_{ML} and C_{MD}-C_{MT} obtained for all the models (Triangular, Tri-Corner cut, Clover, Square, Pentagon, Hexagon, Octagon, Dodecagon and Circular models). Among all these models, the Hexagon model shows positive value correlation in both absolute and its original value correlation. When we consider the correlation between C_{ML}-C_{MT}, the high correlation shows for the Hexagon and Dodecagon models in both its original and absolute value correlation.

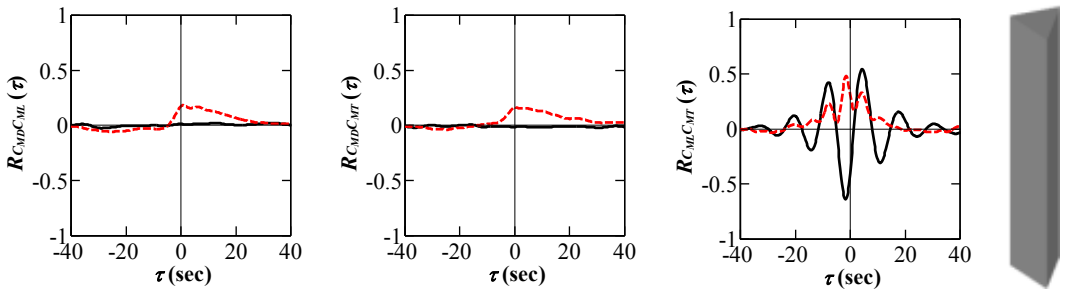

(a) C_{MD} - C_{ML} (b) C_{MD} - C_{MT} (c) C_{ML} - C_{MT}

Figure 7.10 Correlation coefficient (Solid line) and absolute value correlation (dotted line) for Triangular model at 0^o wind direction

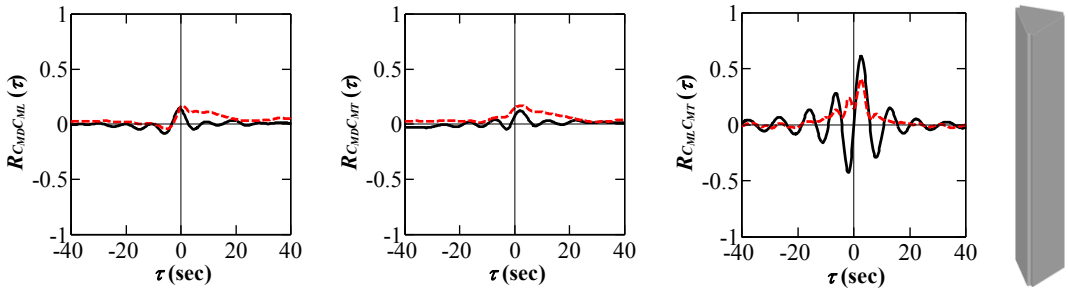

(a) C_{MD} - C_{ML} (b) C_{MD} - C_{MT} (c) C_{ML} - C_{MT}

Figure 7.11 Correlation coefficient (Solid line) and absolute value correlation (dotted line) for Tri-Corner cut model at 0^o wind direction

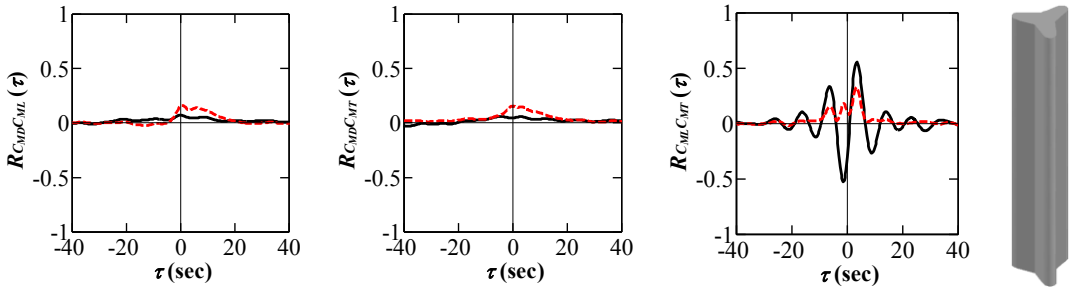

(a) C_{MD} - C_{ML} (b) C_{MD} - C_{MT} (c) C_{ML} - C_{MT}

Figure 7.12 Correlation coefficient (Solid line) and absolute value correlation (dotted line) for Clover model at 0° wind direction

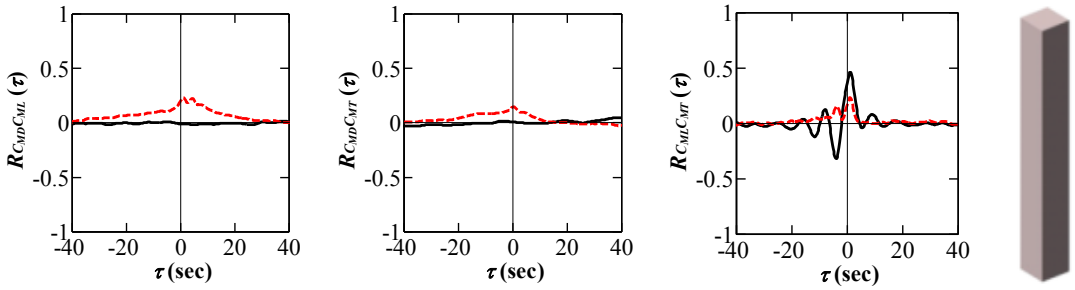

(a) C_{MD} - C_{ML} (b) C_{MD} - C_{MT} (c) C_{ML} - C_{MT}

Figure 7.13 Correlation coefficient (Solid line) and absolute value correlation (dotted line) for Square model at 0° wind direction

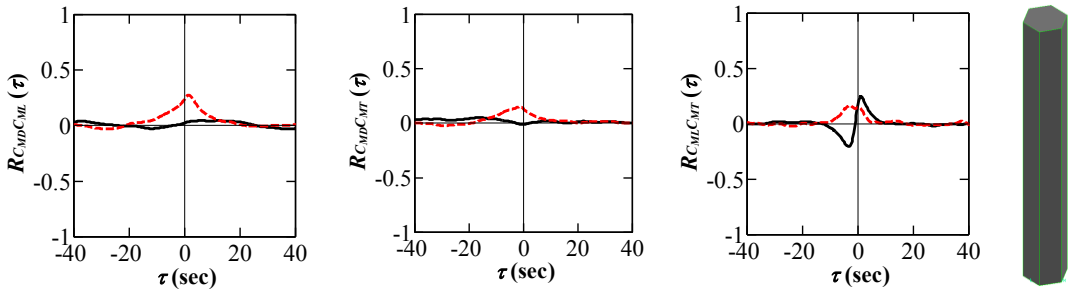

(a) C_{MD} - C_{ML} (b) C_{MD} - C_{MT} (c) C_{ML} - C_{MT}

Figure 7.14 Correlation coefficient (Solid line) and absolute value correlation (dotted line) for Pentagon model at 0° wind direction

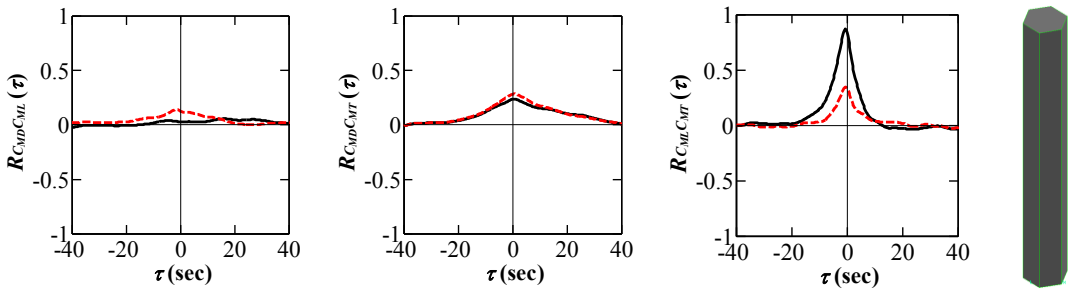

(a) C_{MD} - C_{ML} (b) C_{MD} - C_{MT} (c) C_{ML} - C_{MT}

Figure 7.15 Correlation coefficient (Solid line) and absolute value correlation (dotted line) for Hexagon model at 0° wind direction

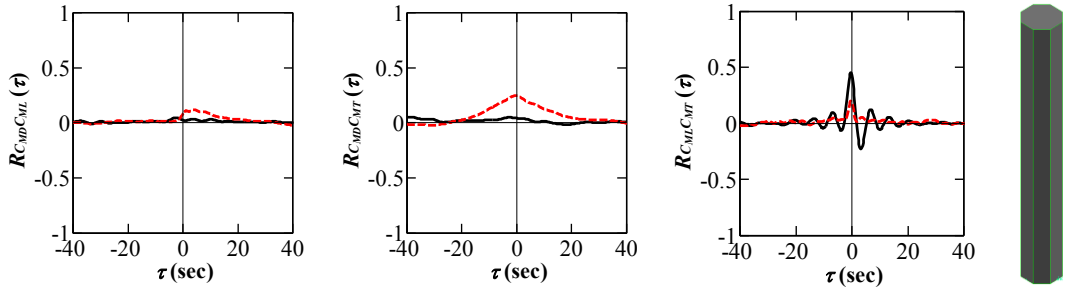

(a) C_{MD} - C_{ML} (b) C_{MD} - C_{MT} (c) C_{ML} - C_{MT}

Figure 7.16 Correlation coefficient (Solid line) and absolute value correlation (dotted line) for Octagon model at 0^o wind direction

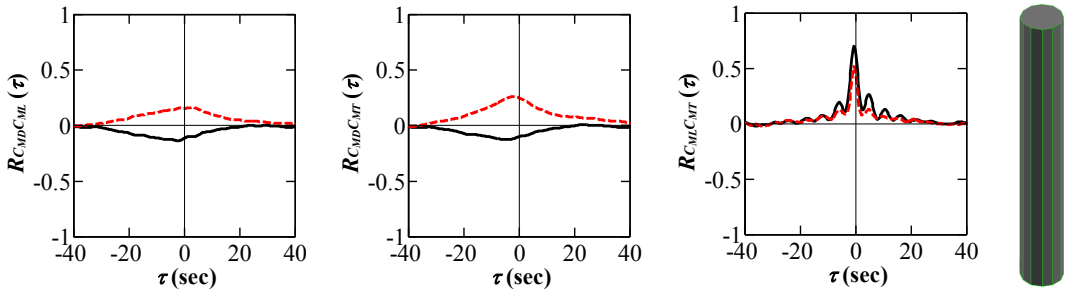

(a) C_{MD} - C_{ML} (b) C_{MD} - C_{MT} (c) C_{ML} - C_{MT}

Figure 7.17 Correlation coefficient (Solid line) and absolute value correlation (dotted line) for Dodecagon model at 0^o wind direction

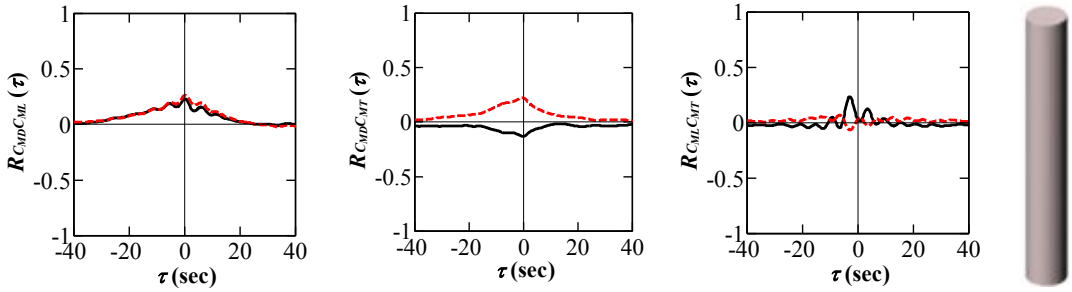

(a) C_{MD} - C_{ML} (b) C_{MD} - C_{MT} (c) C_{ML} - C_{MT}

Figure 7.18 Correlation coefficient (Solid line) and absolute value correlation (dotted line) for Circular model at 0^o wind direction

7.1.3 *Simultaneous wind loadings*

In this research the instantaneous wind forces discussed were obtained by spatial integration of the fluctuating pressures at number of points. Figure 7.19, 7.20 & 7.21 show examples of the results for a Triangular model, on the basis of 33 samples. Figure 7.19 (a) & (b) show the cross-wind force and torsional moment ratios, $C_L(C_{D\max})/C_{L\max}$ and $C_{MT}(C_{D\max})/C_{MT\max}$, when the maximum along-wind force $C_{D\max}$ occurs. They are defined as the ratios of the crosswind force and

torsional moment coefficients $C_L(C_{D\max})$ and $C_{MT}(C_{D\max})$ to their maximum values $C_{L\max}$ and $C_{MT\max}$ for each 10-min sample. 0–30% of the maximum crosswind force coefficient $C_{L\max}$ and 0–30% of the maximum torsional moment coefficient $C_{MT\max}$ were simultaneously recorded with the maximum along-wind force $C_{D\max}$. Fig 6.20 (a) & (b) show the along-wind force and torsional moment ratios, $C_D(C_{L\max})/C_{D\max}$ and $C_T(C_{L\max})/C_{T\max}$, when the maximum across-wind force $C_{L\max}$ occurs. 50–80% of the maximum along-wind forces and 0–40% of the maximum torsional moment coefficients were most likely to appear with the maximum crosswind force $C_{L\max}$. Fig 6.21 (a) & (b) show the cases when the maximum torsional moment $C_{T\max}$ was recorded. When the maximum torsional moment $C_{T\max}$ occurs, around 60-70% of the maximum along-wind force $C_{D\max}$ was simultaneously recorded, as shown in fig 6.21 (a), while a relatively small crosswind force $C_L(C_{T\max})$, i.e. around 0-30% of its maximum value $C_{L\max}$, appears as shown in fig 6.21 (b).

For the models Pentagon, Hexagon and Octagon, the distribution of instantaneous wind forces looks same. For the Circular model, the instantaneous wind forces are distributed uniformly from 0% to 100% for crosswind force coefficient ratio $C_L(C_{D\max})/C_{L\max}$ when along-wind force is maximum ($C_{D\max}$), torsional moment coefficient ratio $C_T(C_{D\max})/C_{T\max}$ when along-wind force is maximum ($C_{D\max}$), torsional moment coefficient ratio $C_T(C_{L\max})/C_{T\max}$ when crosswind force is maximum ($C_{L\max}$) and crosswind force coefficient ratio $C_L(C_{T\max})/C_{L\max}$ when torsional moment is maximum ($C_{T\max}$).

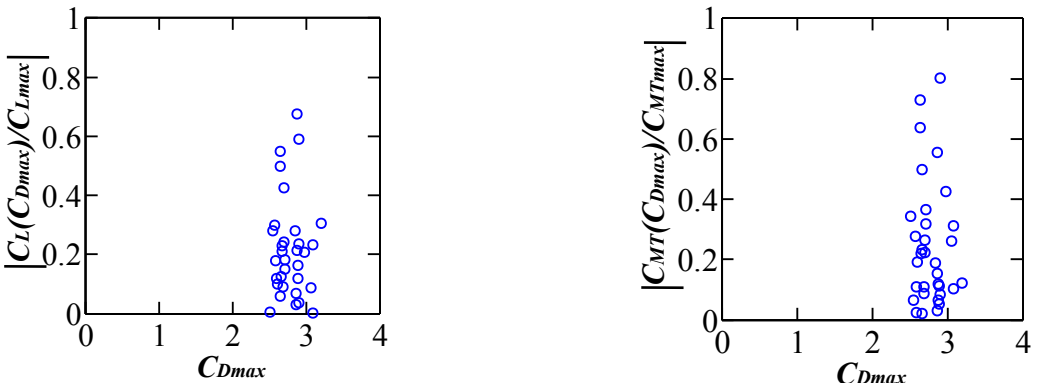

Figure 7.19 Ratio of C_L and C_{MT} accompanied by maximum along-wind force $C_{D\max}$ to their maximum values $C_{L\max}$ and $C_{MT\max}$ for Triangular model (a) C_L $(C_{D\max})/C_{L\max}$, and (b) C_{MT} $(C_{D\max})/C_{MT\max}$.

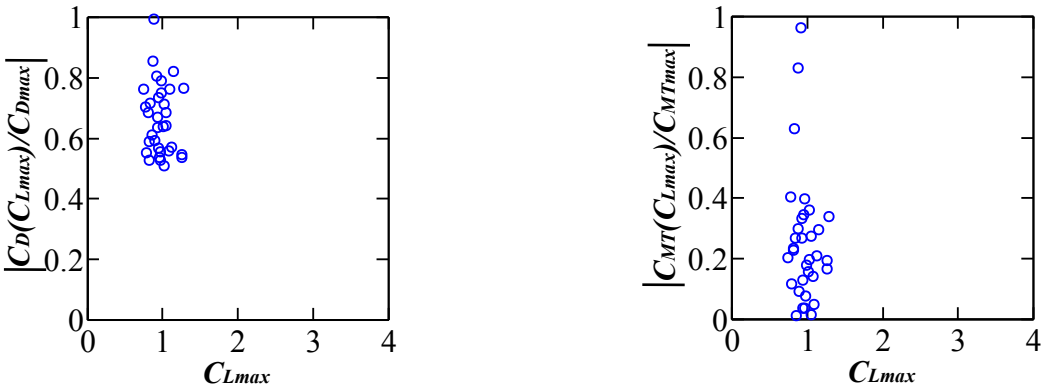

Figure 7.20 Ratio of C_D and C_{MT} accompanied by maximum crosswind force $C_{L\max}$ to their maximum values $C_{D\max}$ and $C_{MT\max}$ for Triangular model (a) C_D ($C_{L\max}$)/$C_{D\max}$, and (b) C_{MT} ($C_{L\max}$)/$C_{MT\max}$.

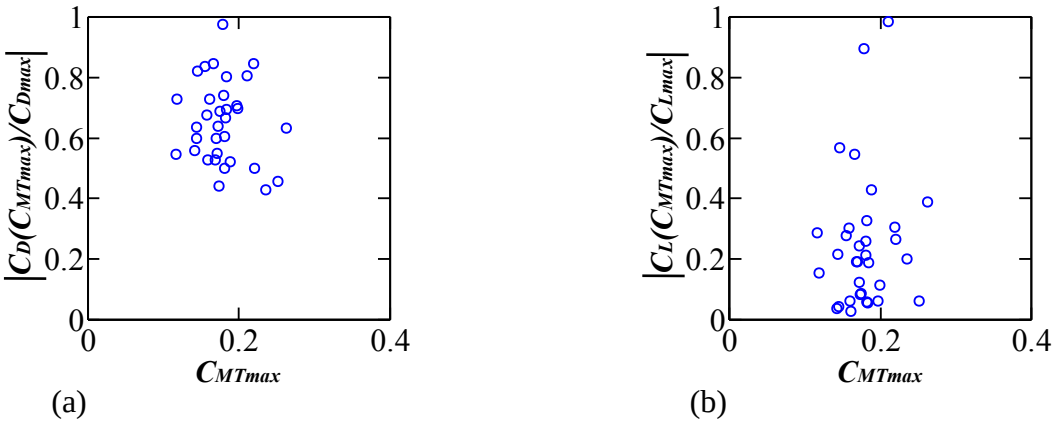

Figure 7.21 Ratio of C_D and C_L accompanied by maximum torsional moment $C_{MT\max}$ to their maximum values $C_{D\max}$ and $C_{L\max}$ for Triangular model (a) C_D ($C_{MT\max}$)/$C_{D\max}$, and (b) C_L ($C_{MT\max}$)/$C_{L\max}$.

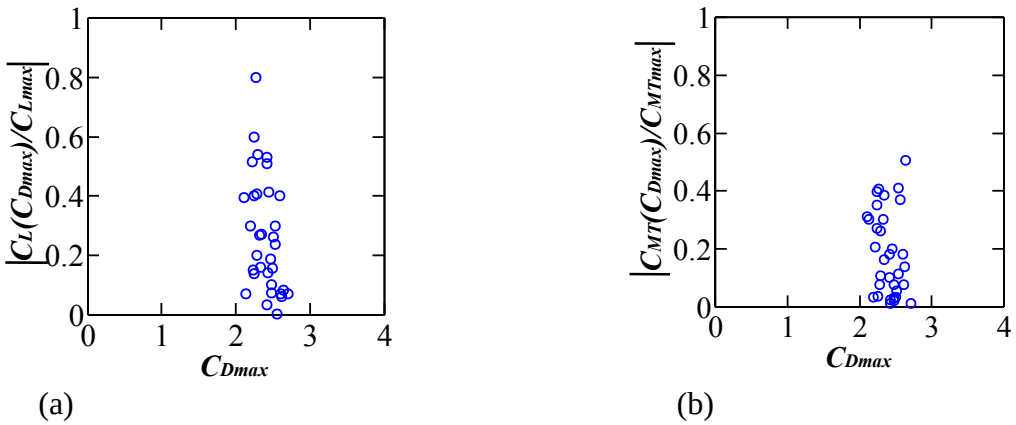

Figure 7.22 Ratio of C_L and C_{MT} accompanied by maximum along-wind force $C_{D\max}$ to their maximum values $C_{L\max}$ and $C_{MT\max}$ for Tri-Croner cut model (a) C_L ($C_{D\max}$)/$C_{L\max}$, and (b) C_{MT} ($C_{D\max}$)/$C_{MT\max}$.

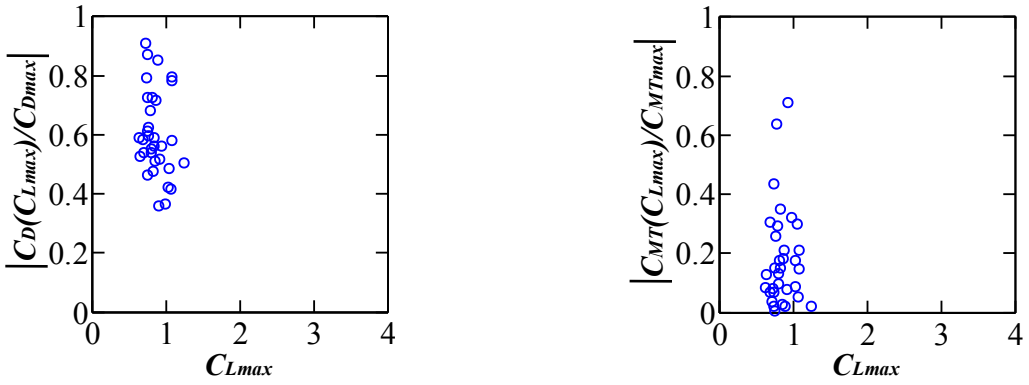

(a) (b)

Figure 7.23 Ratio of C_D and C_{MT} accompanied by maximum crosswind force $C_{L\max}$ to their maximum values $C_{D\max}$ and $C_{MT\max}$ for Tri-Croner cut model (a) C_D ($C_{L\max}$)/$C_{D\max}$, and (b) C_{MT} ($C_{L\max}$)/$C_{MT\max}$.

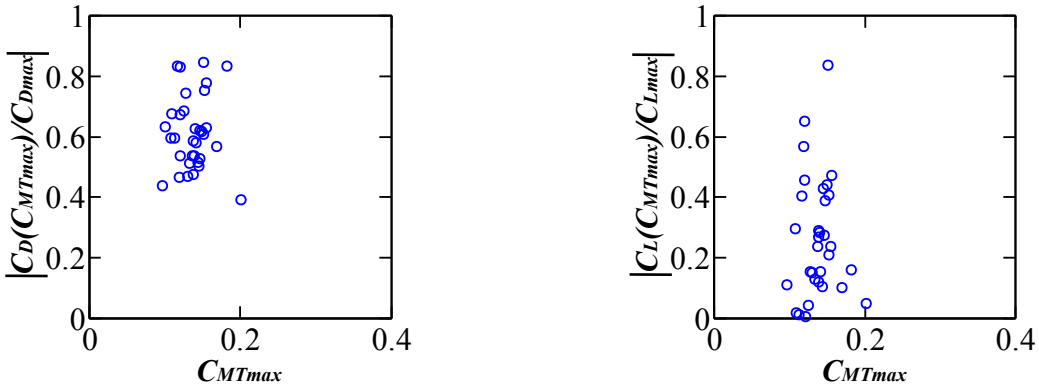

(a) (b)

Figure 7.24 Ratio of C_D and C_L accompanied by maximum torsional moment $C_{MT\max}$ to their maximum values $C_{D\max}$ and $C_{L\max}$ for Tri-Croner cut model (a) C_D ($C_{MT\max}$)/$C_{D\max}$, and (b) C_L ($C_{MT\max}$)/$C_{L\max}$.

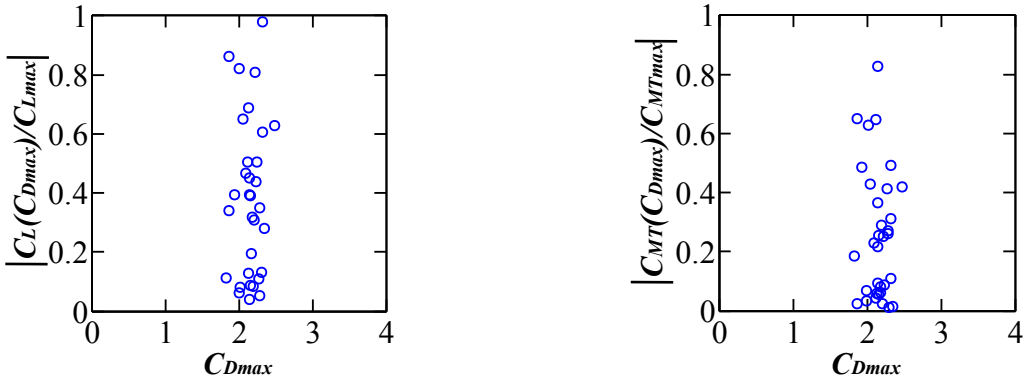

(a) (b)

Figure 7.25 Ratio of C_L and C_{MT} accompanied by maximum along-wind force $C_{D\max}$ to their maximum values $C_{L\max}$ and $C_{MT\max}$ for Clover model (a) C_L ($C_{D\max}$)/$C_{L\max}$, and (b) C_{MT} ($C_{D\max}$)/$C_{MT\max}$.

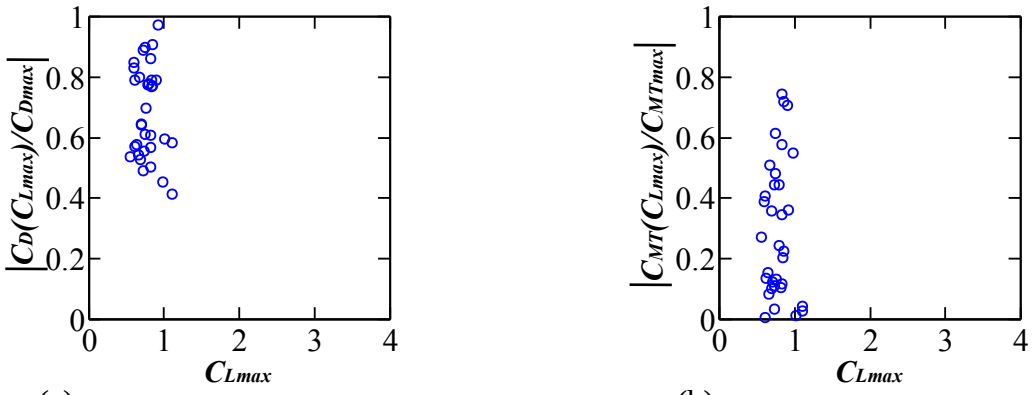

(a) (b)

Figure 7.26 Ratio of C_D and C_{MT} accompanied by maximum crosswind force $C_{L\max}$ to their maximum values $C_{D\max}$ and $C_{MT\max}$ for Clover model (a) C_D ($C_{L\max}$)/$C_{D\max}$, and (b) C_{MT} ($C_{L\max}$)/$C_{MT\max}$.

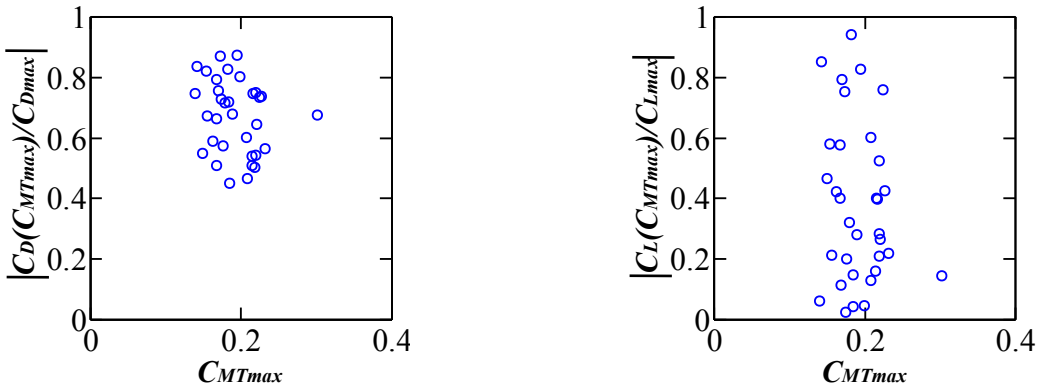

(a) (b)

Figure 7.27 Ratio of C_D and C_L accompanied by maximum torsional moment $C_{MT\max}$ to their maximum values $C_{D\max}$ and $C_{L\max}$ for Clover model (a) C_D ($C_{MT\max}$)/$C_{D\max}$, and (b) C_L ($C_{MT\max}$)/$C_{L\max}$.

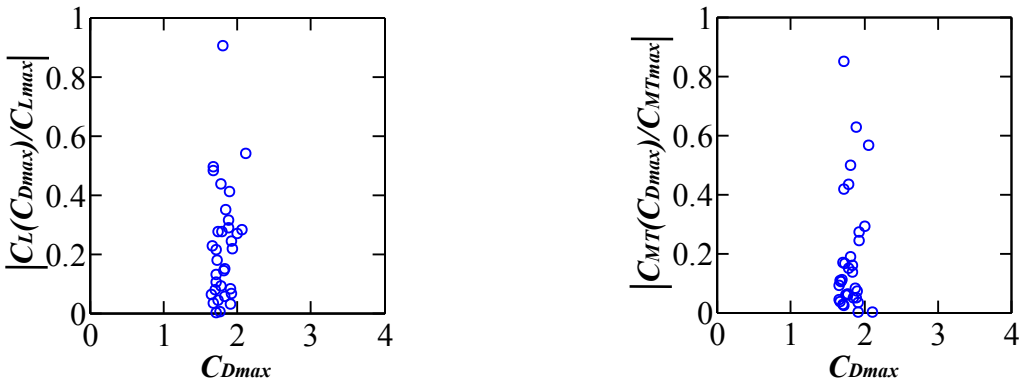

(a) (b)

Figure 7.28 Ratio of C_L and C_{MT} accompanied by maximum along-wind force $C_{D\max}$ to their maximum values $C_{L\max}$ and $C_{MT\max}$ for Square model (a) C_L ($C_{D\max}$)/$C_{L\max}$, and (b) C_{MT} ($C_{D\max}$)/$C_{MT\max}$.

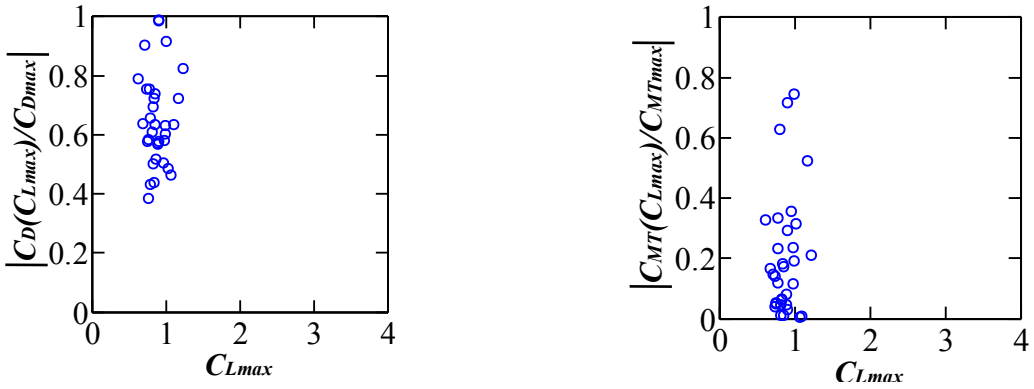

(a) (b)

Figure 7.29 Ratio of C_D and C_{MT} accompanied by maximum crosswind force $C_{L\max}$ to their maximum values $C_{D\max}$ and $C_{MT\max}$ for Square model (a) C_D ($C_{L\max}$)/$C_{D\max}$, and (b) C_{MT} ($C_{L\max}$)/$C_{MT\max}$.

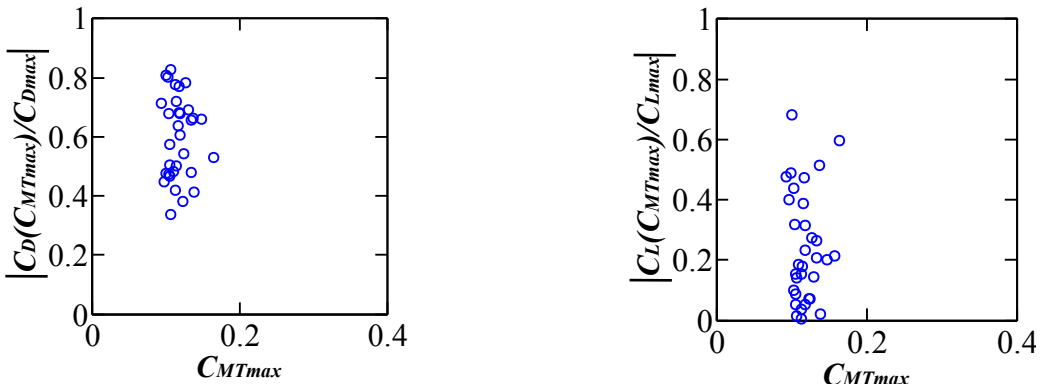

(a) (b)

Figure 7.30 Ratio of C_D and C_L accompanied by maximum torsional moment $C_{MT\max}$ to their maximum values $C_{D\max}$ and $C_{L\max}$ for Square model (a) C_D ($C_{MT\max}$)/$C_{D\max}$, and (b) C_L ($C_{MT\max}$)/$C_{L\max}$.

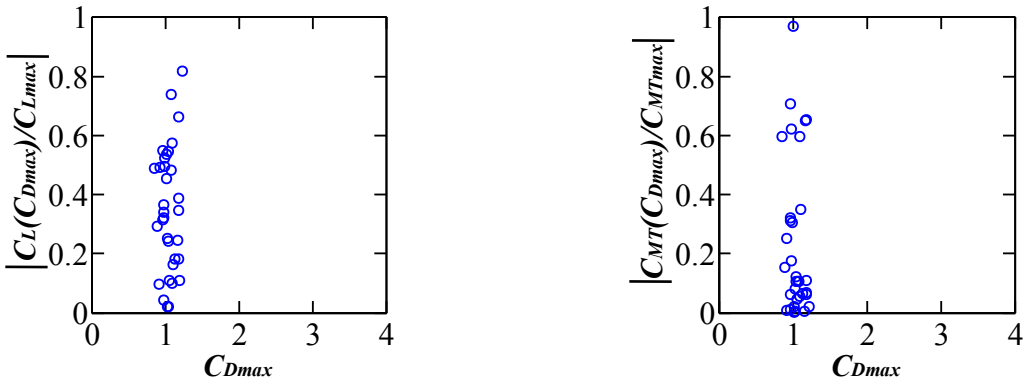

(a) (b)

Figure 7.31 Ratio of C_L and C_{MT} accompanied by maximum along-wind force $C_{D\max}$ to their maximum values $C_{L\max}$ and $C_{MT\max}$ for Pentagon model (a) C_L ($C_{D\max}$)/$C_{L\max}$, and (b) C_{MT} ($C_{D\max}$)/$C_{MT\max}$.

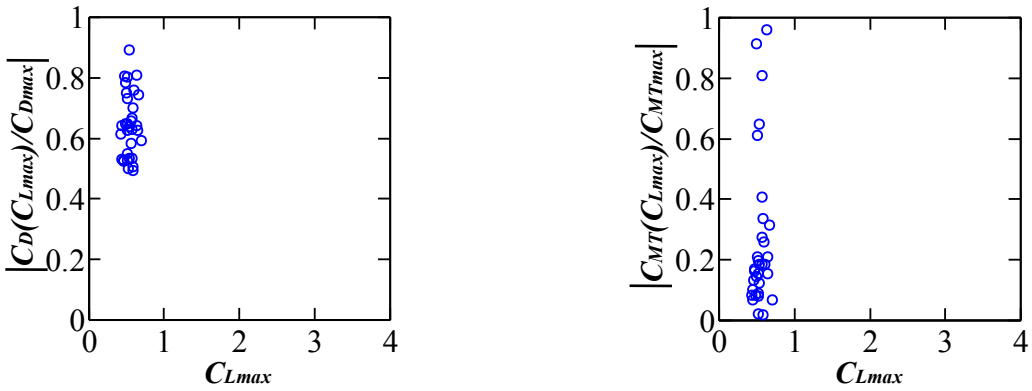

(a) (b)

Figure 7.32 Ratio of C_D and C_{MT} accompanied by maximum crosswind force $C_{L\max}$ to their maximum values $C_{D\max}$ and $C_{MT\max}$ for Pentagon model (a) C_D ($C_{L\max}$)/$C_{D\max}$, and (b) C_{MT} ($C_{L\max}$)/$C_{MT\max}$.

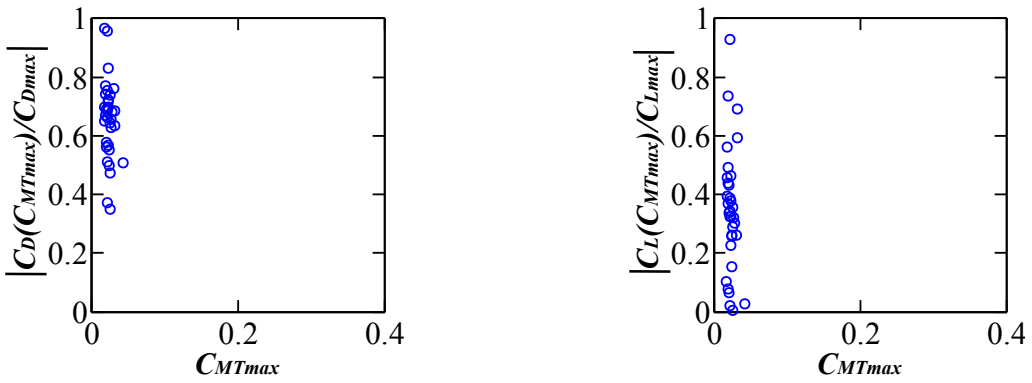

(a) (b)

Figure 7.33 Ratio of C_D and C_L accompanied by maximum torsional moment $C_{MT\max}$ to their maximum values $C_{D\max}$ and $C_{L\max}$ for Pentagon model (a) C_D ($C_{MT\max}$)/$C_{D\max}$, and (b) C_L ($C_{MT\max}$)/$C_{L\max}$.

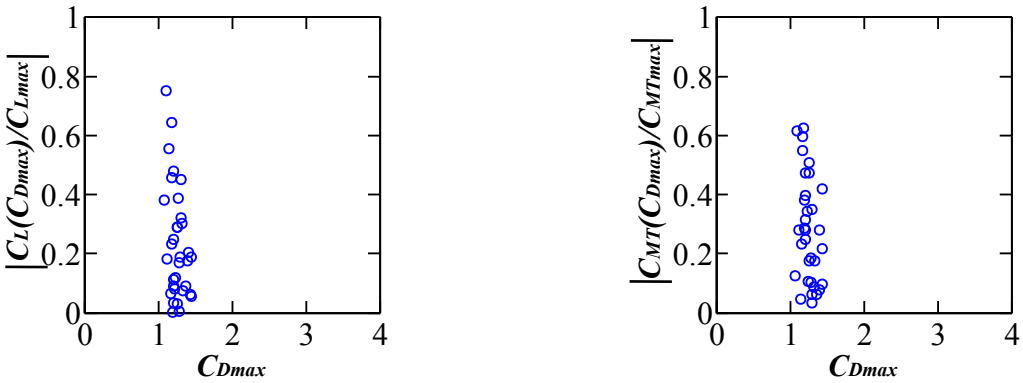

(a) (b)

Figure 7.34 Ratio of C_L and C_{MT} accompanied by maximum along-wind force $C_{D\max}$ to their maximum values $C_{L\max}$ and $C_{MT\max}$ for Hexagon model (a) C_L ($C_{D\max}$)/$C_{L\max}$, and (b) C_{MT} ($C_{D\max}$)/$C_{MT\max}$.

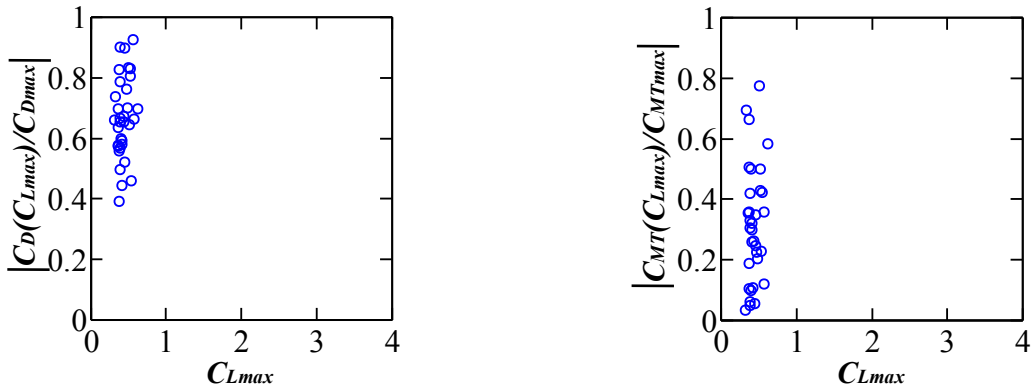

(a) (b)

Figure 7.35 Ratio of C_D and C_{MT} accompanied by maximum crosswind force $C_{L\max}$ to their maximum values $C_{D\max}$ and $C_{MT\max}$ for Hexagon model (a) C_D ($C_{L\max}$)/$C_{D\max}$, and (b) C_{MT} ($C_{L\max}$)/$C_{MT\max}$.

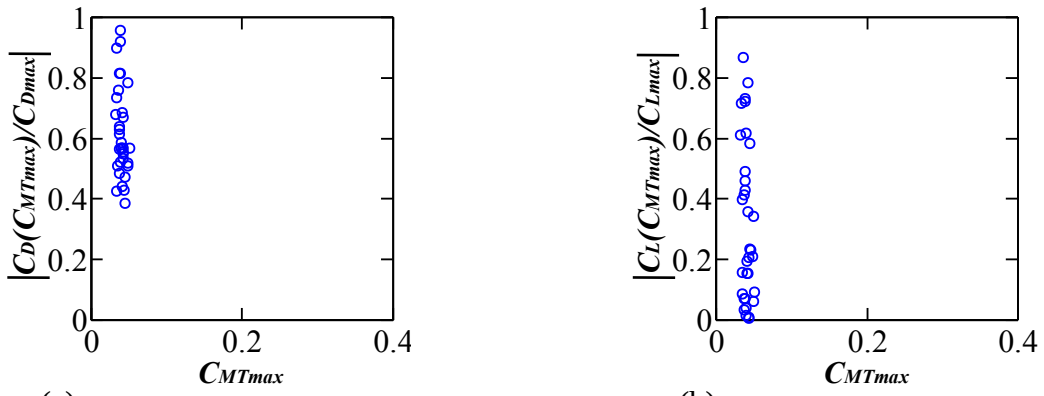

(a) (b)

Figure 7.36 Ratio of C_D and C_L accompanied by maximum torsional moment $C_{MT\max}$ to their maximum values $C_{D\max}$ and $C_{L\max}$ for Hexagon model (a) C_D ($C_{MT\max}$)/$C_{D\max}$, and (b) C_L ($C_{MT\max}$)/$C_{L\max}$.

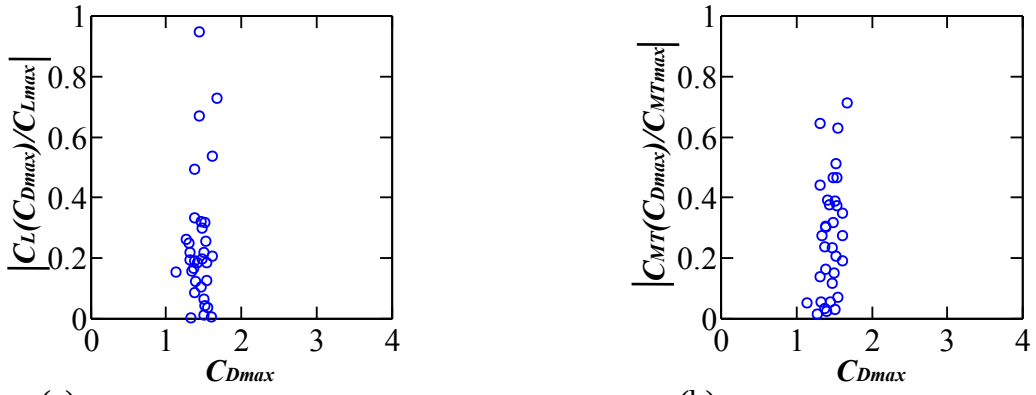

(a) (b)

Figure 7.37 Ratio of C_L and C_{MT} accompanied by maximum along-wind force $C_{D\max}$ to their maximum values $C_{L\max}$ and $C_{MT\max}$ for Octagon model (a) C_L ($C_{D\max}$)/$C_{L\max}$, and (b) C_{MT} ($C_{D\max}$)/$C_{MT\max}$.

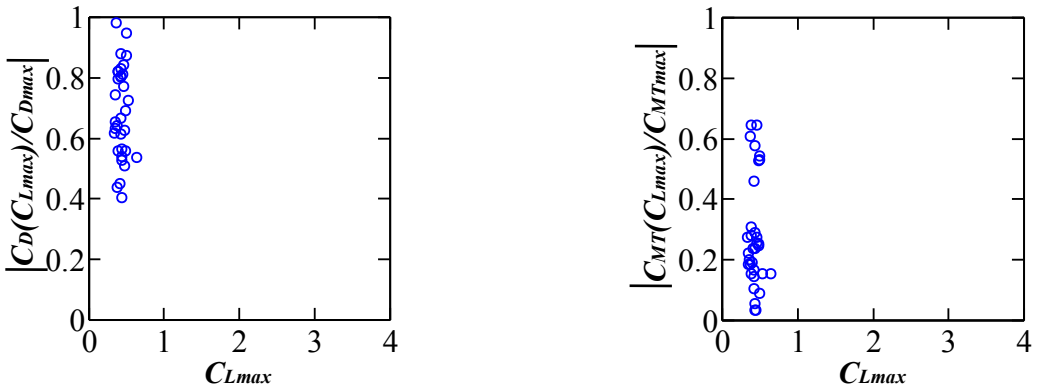

(a) (b)

Figure 7.38 Ratio of C_D and C_{MT} accompanied by maximum crosswind force $C_{L\max}$ to their maximum values $C_{D\max}$ and $C_{MT\max}$ for Octagon model (a) C_D ($C_{L\max}$)/$C_{D\max}$, and (b) C_{MT} ($C_{L\max}$)/$C_{MT\max}$.

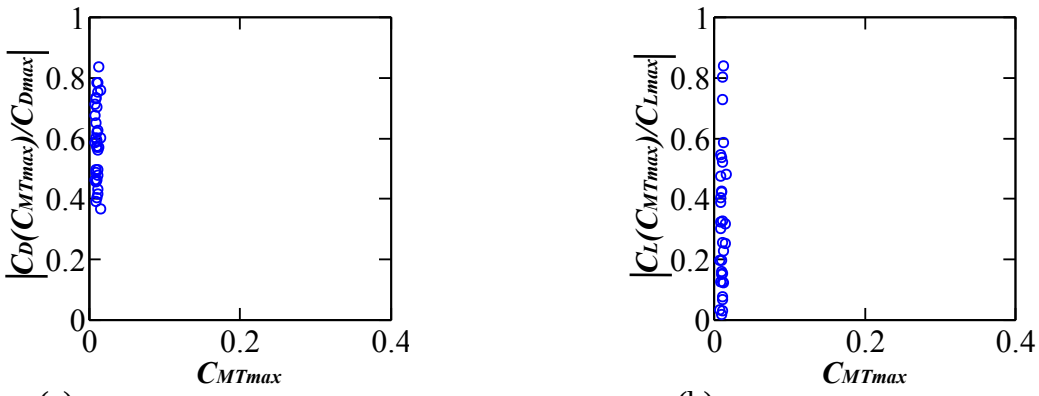

(a) (b)

Figure 7.39 Ratio of C_D and C_L accompanied by maximum torsional moment $C_{MT\max}$ to their maximum values $C_{D\max}$ and $C_{L\max}$ for Octagon model (a) C_D ($C_{MT\max}$)/$C_{D\max}$, and (b) C_L ($C_{MT\max}$)/$C_{L\max}$.

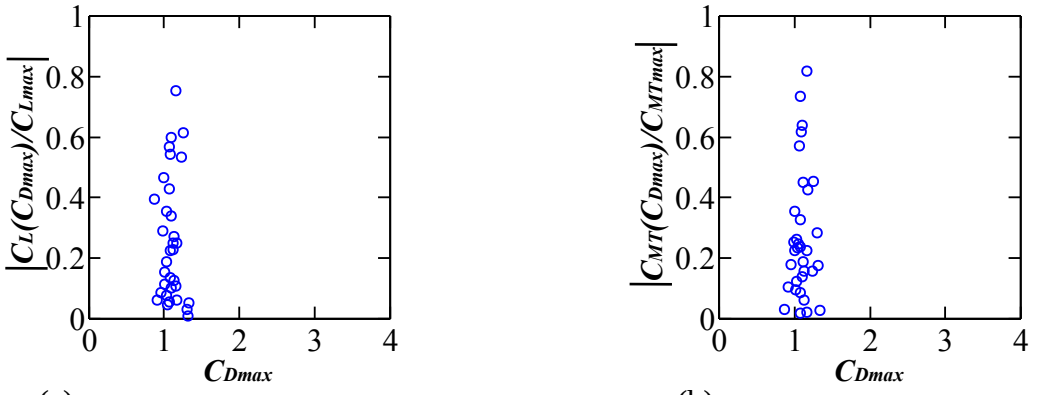

(a) (b)

Figure 7.40 Ratio of C_L and C_{MT} accompanied by maximum along-wind force $C_{D\max}$ to their maximum values $C_{L\max}$ and $C_{MT\max}$ for Dodecagon model (a) C_L ($C_{D\max}$)/$C_{L\max}$, and (b) C_{MT} ($C_{D\max}$)/$C_{MT\max}$.

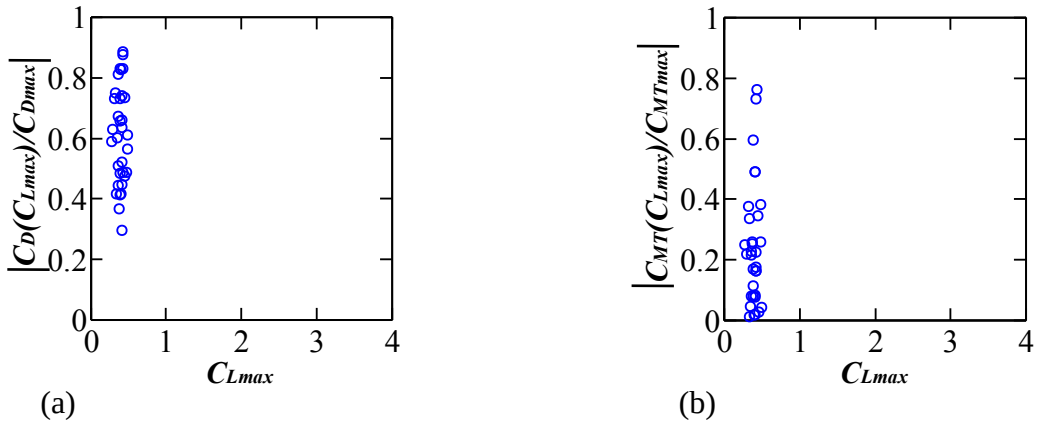

Figure 7.41 Ratio of C_D and C_{MT} accompanied by maximum crosswind force $C_{L\max}$ to their maximum values $C_{D\max}$ and $C_{MT\max}$ for Dodecagon model (a) C_D ($C_{L\max}$)/$C_{D\max}$, and (b) C_{MT} ($C_{L\max}$)/$C_{MT\max}$.

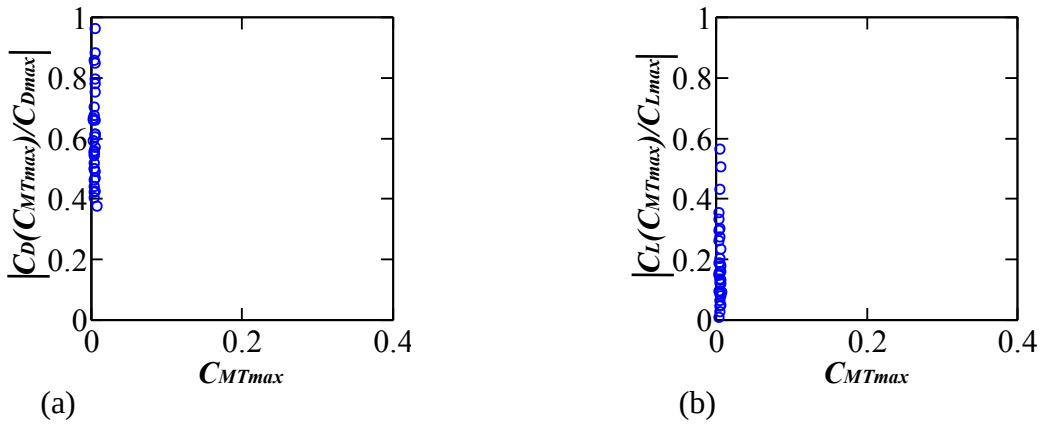

Figure 7.42 Ratio of C_D and C_L accompanied by maximum torsional moment $C_{MT\max}$ to their maximum values $C_{D\max}$ and $C_{L\max}$ for Dodecagon model (a) C_D ($C_{MT\max}$)/$C_{D\max}$, and (b) C_L ($C_{MT\max}$)/$C_{L\max}$.

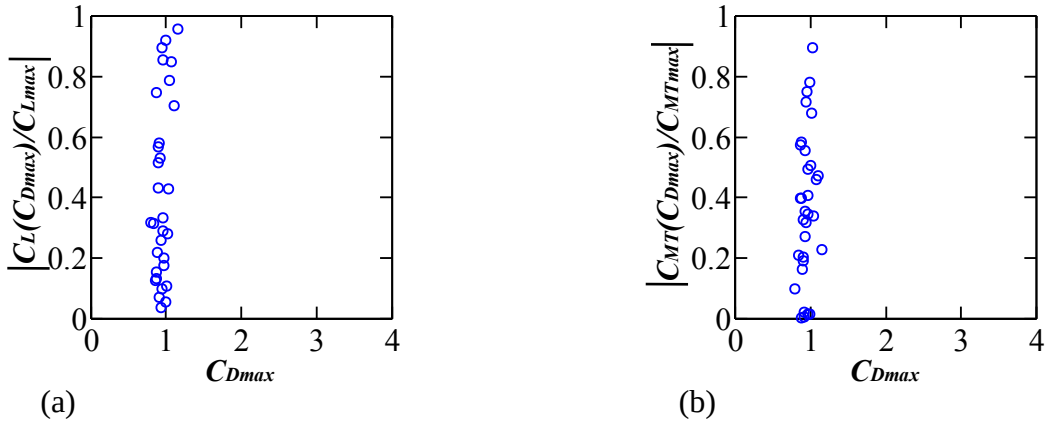

Figure 7.43 Ratio of C_L and C_{MT} accompanied by maximum along-wind force $C_{D\max}$ to their maximum values $C_{L\max}$ and $C_{MT\max}$ for Circular model (a) C_L ($C_{D\max}$)/$C_{L\max}$, and (b) C_{MT} ($C_{D\max}$)/$C_{MT\max}$.

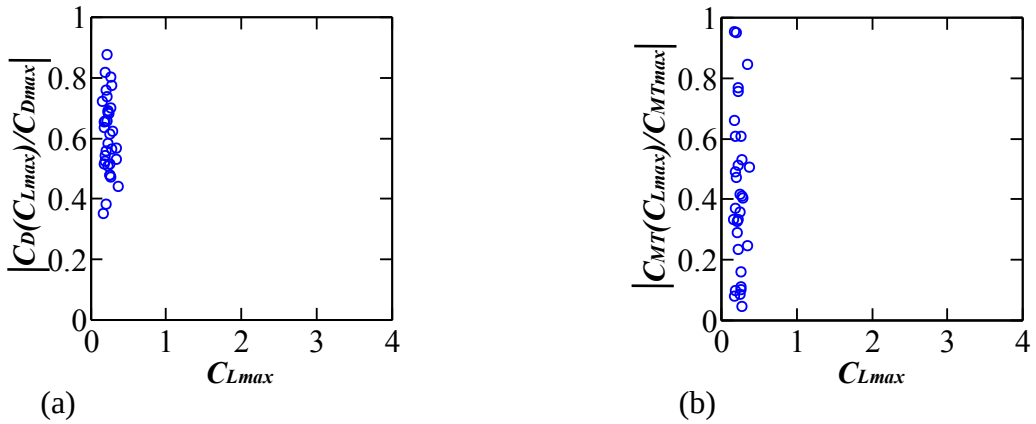

Figure 7.44 Ratio of C_D and C_{MT} accompanied by maximum crosswind force $C_{L\max}$ to their maximum values $C_{D\max}$ and $C_{MT\max}$ for Circular model (a) C_D ($C_{L\max}$)/$C_{D\max}$, and (b) C_{MT} ($C_{L\max}$)/$C_{MT\max}$.

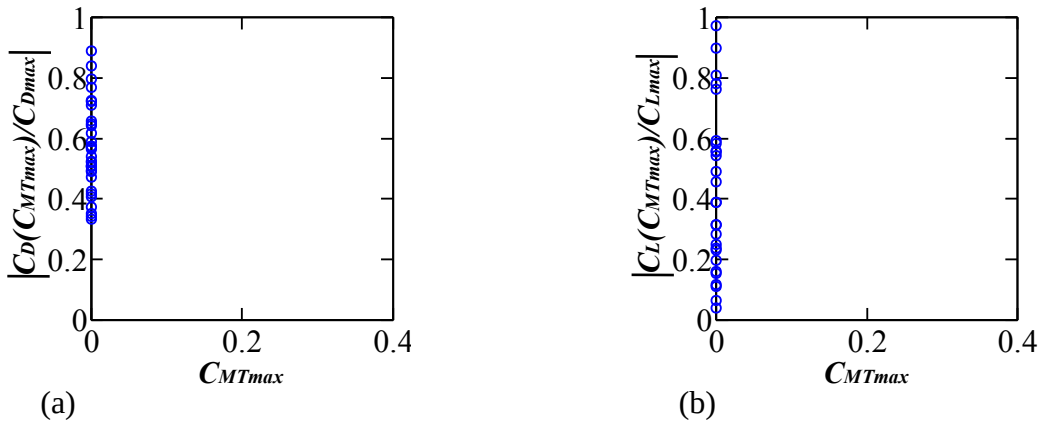

Figure 7.45 Ratio of C_D and C_L accompanied by maximum torsional moment $C_{MT\max}$ to their maximum values $C_{D\max}$ and $C_{L\max}$ for Circular model (a) C_D ($C_{MT\max}$)/$C_{D\max}$, and (b) C_L ($C_{MT\max}$)/$C_{L\max}$.

7.2 **Wind force combinations of helical models with various cross-sections**

7.2.1 *Trajectories of various overturning moment coefficients*

Figure 7.46 to 7.53 shows the trajectories of time series of various overturning moment coefficients for Tri-60°Hel, Tri-180°Hel, Tri-360°Hel, Sq-180°Hel, Penta-180°Hel, Hexa-180°Hel, Octa-180°Hel and Dodeca-180°Hel models. Trajectories of overturning moment coefficients have been plotted for wind direction where the mean over turning moment in crosswind direction ($\overline{C_{ML}}$) becomes zero.

The trajectories of Tri-60°Hel model shows similar trend like Triangular model. The Tri-180°Hel shows some correlation between C_{ML}-C_{MT}. The trajectory of C_{MD}-C_{ML} of all helical models shows a circle shape, implying no correlation between them. There is some correlation between C_{MD}-C_{MT} for Tri-360°Hel, Hexa-180°Hel and Dodeca-180°Hel models. It is very inter-

esting to note that the trajectory of C_{MD}-C_{MT} is elliptic shaped which become thinner and thinner as number of side faces increase from Penta-180^{o}Hel to Dodeca-180^{o}Hel models. We can see some correlation between C_{ML}-C_{MT} for all the models except Sq-180^{o}Hel model whereas Octa-180^{o}Hel and Dodeca-180^{o}Hel models show bit higher correlation. It is very interesting to note that, the trajectory shapes between C_{ML}-C_{MT} becomes elliptic with some inclination in shape and becomes thinner and thinner and also becomes very flat with abscissa as the number of side faces increases from Penta-180^{o}Hel to Dodeca-180^{o}Hel models.

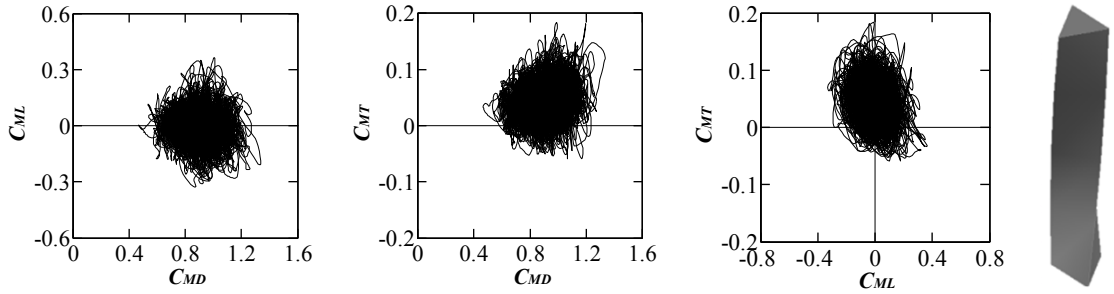

(a) C_{MD} - C_{ML} (b) C_{MD} - C_{MT} (c) C_{ML} - C_{MT}

Figure 7.46 Trajectory of overturning moment coefficients for Tri-60^{o}Hel model at 40^o wind direction

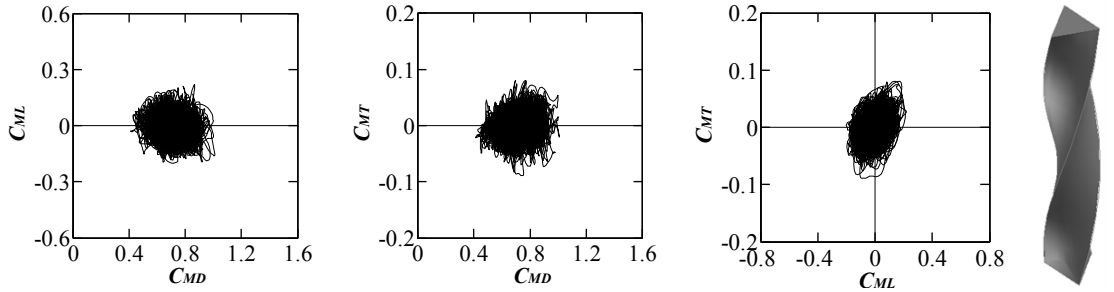

(a) C_{MD} - C_{ML} (b) C_{MD} - C_{MT} (c) C_{ML} - C_{MT}

Figure 7.47 Trajectory of overturning moment coefficients for Tri-180^{o}Hel model at 20^o wind direction

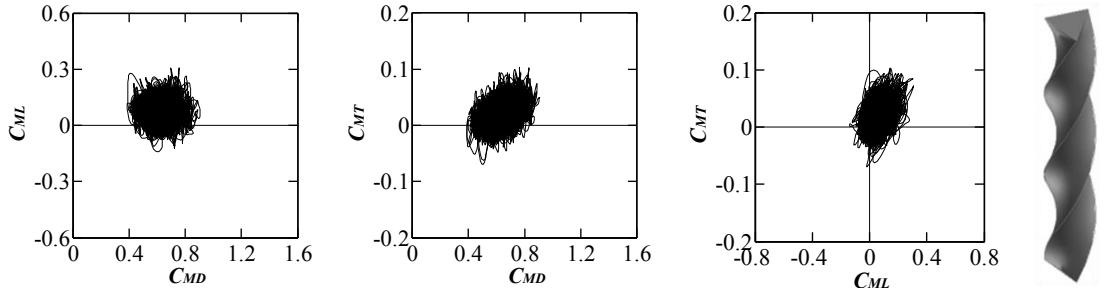

(a) C_{MD} - C_{ML} (b) C_{MD} - C_{MT} (c) C_{ML} - C_{MT}

Figure 7.48 Trajectory of overturning moment coefficients for Tri-360^{o}Hel model at 65^o wind direction

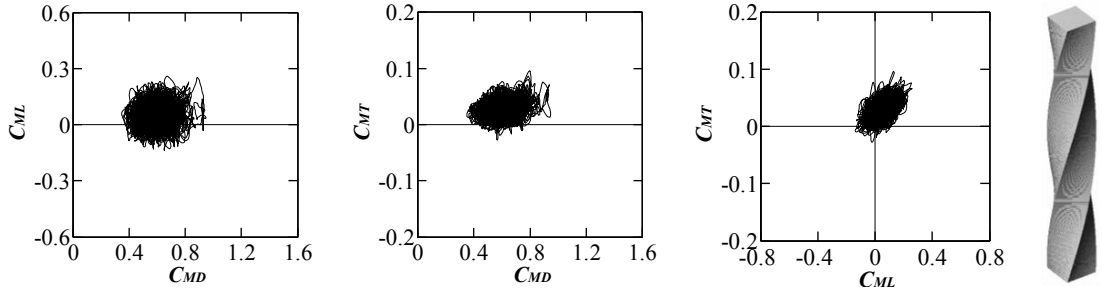

(a) C_{MD} - C_{ML} (b) C_{MD} - C_{MT} (c) C_{ML} - C_{MT}

Figure 7.49 Trajectory of overturning moment coefficients for Sq-180°Hel model at 30° wind direction

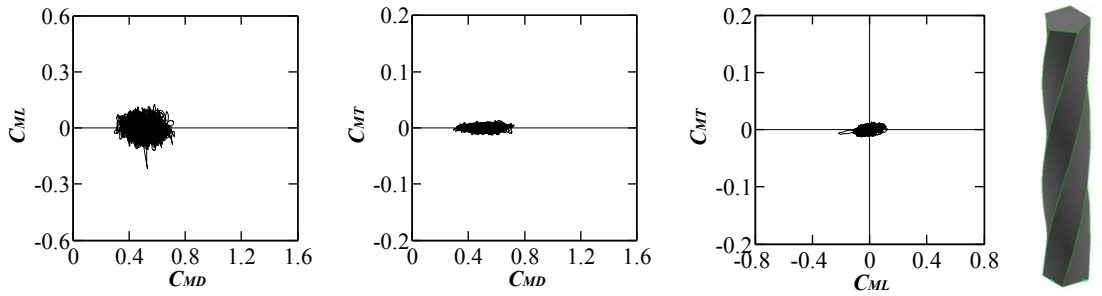

(a) C_{MD} - C_{ML} (b) C_{MD} - C_{MT} (c) C_{ML} - C_{MT}

Figure 7.50 Trajectory of overturning moment coefficients for Penta-180°Hel model at 50° wind direction

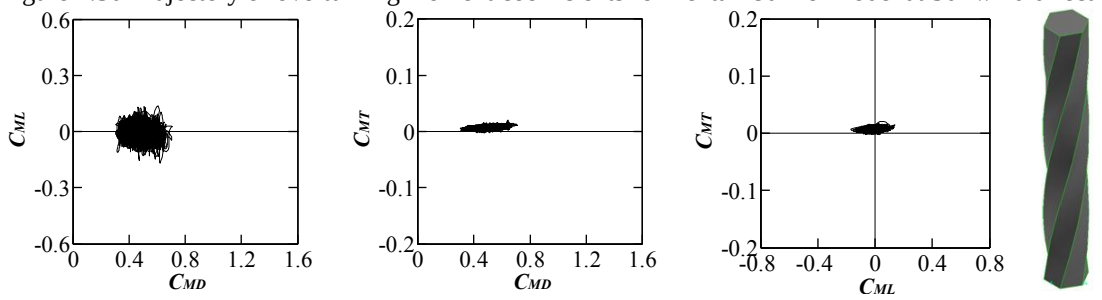

(a) C_{MD} - C_{ML} (b) C_{MD} - C_{MT} (c) C_{ML} - C_{MT}

Figure 7.51 Trajectory of overturning moment coefficients for Hexa-180° model at 70° wind direction

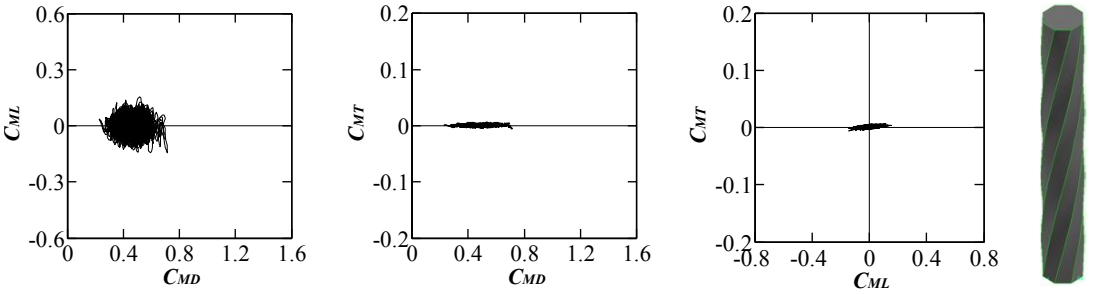

(a) C_{MD} - C_{ML} (b) C_{MD} - C_{MT} (c) C_{ML} - C_{MT}

Figure 7.52 Trajectory of overturning moment coefficients for Octa-180°Hel model at 75° wind direction

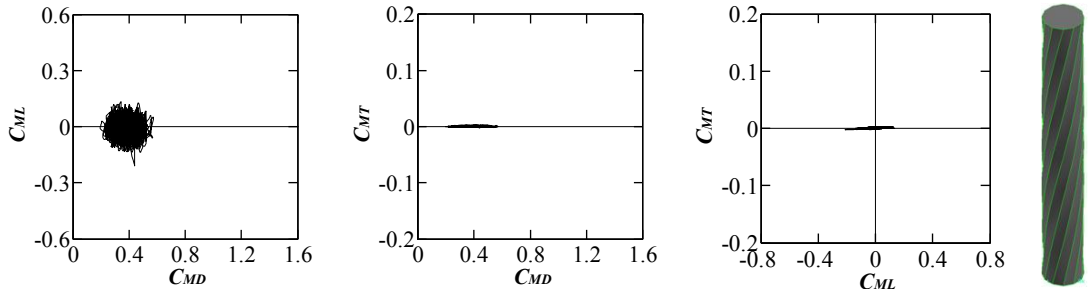

(a) C_{MD} - C_{ML} (b) C_{MD} - C_{MT} (c) C_{ML} - C_{MT}

Figure 7.53 Trajectory of overturning moment coefficients for Dodeca-180°Hel model at 80° wind direction

7.2.2 *Correlation and absolute value correlation*

In this section, helical models have been considered for correlation and absolute value correlation. In order to understand the real relationship between the various overturning moments, the absolute value correlation is also calculated and shown in Figure 7.54-7.61 for the models Tri-60°Hel, Tri-180°Hel, Tri-360°Hel, Sq-180°Hel, penta-180°Hel, Hexa-180°Hel, Octa-180°Hel and Dodeca-180°Hel models respectively. The value of the correlation coefficient can be well compared with the shape of the trajectories of overturning moments discussed in section 7.2.1. In the following figures, solid line shows correlation curve and dotted line shows absolute value correlation. Considering the absolute value correlation, there is slight correlation between C_{MD}-C_{ML} obtained for all the helical models, whereas considering the original value correlation, there are some correlation between C_{ML}-C_{MT} for all helical models except Sq-180°Hel model. Considering the absolute value correlation, there are higher correlations of C_{MD}-C_{MT} for all the models than C_{MD}-C_{ML} and C_{ML}-C_{MT}.

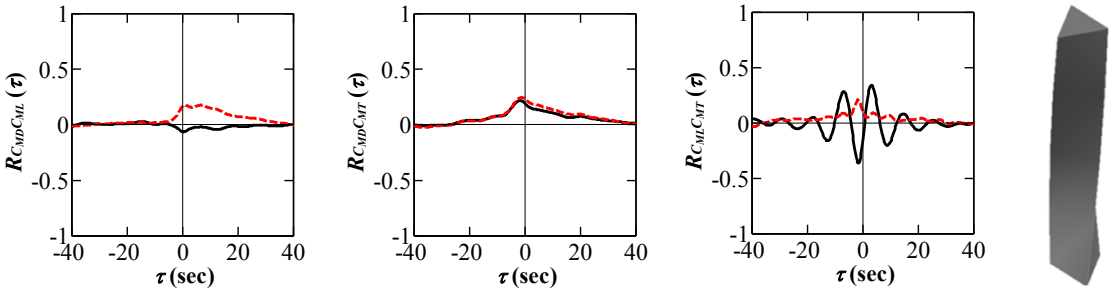

(a) C_{MD} - C_{ML} (b) C_{MD} - C_{MT} (c) C_{ML} - C_{MT}

Figure 7.54 Correlation coefficient (Solid line) and absolute value correlation (dotted line) for Tri-60°Hel model at 40° wind direction

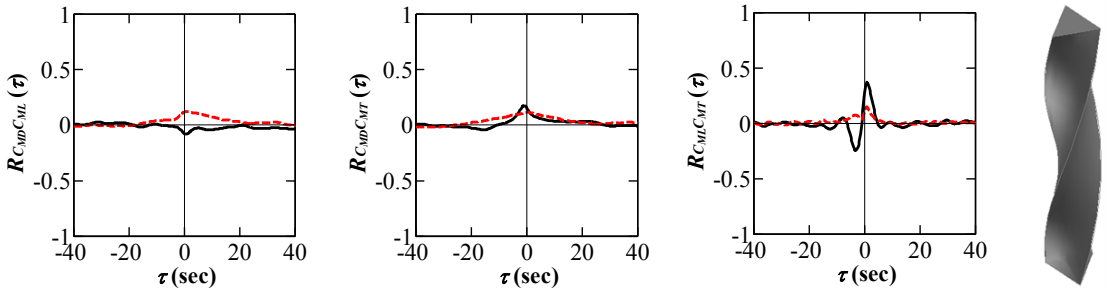

(a) C_{MD} - C_{ML} (b) C_{MD} - C_{MT} (c) C_{ML} - C_{MT}

Figure 7.55 Correlation coefficient (Solid line) and absolute value correlation (dotted line) for Tri-180^{o}Hel model at 20^o wind direction

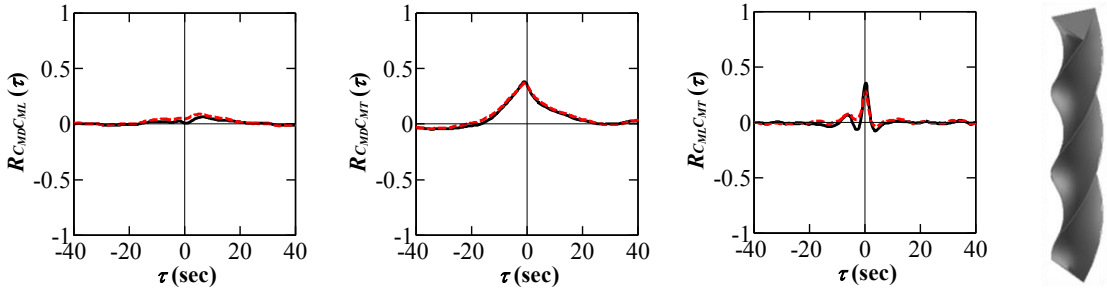

(a) C_{MD} - C_{ML} (b) C_{MD} - C_{MT} (c) C_{ML} - C_{MT}

Figure 7.56 Correlation coefficient (Solid line) and absolute value correlation (dotted line) for Tri-360^{o}Hel model at 65^o wind direction

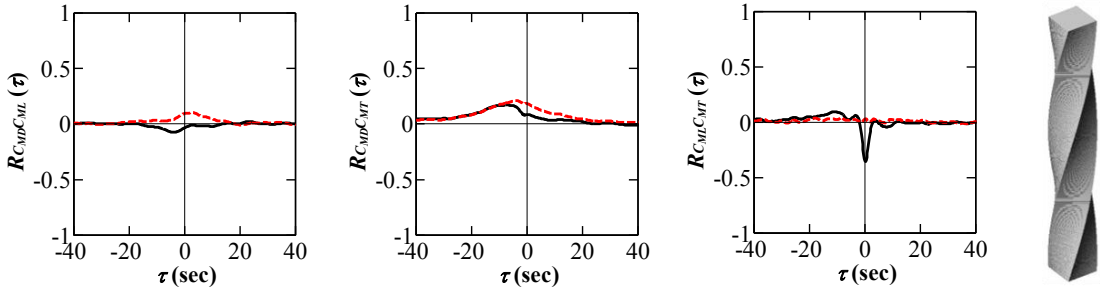

(a) C_{MD} - C_{ML} (b) C_{MD} - C_{MT} (c) C_{ML} - C_{MT}

Figure 7.57 Correlation coefficient (Solid line) and absolute value correlation (dotted line) for Sq-180^{o}Hel model at 30^o wind direction

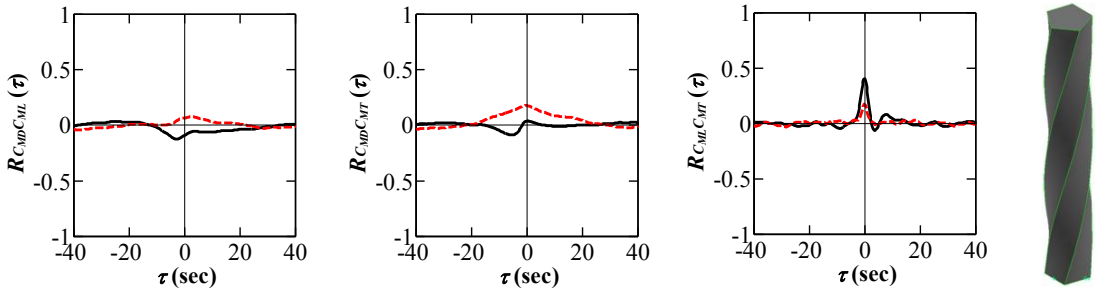

(a) C_{MD} - C_{ML} (b) C_{MD} - C_{MT} (c) C_{ML} - C_{MT}

Figure 7.58 Correlation coefficient (Solid line) and absolute value correlation (dotted line) for Penta-180^{o}Hel model at 50^o wind direction

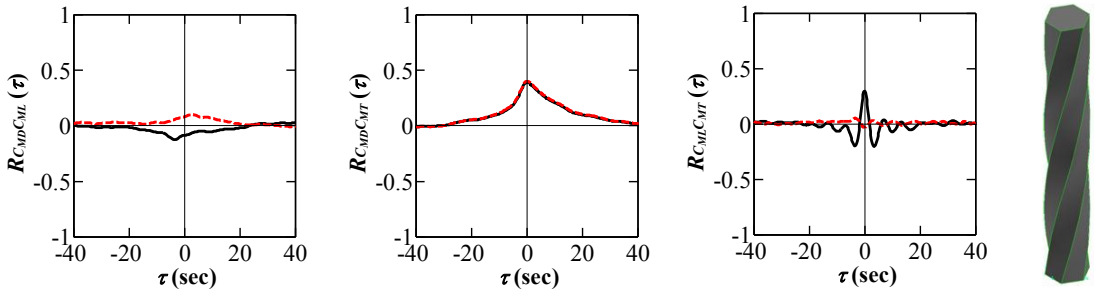

(a) C_{MD} - C_{ML} (b) C_{MD} - C_{MT} (c) C_{ML} - C_{MT}

Figure 7.59 Correlation coefficient (Solid line) and absolute value correlation (dotted line) for Hexa-180°Hel model at 70° wind direction

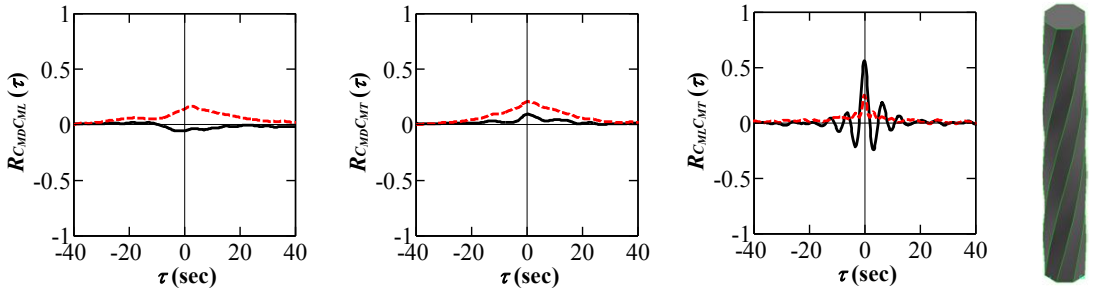

(a) C_{MD} - C_{ML} (b) C_{MD} - C_{MT} (c) C_{ML} - C_{MT}

Figure 7.60 Correlation coefficient (Solid line) and absolute value correlation (dotted line) for Octa-180°Hel model at 75° wind direction

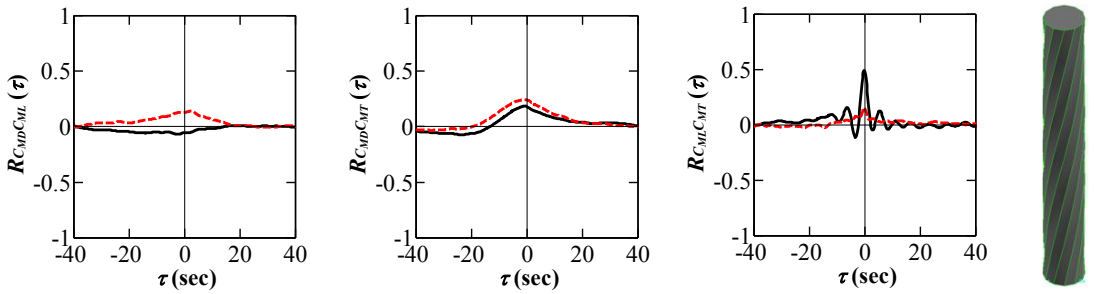

(a) C_{MD} - C_{ML} (b) C_{MD} - C_{MT} (c) C_{ML} - C_{MT}

Figure 7.61 Correlation coefficient (Solid line) and absolute value correlation (dotted line) for Dodeca-180°Hel model at 80° wind direction

7.2.3 *Simultaneous wind loading*

In this research the instantaneous wind forces discussed were obtained by spatial integration of the fluctuating pressures at number of points. Figure 7.62, 7.63 & 7.64 show examples of the results for a Tri-180°Hel model, on the basis of 33 samples. Figure 7.62 (a) & (b) show the cross-wind force and torsional moment ratios, $C_L(C_{D\max})/C_{L\max}$ and $C_{MT}(C_{D\max})/C_{MT\max}$, when the maximum along-wind force $C_{D\max}$ occurs. They are defined as the ratios of the crosswind force and

torsional moment coefficients $C_L(C_{D\max})$ and $C_{MT}(C_{D\max})$ to their maximum values $C_{L\max}$ and $C_{MT\max}$ for each 10-min sample. 0–30% of the maximum crosswind force coefficient $C_{L\max}$ and 0–100% of the maximum torsional moment coefficient $C_{MT\max}$ were simultaneously recorded with the maximum along-wind force $C_{D\max}$. Fig 6.63 (a) & (b) show the along-wind force and torsional moment ratios, $C_D(C_{L\max})/C_{D\max}$ and $C_T(C_{L\max})/C_{T\max}$, when the maximum crosswind force $C_{L\max}$ occurs. 50–80% of the maximum along-wind forces and 0–60% of the maximum torsional moment coefficients were most likely to appear with the maximum crosswind force $C_{L\max}$. Fig 6.64 (a) & (b) show the cases when the maximum torsional moment $C_{T\max}$ was recorded. When the maximum torsional moment $C_{T\max}$ occurs, around 60-80% of the maximum along-wind force $C_{D\max}$ was simultaneously recorded, as shown in fig 6.64 (a), while a relatively small crosswind force $C_L(C_{T\max})$, i.e. around 0-20% of its maximum value $C_{L\max}$, appears as shown in fig 6.64 (b).

For the models Penta-180°Hel, Hexa-180°Hel, Octa-180°Hel and Dodeca-180°Hel, the distribution of instantaneous wind forces looks almost same. The instantaneous wind forces are distributed uniformly from 0% to 100% for torsional moment coefficient ratio $C_{MT}(C_{D\max})/C_{MT\max}$ when along-wind force is maximum ($C_{D\max}$) and torsional moment coefficient ratio $C_{MT}(C_{L\max})/C_{MT\max}$ when crosswind force is maximum ($C_{D\max}$) for Tri-180°Hel and Sq-180°Hel models.

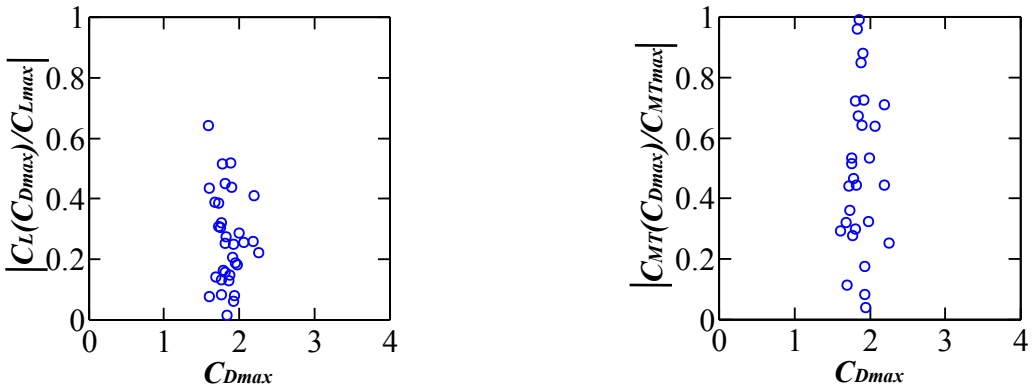

Figure 7.62 Ratio of C_L and C_{MT} accompanied by maximum along-wind force $C_{D\max}$ to their maximum values $C_{L\max}$ and $C_{MT\max}$ for Tri-180°Hel model (a) C_L $(C_{D\max})/C_{L\max}$, and (b) C_{MT} $(C_{D\max})/C_{MT\max}$.

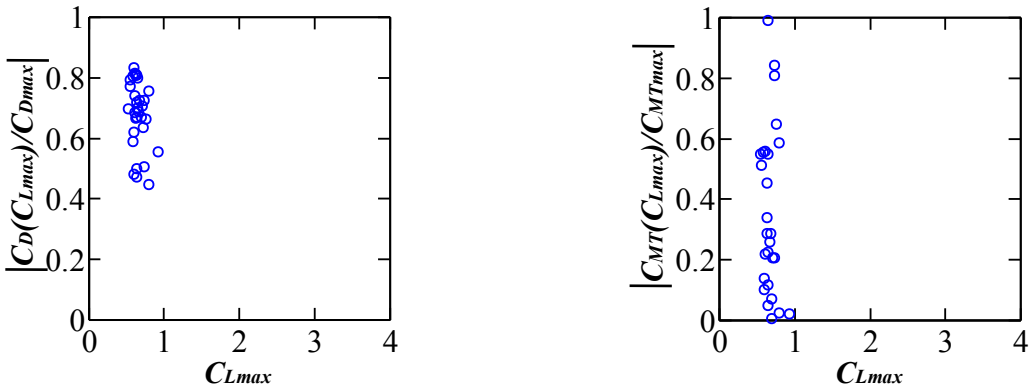

(a) (b)

Figure 7.63 Ratio of C_D and C_{MT} accompanied by maximum crosswind force $C_{L\max}$ to their maximum values $C_{D\max}$ and $C_{MT\max}$ for Tri-180°Hel model (a) C_D ($C_{L\max}$)/$C_{D\max}$, and (b) C_{MT} ($C_{L\max}$)/$C_{MT\max}$.

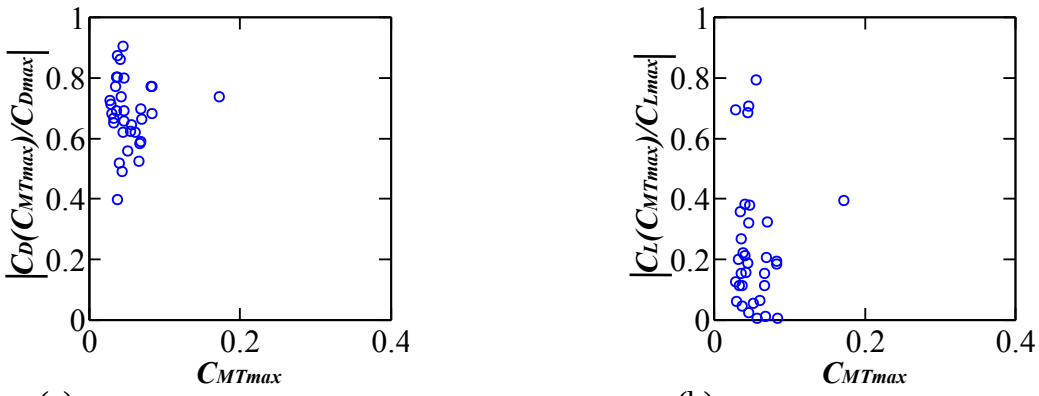

(a) (b)

Figure 7.64 Ratio of C_D and C_L accompanied by maximum torsional moment $C_{MT\max}$ to their maximum values $C_{D\max}$ and $C_{L\max}$ for Tri-180°Hel model (a) C_D ($C_{MT\max}$)/$C_{D\max}$, and (b) C_L ($C_{MT\max}$)/$C_{L\max}$.

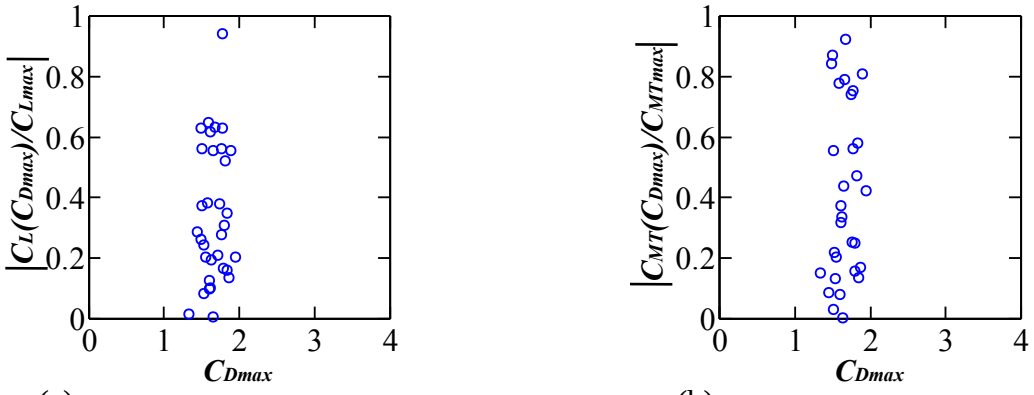

(a) (b)

Figure 7.65 Ratio of C_L and C_{MT} accompanied by maximum along-wind force $C_{D\max}$ to their maximum values $C_{L\max}$ and $C_{MT\max}$ for Sq-180°Hel model (a) C_L ($C_{D\max}$)/$C_{L\max}$, and (b) C_{MT} ($C_{D\max}$)/$C_{MT\max}$.

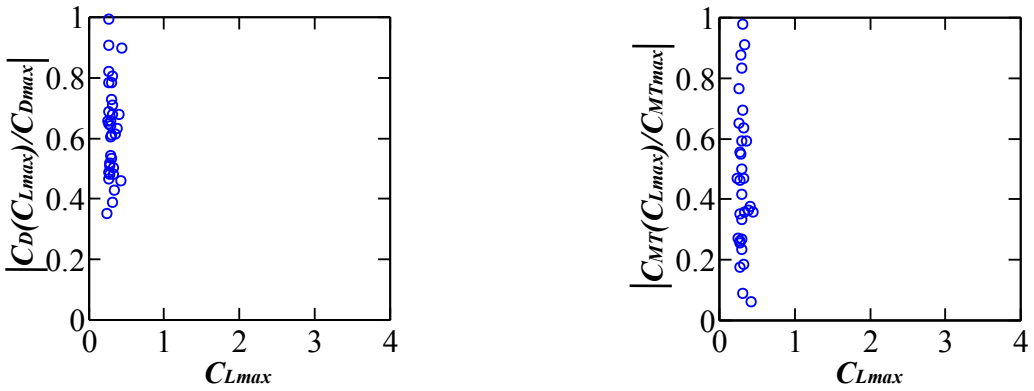

Figure 7.66 Ratio of C_D and C_{MT} accompanied by maximum crosswind force $C_{L\max}$ to their maximum values $C_{D\max}$ and $C_{MT\max}$ for Sq-180°Hel model (a) C_D ($C_{L\max}$)/$C_{D\max}$, and (b) C_{MT} ($C_{L\max}$)/$C_{MT\max}$.

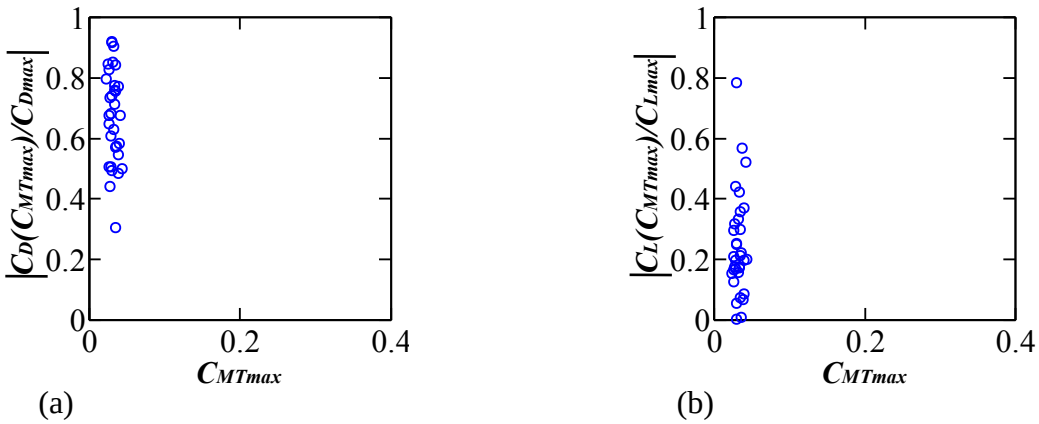

Figure 7.67 Ratio of C_D and C_L accompanied by maximum torsional moment $C_{MT\max}$ to their maximum values $C_{D\max}$ and $C_{L\max}$ for Sq-180°Hel model (a) C_D ($C_{MT\max}$)/$C_{D\max}$, and (b) C_L ($C_{MT\max}$)/$C_{L\max}$.

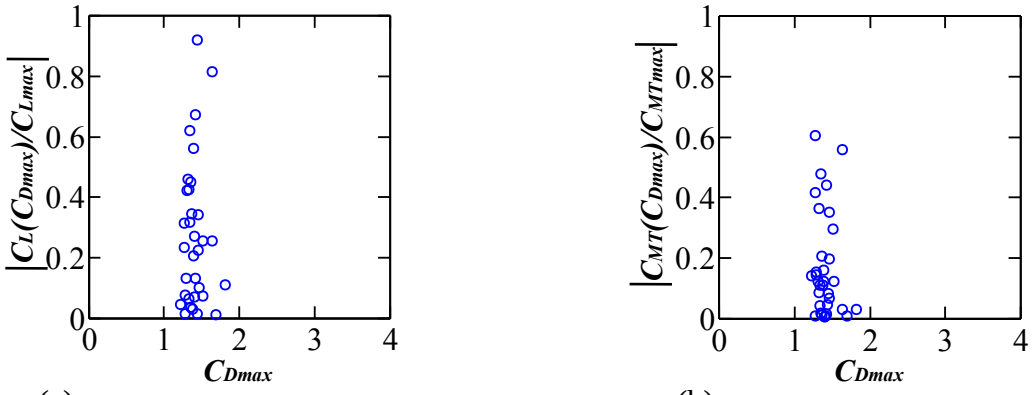

Figure 7.68 Ratio of C_L and C_{MT} accompanied by maximum along-wind force $C_{D\max}$ to their maximum values $C_{L\max}$ and $C_{MT\max}$ for Penta-180°Hel model (a) C_L ($C_{D\max}$)/$C_{L\max}$, and (b) C_{MT} ($C_{D\max}$)/$C_{MT\max}$.

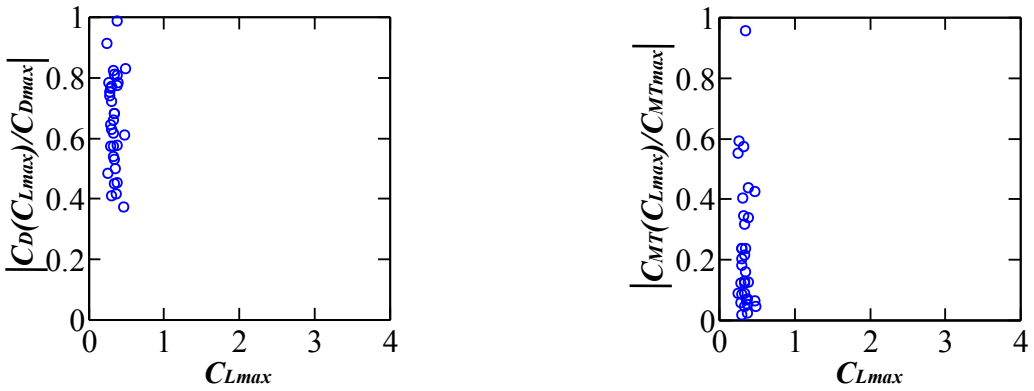

(a) (b)

Figure 7.69 Ratio of C_D and C_{MT} accompanied by maximum crosswind force $C_{L\max}$ to their maximum values $C_{D\max}$ and $C_{MT\max}$ for Penta-180°Hel model (a) C_D ($C_{L\max}$)/$C_{D\max}$, and (b) C_{MT} ($C_{L\max}$)/$C_{MT\max}$.

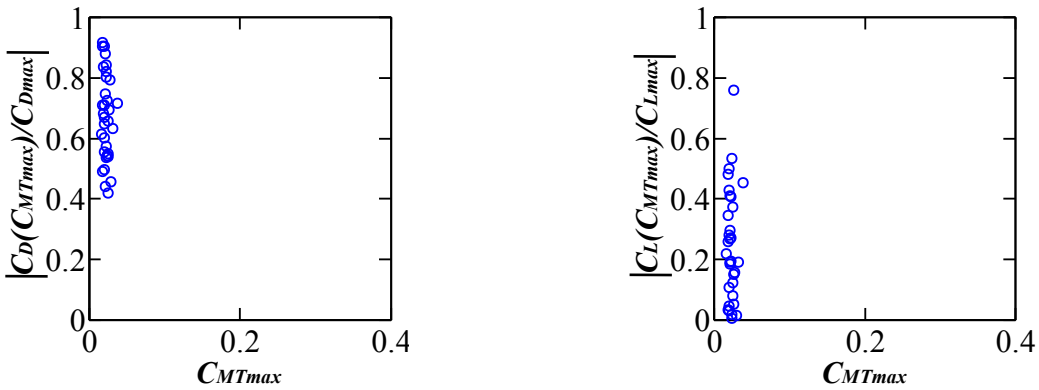

(a) (b)

Figure 7.70 Ratio of C_D and C_L accompanied by maximum torsional moment $C_{MT\max}$ to their maximum values $C_{D\max}$ and $C_{L\max}$ for Penta-180°Hel model (a) C_D ($C_{MT\max}$)/$C_{D\max}$, and (b) C_L ($C_{MT\max}$)/$C_{L\max}$.

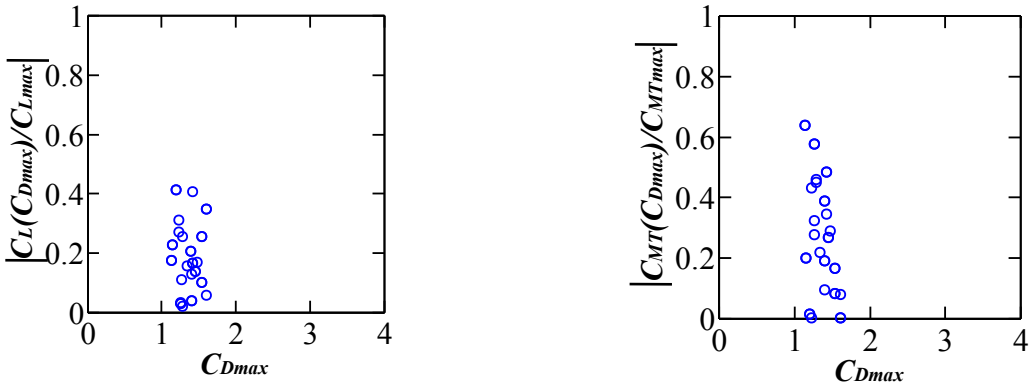

(a) (b)

Figure 7.71 Ratio of C_L and C_{MT} accompanied by maximum along-wind force $C_{D\max}$ to their maximum values $C_{L\max}$ and $C_{MT\max}$ for Hexa-180°Hel model (a) C_L ($C_{D\max}$)/$C_{L\max}$, and (b) C_{MT} ($C_{D\max}$)/$C_{MT\max}$.

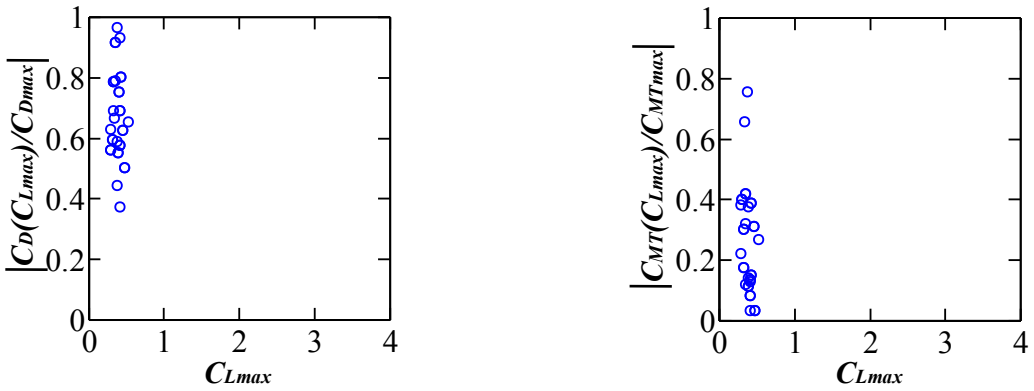

(a) (b)

Figure 7.72 Ratio of C_D and C_{MT} accompanied by maximum crosswind force $C_{L\max}$ to their maximum values $C_{D\max}$ and $C_{MT\max}$ for Hexa-180°Hel model (a) C_D ($C_{L\max}$)/$C_{D\max}$, and (b) C_{MT} ($C_{L\max}$)/$C_{MT\max}$.

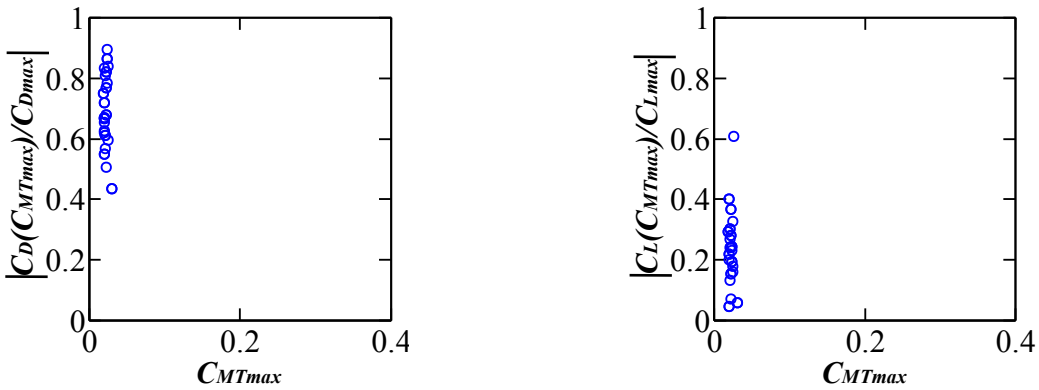

(a) (b)

Figure 7.73 Ratio of C_D and C_L accompanied by maximum torsional moment $C_{MT\max}$ to their maximum values $C_{D\max}$ and $C_{L\max}$ for Hexa-180°Hel model (a) C_D ($C_{MT\max}$)/$C_{D\max}$, and (b) C_L ($C_{MT\max}$)/$C_{L\max}$.

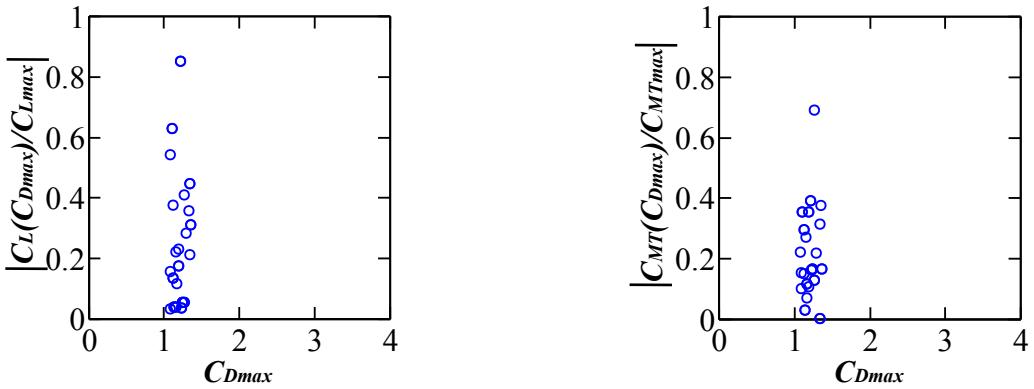

(a) (b)

Figure 7.74 Ratio of C_L and C_{MT} accompanied by maximum along-wind force $C_{D\max}$ to their maximum values $C_{L\max}$ and $C_{MT\max}$ for Octa-180°Hel model (a) C_L ($C_{D\max}$)/$C_{L\max}$, and (b) C_{MT} ($C_{D\max}$)/$C_{MT\max}$.

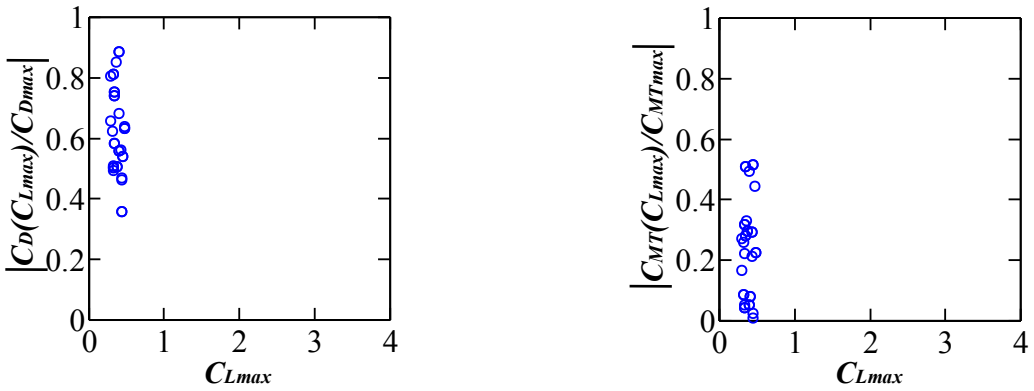

(a) (b)

Figure 7.75 Ratio of C_D and C_{MT} accompanied by maximum crosswind force $C_{L\max}$ to their maximum values $C_{D\max}$ and $C_{MT\max}$ for Octa-180°Hel model (a) C_D ($C_{L\max}$)/$C_{D\max}$, and (b) C_{MT} ($C_{L\max}$)/$C_{MT\max}$.

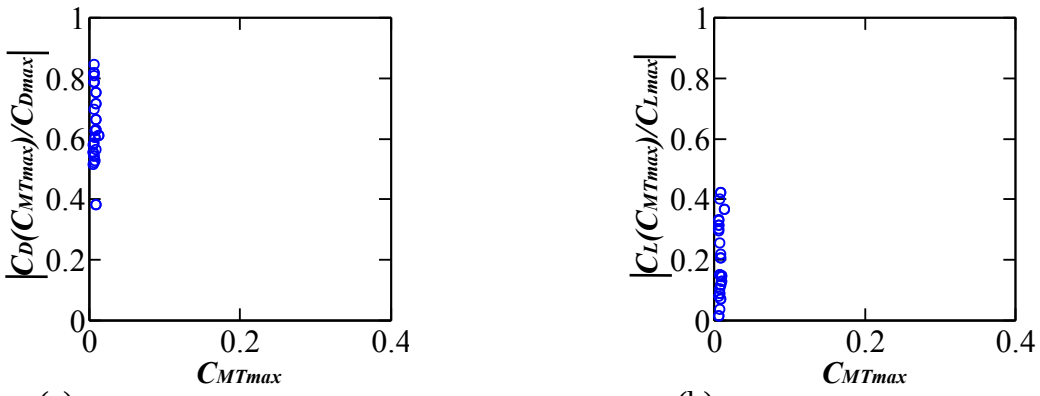

(a) (b)

Figure 7.76 Ratio of C_D and C_L accompanied by maximum torsional moment $C_{MT\max}$ to their maximum values $C_{D\max}$ and $C_{L\max}$ for Octa-180°Hel model (a) C_D ($C_{MT\max}$)/$C_{D\max}$, and (b) C_L ($C_{MT\max}$)/$C_{L\max}$.

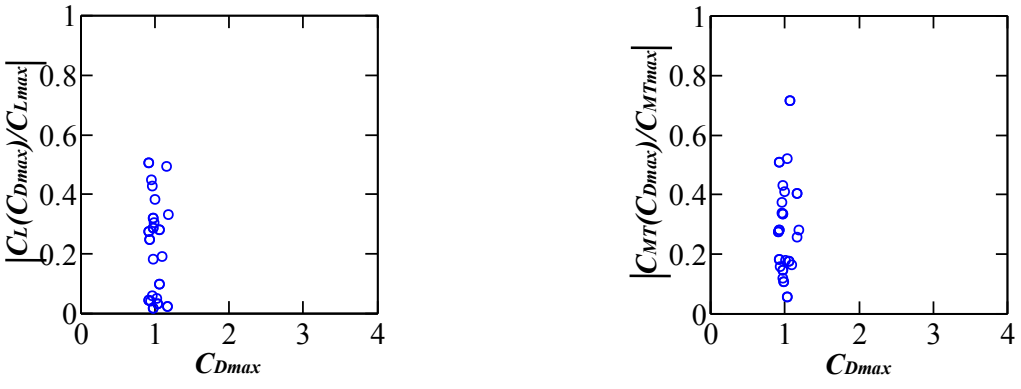

(a) (b)

Figure 7.77 Ratio of C_L and C_{MT} accompanied by maximum along-wind force $C_{D\max}$ to their maximum values $C_{L\max}$ and $C_{MT\max}$ for Dodeca-180°Hel model (a) C_L ($C_{D\max}$)/$C_{L\max}$, and (b) C_{MT} ($C_{D\max}$)/$C_{MT\max}$.

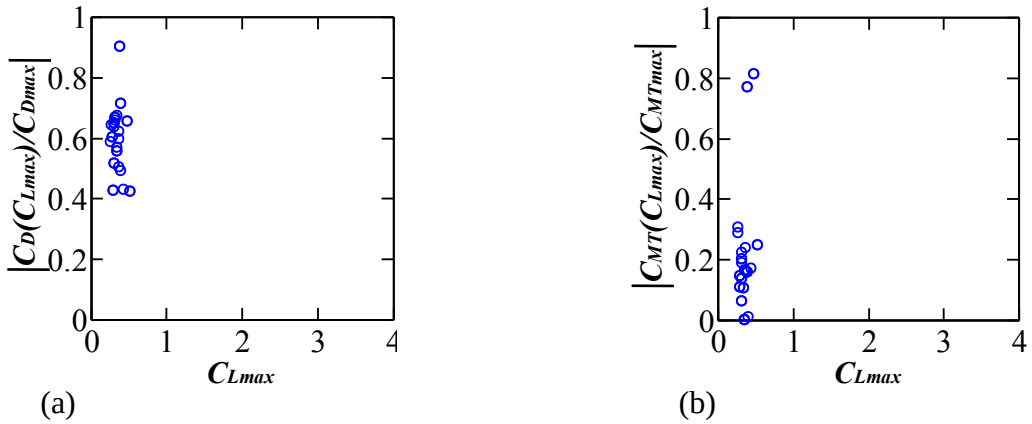

Figure 7.78 Ratio of C_D and C_{MT} accompanied by maximum crosswind force $C_{L\max}$ to their maximum values $C_{D\max}$ and $C_{MT\max}$ for Dodeca-180°Hel model (a) C_D ($C_{L\max}$)/$C_{D\max}$, and (b) C_{MT} ($C_{L\max}$)/$C_{MT\max}$.

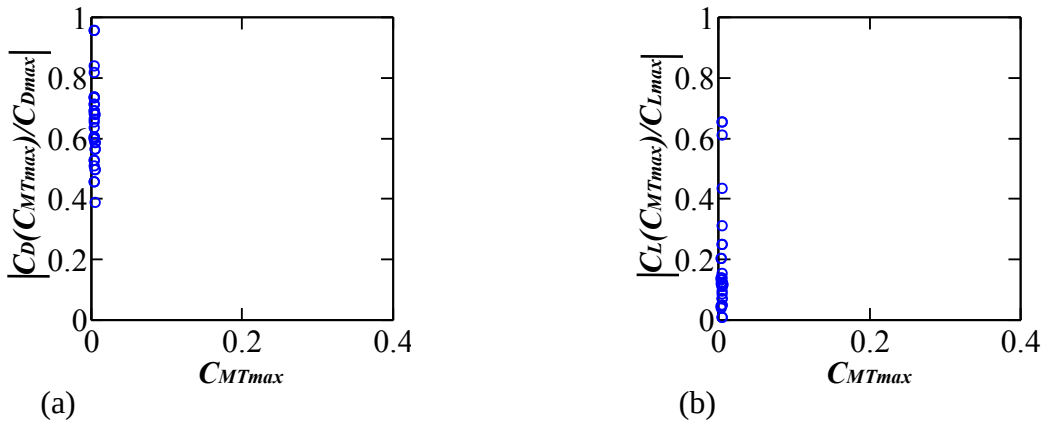

Figure 7.79 Ratio of C_D and C_L accompanied by maximum torsional moment $C_{MT\max}$ to their maximum values $C_{D\max}$ and $C_{L\max}$ for Dodeca-180°Hel model (a) C_D ($C_{MT\max}$)/$C_{D\max}$, and (b) C_L ($C_{MT\max}$)/$C_{L\max}$.

7.3 **Internal Forces and Peak normal stresses in columns**

Local wind forces at each level were calculated using wind pressures, and input to the frame model to examine the effects of loading conditions, and damping ratio on peak normal stresses in columns. All the beams are assumed to be rigid, and the columns are assumed to be square tubes of the same size for all heights. The column size was determined such that the first natural period becomes $H/50$ (Tamura, 2012), and all connections were assumed to be rigid. The local wind forces at each level were applied at the center of the floor. The analyses were made in two ways: quasi-static analyses and dynamic response analyses considering the resonant effect for various damping ratios. To examine the various loading conditions, 3 different loading conditions were considered. The loading conditions are *ALL* (*Fx*, *Fy* and *Mz* loads applied simultaneously at the

center of each floor), only *Fx*, only *Fy* and only *Mz*. In the study, no dead load and no live load were applied.

The effects of damping ratios and various wind loading conditions on internal forces and normal stresses of columns were studies in the following sections for each model. Frame models of various models are shown in Figure.

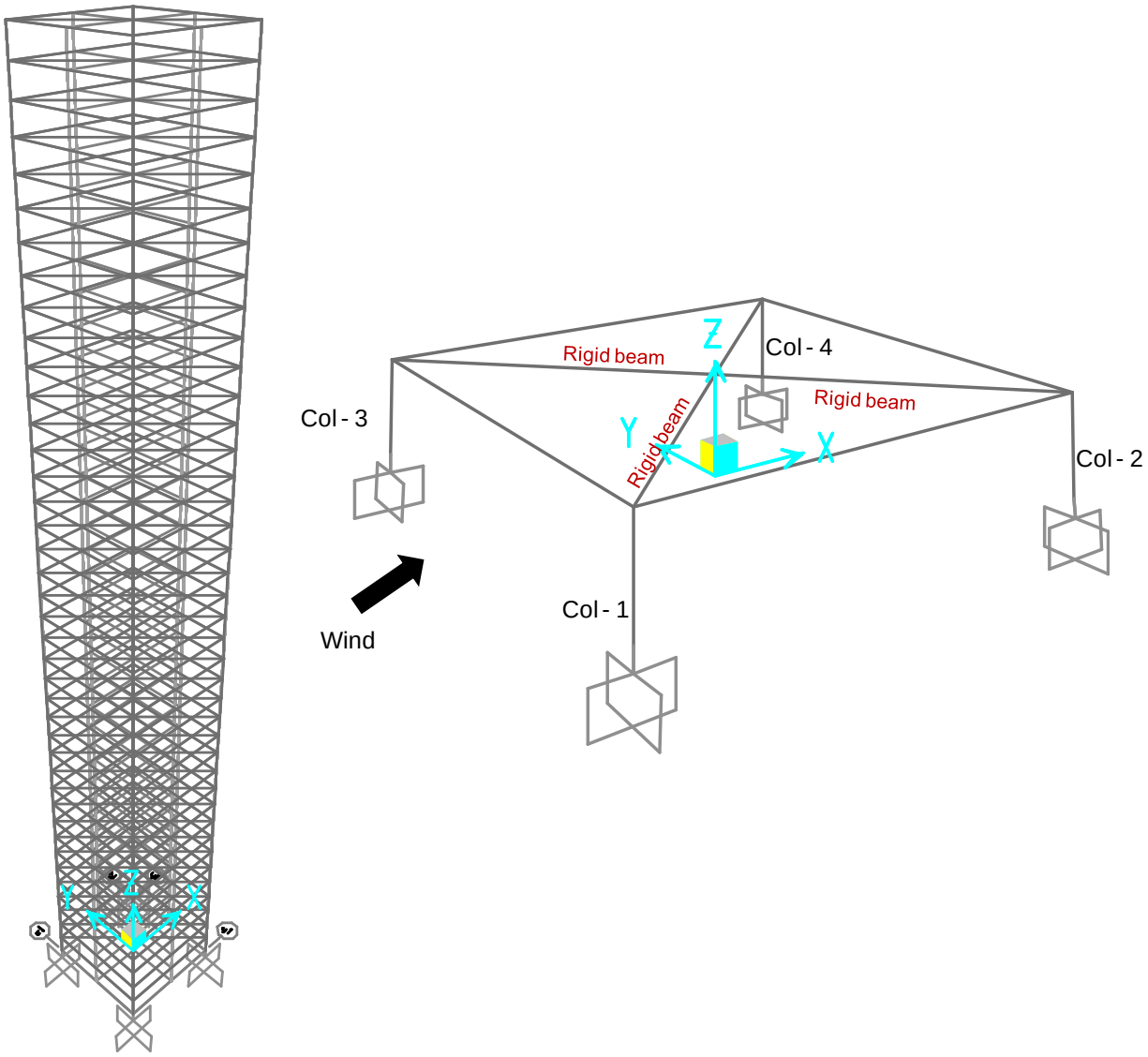

Figure 7.80 Frame model for Square model

7.3.1 *Effect of damping ratio on internal forces of columns*

Effects of damping ratios on internal forces of columns are investigated for the various models. There are 3 damping ratios were used for this study namely ζ = 0.3%, 1% and quasi-static (high damping).

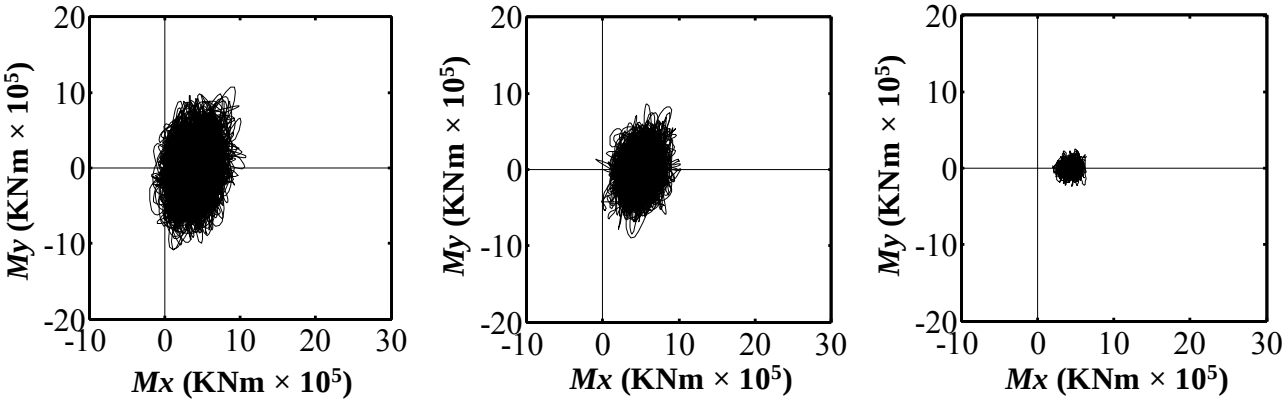

(a) ζ = 0.3% (b) ζ = 1% (c) Quasi-static

Figure 7.81 Effect of damping ratios on phase plane expression of internal forces for *ALL* loading condition (θ=0°) – Square model

7.3.2 *Effect of wind direction on peak tensile stress of columns for ALL loading conditions and damping ratio, ζ=1%*

The effects of wind direction on the peak normal stress of a square model are shown in Figure 7.82 for *ALL* loading condition and the damping ratio considered here, ζ=1%.

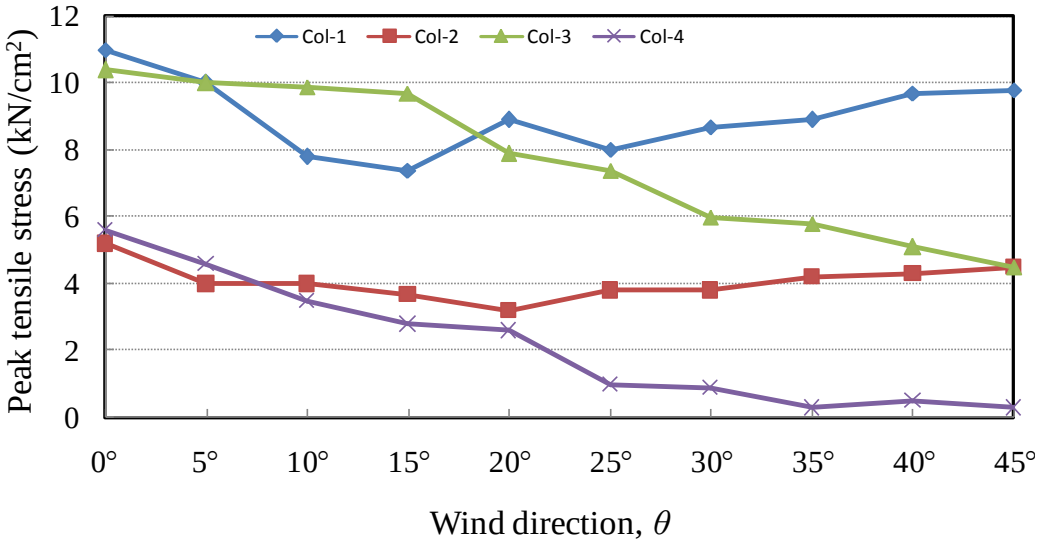

Figure 7.82 Effect of wind direction on peak tensile stress for *ALL* loading condition, and damping ratio, ζ=1% – Square model

ALL loading condition means that *Fx*, *Fy* and *Mz* were applied to the frame mode simultaneously. Peak tensile stresses generally decrease with increasing wind directions, and those of Col 1 and Col 3, which are located at the leading edges, show larger values than those of Col 2 and Col 4.The largest value is shown for wind direction θ=0^o for Col 1 and Col 3, showing nearly 11 kN/cm^2. When wind direction θ becomes 45^o, the peak normal stresses of Col 2 and Col 3 show similar values. The peak compressive stress show similar trends with wind direction, but the largest value is found for Col 2 and Col 4 for wind direction θ=0^o.

The effects of seven different loading conditions on peak tensile stresses are shown in Table 7.2 and 7.3 for quasi-static analysis and dynamic analysis respectively, with damping ratio, ζ=1% for wind direction θ=0^o. As expected, the results from dynamic response analysis are larger than those of quasi-static analysis, and the contribution of *Fx* is the largest, and that of *Mz* is the smallest. It seems that the effect of *Mz* can be ignored, because the peak tensile stresses from *ALL* loading condition and *Fx+Fy* are almost same. As the aspect ratio of the frame model is large, the increasing ratios for *Fy* and *Mz* are much larger than that for *Fx* when the resonant component is considered. For the only *Fx* condition, larger differences in Col 1 and Col 2 (or Col 3 and Col 4) are caused by the larger axial force. This means that the contribution of axial force is large in the frame model used in the present study.

Table 7.1 Effect of various loading conditions on peak tensile stress for quasi-static (wind direction of θ=0^o, kN/cm^2)

Peak tensile stress	*ALL* loading	Only *Fx*	Only *Fy*	Only *Mz*	*Fx+Fy*	*Fx+Mz*	*Fy+Mz*
Col 1	6.0	4.9	1.6	0.2	6.0	4.9	1.6
Col 2	0.6	-0.5	1.6	0.2	0.6	-0.5	1.6
Col 3	5.7	4.9	1.5	0.2	5.7	5.0	1.5
Col 4	0.4	-0.5	1.5	0.2	0.4	-0.5	1.5

Table 7.2 Effect of various loading conditions on peak tensile stress for ζ=1% (wind direction of θ=0^o, kN/cm^2)

Peak tensile stress	*ALL* loading	Only *Fx*	Only *Fy*	Only *Mz*	*Fx+Fy*	*Fx+Mz*	*Fy+Mz*
Col 1	11.0	7.3	6.3	0.4	11.0	7.4	6.3
Col 2	5.2	0.6	6.3	0.4	5.1	0.7	6.4
Col 3	10.4	7.3	6.4	0.4	10.4	7.4	6.5
Col 4	5.6	0.6	6.4	0.4	5.6	0.6	6.5

7.4 **Summary**

In this chapter, seventeen models with different cross-sections with twisting angle of 180^o were used to study the wind load combinations. The models are Triangular, Tri-Corner cut, Clover, Square, Pentagon, Hexagon, Octagon, Dodecagon, Circular, Tri-60^oHel, Tri-180^oHel, Tri-360^oHel, Sq-180^oHel, Penta-180^oHel, Hexa-180^oHel, Octa-180^oHel and Dodeca-180^oHel models.

Wind force combination in the super-tall buildings were discussed in terms of trajectories, correlation coefficient, absolute value correlation and simultaneously acting wind forces.

7.4.1 *Ratio of wind force coefficients to their maximum values when C_L, C_D and C_{MT} are maximum – Helical models*

	*CD*max		*CL*max		*CMT*max	
	CL (*CD*max)/ *CL*max	*CMT* (*CD*max)/ *CMT*max	*CD*(*CL*max)/ *CD*max	*CMT*(*CL*max)/ *CMT*max	*CD*(CMTmax)/ *CD*max	*CL*(*CMT*max)/ *CL*max
Tri-180^{o}Hel	0-60%	0-100%	40-80%	0-100%	40-90%	0-80%
Sq-180^{o}Hel	0-90%	0-90%	40-100%	0-100%	30-90%	0-80%
Penta-180^{o}Hel	0-90%	0-60%	40-100%	0-100%	40-90%	0-80%
Hexa-180^{o}Hel	0-40%	0-60%	40-100%	0-80%	40-90%	0-60%
Octa-180^{o}Hel	0-90%	0-70%	40-90%	0-50%	40-80%	0-40%
Dodeca-180^{o}Hel	0-50%	0-70%	40-90%	0-30%	40-100%	0-70%

Table 7.3 Ratio of wind force coefficients to their maximum values when C_L, C_D and C_{MT} are maximum – Helical models

7.5 **References**

1. Alberto Zasso, Aly Mousaad Aly, Lorenzo Rosa and Gisella Tomasini, Wind induced dynamics of a prismatic slender building with 1:3 rectangular sections, BBAA VI International Colloquium on Bluff-Bodies Aerodynamics & Applications, Milano, Italy, July, 20-24, 2008.

2. H.Tsukagoshi, Y.Tamura, A.Sasaki, H.Kanai, 1993, Response analyses on along-wind and across-wind vibrations of tall buildings in time domain, Journal of Wind Engineering and Industrial Aerodynamics, 46 & 47, 497-506.

3. S.T. Thoroddsen, J.A.Peterk and J.E. Cermak, 1998, Correlation of the components of wind-loading on tall buildings, Journal of Wind Engineering and Industrial Aerodynamics, 28, 351-360.

4. Yong Cgul Kim, Yukio Tamura, Akihito Yoshida 2013, Shielding effects on wind force correlations and quawi-static wind load combinations for low-rise building in large group, Journal of Wind Engineering and Industrial Aerodynamics, 112, 58-70.

5. Y.C.Kim and J.Kanda., 2008, The Structural Design of Tall and Special Buildings, 17, 683-718.

6. Y.Tamura, H.Kikuchi, K.Hibi, 2003, Quasi-static wind load combinations for low- and middle-rise buildings, Journal of Wind Engineering and Industrial Aerodynamics, 91, 1613-1625.

7. Y.Tamura, H.Kikuchi, K.Hibi, 2001, Extreme wind pressure distributions on low-rise building models, Journal of Wind Engineering and Industrial Aerodynamics, 89, 1635-1646.

Chapter VIII

CONCLUSIONS

A detailed comprehensive study of various cross-sectional shapes, various corner modifications, tapering and twisting effects on local peak pressures and wind forces have been carried out. Research developments in this area were analyzed.

Twenty six pressure models of super-tall buildings with various cross-sections including twisted models were tested in a boundary layer wind tunnel. The cross-sections of the configurations are triangular, square, pentagon, hexagon, octagon, dodecagon, circular, and clover. Primarily this study investigated the effect of corner modifications, tapering, number of surfaces and twisting angle on local peak pressures. Also studied the combined effect of corner modification, tapering and twisting on local peak pressures. Later we investigated the effect of increasing number of surfaces, corner modification (Tri-Corner cut model), surface modification (Clover model) and helical models on wind forces. The following are the main conclusions were derived based on the experimental study.

8.1 Chapter II

It discusses about the effect of various polygonal shapes, corner modification, tapering on local peak pressures.

For the models Triangular, Tri-Corner cut, Clover, Square, Sq-Corner cut, Sq-Chamfered model, the $\check{C}_P(i)$ occurred at the corner regions. For Sq-Tapered model, the $\check{C}_P(i)$ occurred even at the center of the surface at around 0.5*H* to 0.6*H* whereas for Sq-Setback model, the $\check{C}_P(i)$ occurred upper side corners of each step. The maximum of $\check{C}_P$ occurred for Triangular model among all the straight polygonal models.

For all the models, the $\hat{C}_P(i)$ values vary very smoothly for all the models. The largest negative peak ($\check{C}_P(i)$) occurs at the corner cut portion for both Tri-Corner cut and Sq-Corner cut models at 0.85*H*. The maximum largest negative peak pressure coefficient ($\check{C}_{p,\max}$) for the Tri-Corner cut model is less than that for the Triangular model whereas for the Sq-Corner cut model is greater than that for the square model. The distribution of $\hat{C}_P(i)$ is smooth for all the straight models whereas for the Sq-Setback model it varies widely and the peak suctions occur at all the corners of each set-back step, and $\check{C}_{p,\max}$ of the Square model is around 88% that of the Sq-Setback model.

The overall trend of $\check{C}_{p,\max}$ is reducing from Triangular model to Circular model. When the number of surfaces increases (polygonal models), $\check{C}_{p,\max}$ decreases.

8.2 Chapter III

It discusses about the effect of various helical models of polygonal shapes on local peak pressures.

For helical models, the distribution of $\check{C}_P(i)$ varies widely and peak suctions occurred at the corners and even on the surfaces, but the area occupied by the peak suctions is very limited comparatively with the straight polygon models. When the twisting angle of helical model increases, the $\check{C}_P(i)$ value and height at which it occurs also increases for both Triangular (Tri-60^{o}Hel, Tri-180^{o}Hel and Tri-360^{o}Hel) and Square cross-sectional models (Sq-90^{o}Hel and Sq-180^{o}Hel). Helical models of polygonal models with 180^o twisting, the trend of $\check{C}_{p,\max}$ is same as straight polygonal models. The variation of $\check{C}_P(i)$ between upper and lower levels decreases as the number of surfaces increases for the polygonal helical models.

The $\hat{C}_P(i)$ values are very smooth for Square, Squ-90^{o}Hel, Squ-180^{o}Hel models than Triangular, Tri-60^{o}Hel, Tri-180^{o}Hel and Tri-360^{o}Hel models.

When the number of surfaces increases (polygonal 180^o helical models from Triangular to Circular model), $\check{C}_{p,\max}$ decreases as in the case of polygonal straight models.

8.3 **Chapter IV**

It discusses about the effect of four types of composite models. The combinations of twisting with corner cut, taper with twisting, taper with corner cut and twisting and setback with rotation were considered. The composite models with various twisting angles were considered to investigate the effect of combination effect on local peak pressure coefficients.

Among all the combination models, the helical and corner cut combination shows much reduction in $\check{C}_{p,\max}$ than that for the Square model.

Among all the combination models, the Setback & 45^{o}Rotate model has the highest value of $\check{C}_{p,\max}$, but the distribution of $\check{C}_P(i)$ looks the same as that of the Sq-Setback

model. $\hat{C}_{p,\max}$ for the Setback model is just 5% less than that of the Setback & 45^{o}Rotate model.

There is significant effect of corner cut with twisting angle of 180^o on the $\hat{C}_{p,\max}$ value. The $\hat{C}_{p,\max}$ value of Sq-180^{o}Hel & Corner cut model is around 22% less than that of Squ-Corner cut model.

Also there is significant effect of twisting the taper model to 180^o, the $\hat{C}_{p,\max}$ value is increases more than around 25% than that of Squ-Taper model. The combination of corner cut with twisting has more effect on $\hat{C}_{p,\max}$ value than tapered with twisting.

8.4 **Chapter V**

It discusses about the effect of, various polygonal and corner modification models on wind forces. The models analyzed in this chapter are Triangular, Tri-Corner cut, Clover, Square, Pentagon, Hexagon, Octagon, Dodecagon and Circular models which are shown in Table 5.1-5.2.

The maximum mean and fluctuating over turning moment coefficients becomes decreasing as the number of surfaces increases for the straight polygonal models (Triangular to Circular models) in both along-wind and crosswind directions.

Maximum peak of crosswind overturning moment (fS_{CML}) reduces as the number of surfaces increases for straight polygonal models, but the maximum peak shows for Square model than all other models. The peak of Power spectral densities of crosswind local wind force coefficients (fS_{CfL}) decreases for the polygonal models as the number of surfaces increases except for Pentagon model. The peak also shifts to higher reduced frequency ranges for the polygonal models as the number of surfaces increases.

The peak of fS_{CfL} increases for the Tri-Corner cut and Clover models than the Triangular model.

8.5 **Chapter VI**

It discusses about the effect of various polygonal helical models with different twisting angles on wind forces. The models analyzed in this chapter are Tri-60^{o}Hel, Tri-180^{o}Hel, Tri-360^{o}Hel, Penta-180^{o}Hel, Hexa-180^{o}Hel, Octa-180^{o}Hel and Dodeca-180^{o}Hel models which are shown in Table 6.1.

The maximum mean and fluctuating over turning moment coefficients becomes decreasing as the number of surfaces increases for the polygonal helical models (Triangular to Circular models) in both along-wind and crosswind directions as in the case of straight polygonal models discussed in Chapter V. If the twisting angle increases (60^o to 360^o for triangular model) we found more reduction in maximum mean and fluctuating overturning moment coefficients in both along-wind and cross wind directions. Maximum fluctuating overturning moment coefficients in crosswind direction is almost constant in both along-wind and crosswind directions for the Pent-180^{o}Hel, Hexa-180^{o}Hel, Octa-180^{o}Hel, Dodeca-180^{o}Hel and Circular models. The polygonal models with twist angle 180^o don't show much effect on crosswind fluctuating overturning moment coefficients.

Maximum peak of crosswind overturning moment (fS_{CML}) and its band width reduces as the twisting angle of helical model increases (60^o to 360^o for triangular model). We found very little difference in fS_{CML} peak for the polygonal helical models with 180^o twisting. The peak of Power spectral densities of crosswind local wind force coefficients (fS_{CfL}) decreases for the polygonal helical models as in the case of straight polygonal models discussed in Chapter V. The peak also shifts to higher reduced frequency ranges for the polygonal models as the number of surfaces increases.

The peak of Power spectral densities of crosswind local wind force coefficients (fS_{CfL}) found same trend as straight polygonal models discussed in Chapter V, but the peak reduces for polygonal helical models than the straight polygonal models.

8.6 **Chapter VII**

It discusses about the wind load combination and its importance. The trajectories of overturning moment coefficients, simultaneous wind loading, correlation coefficient and

absolute value correlation discussions are made for super-tall building models with various cross-sectional shapes and helical models. It is understood from the trajectories, that for combination the absolute value correlation is more important than the ordinary correlation. Also the shape of the trajectory shows the characteristics of the combination.

For Square model, peak normal stresses in columns show the largest values when wind direction of $\theta=0^{o}$, and decrease with increasing wind directions. The contribution of *Fx* to peak normal stress is the largest, and the effect of *Mz* seems to be negligible. The ration of *ALL*/*Only Fx* is small discrepancies between quasi-static analysis and for dynamic analysis. And it was found that as the damping ratio decreases, the effect of *Fy* increase significantly.

Appendix

COMPARISON OF PEAK PRESSURES AND WIND FORCES

Since the local peak pressures are very important for cladding design, we compared the largest negative and largest positive peak pressure coefficients of all models. And also we made the comparison of wind force coefficients of all models of the present study with the models of previous studies (Tanaka et.al., 2012)

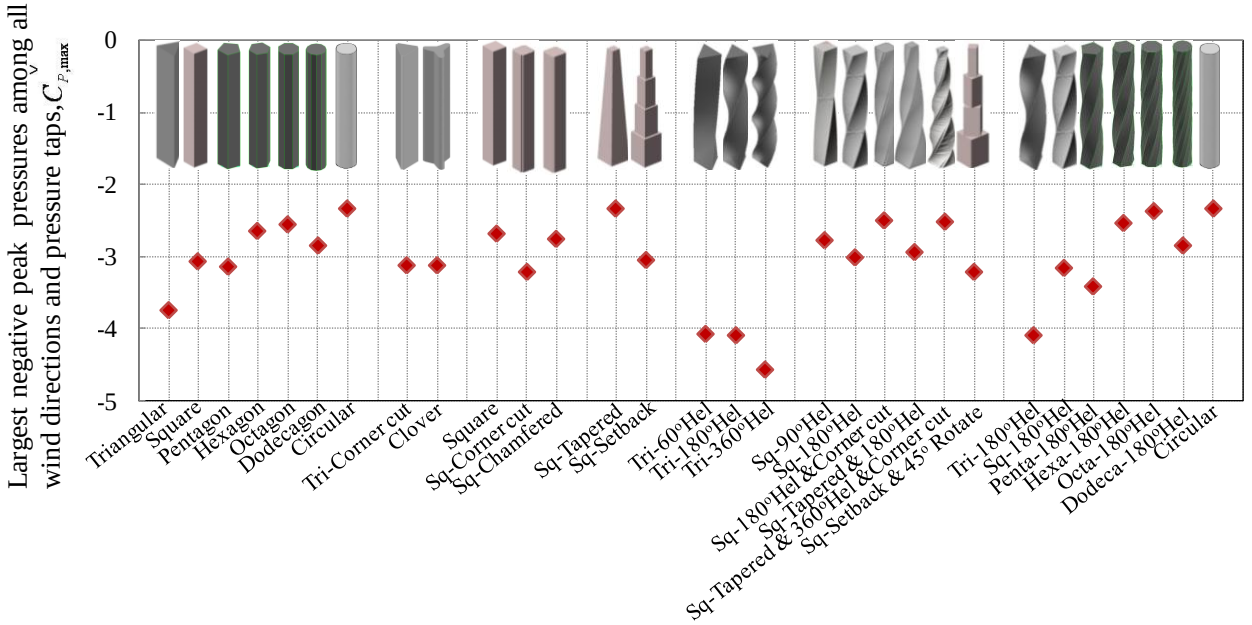

Figure A.1 Largest negative peak ($C_{p,\max}^{\vee}$) among all wind directions and all pressure taps of all the models

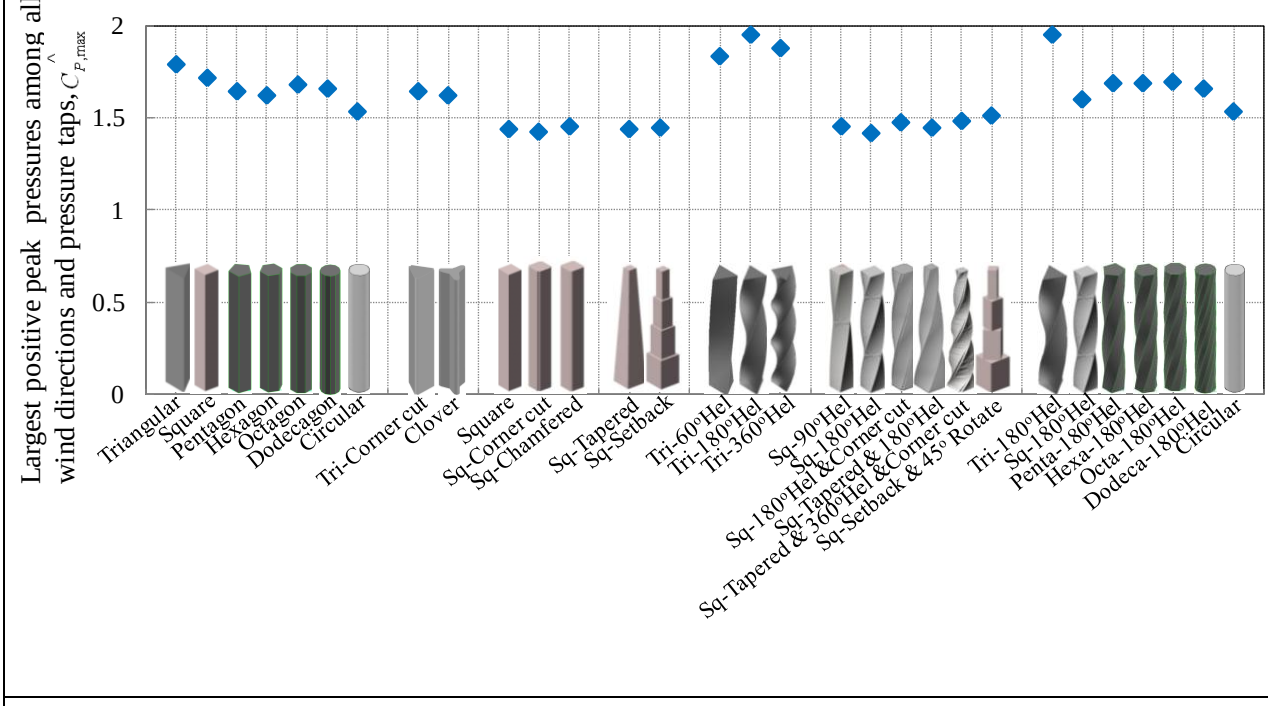

Figure A.2 Largest positive peak ($C_{p,\max}^{\wedge}$) among all wind directions and all pressure taps of all the models

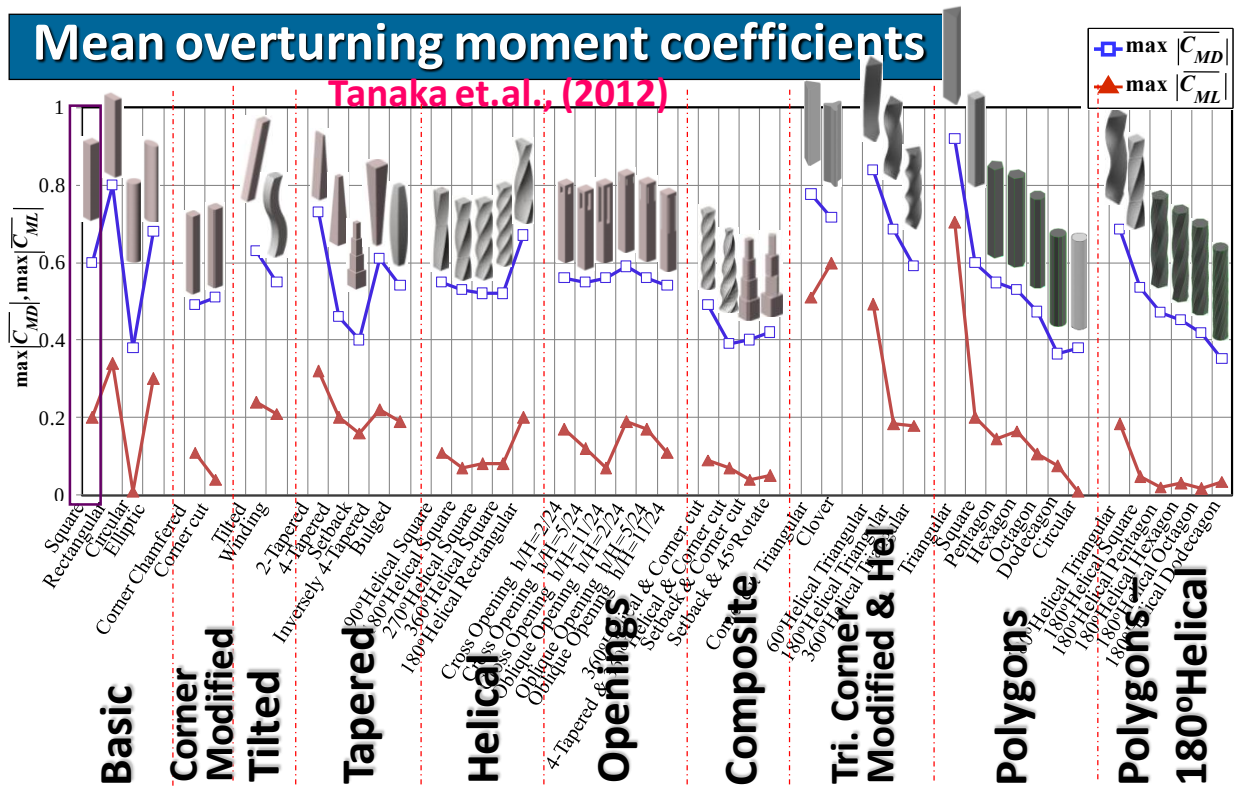

Figure A.3 Comparison of mean overturning moment coefficients among all wind directions of all models

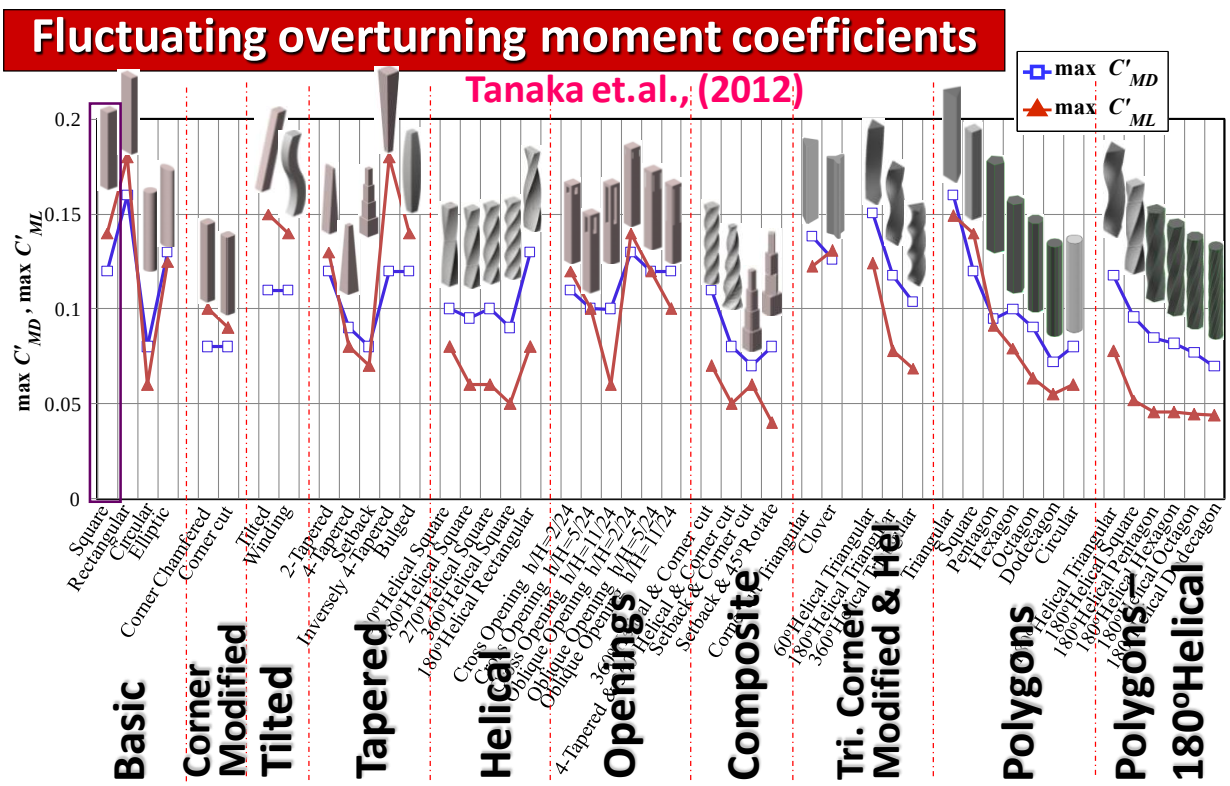

Figure A.4 Comparison of fluctuating overturning moment coefficients among all wind directions of all models

PUBLICATIONS

A. Journal Papers Published

1. Eswara Kumar Bandi, Yukio Tamura, Akihito Yoshida, Yong Chul Kim, Q. Yang, 2013, Experimental investigation on aerodynamic characteristics of various triangular-section high-rise buildings, Journal of Wind Engineering and Industrial Aerodynamics.
2. Eswara Kumar Bandi, Hideyuki Tanaka, Yong Chul Kim, Kazuo Ohtake, Akihito Yoshida, Yukio Tamura(2013), Peak pressures acting on tall buildings with various configurations, International Journal of High-Rise Buildings, September 2013, Vol2, No 3, 229-244.

B. Conference Proceedings/Symposiums

1. Eswara Kumar Bandi, Yukio Tamura, Akihito Yoshida, Yong Chul Kim, Qingshan Yang, 2012, *Local and total wind force characteristics of triangular-section tall buildings*, The 22nd National Symposium on Wind Engineering, Tokyo, Japan.

2. Eswara Kumar Bandi, Yong Chul Kim, Akihito Yoshida, Yukio Tamura, 2011, *Aerodynamic characteristics of triangular-section tall buildings with different helical angles* , International Conference on Wind Engineering (ICWE13) held at Amsterdam, The Nederlands

3. Akihito Yoshida, Eswara Kumar Bandi, Yukio Tamura, Yong Chul Kim, Qingshan Yang, 2012, *Experimental investigation on aerodynamic characteristics of various triangular-section high-rise buildings*, Bluff Body Aerodynamics (BBAA7), Shanghai, China.

4. Yong Chul Kim, Yukio Tamura, Hideyuki Tanaka, Kazuo Ohtake, Bandi Eswara Kumar, Akihito Yoshida, 2013, *Aerodynamic characteristics of tall buildings with*

unconventional configurations, 12th Americas Conference on Wind Engineering (12th ACWE), Seattel, Washington, USA.

5. Yukio Tamura, Yong Chul Kim, Bandi Eswara Kumar, Hideyuki Tanaka, Kazuo Ohtake, 2012, *Aerodynamic characteristics of Tall Building Models with Unconventional Configurations*, Structures Congress, USA.

.